2013

Laser Vaporization Methods for the Synthesis of Metal and Semiconductor Nanoparticles; Graphene, Doped Graphene and Nanoparticles Supported on Graphene

Parichehr Afshani
Virginia Commonwealth University

Laser Vaporization Methods for the Synthesis of Metal and Semiconductor Nanoparticles; Graphene, Doped Graphene and Nanoparticles Supported on Graphene

A dissertation submitted in partial fulfillment of the requirements for the degree of doctor of philosophy at Virginia Commonwealth University

by

Parichehr Afshani
M.S., University of Shahid Beheshti, Tehran, Iran, 1996
B.S., Araak University, Araak, Iran, 1993

Director: M. Samy El-Shall
Professor, Department of Chemistry

Virginia Commonwealth University
Richmond, Virginia
October, 2013

This dissertation is dedicated to my husband:

Mohammad Reza Hajaligol

for his constant support and unconditional love

Acknowledgments

I would like to express my deepest gratitude to my advisor Professor El-Shall for his excellent guidance, care, and patience as well as providing me with a challenging atmosphere to do research. Without his guidance and persistent help, this dissertation would not have been possible.

My special appreciation goes to my committee members for their time, interest, support, and helpful comments. Special thanks go to Dr. James Terner who had spent his precious time helping me to get Raman data and to Dr. Sally Hunnicutt who always responded me with a smile, encouraged my passion for teaching, and provided me with valuable comments on my thesis. I would like to thank Drs. Frank Gupton and Kenneth Wynne who kindly accepted to be part of my research committee. I would also like to express my special gratitude to Dr. Ali Siamaki who performed Suzuki reaction for my catalyst samples in Dr. Gupton laboratory.

It has been a great pleasure working with my group mates for the last several years. I am grateful to Dr. Sherif Moussa for all his assistance and advice, especially for XPS measurements of this work and for directing semiconductors nanoparticles on graphene project. Mr. Jason Wright did most of the experimental work for semiconductors nanoparticles on graphene project (using LVSC and MW) and I greatly appreciate his contributions. My special gratitude goes to Dr. L.S. Panchakarla, for his contribution to heteroatoms doping project and electrochemical measurement of the doped graphene samples. I would also like to thank Mr. Minh Ho for conducting some of electrochemical measurements. I am grateful to Dr. Khaled AbouZeid who was always willing to help me in any way possible. Many thanks go to others who worked in Dr. El-Shall's laboratory; my research would not have been possible without their help.

The financial support of the National Science Foundation (CHE-0911146) for this work is acknowledged. I would also like to acknowledge the financial, academic, and technical support of Virginia Commonwealth University, Chemistry Department and their staff.

Last but not least, I would like to thank my family: my dearly loved parents, two younger sisters, and two brothers for their support, encouragement, and best wishes. In particular, I would never have been able to carry out my doctoral study without the unconditional support of my beloved husband, Mohammad Hajaligol. He has always been there cheering me up and standing by me through the good times and bad. My deepest appreciation is expressed to him for his love, understanding, and inspiration. Without my husband and my little precious daughter (Kiana) blessings, sacrifices and encouragements, I would not have been able to complete my dissertation.

Table of Contents

List of Figures

List of Tables

List of Abbreviations

2-D	2-Dimensional
AN	Acetonitrile
ASPL	Anti-stock photoluminescence
B	Boron
BG	Boron doped graphene
BG-150	150 Torr B_2H_6 in He
BG-300	300 Torr B_2H_6 in He
BG-400	400 Torr B_2H_6 in He
BNG	Boron nitrogen doped graphene
CNT	Carbon nano-tube
CNT	Classical nucleation theory
CO	Carbon monoxide
CV	Cyclic voltammetry
CVD	Chemical vapor deposition
DC	Direct current
FRGO	Functionalized reduced graphene oxide
FTIR	Fourier transform infrared spectroscopy
FWHM	Full width half maximum
G	Graphene

GCE	Glassy carbon electrode
GO	Graphite oxide
GQDs	Graphene quantum dots
HOMO	Highest occupied molecular orbital
HOPG	Highly ordered pyrolytic graphite
HTG	Hydrogen terminated graphene
LUMO	Lowest unoccupied molecular orbital
LVCC	Laser vaporization control condensation
LVSC	Laser vaporization solvent capturing
N	Nitrogen
Nd-YAG	Neodymium-doped yttrium aluminum garnet
NG	Nitrogen doped graphene
N-GQDs	Nitrogen graphene quantum dots
OLED	Organic light-emitting diodes
PL	Photoluminescence
PPA	Propargylamine
RGO	Reduced graphene oxide
SEM	Scanning electron microscopy
TEM	Transmission electron microscopy
TGA	Thermal gravimetric analysis
THF	Tetrahydrofuran
XPS	X-ray photoelectron spectroscopy
XRD	X-ray diffraction

ZGNR	Zigzag graphene nanoribbon

Abstract

LASER VAPORIZATION METHODS FOR THE SYNTHESIS OF METAL AND SEMICONDUCTOR NANOPARTICLES; GRAPHENE, DOPED GRAPHENE AND NANOPARTICLES SUPPORTED ON GRAPHENE

By: Parichehr Afshani

A dissertation submitted in partial fulfillment of the requirements for the degree of Doctor of philosophy at Virginia Commonwealth University

Director: M. Samy El-Shall, Professor, Department of Chemistry

The major objective of the research described in this dissertation is the development of new laser vaporization methods for the synthesis of metal and semiconductor nanoparticles, graphene, B- and N-doped graphene, and metal and semiconductor nanoparticles supported on graphene. These methods include the Laser Vaporization Controlled Condensation (LVCC) approach, which has been used in this work for the synthesis of: (1) gold nanoparticles supported on ceria and zirconia nanoparticles for the low temperature oxidation of carbon monoxide, and (2) graphene, boron- and nitrogen-doped graphene, hydrogen-terminated graphene (HTG), metal nanoparticles supported on graphene, and graphene quantum dots.

The gold nanoparticles supported on ceria prepared by the LVCC method exhibit high activity for CO oxidation with a 100% conversion of CO to CO_2 at about 60 °C. The first application of the LVCC method for the synthesis of these graphene and graphene-based nanomaterials is reported in this dissertation. Complete characterizations of the graphene-based nanomaterials using a variety of techniques including spectroscopic, X-ray diffraction, mass spectrometric and microscopic methods such as Raman, FTIR, UV-Vis, PL, XRD, XPS, TOF-MS, and TEM. The application of B- and N-doped graphene as catalysts for the oxygen reduction reaction in fuel cell applications is reported. The application of Pd nanoparticles

supported on graphene for the Suzuki carbon-carbon cross-coupling reaction is reported. A new method is described for the synthesis of graphene quantum dots based on the combination of the LVCC method with oxidation/reduction sequences in solution. The N-doped graphene quantum dots emit strong blue luminescence, which can be tuned to produce different emission colors that could be used in biomedical imagining and other optoelectronic applications.

The second method used in the research described in this dissertation is based on the Laser Vaporization Solvent Capturing (LVSC) approach, which has been introduced and developed, for the first time, for the synthesis of solvent-capped semiconductor and metal oxide nanoparticles. The method has been demonstrated for the synthesis of V, Mo, and W oxide nanoparticles capped by different solvent molecules such as acetonitrile and methanol. The LVSC method has also been applied for the synthesis of Si nanocrystals capped by acetonitrile clusters. The acetonitrile-capped Si nanocrystals exhibit strong emissions, which depend on the excitation wavelength and indicate the presence of Si quantum dots with different sizes. The Si and the metal oxide nanoparticles prepared by the LVSC method have been incorporated into graphene in order to synthesize graphene nanosheets with tunable properties depending on graphene-nanoparticle interactions.

Chapter 1: Introduction

1.1 Nanoparticles by Laser Vaporization

It is now well established that nanoparticles (1-100 nm) exhibit unique chemical and physical properties that differ from those of the corresponding bulk materials. Semiconductor nanoparticles from ~1 to ~10 nm in diameter are often called quantum dots, nanoparticles, or Q-particles. In this size regime, the particles possess short-range structures that are essentially the same as the bulk semiconductors, yet have optical and/or electronics properties that are dramatically different from the bulk. The confinement of electrons within a semiconductor nanocrystal results in the shift of the band gap to higher energy with smaller crystalline size. This effect is known as the quantum size effect. In the strong confinement regime, the actual size of the semiconductor particle determines the allowed energy levels and thus the optical and electronic properties of the material.[1]

Owing to their finite small size and the high surface-to-volume ratio, nanoparticles often exhibit novel and sometimes unique properties. The characterization of these properties can ultimately lead to identification of many potential uses and applications including catalysis, ceramics, microelectronics, sensors, pigments, and biomedical The application of nanoparticles are thus expected to enhance many fields of advanced technology particularly in the case of catalysis, chemical and biological sensors, optoelectronics, drug delivery, and media storage.[1]

A wide range of scientifically interesting and technologically important nanoparticles have been produced by both chemical and physical methods. The synthesis of nanocrystals by colloidal methods involves nucleation (the initial formation of the appropriate semiconductor bond), growth (the formation of a highly crystalline core), and passivation of the nanocrystal surface. The passivation step is important in stabilizing the colloid and controlling the growth of the nanoparticles, preventing the agglomeration and fusing of the particles, and allowing the solubility of the nanoparticles in common solvents.[1]

The formation of nanoparticles from the vapor phase involves creating a supersaturation condition. This condition is created where the vapor phase mixture is thermodynamically metastable relative to formation of the solid material to be prepared in nano-particulate form. Nuclei are expected to form homogeneously if the degree of supersaturation is sufficient to permit condensation. This condition occurs via physical and/or chemical means. Physical methods require some form of cooling of the vapor molecules either by expansion, mixing with a cooler gas, or heat transfer to the surroundings. Once nucleation occurs, remaining supersaturation can be relieved by condensation or reaction of the vapor molecules on the resulting nucleus and particle growth will occur rather than further nucleation. Therefore, to prepare smaller nanoparticles, one may create a high degree of supersaturation where the condensation nuclei can be very small, and preventing the particle growth by immediately quenching the system. The system can be quenched by either removing the source of supersaturation or slowing the kinetics down. In most cases, this process takes place rapidly (e.g., in the orders of milliseconds) in a relatively uncontrolled fashion, and presents itself as a quasi-continuous operation.[2]

Once nanoparticles are formed in the gas phase, they can coagulate to form larger particles. The coagulation rate is proportional to the square of nanoparticles number concentration but a weak function of particle size. The control of coagulation is crucial where individual non-agglomerated nanoparticles are desired. At sufficiently high temperatures, particles coalesce (sinter) faster than they coagulate, and spherical particles are produced. At lower temperatures, where coalescence is almost absent, loose agglomerates with quite open structures are formed. At intermediate temperatures, partially sintered non-spherical particles are produced. The nanoparticles agglomeration in gas phase always occurs, which is in contrast to the liquid phase where a dispersion of nanoparticles can be stabilized indefinitely by capping the particles with appropriate ligands.[2]

Various heating and evaporation methods are used to achieve the required supersaturation for inducing nucleation. After vaporizing a material into a background gas, rapid cooling processes become especially important when very small particles are desired and the formation of hard agglomerates has to be avoided. There are various methods for gas phase synthesis of nanoparticles that are principally based on the source of energy and the phase of precursor.[3]

Perhaps the most straightforward method of achieving supersaturation is to heat a solid and evaporate it into a background gas; then, mix the vapor with a cold gas usually helium or argon to reduce the temperature. This method is suited for production of some metal nanoparticles where metals can evaporate at reasonable rates and attainable temperatures. By including a reactive gas such as oxygen in the gas stream, oxides or other compounds of the evaporated material can be prepared.[4] Rather than steadily evaporating a material to produce a supersaturated vapor, one may use a pulsed laser to instantly vaporize a plume of material that is both dense and confined spatially. This method can generally only produce small amounts of

nanoparticles. However, laser ablation can vaporize materials that cannot readily be evaporated. Another means of vaporizing metals is to charge electrodes made of the metal to be vaporized in the presence of an inert background gas until the breakdown voltage is reached. The arc (spark) formed across the electrodes vaporizes a small amount of metal to form a plasma, which produces a very small amount of nanoparticles.[5] Another means for vaporizing a solid at low pressure is sputtering. Sputtering vaporizes materials from a solid surface by bombardment with high velocity ions of an inert gas, causing an ejection of atoms and clusters.[6]

Alternative to physical methods in achieving a required supersaturation is chemical methods. Chemical precursors are heated and/or mixed to induce gas phase reactions that produce a state of supersaturation in the gas phase. In chemical vapor synthesis, vapor phase precursors are brought into a hot-wall reactor under conditions that favor nucleation of particles in the vapor phase and prevent deposition of a film on the wall. This method has remarkable flexibility in producing a wide range of materials and can take advantage of the huge database of precursor chemistries that have been developed for chemical vapor deposition (CVD) processes. The precursors can be solid, liquid or gas at ambient conditions, but are delivered to the reactor as a vapor. For instance, a two-stage reactor was successfully used for producing high quality oxide-coated silicon nanoparticles.[7] In spray pyrolysis or aerosol decomposition synthesis, a nebulizer directly injects a small amount of fine droplets of precursor solution into a hot reactor to form a vapor.[8] In the laser pyrolysis method, a portion of gas is heated using an infrared (CO_2) laser. The source molecules are heated by absorption of the laser beam energy. This method allows highly localized heating and rapid cooling when mixed with the inert surrounding gases. A gas phase decomposition of the reactants takes place due to the temperature increase and leading to the formation of a supersaturation condition.[9]

There is yet another approach that combines both chemical and physical methods to create supersaturation and form nanoparticles, which is called thermal plasma synthesis. In this method the precursors are injected into the thermal plasma and nanoparticles are formed upon cooling while exiting the plasma region. As a result of both heat and decomposition, atoms and molecules are produced, which then react or condense to form nanoparticles when cooled by mixing with a cold inert gas flow.[9] The required heat for the synthesis of particles is produced in situ by the combustion reactions within a flame such as synthesis of carbon black and metal oxide.[10] If liquid is directly sprayed into the flame instead of injecting vapor, it is called flame spray pyrolysis.[11] In low temperature reactive synthesis, the heat of reaction is expected to be high enough to allow the vapor phase to directly react without external heat. An example of such synthesis is preparing nanoparticles such as ZnSe from dimethylzinc-trimethyamine and hydrogen selenide.[12]

Laser vaporization provides several advantages over other heating methods including the production of a high density vapor of material, generation of a directional high speed vapor from the solid target that can be useful for directional deposition of the particles, control of the evaporation from specific spots on the target, and the simultaneous or sequential evaporation of several different targets. [13] In 1994, El-Shall group introduced a novel technique called laser vaporization controlled condensation (LVCC) to synthesize nanoparticles of controlled size and composition.[1] The further advantage of pulsed laser vaporization with controlled condensation (LVCC) over other laser employed methods is in generating a diffusion cloud chamber under well-defined conditions of temperatures and pressures. The LVCC method has been successfully used for the preparation of a variety of supported and unsupported metallic and bimetallic nanoparticle such as Au on different oxide support of CeO_2, Al_2O_3, and SiO_2.[1, 14-42]

In laser vaporization, a high energy pulsed laser with an intensity flux of about 10^6-10^7 W/cm^2 is focused on a metal target of interest. The resulting plasma causes highly efficient vaporization, and the temperature at the focusing spot can exceed 10,000 K. This high intensity heating can vaporize all known substances quickly while the surrounding gas stays at an ambient temperature. Typical yields are 10^{14}-10^{15} atoms from a surface area of 0.01 cm^2 for a 10^{-8} s pulse. The local atomic vapor density can exceed 10^{18} atoms/cm^3 (equivalent to 100 Torr) for a microsecond following the laser pulse. Laser vaporization provides several advantages as an approach for producing nanoparticles including production of a high density vapor of any metal or metal oxide within an extremely short time (10^{-8} s) and generation of a directional, high speed, vapor stream from the solid targets. The limitation of this approach includes the difficulty in scaling up production and the cost of the produced nanoparticles.

The foundation of the gas phase synthesis of nanostructured materials is the generation of gas-born nanosized "embryos." In gas phase synthesis of nanoparticles, conditions are created such that the vapor phase is thermodynamically metastable in relation to the formation of the material to be produced in nanosized particulate form. This condition includes the typical condition of a supersaturated vapor. Nucleation of new particles from a continuous phase can occur either homogeneously or heterogeneously. Homogeneous and heterogeneous nucleations are a non-equilibrium process of a stable phase formation from an unstable or a meta-stable phase. Most synthesis methods of pure nanoparticles from the gas phase are based on homogeneous nucleation in the gas phase with subsequent condensation and coagulation.

The formation of nanostructure in this work is based on both homogeneous nucleation and heterogeneous. Thus, it is essential to briefly cover the principles of both nucleations before describing nanoparticles syntheses of interest in the gas phase.

1.2 Homogenous Nucleation

The ability to predict the onset of nucleation is important for a wide variety of first order phase transitions from industrial crystallization to gas-phase nanoparticle formation. There are various systems that can be held in a supersaturated state for significant periods of time before a phase transition occurs. Distilled water can be held indefinitely at -10 ºC without freezing, and with further purification it can be cooled to -30 ºC without freezing. Theoretically, homogeneous nucleation can occur in the absence of any foreign object in a system where the vapor atoms or molecules condense to form embryonic nuclei or clusters. The creation of a nucleus implies the formation of an interface at the boundaries of a new phase. There are various theories and models to describe the formation of this interface, which have been developed over the years.[43-45] The most well-known theory, called classical nucleation theory (CNT), is based on the assumption that embryonic nucleus of the new phase can be described as spherical liquid particles with the bulk liquid density inside and the vapor density outside.[1] For homogeneous nucleation, classical nucleation theory suggests that the free energy of a nucleus at first increases with the nucleus size until a maximum is reached at a size called nucleus critical size, and then the free energy monotonically decreases. As a result, the rate of homogeneous nucleation is determined by the rate of formation of nuclei, which maximize the free energy with respect to nuclei radius. After a nucleus reaches this critical radius, further growth becomes energetically favorable. For a single component system, this maximum in free energy arises from the contributions from the surface and the bulk contributions. Therefore, the phase transition occurs if a nucleus exceeds the critical size and overcomes the nucleation free energy barrier due to the competition between the surface and bulk free energies.[2] The free energy of these nuclei, relative to the vapor, can be described by ΔG given in Equation 1,

$$\Delta G = \gamma A + \Delta g V \quad (1)$$

where the first term is the contribution of surface energy with γ representing the surface tension (surface excess free energy) and A the surface area of the nucleus. The second term is the free energy difference between the supersaturation and bulk states, where Δg is the difference per unit volume and V volume of the nucleus. As discussed above, a nucleus has a spherical shape with $A=4\pi r^2$ and $V=(4/3)\pi r^3$, where r is the radius of the nucleus.[46] The surface free energy results from the reversible work in forming the interface between the liquid droplet and vapor; and for a nucleus containing n atoms or molecules the interface energy is given by Equation 2,

$$\sigma A(n)=4\sigma\pi(3\upsilon/4\pi)^{2/3}n^{2/3} \quad (2)$$

where σ is the interfacial tension or surface free energy per unit area, A(n) is the surface area of the nucleus, and υ is the volume per molecule in the bulk liquid. Because n molecules are transferred from the vapor to the nucleus, the bulk contribution to the free energy of formation is $n(\mu_l-\mu_\upsilon)$ where μ_l and μ_υ are the chemical potentials in the bulk liquid and vapor, respectively. Assuming a supersaturated ideal vapor, then it can be written,

$$n(\mu_l-\mu_\upsilon) = -nk_BT\ln S \quad (3)$$

where k_B is the Boltzmann constant, T is temperature, and S is supersaturation defined by Equation 4,

$$S=P/P_e \quad (4)$$

where P and P_e are vapor pressure and equilibrium (or saturation) vapor pressure of the condensing material at a given operating temperature. Supersaturation (S) can be increased by increasing P or deceasing P_e. The vapor pressure P can be increased by increasing the rate at

which atoms are placed in the vapor or decreasing the rate at which they leave the region where the particle nucleation and growth is occurring. The saturation pressure P_e can be decreased by decreasing T since P_e is approximately given by Equation 5

$$P_e=P_0e^{-L(0)/RT} \tag{5}$$

where the latent heat per mole has been approximated by its zero-temperature value L(0), P_0 is a constant , and R is the universal gas constant. The sum of the contributions in Equations 1 and 2 is the reversible work, W(n), for the formation of a nucleus containing n molecules, and it is given by

$$W(n)=-nK_BTLnS+4\sigma\pi(3\upsilon/4\ \pi\ )^{2/3}n^{2/3} \tag{6}$$

Equation 6 expresses the competition between "bulk" and "surface" behavior in determining nucleus stability and, ultimately, nucleus concentration in the supersaturated vapor. For a saturated vapor S = 1, the bulk contribution vanishes and W(n) becomes proportional to $n^{2/3}$.

Because of the many impractical assumptions of classical nucleation theory (CNT), it has limited applicability to the solution of many practical problems when compared with experimental work. One set of limitations arise mainly because CNT assumes that macroscopic properties of molecules can be applied to the microscopic behavior. This can be a major drawback when dealing with characteristics such as density, surface tension, and saturated vapor pressure of clusters consisting of only several tens of molecules. Classical nucleation theory also does not take into account the interaction of molecules around the nuclei. In situations where the size of critical nucleus is very small (often 20-50 molecules), or the molecules are polar, classical nucleation approach also fails. In latter cases, the sharp curvature of the surface will have a

significant effect on the interfacial energy and thus, the structure and corresponding energy of the nucleus may be significantly different from the bulk of the new phase.

The most widely applied advancement to the classical approach has been the use of Density Functional Theory (DFT). The density functional approach assumes that the free energy of the nucleus, ΔG, depends on the average spherical density profile $\rho(r)$ rather than just the radius.

There are many factors controlling nucleation and growth, which among them diffusion can be the most critical one. When diffusion is too fast the generated vapors are removed very quickly from the nucleation region and an adequate supersaturation may not reach to form a sufficient number of nuclei. On the other hand, if diffusion is too slow then the formed nucleus could grow very rapidly, which may lead to a larger particle size and an undesirable particle size distribution. Vacuum is generally employed for most of gas phase synthesis to adjust the diffusion rate. Alternatively, a higher pressure of an inert gas is used in some other gas phase synthesis. The inert gas atmosphere increases the collisions rates of atoms to decrease their diffusion rate of atoms, cools them down, and prevents undesirable growth. If the diffusion rate is not controlled sufficiently, then supersaturation may not achieved and only very small clusters of atoms are deposited on the collecting surfaces.

1.3 Heterogeneous Nucleation

Heterogeneous nucleation or nucleated condensation from a vapor phase can occur on any foreign material acting as a nucleus such as dust particles, a cluster ions or surface of a liquid droplet. Nucleation of water in the atmosphere, such as ice, fog, snow and rain formation, as well as the formation of secondary atmospheric aerosols and minerals in the Earth's crust due to solidification, are examples of heterogeneous nucleation. An earlier theory of water nucleation

on insoluble spherical particles with uniform surfaces was developed by Fletcher.[47] This theory makes it possible to calculate the critical supersaturation and nucleation rate using the contact angle of a water droplet on the surface of a uniform aerosol particle as a function of particle radius. Later, this theory was adopted for heterogeneous nucleation of ice (on nuclei with non-uniform surfaces) and was extended to other substances.[48]

In heterogeneous nucleation, the concentration of foreign particles could be high and the required supersaturation low, so condensation occurs at nucleating sites of existing particles without forming new nuclei. Homogeneous nucleation usually requires saturation ratios of 2-10, but nucleated condensation can occur at a supersaturation of only a few percent. The deviation from equilibrium is crucial in homogeneous condensation as it is required for the compensation of the work necessary to form an embryo of the stable growing phase. In heterogeneous nucleation, the foreign material that is also called nucleation catalyst reduces the interfacial energy and thus increases the probability of nucleation. Cracks and defects in a material surface can further increase the phase transition rate because filling these cracks can decrease the surface energy. This explains why heterogeneous nucleation is much more common than homogeneous nucleation where the probability of nucleation is determined by the deviation of the meta-stable phase from the equilibrium state.[49] In first order phase transitions, such as condensation and crystallization, heterogeneous nucleation occurs much more often than homogeneous nucleation because the former often leads to a lower nucleation barrier. When a foreign material is very efficient, heterogeneous nucleation can be considered an adsorption process.

The heterogeneous nucleation of supercooled or supersaturated solutions by foreign particles is of a great interest in many fields. Thus, an understanding of the dependence of nucleation efficiency on the size and the surface of the nucleating particles is of great

importance.[47] The classical heterogeneous nucleation theory was developed for nucleation of liquid droplet on a solid particle. The free energy required for heterogeneous nucleation is frequently assumed to be the product of the homogeneous nucleation and a function of the contact angle, θ,

$$\Delta G_{heterogeneous} = \Delta G_{homogeneous} f(\theta) \quad (7)$$

or a function of homogeneous nucleation and interfacial tensions between gas, liquid and solid,

$$\Delta G_{heterogeneous} = \Delta G_{homogeneous} f(m, x) \quad (8)$$

where m is related to the interfacial tension and x is the relative size of foreign particles. The correlation function, $f(\theta)$ or $f(m, x)$, which reflects the direct correlation between the nucleating phase and substrates in the formation of critical nuclei, varies between 1 and 0. If $f(\theta) = 1$, no wetting of the surface occur, so the nucleation falls under the case of homogeneous nucleation. If $f(\theta) = 0$, there is full wetting, and there is no barrier for nucleation at surface and nucleation is considered fully heterogeneous. Another assumption in heterogeneous nucleation is that, in comparison to homogeneous nucleation, the radius of the critical nucleus for heterogeneous nucleation remains unchanged.[2] Problems with classical heterogeneous nucleation theory includes the situation when the condensation efficiency of vapor on the material is high, i.e. when θ, $f(\theta)$ and ΔG approach zero, the nucleus of the condensed phase is only a few atoms thick or falls below a monolayer. A spherical cap shaped nucleus becomes impossible, and $f(\theta)$ is no longer an adequate measure of condensation efficiency for heterogeneous nucleation.

1.4. Graphene-based Nanomaterials by Laser Approaches

Graphene consists of a hexagonal monolayer network of sp^2-hybridized carbon atoms, and it is the building block of all graphitic forms of carbon nano-materials. Graphene is a single-atom-thick planar sheet of bonded carbon atoms that is densely packed in a honeycomb type

crystal lattice. A perfect graphene sheet is a single layer of a two-dimensional hexagonal sheet of carbon atoms, but it commonly exists in two or more layers called bi-layer or multi-layer graphene.[50] Although graphene sheets are expected to be ideally flat, ripples occur due to the processing effects. Graphene can corrugate, wrapped into 0D fullerenic carbon, rolled into 1D nanotubes or stacked into 3D graphitic material. Graphene (or 2D graphite) has been studied theoretically for almost sixty years.

The unique properties of this 2D material include the highest intrinsic carrier mobility at room temperature of all known materials and very high mechanical strength and thermal stability. Electrons in graphene have zero effective masses and can travel for micrometers without scattering at room temperature allowing them to behave ballistically, similar to massless particles.[51] Furthermore, graphene also conducts heat ballistically. Phonons move like electrons across the solid giving graphene unusual thermal capabilities. Most of the outstanding electronic properties of graphene can only be observed in samples with high perfection of the atomic lattice because structural defects that may appear during growth or processing deteriorate the performance of graphene electronic devices. These properties inspire many new applications in a wide range of areas including nanoelectronics, supercapacitors, batteries, photovoltaic, solar cells, fuel cells, transparent conducting films, sensors, and many others.

In addition to the unique electronic properties of graphene, other properties such as high thermal, chemical, and mechanical stability as well as high surface area also represent desirable characteristics as 2D support layers for metallic and bimetallic nanoparticles in heterogeneous catalysis. Supporting metal nanoparticles on graphene sheets could provide a large surface area and thermally stable system for potential applications in catalysis, fuel cells, chemical sensors, and hydrogen storage.

The synthesis of monolayer graphite was attempted as early as 1975 by Lang,[52] who showed the formation of mono- and multilayered graphite by thermal decomposition of carbon on single crystal platinum substrates. Scattered attempts to produce graphene were reported from 1975 to 2004. Novoselov et al.[53] were credited for the discovery of graphene in 2004. Despite of more than a decade of extensive research and innovation, this area demands more theoretical and experimental research work from synthesizing to scaling up production methods to fundamental understanding of chemical and electronic behavior of the synthesized graphene based materials.

The deposition of inorganic nanoparticles including metals or semiconductors on the surfaces of graphene sheets presents special features in new hybrid materials. The resulting composites can be useful in various products such as optical and electronic devices, catalysts, and sensors. Recently, composites of graphene with precious metal nanoparticles such as Ag and Pt were prepared[54] and used as catalysts for oxygen reduction[55] and methanol oxidation.[56] In addition to making composite catalysts, decoration of graphene surface with metallic nanoparticles makes it more suitable for usage in electronics, optics, and biotechnology related applications. For instance, graphene containing a few layers of carbon atoms was found to be easily decorated with Pt, Ag, and Au nanoparticles where decoration enhances its application in opto-electonics.[57] However, comparatively, a few publications concerning the loading of metal nanoparticles on graphene sheets signifying opportunities for further scientific research.

Substitutional doping refers to substitution of carbon atoms in the honeycomb lattice of graphene by atoms with different number of valence electrons such as nitrogen and boron. The incorporation of foreign atoms interrupts sp^2 hybridization of carbon atoms.[58] Adding atoms with fewer valence electrons than carbon, like boron, makes a p-type semiconductor, while adding atoms with more valence electrons than carbon, like nitrogen, makes an n-type semiconductor.

There are various processes for graphene preparation including chemical vapor deposition (CVD),[59] arc discharge of graphite,[60] micromechanical exfoliation of graphite,[61] epitaxial growth on electrically insulating surface such as SiC, solvothermal synthesis,[62] laser excitation of graphite oxide (GO) in solution,[63] and the reduction of graphene oxide (GO).[64-65] The reduction of GO has generally been carried out in liquid phase by chemical methods using different reducing agents such as hydrazine,[66] hydroquinone,[67] and $NaBH_4$.[68] Reduction of GO was recently reported under alternative conditions such as alkaline conditions,[69] ultraviolet-assisted methods,[70] and thermal methods.[71 -72] Among them, thermal treatment is a green process where no hazardous chemicals are used, but the process requires rapid heating rate of over 2000 °C min^{-1} for a temperature of up to 1050 °C in an oven under an inert atmosphere like argon[73] or up to 800 °C under hydrogen.[74] Though the rapid reduction of graphite oxide (GO) under mild conditions seems to be very difficult, Fozooni et al.[25] reported that a microwave can heat the graphite or amorphous carbon (in powder form) to a high temperature in a short period of time, and it has been successfully applied in the pre-exfoliation of the graphite.[75]

Recent advances in the synthesis of graphene sheets through the reduction of GO have presented efficient approaches for somewhat larger scale production of chemically converted graphene in solution.[72] However, chemical reduction methods suffer from the difficulty of controlling the reduction process and the potential for residual contamination by the chemical reducing agents, which necessitates the use of multiple solvents and several post synthesis treatments such as drying and thermal annealing.[59] Other methods such as thermal annealing at high temperatures, laser photoreduction, and plasma discharge processes offer several advantages over chemical reduction including efficient removal of oxygen from GO without using toxic chemical reducing agents.[76] However, thermal annealing requires high temperatures

and use of ultrahigh vacuum equipment for the efficient removal of oxygen from GO.[76] On the other hand, photoreduction methods including flash photolysis and laser irradiation have been demonstrated to be effective only in GO solutions[76] or on thin films of GO supported on substrates.[77] Similarly, a plasma-assisted reduction method has been recently applied to films of GO casted on polymeric substrates.[78] The formation of freestanding 2D- graphene was achieved through laser exfoliation of highly ordered pyrolytic graphite (HOPG) using a pulsed neodymium-doped yttrium aluminum garnet (Nd-YAG) laser.[79] When the applied laser flux ranges from 1.0 to10.0 J /cm^2, ultrathin sheet fragments are peeled off the HOPG and deposited on the substrate as graphene. The chamber needs to be evacuated to 10^{-5} Torr and then filled with argon gas to 1 Torr.

To overcome some of the limitations reported above, and as an objective of this work, a larger scale production of hydrogen-terminated graphene (HTG) nanosheets was achieved by the laser synthesis approach. The approach employs Nd-YAG laser to irradiate a compressed target of graphene oxide in a confined volume containing an inert gas or a mixture of reducing and inert gases. The technique is known as laser vaporization controlled condensation (LVCC) and was developed in El-Shall's laboratory in 1994 for the synthesis of variety of nanoparticles.[1] For the first time, the syntheses of hydrogen-terminated graphene and reduced graphene oxide from preformed graphite oxide (GO) targets were achieved using the so-called laser vaporization controlled condensation (LVCC) technique.

1.5 Objective

1.5.1 LVCC

One major objective of the work reported in this thesis is the development of laser methods for synthesis of nanoparticles and nanoparticles-graphene composites. These methods

are based on the Laser Vaporization Controlled Condensation (LVCC) where the laser is used to vaporize a semiconductor or a metal target in an inert atmosphere followed by rapid condensations to form semiconductor or metal nanoparticles. The LVCC method is applied in Chapter 3 for the synthesis of Au nanoparticles catalysts supported on ceria and zirconia for the low temperature catalytic oxidation of CO. This method is extended in Chapter 4 for the synthesis of graphene, hydrogen terminated graphene, nitrogen-and boron doped graphene, and metal nanoparticles supported on graphene. The synthesis of these graphene –based materials by the LVCC method is reported for the first time in this thesis.

1.5.2 LVSC

The second method developed in this work is called "Laser Vaporization-Solvent Capturing" (LVSC). This method represents a logical extension of LVCC where the nanoparticles formed in the vapor phase are quickly captured by liquid solvents, which provide surface passivation of the nanoparticles through the attachment of weakly bounded ligand molecules to the surfaces. This method is applied, for the first time, for the synthesis of vanadium (V), molybdenum (Mo), and tungsten (W) oxide nanoparticles capped by acetonitrile, methanol, and THF. The properties of these nanoparticles are compared with those made by the LVCC method. Results are presented in Chapter 5 of this dissertation.

In order to provide a comparison between the LVCC and LVSC methods for the synthesis of semiconductors, silicon (Si) nanoparticles were used as model semiconductor nanoparticles to investigate their optical and photoluminescence (PL) properties. This comparison is provided in Chapter 6. The silicon nanoparticles synthesized by both LVCC and LVSC methods are incorporated into graphene sheets and their chemical properties are measured and compared to the free and solvent capped Si nanoparticles. The incorporation of Si

nanoparticles in graphene sheets could lead to new applications where the photoluminescence properties of Si can be utilized in combination with the exceptional electronic, thermal and chemical properties of graphene. These applications could be sensors, optical devices, and electronic.

At this point, it is useful to provide a summary of the chapters presented in this thesis. Chapter 2 thoroughly describes the experimental parts of work including materials used, LVCC setups and its modifications to LVSC, experimental procedures, and characterization techniques used to analyze all the synthesized materials throughout the work. Chapter 3 describes the formation, characterization and performance analysis of two catalysts based on gold nanoparticles deposited on metal oxide supports namely ceria (Au/CeO_2) and zirconia (Au/ZrO_2). Chapter 4 covers the synthesis and characterization of hydrogen terminated graphene (HTG) from graphite oxide (GO), substitution doping of graphene with heteroatom like nitrogen, boron and nitrogen-boron mixture, graphene-metal nanoparticle composites, and the preparation and characterization of graphene quantum dots (GQD) and nitrogen-doped graphene quantum dots (N-GQDs). Chapter 5 begins with the formation and characterization of nanoparticles of several metals (V, Mo, and W) and their oxide; then, it continues with the formation and characterization of the capped nanoparticles of these metals (V, Mo, and W) and their oxides with different organic molecules (ligands) namely acetonitrile, tetrahydrofuran and methanol; and in the final section, it describes the formation and characterization of nanocomposites of graphene with vanadium, molybdenum and tungsten oxide nanoparticles capped by acetonitrile. Chapter 6 first describes the formation of silicone nanoparticles, then discusses silicon quantum dots capped with various organic molecules and finally covers the formation of nanocomposite

of graphene with capped silicon nanoparticles with acetonitrile. Last chapter, Chapter 7, provides a summary for all the major conclusions reached throughout this study.

Chapter 2: Experimental

This chapter is comprised of several sections. (1) The materials used (e.g., graphite, pure metals, etc.) in the processing of making products such as hydrogen terminated graphene (HTG), reduced graphene oxide (RGO), graphene-metal nanoparticles composites, and graphene doped with heteroatoms. (2) The experimental setups including mainly laser vaporization controlled condensation (LVCC) and laser vaporization solvent capturing (LVSC), hydrothermal, chemical and microwave (MW) and their working procedures. (3) The instrumentation such as X-ray, XPS, FTIR, Raman, TEM, SEM, and etc. used to characterize the materials produced in this work. (4) The methods and procedures for performance assessment of the materials synthesized.

2.1 Materials

Graphite was the key material used in the preparation of graphite oxide (GO), which was subsequently used in preparing the experimental materials of interest for this research study. These materials include reduced graphene oxide, hydrogen terminated graphene, metal nanoparticles supported graphene, and nitrogen and boron doped graphenes. High purity graphite (99.99%) was purchase from Alfa Aesar and employed in preparing graphite oxide (GO) using $H_2SO_4/KMnO_4$ according to the method of Hummers and Offeman.[80] Other essential materials used in this work were pure metals including Pd, Fe, Co, Ni, Cu, Au, Mo, and W in the form of powder and rod; all were purchased from Sigma Aldrich with a better than 99.9% purity.

Organic solvents such as acetonitrile (AN), methanol, and tetrahydrofuran (THF) were purchased from Sigma Aldrich with a purity of better than 99%. All gases such as He, H_2, NH_3, and O_2 were ultra-high purity.

2.2 Experimental Setup and Procedures

2.2.1 Formation of Graphite Oxide

High purity graphite with a mesh size of 200 was employed in the preparation of graphite oxide (GO) using $H_2SO_4/KMnO_4$ according to the method of Hummers and Offeman.[80] Briefly, the oxidation of graphite was carried out under a hood in an Erlenmeyer flask containing $H_2SO_4/KMnO_4$ and graphite. The mixture was stirred until it turned into yellowish brown color. The stirring was stopped and let the solids to precipitate; a yellowish-brown cake in the bottom of the container was the confirmation of formed graphite oxide (GO). This cake was repeatedly and at least 6 times washed with de-ionized hot water, and the resulting powders were dried under vacuum and at room temperature for overnight. A flaky sheet like product was formed that was manually ground to a much finer size particles before using it in making targets for the laser irradiation experiments.

2.2.2 Laser Vaporization Controlled Condensation (LVCC)

LVCC is the fundamental process used in this study to synthesize the experimental materials. This process was first developed by El-Shall group in 1994 to synthesize various nanoparticles by vaporization of a given material or a mixture of materials with the subsequent particle formation from the controlled condensation of the vapor phase. The LVCC process as described by El-Shall et al.,[1, 16] consists of a pulsed laser for vaporization, a cylindrical vessel for synthesis and collection of nanomaterials and some accessories such as vacuum pump and gases. The pulsed laser is the second harmonic (532 nm) of a Nd-YAG laser (15-30 mJ/pulse, 10^{-8} s

pulse) that is used for vaporization of the targets. A schematic diagram of the vessel with the relevant components for gases and vacuum is shown in Figure 2.1. The chamber consists of two circular stainless-steel plates assembled horizontally and separated by a quartz ring. The upper and lower plates have assemblies that allow them to be heated or cooled before any operation. The target and the lower plate are generally maintained at a temperature higher than that of the upper one. The lower plate temperature was controlled by circulating a fluid like hot water and was normally held at room up to the water boiling temperatures. In most experiments, the top plate was cooled down to less than 230 K using liquid nitrogen. However, there were experiments where the top plate was held at room temperature and the bottom plate was cooled down to a sub-ambient temperature. The large temperature gradient between the bottom and top plates creates a steady convective gas flow, which can be enhanced by using a heavier carrier gas such as Ar under a higher than atmospheric pressures (e.g.,10^3 Torr).

The target was made with a pure or a mixture of pure materials by well blending the solid materials first and then pressing into a cylindrical shape using a given die and a hydrolytic press. For this work, the die diameter was about 15 mm; and, the total mass of the starting materials was roughly between 0.5 to 1.0 grams, depending on their densities and particle sizes of starting materials. By applying a proper amount of load on the powders in the die, a cylindrical shape target having a height of about 2 to 10 mm was made. Pure metal received in the form of rods did not need to be pelletized again.

To operate the LVCC, a pre-formed target or a rod was first placed on the bottom plate. The chamber gaseous content was vacuumed and purged with helium for at least five times before filling the chamber to a given pressure of between 100 to 1000 Torr. The chamber, depending on the type of experiment and material to be synthesized, was filled with a pure gas

such as He, Ar or a mixture of gases with a known composition (e.g., 20% H_2-He in the case of reduction, O_2 in the case of oxides formation, or N_2 or NH_3 for nitrides formation). As indicated above, the upper and lower plates can be heated or cooled to different temperatures. This gives an important feature to this setup, which is the use of an upward diffusion cloud at a well-defined temperature and pressure for nanoparticle formation. The vapor is generated by pulsed laser vaporization using the second harmonic (532 nm) of a Nd-YAG laser (15-30 mJ/pulse, 10^{-8} s pulse). The laser vaporization produces a high density vapor in a very short period of time, typically 10^{-8} s, in a directional jet that allows directed deposition. The laser beam was moved on the target surface to expose new areas to the beam and assure good reproducibility of the amount of vapor produced. Following the laser pulse, the ejected pulse of the atoms or molecules interacts with the gas mixture in the chamber and forms a cloud of nucleus before growing into nanoparticles of desired size. Both diffusion and convection affect the removal of the nucleus and small nanoparticles away from the nucleation zone before they can grow into larger particles. It is possible to control the size of the initial nucleus and final nanoparticles by controlling the temperature gradient, the total pressure and the laser power. The later factor determines the number density of the atoms or molecules released into the vapor phase. Generally, no particles were found anywhere else in the chamber except on the top plate where the products were collected. This supports the assumption that nucleation takes place in the upper part of the chamber and that the convective flow of gas carries the formed nanoparticles upward to the top plate where deposition occurs.

2.2.3 Reduction of Graphite Oxide

Hydrogen terminated graphene (HTG), which may also be called graphene (G) and reduced graphite oxide (RGO) were synthesized using primarily LVCC. First a target of graphite

oxide was made and placed on the bottom plate. The vessel was purged several times and filled to a given pressure with a desired gas mixture. The bottom and top plates were heated and cooled to about 363 K and 230 K, respectively. A portion of GO sheets was blasted into the gas phase by focusing a Nd-YAG laser on the target continuously. It was expected that LVCC process exfoliates the GO sheets from the GO target where they undergo deoxygenation and reduction without the destruction of their layer structures or atomization to produce carbon nanoparticles. The formed graphene nanosheets were collected on the top plate. To find the most optimum conditions for reduction of GO to graphene sheets, experiments were carried out under different conditions of laser power (1, 3, and 5 W), gaseous composition (H_2/He), and total pressure (100 to 1000 Torr). As this will be further discussed in the following chapters, a minimum laser power of about 2 W, a gaseous atmosphere of 20% H_2 and a total pressure of 800 Torr were required to achieve the best reduction of graphite oxide (GO) to graphene. The material synthesized under these conditions is called hydrogen terminated graphene (HTG).

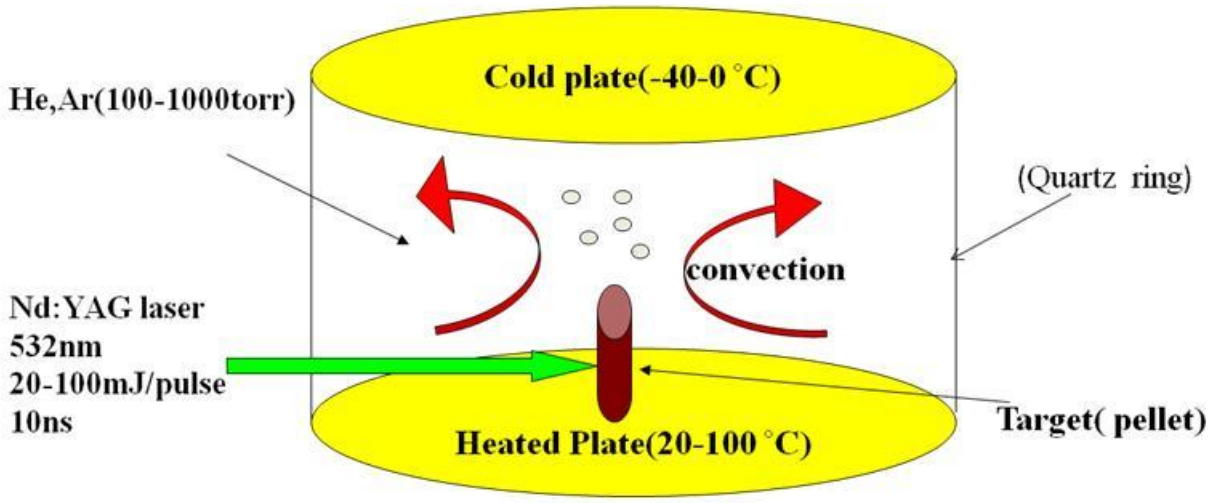

Figure 2.1. Schematic of a pulsed laser vaporization controlled condensation (LVCC) system.

2.2.4 Nanocomposites of Metal Nanoparticle with Graphene and Metal Oxide

For the preparation of a metal (e.g., Pd, Au) nanoparticles deposited on graphene, an appropriate amount of a metal such as palladium (e.g. 5% by weight) was thoroughly mixed with graphene oxide sheets and then compressed into a target. The same procedure was followed to make targets containing metals such as Au and oxides such as ZrO_2. In either case, the target was placed on the bottom plate; chamber was purged several times and brought to a desired total pressure of a known gas composition. Plates were set at desired temperatures and then laser began to irradiate on the target as described above to form graphene or metal oxide supported metals nanoparticles. It is well established that metals and metal oxides such as ceria evaporate with pulsed laser used in LVCC, which in this case the nucleation is expected to be mostly homogeneous with respect to oxide and heterogeneous with respect to metal. This situation for graphite oxide and metals are different and the nucleation of metal nanoparticles on graphene is supposed to be heterogeneous. One reason is the conversion of graphite oxide to graphene and high vaporization temperatures of these two materials that would not allow for these materials to evaporate. Furthermore, it is clear from the characterization of the products that formed graphene has retained its structural integrity and contain little to no amorphous carbon particles.

2.2.5 Graphene Doped with Nitrogen, Boron, and Nitrogen-Boron

The syntheses of nitrogen doped graphene (NG), boron doped graphene (BG), and boron –nitrogen doped graphene (BNG) from graphite oxide (GO) were carried out using laser vaporization controlled condensation (LVCC). In this section of the work, a target of graphite oxide was placed on the lower plate and the top plate was the depository area for the formed products. The lower plate and target were heated and maintained at around 363 °K temperature

while the upper plate was kept at room temperature. The chamber after being purged with helium at least five time was filled with a given gas mixture to a total pressure of 800 Torr. A gaseous mixture comprising of He and a known amount of a reactant gas was employed for doping studies, which included NH_3 in case of nitrogen doped graphene, B_2H_6 for born, and B_2H_6-NH_3 for boron –nitrogen doped graphenes.

For the synthesis of nitrogen doped graphene samples, LVCC chamber was filled with a mixture of ammonia and helium to a total pressure of 800 Torr. The partial pressure of NH_3 used as a variable to find how it affects the extent of nitrogen doping. Graphite oxide was expected to interact with ammonia in the chamber before and during the laser irradiation. The interaction of graphite oxide with NH_3 and the extent of reaction were expected to be affected by the ammonia partial pressure in the chamber, the exposure time of GO to NH_3 and the lower plate temperature. The LVCC chamber and gaseous atmosphere remained at room temperature until the lower plate and the target were heated. The heating of the lower plate could elevate the gas temperature to above room temperature. The average laser power for this experimental work was 1.94±0.12 W (Range: 1.75 to 2.13 W). Table 2.1 presents different experimental conditions including laser power and gaseous atmospheres used in this work. Nitrogen doped graphene deposited on the top plate was collected and stored in an inert atmosphere to be analyzed by various spectroscopic techniques. In experiment 3 (Table 2.1), the chamber was first filled with NH_3 to a pressure of 800 Torr and kept for about 15 hrs without heating the bottom plate. During this time, ammonia pressure was dropped to 550 Torr indicating the adsorption of NH_3 onto GO surfaces. At this point, the chamber was quickly evacuated and filled with He to a total pressure of 800 Torr. The bottom plate was heated to 90 °C before the laser irradiation of the target.

For the synthesis of boron doped graphene and boron-nitrogen doped graphene samples, LVCC chamber was filled with the gaseous mixtures of interest, e.g., B_2H_6-He and B_2H_6-NH_3-He to a total chamber pressure of 800 Torr. B_2H_6 was prepared in the lab and in a simple apparatus according to the reaction given by Equation 7. About 2 - 4 mL of boron trifluoride diethyl ether ($BF_3.C_4H_{10}O$) was added to 1 - 2 grams of sodium borohydride ($NaBH_4$) and allowed the reaction to proceed to form B_2H_6. The formed B_2H_6 in the apparatus was directed into the LVCC chamber using right tubing and valves.

No.	Sample ID	Target	NH_3 Partial Pressure (Torr)	He Partial Pressure (Torr)	Total Pressure (Torr)	Laser power (W)
1	NG-100	GO	100	700	800	1.75
2	NG-250	GO	250	550	800	2.01
3	NG-250 ad*	GO	0	800	800	1.97
4	NG-500	GO	500	300	800	1.85
5	NG-600	GO	600	200	800	2.13

Table 2.1. List of experimental conditions including laser power and chamber atmosphere used in LVCC to produce nitrogen-doped graphene from graphite oxide.

$$3\ NaBH_4\ (s) + 4\ BF_3{\bullet}OEt_2\ (l) \rightarrow 3\ NaBF_4\ (s) + 2\ B_2H_6\ (g) + 4\ Et_2O\ (l) \quad (7)$$

Table 2.2 presents a list of experimental conditions including laser power with an average value of 1.7±0.12 W and gaseous atmospheres used to produce boron and boron-nitrogen doped graphene. Boron or boron-nitrogen doped graphene samples deposited on the top plate were collected and stored in an inert atmosphere to be analyzed by various spectroscopic techniques. Again partial pressures of B_2H_6 and NH_3 were used as parameters to study the impacts of reactants partial pressures. In experiments number 5, 6 and 7 (Table 2.2), the chamber was first

filled to a given pressure of B_2H_6 and then He was added. After heating the bottom plate to 90 ºC, sufficient amount of NH_3 was added to bring the vessel pressure to a total pressure of 800 Torr. At this point laser irradiation of the target began.

No.	Sample ID	B_2H_6 partial Pressure (Torr)	NH_3 Partial Pressure (Torr)	He Partial Pressure (Torr)	Total Pressure (Torr)	Laser Power (W)
1	BG	800	0	0	800	2.57
2	BG-150	150	0	650	800	1.4
3	BG-300	300	0	500	800	1.38
4	BG-400	400	0	400	800	1.48
5	BNG (100B-100N)	100	100	600	800	1.6
6	BNG (100B-200N)	100	200	500	800	1.4
7	BNG (200B-200N)	200	200	400	800	2.1

Table 2.2. List of experimental conditions including laser power and chamber atmosphere used in LVCC to produce boron and boron-nitrogen doped graphenes from graphite oxide.

2.2.6 Laser Vaporization-Solvent Capturing (LVSC)

Laser vaporization solvent capturing (LVSC) was the primary technique used to synthesize the nanoparticles of metal and metal oxide capped with various organic solvents and their nanocomposites with graphene. This method is a modified version of laser vaporization controlled condensation (LVCC). It consists of a pulsed laser, a chamber and accessories similar to LVCC. Unlike LVCC, the bottom plate is cooled to a sub-ambient temperature while the top plate is kept at room temperature. A large petri dish contain a desirable solvent is positioned on the bottom plate before putting the target in place. Advantages of LVSC over LVCC are in better

controlling of the nanoparticle size and surface chemistry (e.g., degree of oxidation) , which is due to in-situ usage of a solvent as the capping agent for nanoparticles. A nice feature of LVSC is in combining the gas phase and chemical approaches for synthesizing nanoparticles. A schematic diagram of the LVSC chamber with the relevant components is given in Figure 2.2.

Experimental procedures for synthesizing metal nanoparticles by LVSC are very similar to LVCC. Like LVCC, a pulsed-laser vaporizes a metal target to produce a high-density vapor of that metal, e.g., molybdenum, in a very short period of time during a LVSC experiment. This vapor condenses and forms nanoparticles, which is captured by the solvent in the petri dish. To improve the capturing of the condensed vapors and nanoparticles by the solvent, the top plate was kept at room temperature while the bottom plate was cooled to about 243 K temperature to prevent an upward flow of gases and nanoparticles. The further growth of nanoparticles is expected to be prevented by capping of nanoparticles by solvent molecules and probably by forming a weak chemical bond between solvent and nanoparticles. No detectable particles are found anywhere else in the chamber except in the solvent and on the surfaces of petri dish. This observation supports the assumption that nucleation takes place around the target and above the solvent surface and that the nanoparticles diffuse into the solvent where deposition and interaction with solvent occur. The petri dish in the chamber may contain different solvents such as tetrahydrofuran (THF), acetonitrile (AN), and methanol (Met). In the case of metal- or metal oxide composited with graphene, petri dish contains graphene oxide suspended in a solvent like acetonitrile.

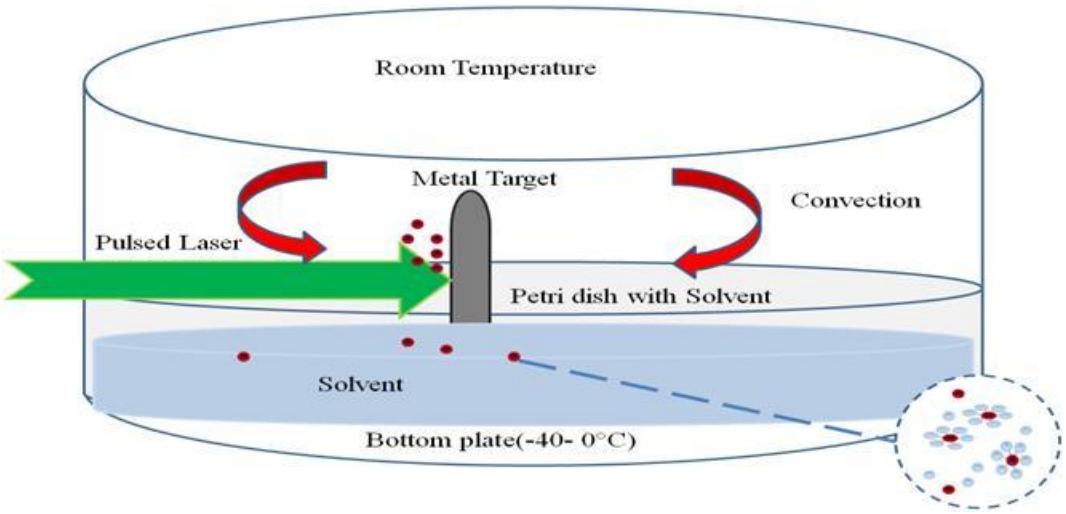

Figure 2.2. Schematic of a pulsed laser vaporization solvent capturing (LVSC) system.

2.2.6.1 Synthesis of Capped Metal and Metal Oxide Semiconductors Using LVSC Methods

Procedures used to form capped V, MO, W, and Si nanoparticles and their oxides are identical to the procedures presented in section 2.2.6.

2.2.6.2 Synthesis of Capped Metal and Metal Oxide Semiconductors Supported on Graphene Using LVSC and MW Techniques

A combination of laser vaporization solvent capturing (LVSC) and chemical (hydrazine hydrate) reduction by microwave irradiation were used to synthesize metal (Si) or metal oxide (Mo_xO_y, V_xO_y, and W_xO_y) nanoparticles capped by acetonitrile and supported on graphene. First in a petri dish, 2 grams of GO were dispersed in 10 ml of acetonitrile, and placed on the bottom plate. The target, which could be Si, Mo, V, or W was placed in position on the bottom plate. The gas in the chamber was He for metal and 10-20% O_2-He for metal oxide nanoparticle formation. The total chamber pressure was kept at 800 Torr for all the experiments, and laser power was held around 4 W. After irradiation of the metal target with laser beam in the appropriate atmosphere, the formed nanoparticles in the gas phase were captured by the solvent (AN) containing graphite oxide (GO). This mixture containing suspended GO and metal (or

metal oxide) nanoparticles in acetonitrile was transferrd into an Erlenmeyer. The mixture was stirred for 15 minutes to make a suspension. Then 40-100 μL of hydrazine hydrate was added to this suspension. Next the suspension was heated in an Avanti MO7191TW microwave oven with a maximum power of 1.05 kW for 1-2 minutes.

2.3 Characterization Techniques

The samples of reduced graphite oxide, graphene metal nanoparticles composites, doped graphene, metal and metal oxides capped with different organic molecules were analyzed using a series of spectroscopic, microscopic and mass spectrometric techniques. A summary of the characterization techniques and their general procedures are given below.

2.3.1 Raman Spectroscopy

The Raman spectroscopy is one of the most widely used techniques to characterize the structural and electronic properties of graphene including disorder and defect structures, defect density and doping levels. It has been successfully used to characterize graphene, other carbon–based materials and functionalized graphene and metal nanoparticles. It can also provide useful information about the crystallinity and the number of layers present in a graphene sample[81].

Two Raman spectrometers were used in this study. The first one has a Princeton Instruments 1340 x 400 liquid nitrogen CCD detector, attached to a Spex model 1870 0.5 meter single spectrograph with interchangeable 1800, 1200, 600, and 300 lines/mm holographic gratings (Jobin-Yvon). The Raman spectra were measured using an excitation wavelength of 406.7 nm krypton (Coherent Sabre) and a power of 0.072 W, which was provided by a Spectra-Physics model 2025 argon ion laser for 457.9 nm and 514.5 nm. The samples were pressed into a depression at the end of a 3 mm diameter stainless steel rod. The Raman scattered light was

collected by a Canon 50 mm f/0.95 camera lens. The second Raman spectrometer was the Thermo- DXR Raman system, which has excitation wavelengths of 532 nm and 780 nm.

2.3.2 X-Ray Diffraction (XRD)

X-ray scattering techniques are a family of non-destructive analytical techniques that reveal information about the crystallographic structure, chemical composition and size of particles. X-ray diffraction yields the atomic structure of materials and is based on the elastic scattering of X-rays from the electron clouds of the individual atoms in the system. The crystallite diameter was determined by the Debye-Scherrer equation.

The X-ray diffraction (XRD) patterns of samples were measured at room temperature with an X'pert Philip Materials Research Diffractometer using Cu K_α radiation (λ = 1.54 °A) at 45 kV and 40 mA, in the range of 2θ = 5°- 80°. The particle size of the investigated solids was calculated from the line broadening analysis of some diffraction line using Scherrer equation:

$$D = k\lambda / B_{1/2} \cos\theta \qquad (9)$$

where D is the mean crystallite diameter, λ the X-ray wavelength, k the Scherrer constant (0.89) and $B_{1/2}$ is the full width half maximum (FWHM) of the nanoparticles diffraction peaks and θ is the diffraction angle.

2.3.3 X-Ray Photoelectron Spectrometer (XPS)

The X-ray photoelectron spectrometer (XPS) is a suitable technique for studying the surface chemistry of materials. The XPS used in this work was a Thermo Fisher ESCALAB 250 X-ray photoelectron spectrometer with a monochromatic Al KR. The instrument is equipped with a 95 nm spatial resolution and a UV photoelectron lamp. The system includes an argon ion sputtering gun for depth profiling. The instrument includes a field emission electron gun , which

allows for scanning electron microscopy (SEM) imaging. The TEM grids containing samples were glued using carbon glue onto the surface of SEM sample holder and then used in SEM analysis.

2.3.4 Fourier Transform Infrared Spectroscopy (FTIR)

The FTIR spectroscopy is one of the most widely used techniques to characterize the structural and functional groups in a compound by measuring vibrational absorption. It has been successfully used to characterize graphene and other carbon–based materials and it can also provide useful information about the structure of a sample.

The instrument used in this work was a Nicolet-Nexus 670 FTIR equipped with a deuterated triglycine sulfate (DTGS) detector. The instrument has an Ever Glo (black body radiation) light source and a XT-KBr beam splitter for near- and mid-infrared measurement. The samples were prepared for analyses by mixing powders with KBr and pressing them into pellets.

2.3.5 Transmission Electron Microscopy (TEM)

The transmission electron microscopy (TEM) is an instrument that scrutinizes a specimen at an atomic scale, which includes the size, shape and arrangement of atoms and particles that make up the specimen as well as their relationships. A thin (0.5 um or less) layer sample is illuminated by an electron beam and the images are recorded by detecting the electrons that pass through the sample to a system of electromagnetic lenses , which focus and enlarge the image on a digital camera.

The transmission electron microscope (TEM) images in this work were obtained using a Jeol Jem-1230 electron microscope operated at 120 kV equipped with a Gatan UltraScan 4000SP 4K x 4K CCD camera. The sample powders were dispersed in ethanol or water using ultrasonic vibration for 2-5 minutes and a drop of the suspension was placed on a Formvar carbon-coated

300-mesh copper grid (Ted Pella). The solvent evaporated from the sample in air at room temperature.

2.3.6 Ultraviolet –Visible Spectroscopy (UV-Vis)

The ultraviolet –visible spectroscopy refers to absorption spectroscopy in the ultraviolet-visible spectral region. In this region, molecules undergo electronic transitions. UV-Vis is used for the determination of conjugated organic compounds such as graphene.

The instrument used in this work was a Hewlett Packard 8453 UV-visible Spectroscopy Systems, each equipped with a HP Chem Station software. The range of this instrument is 200-980 nm, and the light source is deuterium and tungsten with a diode array detector.

2.3.7 Thermal Gravimetric Analysis (TGA)

TGA was used in this study to test the thermal stability of some synthesized samples. Samples were tested in a TA Instruments Q-5000IR series thermal gravimetric analyzer. Sample was placed in a platinum pan under an atmosphere of nitrogen. Then it was heated at a heating rate of 5 ºC/min up to a desired temperature of 500 °C, and the carrier gas flow rate was kept at about 50 ml/min in all tests.

2.3.8 Photoluminescence (PL)

To study the optical properties of the samples as well as specific transition in molecules, photoluminescence is a useful instrument and was the instrument of choice in this research. The photoluminescence (PL) spectra were obtained using a Varian photoluminescence, which the instrument is equipped with a Xenon flash and two monochromators, excitation and emission and a photomultiplier tube detector.

2.3.9 Mass Spectrometry

A laser desorption time-of-flight mass spectrometer (TOF-MS) was used for measuring mass spectra of metal and metal oxide nanoparticles capped with acetonitrile using LVSC. This instrument was designed in a laboratory of the University of Georgia specifically for laser desorption of large molecules. A few drops of the collected suspension were placed on a stainless steel probe tip, which was then inserted directly within the acceleration region of the TOF. Samples were desorbed with a Nd-YAG laser (New Wave Research, Polaris II) at 532 and 355 nm with pulse energies of ~ 400 μ J/pulse.

2.4 Performance Analyses

CO conversion and Suzuki reaction were used to evaluate the catalytic activities of the synthesized nanocomposite materials in this work.

2.4.1 CO Oxidation

The catalytic reactivity of prepared materials for CO oxidation was measured using a home-made assembly. The full description of the set up is given elsewhere.[82] Briefly, it consists of a Thermolyne 2100 programmable tube furnace reactor (50 cm length and 0.9 cm ID) for a controlled heating of the samples. For the CO oxidation reaction, the reactant gas mixture contains 3.40 vol. % CO and 20.0 vol. % O_2 in Ar mixture that is flown at a rate of 100 cm^3/min over a bed of the sample while sample is heated to different temperatures. The sample temperature is recorded using an Omega K-type thermocouple embedded in the middle of the sample. The flow of gas mixture is controlled by a digital flow meter. The temperature and concentration data are recorded using a Lab view-based program. The conversion of CO to CO_2 was monitored using an infrared gas analyzer. All the catalytic activities were measured using 10 mg of catalyst and after heat treatment of the catalysts at 200 °C in the reactant gas mixture.

The CO conversion was calculated based on the converted CO in the reactor according to

$$\% \text{ Conversion of CO} = [CO_{in} - CO_{out}]/[CO_{in}]*100 \quad (10)$$

where CO_{in} is the concentration of CO in the inlet gas and CO_{out} is the concentration of CO in the outlet gas.[83]

2.4.2 Suzuki Reaction

The carbon-carbon coupling-Suzuki reactions have been used for the assembly of complex organic molecules for a wide variety of applications with considerable impact on the chemical and pharmaceutical industries. The Suzuki reaction is a heterogeneous catalytic reaction and has many advantages such as simplicity, cleanliness and low cost. The cross coupling reaction is between an aryl or vinyl-boronic acid with an aryl or vinyl-halide, and is predominately catalyzed by palladium (Pd) catalysts. In some studies other catalysts such as Ni on charcoal,[84] Pd-graphene hybride,[85] and Au-graphene hybrids[86] have also been used. Palladium nanoparticles with high activity, stability, and recyclability are good candidate for these type reactions. After the discovery of carbon nano-materials especially graphene with a large surface area, carbon materials have been considered as potential support system for palladium nanoparticles. This reaction is a powerful and convenient synthetic method in organic chemistry for the generation of biaryls, conducting polymers, and liquid crystals.[87] A schematic presentation of this reaction is given below.

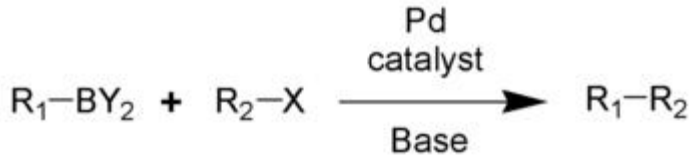

Figure 2.3. A typical carbon-carbon coupling reaction in solution using Pd catalyst.

To test a catalysts, a small quantity of bromobenzene (50 mg/0.32 mmol) was dissolved in a mixture of 4 mL H_2O:EtOH (1:1) and placed in a 35 mL microwave tube. First phenyl boronic acid (47 mg, 0.382 mmol, 1.2 eq.), and then potassium carbonate (133 mg, 0.96 mmol) was added to this solution. The metal catalyst (3 mol %) was added at the end. The test tube was sealed and heated under microwave irradiation (250 W, 2.45 MHz) at 150 °C for 5 min. A CEM Discover microwave instrument was used for cross coupling reactions. The reactions were performed at operator selectable power output of 250 W. Upon the end of reaction period, an aliquot of the reaction mixture was diluted with 10 mL of acetonitrile and injected into a GC-MS port. GC-MS analyses were performed on an Agilent 6890 gas Chromatogram equipped with an Agilent 5973 mass selective detector. The percentage conversion of the product was determined based on the consumption of the bromobenzene. Figure 2.4 presents a schematic of a typical carbon-carbon coupling reaction.

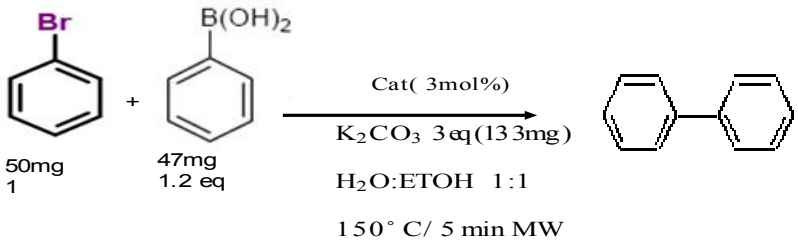

Figure 2.4. A schematic of Suzuki reaction used in this study.

To repeat the test, after the completion of the reaction, 10 mL of EtOH was added to the mixture and vigorously shaken. The entire mixture was centrifuged and the solvent above the

metal nanoparticle catalyst was completely decanted. EtOH washing followed by centrifugation was repeated two additional times to assure the removal of all products from the solution and catalyst surface. The metal nanoparticle catalyst was then transferred to another microwave tube along with fresh reagents for the next test.

2.4.3 Electrochemical Measurements

Cyclic voltammograms were obtained in a three-electrode system using glassy carbon electrode (GCE) with a potential of -0.44 V as the working electrode, a Pt wire as counter electrode and an Ag/AgCl electrode at room temperature. All the electrochemical measurements were carried out in a standard electrochemical cell with CH instruments Picocamp Booster & Faraday cage, and 0.1 M KOH aqueous solution saturated with oxygen as the electrolyte. The scan rate was 100 mV/s. The working electrode was fabricated by casting heteroatom (B, N, and BN) doped graphene onto a 5 mm diameter glassy carbon electrode. To prepare the sample, 1mg of the NG, BG, or BNG samples was ultrasonically dispersed into 5μL of Nafion solution for 1-2h. The glassy carbon electrode was coated by this mixture and then dried at room temperature. The reaction was carried out in a electrochemical cell by the known oxygen reduction mechanism, which happens in most of the fuel cell.

Chapter 3: CO Oxidation by Au/CeO_2 and Au/ZrO_2

3.1 Introduction

Low temperature catalytic activity, selectivity and stability during an operation are critical characteristics that could make nanoparticles among the great candidates for catalysis. As discussed in previous chapters, metallic nanoparticles have many applications including in catalysis. Metal particles deposited on metal oxide supports are a category of catalysts used for decades. Metal nanoparticles deposited on metal oxide catalysts with controlled particle size, high surface area and more densely populated unsaturated surface coordination sites could potentially provide significantly improved catalytic performance over conventional metal-metal oxide catalysts.[88]

CO oxidation at low temperature is of great environmental concern due to the poisonous and deadly nature of very small exposure (ppm) to this odorless and invisible gas.[89] Therefore, there is a need to develop highly active CO oxidation catalysts to remove even the trace amount of CO from the local environment at low temperatures.

Gold (Au), a noble metal and chemically inert element has shown catalytic activity for reactions such as CO oxidation at low temperature.[16] Gold supported on manganese oxides prepared in hydrogen atmosphere can oxidize CO.[90] Ceria (CeO_2) has shown remarkable redox properties, which have been used as a catalyst support in the synthesis of many catalysts. CeO_2,

as an oxygen buffer can release or adsorb oxygen through $Ce^{4+/}$ Ce^{3+} couple by redox process.[91] Highly non stoichiometric oxide nanoparticles such as CeO_{2-x} provide a high oxygen vacancy concentration and active superoxide surface species. It has been shown that for reduction of sulfur dioxide and the oxidation of carbon monoxide, CeO_2 nanoparticles could carry out the reaction at a low temperature[88] Ceria is an excellent support for gold nanoparticles due to its complex interaction with Au as cation and its particular lattice , which causes to increase redox activity.[92] Oxidation of formaldehyde by CeO_2 supported gold nanoparticles was conducted at a temperature close to 100 °C.[93] The Au/CeO_2 catalyst has shown a good catalytic reactivity toward aerobic oxidation of benzyl alcohol.[94] Gold is a strong and effective catalyst for the CO oxidation reaction but a major limitation is the CO adsorption on the gold surface. To effectively adsorb CO molecules, type of catalyst support, catalyst preparation along with gold-support interaction are important to be considered. It has been reported that Au nanoparticles on CeO_2-nanorodes improved overall catalytic activity more than just CeO_2 nanoparticles during CO oxidation.[95] Zirconia-supported Au catalysts have also been found to be active in many catalytic reactions such as CO oxidation, selective hydrogenation, and the water gas shift reaction. There are important factors influencing the catalytic activity of Au/ZrO_2 including the chemical states and size of Au nanoparticles, and the zirconia crystal phases.[96]

In this chapter the synthesis and characterization of Au nanoparticles catalysts supported on ceria and zirconia are first discussed using LVCC method. Then the performance of the synthesized catalysts for the low temperature oxidation of CO is evaluated.

3.2 Synthesis by Laser Vaporization Controlled Condensation (LVCC)

With the objectives of making catalyst for CO oxidation, gold (Au) nanoparticles supported on two metal oxides, namely CeO_2 and ZrO_2, were synthesized. The laser vaporization

controlled condensation (LVCC) method has been successfully used for the preparation of a variety of supported and unsupported metallic and bimetallic nanoparticle including Au on different oxide supports such as CeO_2, Al_2O_3, and SiO_2.[1] Thus the synthesis was carried out by simultaneous laser vaporization and controlled condensation of metal and metal oxide as was described in Chapter 2. The catalytic activities of the Au/CeO_2 and Au/ZrO_2 nanoparticles were examined for CO oxidation under mild conditions. The procedure for carrying out the performance test was also provided in Chapter 2. The synthesized catalytic samples were characterized using UV-Vis absorption, X-ray diffraction (XRD), transmission electron microscopy (TEM), and X-ray photoelectron spectroscopy (XPS). The activities of the synthesized catalysts were demonstrated by a home-made tubular reactor assembly.[1]

3.3 Results and Discussion

Figure 3.1 shows UV-Vis spectra of Au/CeO_2 and Au/ZrO_2. A peak around 550 nm was detected for all the samples, though it's less visible for 1% Au/CeO_2 sample, which could be due to a lower amount of Au nanoparticles in CeO_2. The weight percentages given here are the nominal percent of metal powders added to the metal oxide before pressing the mixture into a target. This result is consistent with prior work where the gold nanoparticles were suggested to display the characteristic optical signature of a Plasmon resonance in the visible region with 500-550 nm.[97] The absorption spectrum is affected by the size of nanoparticles indicating that the Plasmon resonance could slightly shift to higher energies (blue shift) as the particle size decreases. The aggregation, agglomeration, or changes in the shape of nanoparticles can result in a red shift of the absorption spectra.[98]

The XRD patterns of 1% and 5% Au/CeO_2 as CO oxidation catalysts along with Au and Ceria nanoparticles are shown in Figures 3.2 and 3.3. X-ray spectra were obtained for the

catalysts as prepared and after being used as a catalyst in CO oxidation. The crystal structure of Au/CeO_2 even after being used as a catalyst for CO oxidation remained unchanged meaning that its stability is reasonably well. The ceria (CeO_2) samples prepared by LVCC shows an XRD pattern with peaks at $2\theta = 28.7°$ (111), 33.3° (200), 47.4° (220), and 76.7° (331). The crystal structure of CeO_2 nanoparticles is face-centered cubic based on reference ICCD 00-034-0394.[83]

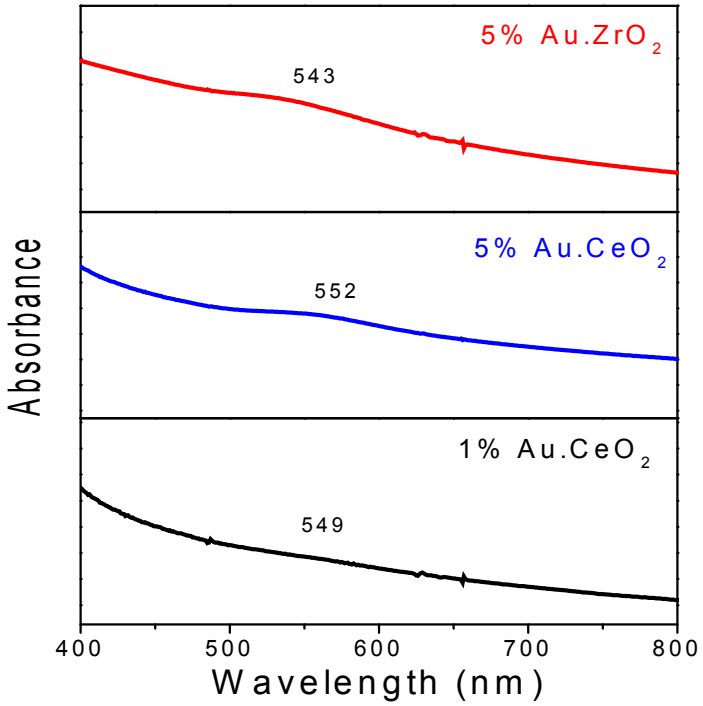

Figure 3.1. UV-Vis spectra of 1% Au/CeO_2, 5% Au/CeO_2, and 5% Au/ZrO_2 prepared by LVCC.

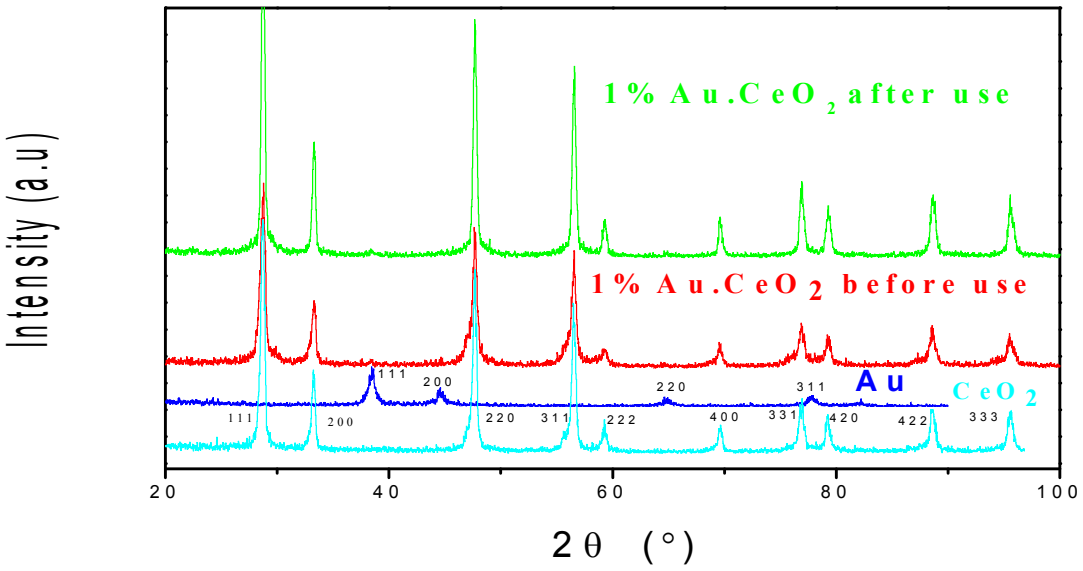

Figure 3.2. X-ray diffraction patterns of Au and CeO_2 nanoparticles as well as 1% Au/CeO_2 nanocomposite for before and after use as a catalyst for CO oxidation.

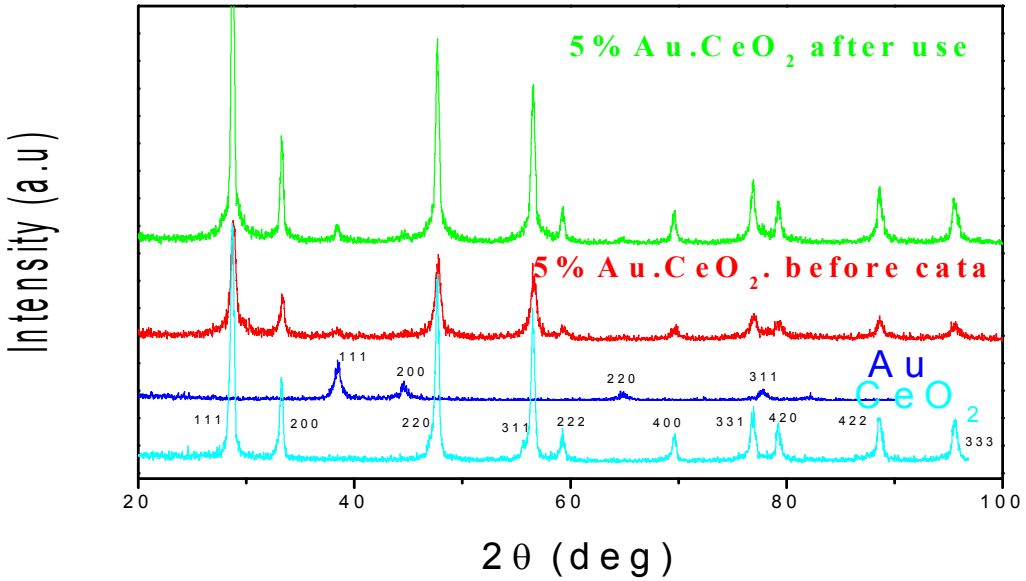

Figure 3.3. X-ray diffraction patterns of CeO_2 and Au nanoparticles as well as 5% Au/CeO_2 nanocomposite for before and after use as a catalyst for CO oxidation.

Figure 3.4 compares the XRD spectra of 5% Au/ZrO_2 catalyst as prepared and after use in CO oxidation testing. Based on the reference codes JCPDS 00-013-0307 and 01-079-0177

ZrO_2 has the monoclinic phase (major) and tetragonal phase (minor), with characteristic diffraction peaks at 2θ = 24.2° (011), 28.3° (-111), 31° (111), 34° (002), 49.3° (022), and 54° (202) representing the monoclinic phase.[99]

Figure 3.5 displays the XPS of 4f and 3d for Au on CeO_2 and ZrO_2 before and after the samples were used for CO oxidation. The gold metal binding energies of $4f_{5/2}$ and $4f_{7/2}$ in Au/ZrO_2 were 87.5 and 83.7 eV before use as a catalyst and after being used in CO oxidation testing were 87.3 and 83.7 eV respectively. No shift was observed for gold particles deposited on ZrO_2 before and after use as a catalyst, which is consistent with the data reported by Radnik et al. [100] The binding energies of gold metal were reported at 87.7 eV and 83.9 eV for $4f_{5/2}$ and $4f_{7/2}$ respectively.[101] The binding energies of Zr 3d spectra show $3d_{3/2}$ and $3d_{5/2}$ at 184.6 and 182.3 eV respectively.

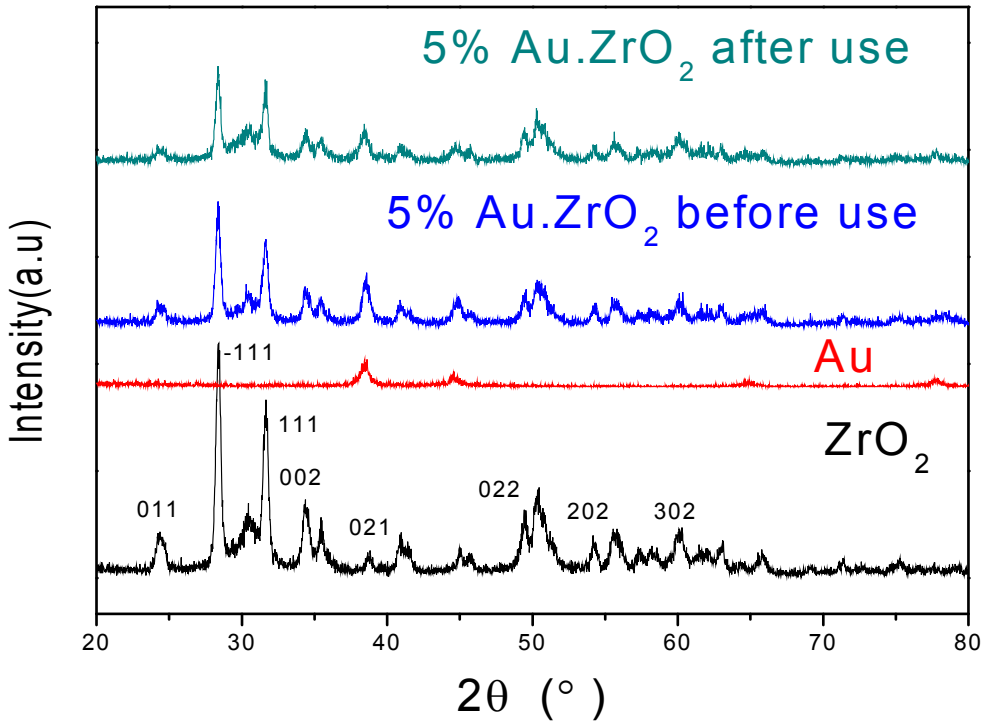

Figure 3.4. X-ray diffraction patterns of Au and ZrO_2 nanoparticles along with 5% Au/ZrO_2 nanocomposite for before and after use as a CO oxidation catalyst.

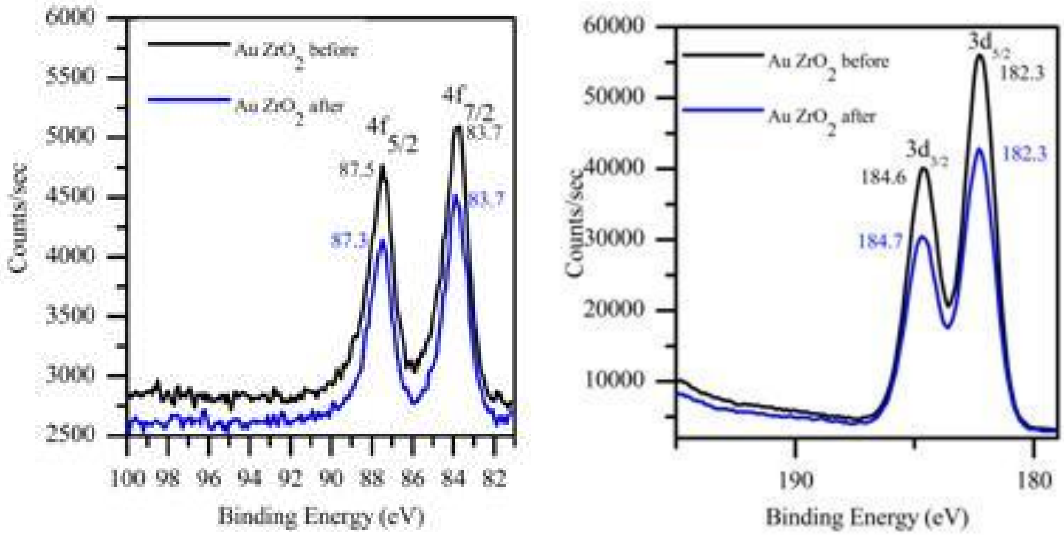

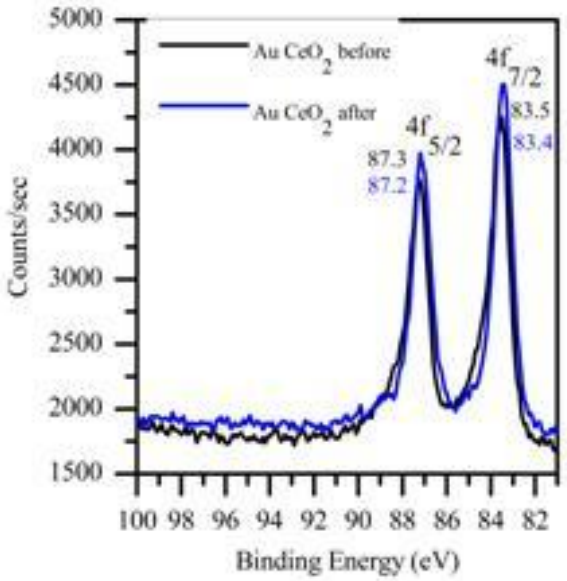

Figure 3.5. XPS spectra of 4f and 3d Au/ZrO_2 and 4f Au/CeO_2.

Figure 3.6 displays representative TEM images of 1% and 5% Au/CeO_2 and 5% Au/ZrO_2 before being tested as CO oxidation catalysts. TEM images of Au/CeO_2 and Au/ ZrO_2 catalysts show that most of Au nanoparticles are in the size range of 2 to 6 nm and well dispersed on the surface of support material with almost no large aggregates of Au nanoparticles. The particle size of 5% Au/CeO_2 was estimated around 6 nm from XRD data, which is comparable to an average size of around 4 nm estimated from TEM images. After catalyst being used, the particles show an increase in size, which can be seen from both XRD and TEM data indicating some aggregation as a result of heating during operation. The estimated average particle size based on TEM images for 5% Au/CeO_2 catalyst are around 4 nm before any testing and 10-12 nm after testing.

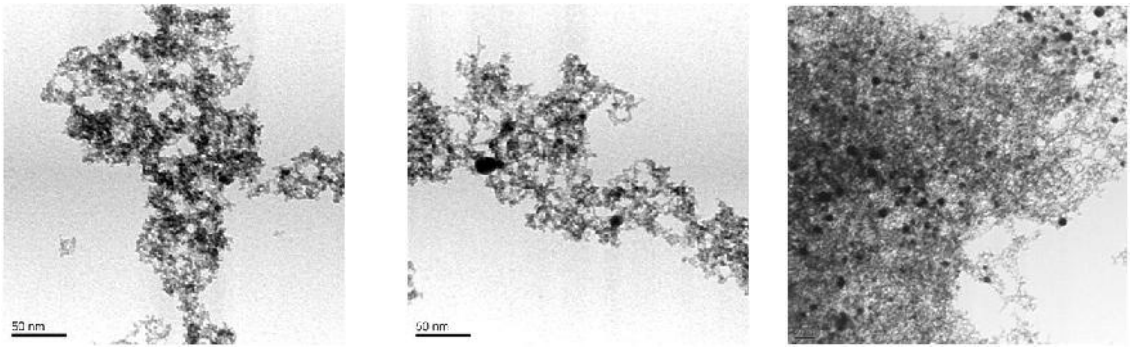

Figure 3.6. Representative TEM images for as prepared samples of 1% Au/CeO_2, 5% Au/CeO_2 and 5% Au/ZrO_2 from left to right respectively.

Figure 3.7a compares the CO oxidation activities of several catalysts including as-prepared 1% Au/CeO_2, 5 % Au/CeO_2 and CeO_2 nanoparticles prepared by LVCC. Figure 3.7b compares catalytic activities of 5% Au/ZrO_2 with pure ZrO_2 nanoparticles prepared by LVCC. The performance results clearly indicate the superior catalytic activity of 5%Au/CeO_2 catalyst with a complete oxidation (100% conversion) of CO at 66 °C. As can be seen from Figure 3.7a, the catalytic activity would be very different when Au powder and CeO_2 powders were physically mixed and used as catalyst. These results further point to the preparation of Au/CeO_2 that can lead to Au nanoparticles supported on CeO_2 nanoparticles with significant metal-support interaction. Next performing catalyst was 5% Au/ZrO_2 with 100% oxidation of CO at 176 °C, and the last performing catalyst was 1%Au/CeO_2 achieving a complete conversion of CO at 188 °C. These performances for the same catalysts are far better than previously reported results.[1]

Both oxides, CeO_2 and ZrO_2, especially as nanoparticles have shown to have redox properties and oxygen storage capacity indicting that enhanced active sites will improve their catalytic activity. Strong interaction between Au nanoparticles and support (CeO_2 or ZrO_2) are expected to be the causes of this high activity of Au/CeO_2 and Au/ZrO_2. Stability and reproducibility under typical reaction condition were tested and the result showed a complete CO

oxidation (100% conversion) at 86 °C for 5% Au/CeO_2 catalyst after one week of continuous use. This retained high activity can be attributed to the large surface area of the support, highly dispersed Au nanoparticles, interaction of Au and support and the nature of CeO_{2-x} surface oxygen species.[102]

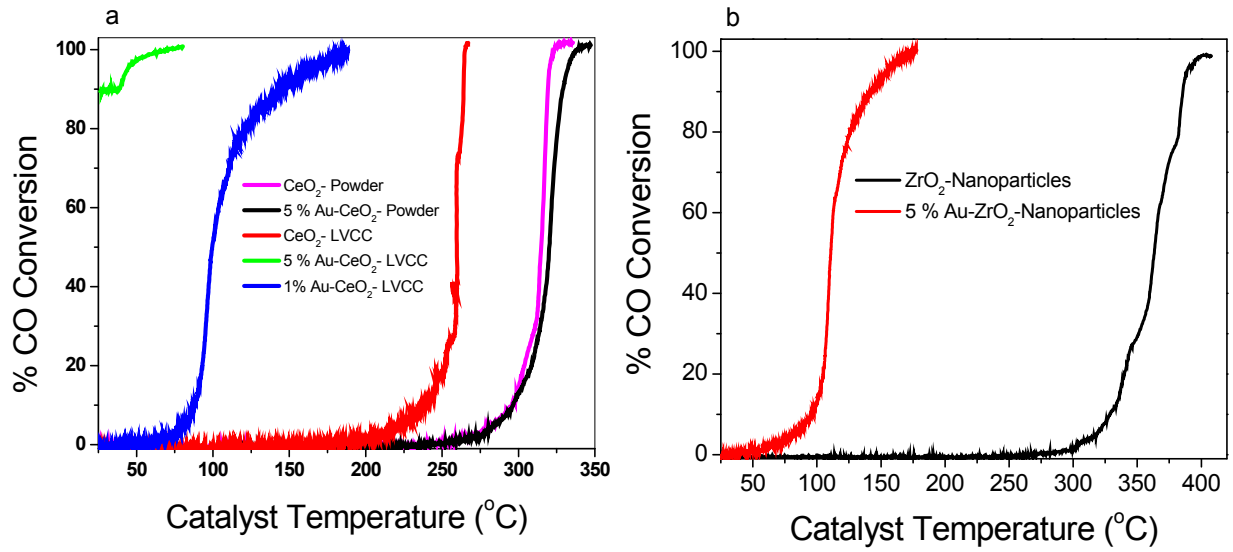

Figure 3.7. Catalysts performance for CO oxidation a as function of temperature for a reactant gas mixture containing 3.5% CO and 20.0 wt% O_2 in helium (20 mg catalyst and a flow rate of 100 cc/min), (a) CeO_2 powder, 5% Au-Ceria powder mixture, CeO_2 nanoparticles, 1% Au/CeO_2, and 5% Au/CeO_2, and (b) ZrO_2 nanoparticles and 5% Au/ZrO_2.

Chapter 4: Synthesis of Graphene, Doped Graphene, Metal-Containing Graphene, and Graphene Quantum Dots

4.1 Introduction

Graphene has become an important topic for research, innovation and technological discovery during the recent years. Graphene is a single-atom-thick planar sheet of bonded carbon atoms that is densely packed in a honeycomb type crystal lattice. An ideal graphene sheet is a single layer of a two-dimensional hexagonal sheet of carbon atoms, but it commonly exists in two or more layers and is called bi-layer and multi-layer graphene (between 2 to 10 layers).[50] Ideal graphene is characterized as a zero band gap semiconductor or semi-metal, and its unique electronic properties produce an unexpectedly high opacity for an atomic monolayer, with an extremely low absorption ratio of 2.3% of white light.[103] Electrical property of a graphene sheet is remarkable with high electron mobility at ambient temperatures, with an experimentally measured value[104] above 200,000 $cm^2V^{-1}S^{-1}$. The corresponding resistivity of the graphene sheet would be on the order of 10^{-6} ohm-cm , which is lower than the resistivity of silver, the lowest resistivity substance known at room temperature.[105] This is due to its exceptional properties , which including the quantum Hall effect at ambient temperature,[53] a bipolar electric field effect along with unique condition of charge carriers,[104] a tunable band gap,[106] a high elasticity,[107] a high current density, chemical inertness, high thermal conductivity (5000 W/mK),[108] optical

transmittance and super hydrophobicity on the nanometer scale.[109] The graphene sheet has a high value of Young's modulus (1100 GPa),[107] fracture strength (125 GPa),[107] and specific surface area (a calculated value of 2630 m^2g^{-1}).[110] Although graphene sheets are expected to be ideally flat, ripples occur due to processing inefficiencies and thermal fluctuations. Graphene sheets can become corrugated, wrapped into 0D fullerenes, rolled into 1D nanotubes or stacked into 3D graphite.

Graphene (or 2D graphite) has been studied for almost sixty years. The synthesis of monolayer graphite was attempted as early as 1975 by Lang[52] who showed the formation of mono- and multi-layered graphite by thermal decomposition of carbon on single crystal platinum substrates. Many years later and during the late 1990's, scattered attempts to produce graphene were reported again. However, Novoselov et al.[111] were credited for the discovery of graphene in 2004. Graphene has shown great application potential in various fields such as electronic devices,[50] nanocomposite materials,[112] sustainable energy storage and conversion (ultra capacitors,[113] batteries,[114] fuel cells,[56] and solar cells[115]).

Deposition of inorganic nanoparticles including metals or semiconductors on the surface of graphene sheets presents special features in new hybrid materials that can be useful in optical and electronic devices, catalysts, and sensors. Supporting metal nanoparticles on the graphene sheets could prevent the formation of stacked graphitic structures because metal nanoparticles can act as spacers to increase the distance between the sheets. This could lead to an increase in the surface area of the nanoparticles-graphene composites.[116] Recently, the composites of graphene with precious metal nanoparticle such as Ag/graphene and Pt/graphene have been reported[54] and used as a catalyst for oxygen reduction[55] and methanol oxidation.[56] El-Shall et al. [51] reported the deposition of metal nanoparticles on graphene surface by laser irradiation of mixture of graphene oxide and metal ion

precursors (gold or silver) in water or other solvents. Apart from making composite catalysts, decoration of graphene with metallic nanoparticles also becomes necessary to make the structure more suitable for usage in electronics, optics and biotechnology related applications. For example, graphene with a few layers was found to be easily decorated with Pt, Ag, and Au nanoparticles where decoration enhances its application in opto-electonics.[57] However, there are few publications concerning the loading of metal nanoparticles on graphene sheets.

Graphene is an excellent candidate for the next generation of electronic materials due to the strict two-dimensionality of its electronic structure as well as its extremely high carrier mobility. A prerequisite for the development of a graphene based electronic device is the reliable control of the type and density of the charge carriers by external (gate voltage) and internal (doping) means.[117] While gating has been successfully demonstrated for graphene flakes, the development of reliable chemical doping methods turns out to be a real challenge. The chemical doping of graphene falls into two categories: surface transfer and substitutional doping. For surface transfer doping, electron exchanges between a graphene and dopants is usually realized by adsorbing atoms or molecules on graphene surface.[118] In this case, dopants do not disrupt the structure of graphene. Molecules with electron withdrawing groups adsorbed on the surface of graphene makes p-type and molecules with donating will lead to n-type doping. The electrical conductivity of graphene varies as a result of interaction with electron-donor molecules (softens G-band or shift to lower frequency in Raman) and electron–acceptor molecules (stiffen G-band Raman, shift to higher frequency). For n-type (or p-type) doping the electrons have to be released into (extracted out of) the graphene layer. P-type doping drives the Dirac points of graphene above the Fermi level, and n-type doping drives the Dirac points below the Fermi level. Substitutional doping refers to the substitution of carbon atoms in the honeycomb lattice of graphene by atoms having different number of valence electrons such as

nitrogen and boron. The incorporation of foreign atoms would disrupt sp^2 hybridization of carbon atoms.[58] Adding atoms with fewer valence electrons than carbon like boron make p-type while adding atoms with more valence electrons than carbon makes n-type like nitrogen. An upshift was reported for the G-band in both nitrogen and boron doped graphene. Figure 4.1 illustrates the doping of graphene; it shows a free-standing graphene layer where the left (Fig 4.1a) and right (Fig 4.1c) panels visualize n-type and p-type doping, respectively. The center panel (Fig 4.1b) shows the pure graphene layers. In this work, the surfaces of graphene sheets were decorated by metal nanoparticles and substitutionally doped with nitrogen, boron, and co-doped with nitrogen and boron.

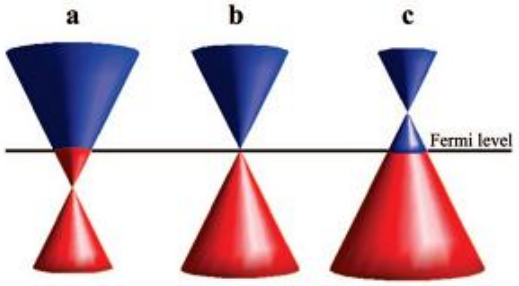

Figure 4.1. An illustration of doping graphene with the position of the Dirac point and the Fermi level of pristine and epitaxial graphene as a function of doping.[117]

Graphene, owing to its large specific surface area and high thermal and electrical conductivities, is also a good candidate as a support material for metal nanoparticles. As a result, one of the objectives of this work was to deposit metal nanoparticles onto the graphene surfaces and investigate the catalytic activities of composite materials towards the Suzuki reaction.

4.1.1 Previous Work on Graphene Synthesis

There are different processes to prepare graphene including chemical vapor deposition (CVD)[59], arc discharge of graphite,[60] micromechanical exfoliation of graphite,[61] epitaxial growth on electrically insulating surfaces such as SiC, solvothermal synthesis,[62] laser excitation of

graphite oxide in solution,[63] and the reduction of graphene oxide (GO).[64-65] The reduction of GO has generally been carried out in liquid phase by chemical methods using different reducing agents such as hydrazine,[66] hydroquinone,[67] and $NaBH_4$.[68] Though the chemical pathways for the GO reduction remain unclear, hydrazine hydrate is one of the best reducing agents for the chemical reduction of exfoliated GO to produce very thin graphene sheets.[51] This reduction leads to deoxygenation of the GO (removal of oxygen functionalities such as hydroxyl and epoxide groups) and to significant restoration of the sp^2 carbon sites and re-establishment of the conjugated graphene network.[119] Reduction of GO was recently reported under alternative conditions such as alkaline conditions,[69] ultraviolet-assisted methods,[70] and thermal methods.[71-72] Among them, thermal treatment is a green process where no hazardous chemicals are used but process requires rapid heating (>2000 °C min^{-1}) up to 1050 °C in an oven under argon[73] or up to 800 °C under hydrogen gas.[74] Though the rapid reduction of GO under mild conditions seems to be very difficult, Fozooni et al.[75] have reported that a microwave can heat the graphite or amorphous carbon (in powder form) to a high temperature in a short period of time, and it had been successfully applied in the exfoliation of the graphite.[75]

Another method for the reduction of GO is laser irradiation in solution to produce laser-converted graphene (LCG) sheets.[120] This method provides a solution processable synthesis of individual graphene sheets in water at ambient conditions without the use of any chemical reducing agent. El-Shall et al. [120] reported that reduction of GO in different mixture such as ethanol-water and PEG-water showed most of the oxygen-containing groups in GO are removed after the laser irradiation. Chemical reduction methods using microwave heating have been employed for the production of metal/metal-oxide nanoparticles supported on the defect sites of reduced graphene oxide (GO) nanosheets.[121] The main advantage of microwave irradiation over

other conventional heating methods is the rapid and uniform heating of the reaction mixture.[122] Unlike conventional thermal heating, MW allows a better control of the extent of GO proceeds by yield a nearly complete reduction of GO. The reduction of GO proceeds by rapid deoxygenation to create C-C and C=C bonds.[51] The occurrence of non-equilibrium local heating of graphite oxide is likely to result in the generation of hot spots (electric discharge) in the reduced graphene oxide, which could lead to the development of structural defects in the graphene lattice. These defect sites act as nucleation centers for the formation of the metal nanoparticles, which can be anchored to the graphene sheets.

Recent advances in the production of graphene sheets through the reduction of GO have provided efficient approaches for the large scale production of chemically converted graphene in solution.[72] However, chemical reduction methods suffer from the difficulty of controlling the reduction process and the potential for residual contamination by the chemical reducing agents , which necessitates the use of multiple solvents and several post synthesis treatments such as drying and thermal annealing.[59] Other methods such as thermal annealing at high temperatures, laser photoreduction, and plasma discharge processes have been attempted and offer several advantages over chemical reduction including the efficient removal of oxygen from GO without the use of toxic chemical reducing agents.[76] However, thermal annealing requires high temperatures and the use of ultrahigh vacuum equipment for the efficient removal of oxygen from GO.[76] On the other hand, photoreduction methods including flash photolysis and laser irradiation have been demonstrated to be effective only in GO solutions[76] or on thin films of GO supported on substrates.[77] Similarly, a plasma-assisted reduction method has been recently applied to films of GO casted on polymeric substrates.[78] The formation of freestanding 2D graphene was achieved through laser exfoliation of highly ordered pyrolytic graphite (HOPG)

using a pulsed neodymium-doped yttrium aluminum garnet (Nd:YAG) laser.[79] If the laser flux ranges from 1.0 to10.0 J/cm^2, ultrathin sheet fragments were peeled off from the HOPG and deposited onto a substrate surface as graphene. The chamber was evacuated to 10^{-5} Torr and then filled with argon gas to 1 Torr.

The objectives of this chapter are the synthesis and characterization of graphene, hydrogen terminated graphene, nitrogen-and boron doped graphene, metals nanoparticles supported on graphene and graphene quantum dots (GQDs). The metals nanoparticles supported on graphene are further evaluated using Suzuki reaction. As indicated earlier, LVCC was used for the first time in this study to synthesize graphene from graphite oxide. In this approach, a large quantity of hydrogen-terminated graphene (HTG) nanosheets was prepared without the need for chemical reducing agents, solvents or high temperatures equipment.[123] Materials, equipment and procedures for preparing graphene were thoroughly described in Chapter 2.

4.1.2 Results and Discussion

The process of laser exfoliation is expected to reduce graphite oxide to graphene. When a pulsed laser irradiates the GO surface, the visible laser photons are absorbed and photothermal and potentially photochemical processes are frequently carried out. The average C–C, C-O, and C=O bond energies are 3.6, 3.7, and 7.69 eV respectively. The pulsed laser used in this study is the second harmonic (532 nm) of a Nd-YAG laser (15-30 mJ/pulse).The photon energy of the this laser equivalent to a wavelength of 532 nm is 2.3 eV, and this energy is not sufficient for direct photochemical bond breaking. Therefore, only photothermal mechanisms play a major role in the laser exfoliation. Absorption of two 532 nm photons by GO excites electrons from valence to conduction bands (2.3 eV). This generates electron-hole pairs within the GO followed by non-radiative recombination, which results in efficient energy conversion. Because electron lattice

temperature equilibrium occurs on the picoseconds time scale, the resulting thermal energy is sufficient for the rapid removal of O, H, and C from the lattice. This removal leads to the formation of deoxygenated GO or hydrogen terminated graphene.[124]

The XRD patterns of graphite oxide (GO), hydrogen terminated graphene (reduced GO) and graphite are compared in Figure 4.2. GO is characterized by a peak at $2\theta = 10.9^{o}$ corresponding to the (002) plane of GO, which exhibits a larger d-spacing of 8.14 Å as compared to the typical value of 3.34 Å in graphite. This larger spacing results from the insertion of hydroxyl and epoxy groups between the carbon sheets and the carboxyl groups along the terminal and lateral sides of the sheets through the oxidation process of graphite.[59] The $2\theta = 10.9^{o}$ peak disappears in all the synthesized graphenes using LVCC. This confirms the loss of a long-range order in the GO stacked layers and implying the deoxygenation of GO and the restoration of the sp^2 carbon sites in the resulting graphene (HTG or RGO) nanosheets.[59] For comparison, the bulk graphite was also processed with LVCC in the presence of helium carrier gas to directly remove graphene nanosheets (Figure 4.2). From the XRD pattern of graphene produced by LVCC processing of graphite that the peak at $2\theta = 27.9^{o}$ corresponding to the (002) plane of hexagonal graphite has disappeared. Therefore, the processing of GO and graphite by LVCC results in the loss of long-range order that are presented by 2θ peaks at 10.9^{o} and 27.9^{o} for GO and graphite, respectively.

The UV-Vis spectra of GO and graphene prepared by LVCC processing of GO in the presence of He or He-H_2 are shown in Figure 4.3a. The samples were suspended in extra methanol before taking their UV-Vis spectra. The UV absorption spectrum of GO shows significant absorption below 400 nm with a characteristic shoulder at 305 nm attributed to $n \rightarrow \pi^*$ transitions of C=O bonds.[63] It is clear that this shoulder disappears after the LVCC processing of

GO, and the absorption peak of GO at 230 nm red shifts to 270 nm and 274 nm in the presence of He and He-H_2 carrier gas, respectively. This finding indicates the presence of $\pi \rightarrow \pi^*$ transitions of extended aromatic C-C bonds, suggesting that the electronic conjugation within the deoxygenated sheets is restored following the processing of GO by LVCC.[63] This result also indicate the presence of H_2 in the He carrier gas enhances the reduction of GO during the LVCC process.

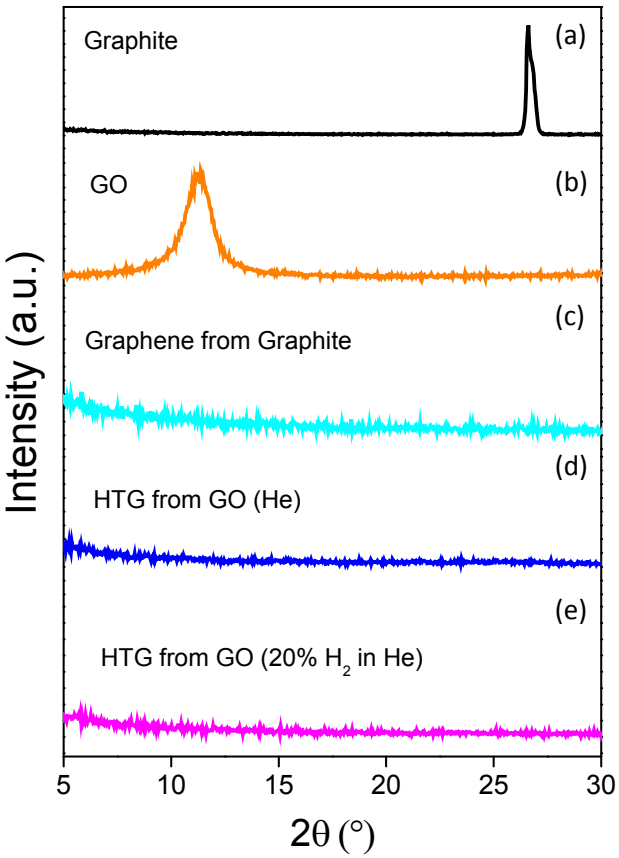

Figure 4.2. X-ray diffraction data of (a) graphite, (b) graphite oxide (GO), (c) graphene produced by LVCC of graphite in helium, and (d) and (e) HTG produced by LVCC of GO in helium and 20% H_2-helium mixture, respectively.

Figure 4.3b compares the FTIR spectra of graphite, graphite oxide (GO), and graphenes prepared by LVCC processing of graphite and GO. The graphite spectrum has no significant

peaks since graphite is an IR inactive solid. Similarly, the spectrum of the graphene produced by LVCC of graphite shows no significant peaks. The GO spectrum shows strong bands corresponding to the C=O stretching vibrations of the COOH groups at 1730 cm^{-1}, the O-H deformations of the C-OH groups at 1350-1390 cm^{-1}, the C-O stretching vibrations at 1060-1100 cm^{-1}, and the epoxide groups at 1230 cm^{-1}.[63] In addition, a strong and broad O-H stretching vibration at 3420 cm^{-1} is observed resulting from water adsorbed on GO. These bands are completely absent from the spectrum of graphene prepared in He or H_2-He, confirming deoxygenation of GO following the LVCC process. The LVCC method can also reduce GO to hydrogen terminated graphene (HTG), which the FTIR clearly confirm this results as shown in Figure 4.3. The spectrum clearly shows aliphatic C−H stretching bands in the 2840−2950 cm^{-1} region, for samples prepared under H_2-He atmosphere. The strong similarity between the FTIR spectra of the bulk graphite and graphene produced by the processing of either graphite or GO with LVCC and the absence of any oxygen-related features in these spectra confirm that the graphene sheets produced by the LVCC process are free of oxygen functional groups.

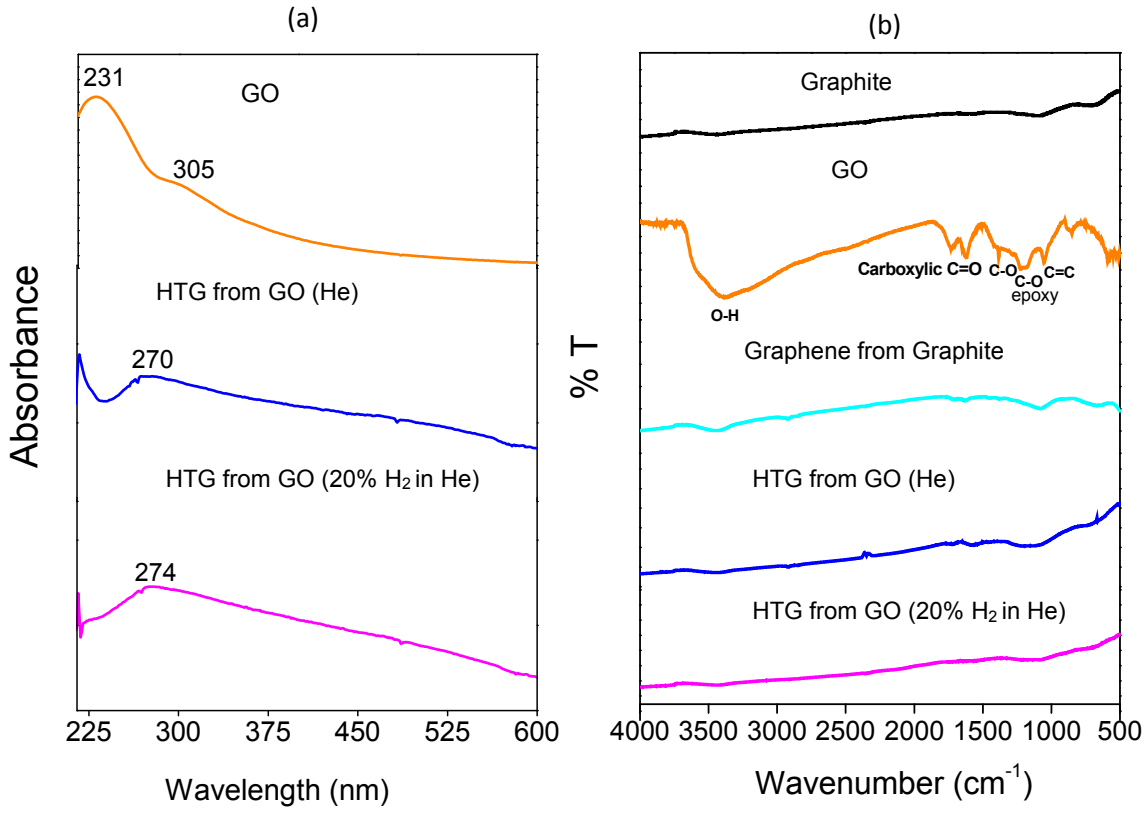

Figure 4.3. (a) UV-Vis spectra of graphene oxide (GO) and graphene prepared by the LVCC of GO in pure He and in a 20% H_2-He mixture, and (b) FTIR spectra of graphite, graphite oxide (GO), and graphene samples from graphite and from GO in He and 20% H_2-He prepared by LVCC.

Figure 4.4 displays the XPS C1s spectra of GO and graphene prepared by the LVCC method using different carrier gases. The GO spectrum shows peaks corresponding to oxygen-containing groups between 285.5 and 289 eV, in addition to the sp^2-bonded carbon C=C at 284.5 eV. Typically, peaks at 285.6, 286.7, 287.7, and 289 eV are assigned to the C1s of C-OH, C-O, C=O, and HO-C=O groups, respectively.[63] The XPS spectrum of graphene clearly indicates the removal of oxygen-containing groups in GO after the LVCC process, particularly in the presence of the H_2-He gas mixture. Based on the XPS curve fitting using a Gaussian-Lorenztian peak shape analysis, the ratio of carbon to oxygen was estimated by dividing the area of the C1s and

O1s peaks and multiplying by the corresponding photoionization cross sections. The calculated atomic percent and C/O atomic ratio for the GO target used in experiments and the graphene

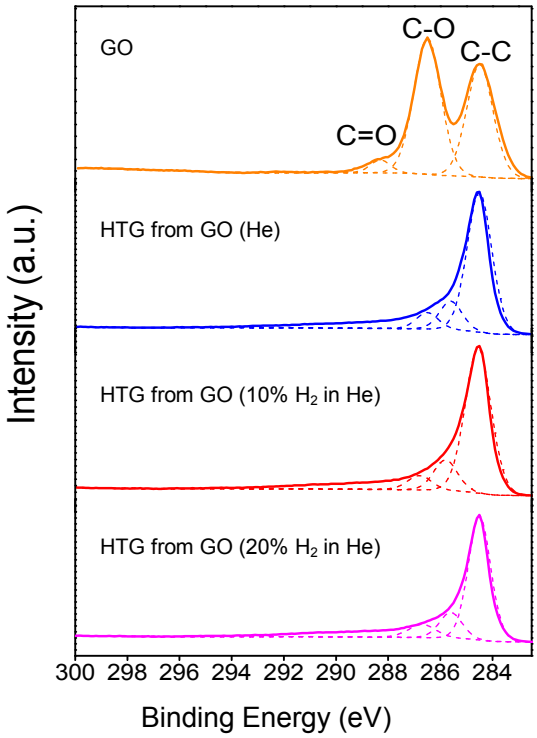

Figure 4.4. XPS C1s spectra of graphite oxide (GO) and graphene prepared by the LVCC processing of GO in pure He and in H_2-He carrier gases.

Samples prepared using pure He and 20% H_2 in He by LVCC are shown in Table 4.1. It is clear that the C/O ratio increases from about 1.91 in the GO to 4.71 in the graphene prepared in pure He by LVCC process. This indicates that laser vaporization of the GO sheets was accompanied by a significant removal of oxygen atoms most likely in the form of CO, CO_2 and H_2O vapors. However, in the presence of 20% H_2 in helium, the resulting graphene sample shows a significant increase in the carbon atomic percent (89.7%), which results in a C/O ratio of about 8.71. This indicates the presence of H_2 in the LVCC process plays an important role in the reduction of the GO nanosheets. This can be explained by the formation of atomic hydrogen

within the plume of the laser vaporization of GO, which can act as an efficient reducing agent for GO. It should be noted that further increase in the amount of H_2 for up to 50% in He did not result in any further increase in the carbon percent of the resulting graphene. Therefore, the 20% H_2 in helium was considered an optical value and used in the preparation of all the graphene samples by LVCC method. The C/O ratios in the graphene samples prepared in He and H_2-He gases can be further increased to 5.67 and 11.50, respectively by annealing the samples at 400 °C in helium for 3 hrs. The increase in the C/O ratio is most likely due to the removal of the residual oxygen functional groups in the graphene samples following the LVCC process.

Sample No.	Sample Description	C (%)	O (%)	C/O
1	GO	65.7	34.3	1.91
2	HTG from GO (He)	82.5	17.5	4.71
3	HTG from GO (He)[a]	85.0	15.0	5.67
4	HTG from GO (20% H_2-He)	89.7	10.3	8.71
5	HTG from GO (20% H_2-He)[a]	92.0	8.0	11.50

Table 4.1. The calculated atomic percent and C/O atomic ratio for the GO target and HTG samples prepared using LVCC. (a) sample was annealed at 400 °C in helium for 3hrs.

In addition to XRD, UV-Vis, FTIR, and XPS data, the successful conversion of GO to graphene using the LVCC method was further confirmed by Raman spectroscopy. Figure 4.5 displays Raman spectra of graphite, GO and graphene prepared by the LVCC processing of graphite and GO. The graphite spectrum shows the typical G-band at about 1568 cm^{-1}, which is common to all sp^2 carbon materials arising from vibrations of sp^2-hybridized carbon atoms. The

spectrum of graphene prepared by the LVCC processing of graphite shows a broader G-band almost at the same frequency as that of bulk graphite, in addition to the disorder-induced D-band at about 1363 cm^{-1} and a D/G intensity ratio of ~0.40. The D-band requires defects for its activation, and therefore, its intensity provides a measure for the amount of disorder in graphene.[125] The intensity ratio of the D-band to the G-band is usually used as a measure of the quality of the graphitic structures since for highly ordered pyrrolitic graphite, this ratio approaches zero.[125] The Raman spectrum of GO shows a broadened and blue shifted G-band (1584 cm^{-1}) as compared to graphite, and a D-band at 1372 cm^{-1}.[126] The spectrum of the graphene prepared by the LVCC processing of GO in the presence of 20% H_2 in He shows a strong G-band around 1571 cm^{-1}, almost at the same frequency as that of graphite, and a relatively weak D-band around 1372 cm^{-1}. This result provides a D/G intensity ratio (I_D/I_G) of ~0.54 as compared to a value of 0.67 in GO, indicating a decrease in the degree of disorder and defect sites following the LVCC processing of GO.[126]

Figure 4.6 displays representative TEM images of the graphene nanosheets prepared by LVCC method from GO in the presence of helium and 20% H_2 in helium. It is apparent from these images that LVCC produces wrinkled and partially folded sheets with a lateral dimension of up to a few microns in length. These images confirm that the LVCC process exfoliates the GO sheets from the GO target where they undergo deoxygenation and reduction without any evidence for the destruction of their layer structures or atomization to produce carbon nanoparticles.

Thermal stability of the hydrogen terminated graphene samples prepared under different LVCC conditions was also examined using TGA and the results were compared to that of GO as shown in Figure 4.7. Samples were heated from room temperature to 700 °C at a heating rate of

10º C/min under high purity nitrogen gas. As can be seen from Figure 4.7, the graphene sample prepared under H_2-He atmosphere shows a much better stability and a lower weight loss comparing to other graphene samples. GO sample in this test showed a weight loss of about 10%

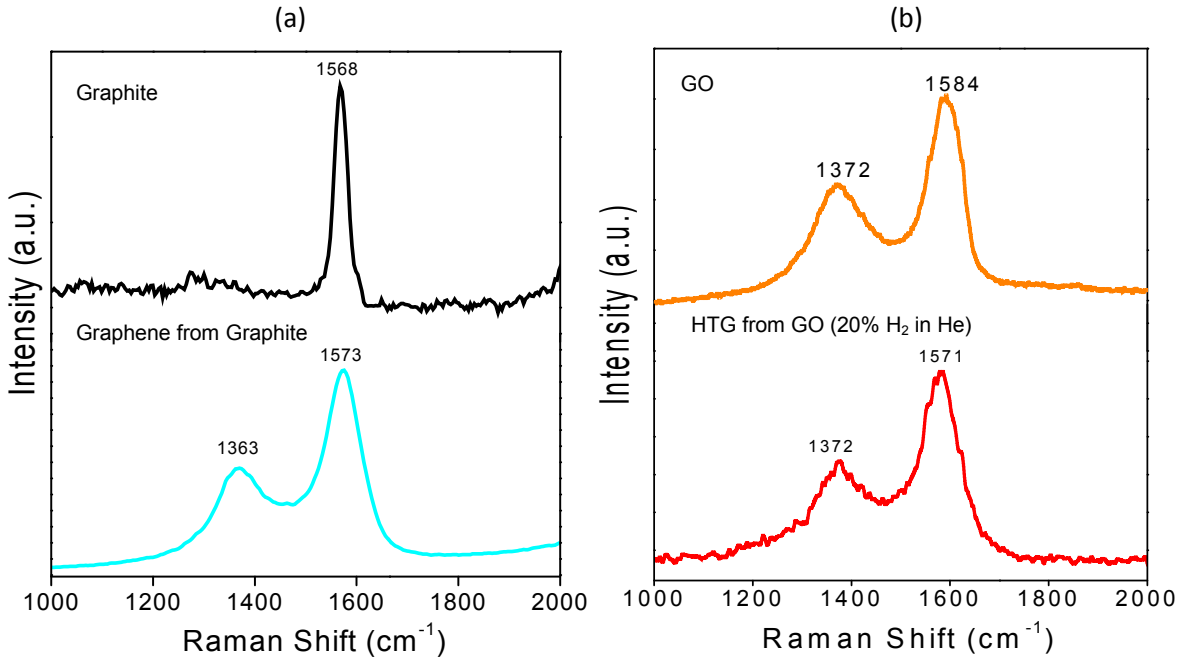

Figure 4.5. Raman spectra of (a) graphite and graphene prepared from graphite, (b) graphite oxide (GO) and HTG prepared under 20% H_2/He atmosphere by LVCC method.

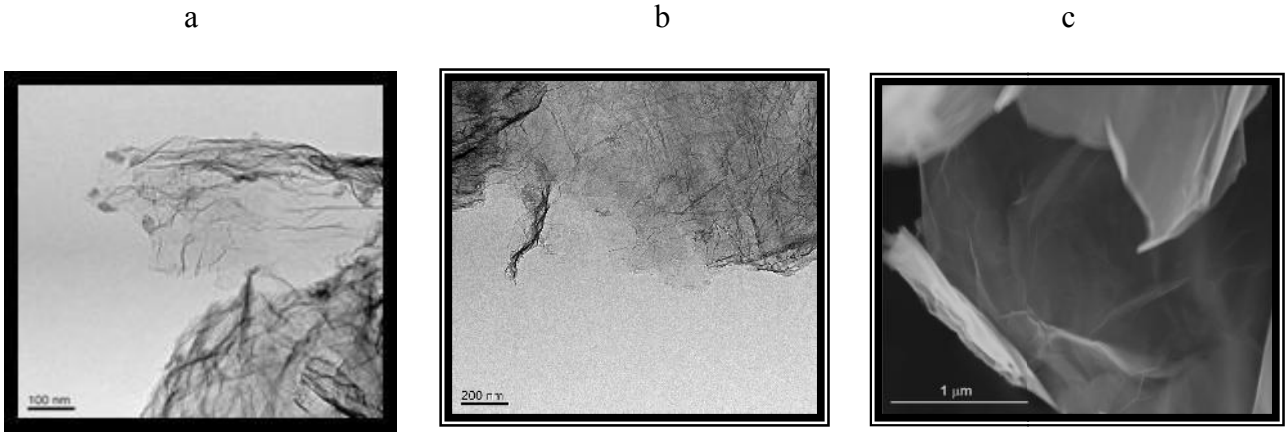

Figure 4. 6. Representative TEM images of HTG nanosheets prepared by the LVCC of GO in (a) pure He, (b) 20 % H_2-He and (c) SEM image of HTG prepared in He.

by about 100 ºC, another 30% by about 200 °C and lost the rest of its weight by about 550 °C. The weight lose is believed to be the results of the removal of adsorbed water and the liable oxygen containing functional groups such as CO and CO_2. This results are consistent with the results given by Chen et al.[127] and somewhat different from that of Shen et al.[128] and Li et al.[129] where they noticed only about 50% weight loss for GO up to 700 °C with most of the weight loss at about 200 °C. In contrast to Li et al.'s results, the reduced graphene oxide samples in this study showed different thermal behavior. The sample prepared under H_2-He showed a better stability and a lower mass loss up to about 500 °C. This sample retained about 20% of its weight when temperature reached 700 °C in TGA.

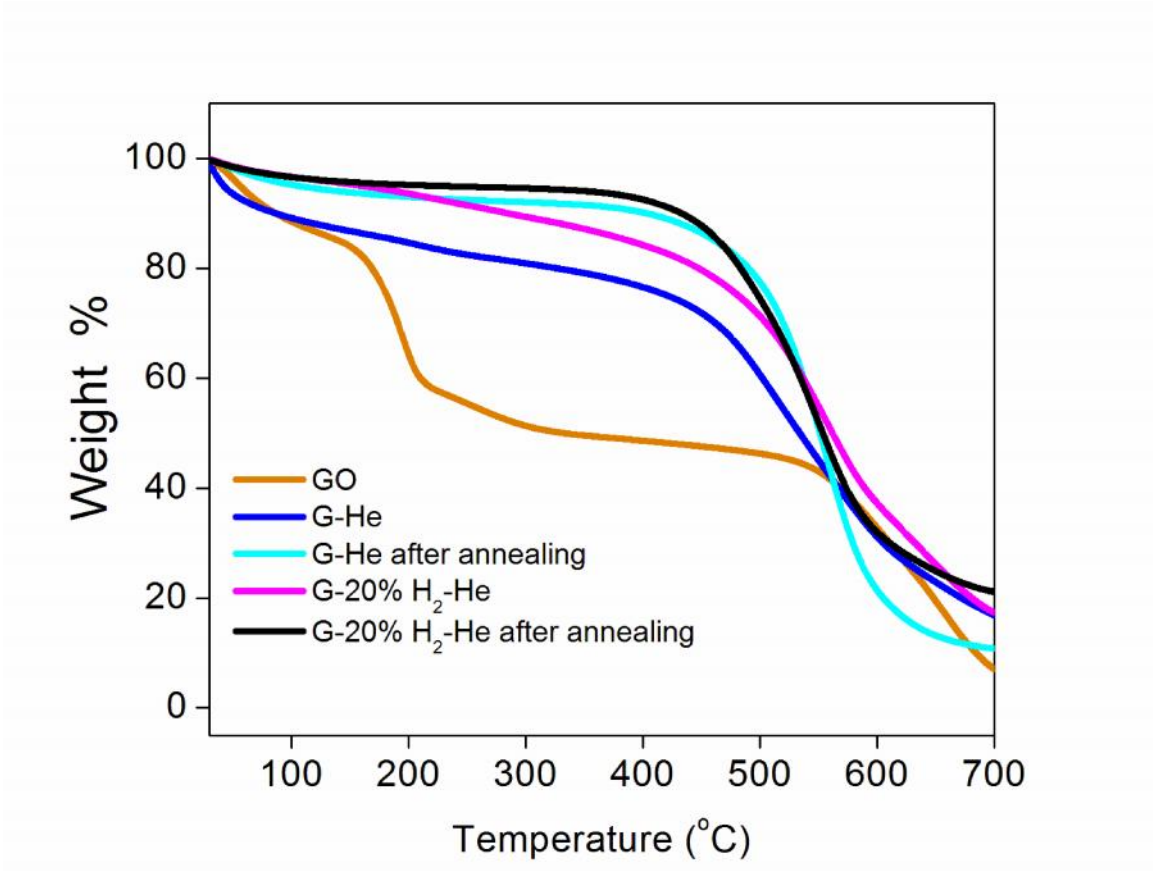

Figure 4.7. Thermal gravimetric analysis of graphene samples prepared by LVCC method.

4.2 Synthesis of Nitrogen, Boron, and Co-Doped Boron-Nitrogen Graphene

Graphene can be considered a semiconductor with a zero band gap semiconductor, which its electronic structure can be altered by opening band gap. There are three groups for opening the band gap: Heteroatom doping, chemical modification, and electrostatic field tuning. Employing the heteroatom doping and chemical modification methods can open the band gap and tune the Fermi level of graphene. Using electrostatic field tuning method, the polarity and value of gate voltage can change the Fermi level of graphene without opening the band gap. The electronic properties of graphene are strongly influenced by a delocalized π electron system, and as a result any chemical modification of the graphene may affect these properties. Thus by proper choice of modification, the electronic properties of graphene can be intentionally tuned. Doping is another term used for tuning of electronic properties.

There are two approaches for chemically doping graphene including adsorption of gases, metals, or organic molecules[130] on graphene surface and substitutional doping, which incorporate heteroatoms into the carbon lattice. Nitrogen and boron atoms are good substitutional dopant for carbon materials due to their atomic size and having five or three valence electrons available to form strong valence bonds; thus, have a reasonable probability to enter into the carbon lattice.[131] These elements can introduce donor (nitrogen) or acceptor (boron) states near the Fermi level. As a result they can change the electronic and transport properties of the resultant graphene. It has been reported that when one nitrogen or boron atom is incorporated into a carbon nanotube (CNT), there will be an impurity level near the conduction band minimum or the valence band maximum. Therefore, the CNT is changed from intrinsic semiconductor to n-type or p-type semiconductor. [132] When a zigzag graphene nanoribbon (ZGNR) is doped with N or B atoms, its electronic properties is also affected strongly. [133]

The inclusion of nitrogen, boron or both into the network of carbon structure may facilitate charge transfer between adjacent carbon atoms and consequently improve the electrochemical performance of the material. Wu et al.[134] reported nitrogen-boron doped graphene. Based on all-solid state super capacitors, doped graphene displays a high specific capacitance (62 Fg^{-1}) and an enhanced energy density (1600 Wkg ^{1}) respect to pure graphene, nitrogen, or boron doped graphene.

Graphene has been effectively doped with nitrogen by different methods.[135] Nitrogen attaches to different configurations in graphene network including pyridinic, pyrolytic, and graphitic; each introduces special property in graphene network. It has been theoretically reported that pyridinic type nitrogen shown to have p-type characteristic whereas graphitic nitrogen has n-type characteristic.[136] Most of the published data so far shown to have at least two kinds of nitrogen present in carbon network adding both n-type and p-type properties simultaneously to graphene. Adding unique property to graphene is achieved by only adding one type of nitrogen into the graphene network, which is being difficult to accomplish. According to Wang et al.[137] by doping graphene with nitrogen or boron, n-type or p-type semiconducting graphene can possibly be obtained.

In the last few years, a number of attempts have been made to prepare nitrogen doped graphene. Nitrogen doped graphene was made by thermal exfoliation of graphite oxide (GO) in the presence of ammonia[138] or melamine,[139] transformation of nano-diamond in the presence of pyridine, and electrothermal annealing of graphene in NH_3.[135] Most the methods except CVD yield both pyridinic and graphitic nitrogen. Chemical vapor deposition (CVD) of CH_4/NH_3 or C_2H_4/NH_3 can dope graphene selectively with graphitic[139] or pyridinic type nitrogen.[140] Selectively preparing one type of nitrogen in the graphene in bulk scale is highly desirable. It is

also important to understand the properties of graphene doped with each type of nitrogen to make use of this for specific applications. Lin et al.[141] synthesized boron doped graphene by reduction of tetrachloromethane and boron tribromide using an alkali metal reductant. Nitrogen and boron-doped graphene have been prepared by arc discharge of graphite electrodes in the presence of H_2 - B_2H_6 for boron doped and H_2-NH_3 for nitrogen doped graphene.[132] Wu et al.[142] produced boron doped monolayer graphene (BG) by chemical vapor deposition of polystyrene, urea and boric acid at 1035 °C. Thermal annealing of graphite oxide in the presence of B_2O_3 is another way of producing boron doped graphene.[143] These methods require complex experimental setup, high temperatures, rigorous conditions and poisonous reagents such as B_2H_6 or BBr_3. Wu et al.[144] reported preparation of heteroatom (N, B, or P) doped carbon nanotubes, graphene and graphite. Wang el al.[137] reported synthesis of vertically aligned carbon nanotubes co-doped with N and B by pyrolysis of melamine diborate. Wang et al. also synthesized N-/B-doped graphene by thermal annealing of graphite oxide in the presence of boric acid under ammonia atmosphere.[145] Hydrothermal reaction and freeze-drying of graphite oxide in ammonia boron trifluoride (NH_3BF_3) gave boron nitrogen doped graphene.[134] Zheng et al.[146] reported synthesis of boron-nitrogen doped graphene from solution – exfoliated graphite oxide by a two step doping method. First nitrogen was added by annealing of GO in NH_3 and then boron was introduced by pyrolysis of H_3BO_3.

The substitution of a number of carbon atoms with heteroatoms such as N, B, S, and P is also an effective way to tailor graphene activity and selectivity as a catalyst for certain catalytic applications. The substitution of carbon with heteroatoms modifies graphene electron transfer properties and consequently enhances its catalytic activity. In particular, co-doping with two elements, one with higher and one with lower electronegativity than that of carbon could create a

synergistic coupling effect. An example of this situation is nitrogen with higher (χ=3.04) and boron with lower (χ=2.04) electronegativities than that of carbon (χ=2.55). This synergistic effect makes such dual-doped graphene catalyst much more catalytically active than singly doped graphene.[146] Reddy et al.[147] suggested that pyridinic nitrogen is responsible for increased oxygen reduction activity as well as increased Li ion storage capacity in graphene. The boron-nitrogen doped graphene can be an efficient catalyst for metal free oxygen reduction reaction in fuel cells and metal–air batteries.[145] Wu et al.[134] reported that a N/B co-doped graphene can potentially be a super capacitor for energy-storage device.

For the first time, laser vaporization controlled condensation was used in this study to synthesize nitrogen, boron, and nitrogen-boron doped graphene (NG, BG, and BNG). The laser exfoliation of graphite oxide by laser ablation and under an appropriate gaseous atmosphere can produce a single- or dual-doped graphene. The advantages of this technique along with the details of the materials, equipment setup and experimental procedure were given in detail in Chapter 2.

4.2.1 Results and Discussion

Figure 4.8 shows X-ray diffraction (XRD) patterns of nitrogen doped graphene samples prepared by laser exfoliation of graphite oxide under different gaseous conditions using LVCC. The XRD spectra of GO, graphite, and HTG were presented in Figure 4.2 and was thoroughly explained. Graphite oxide sample shows a peak at 11°, which is an illustration of the effective conversion of graphite to GO. Briefly, there is no peak around 11° for exfoliated graphene (Figure 4.8) indicating that graphite oxide has been converted to graphene. A weak or no (002) peak between 20-30° in nitrogen doped graphene is indicative of a lower number of layers in NG comparing to graphite oxide sample. The samples represented by NG-100, NG-250, and NG-500

were prepared with an ammonia partial pressure of 100, 250, and 500 Torr respectively. For NG-250ad sample, the chamber was first filled with pure ammonia to a total pressure of 800 Torr and held for overnight (about 15 hrs). The ammonia pressure was dropped to 550 Torr during the holding time indicating a significant adsorption of ammonia by graphite oxide. The chamber was then purged and filled with helium to a total pressure of 800 Torr, and the bottom plate was heated to about 90 °C.

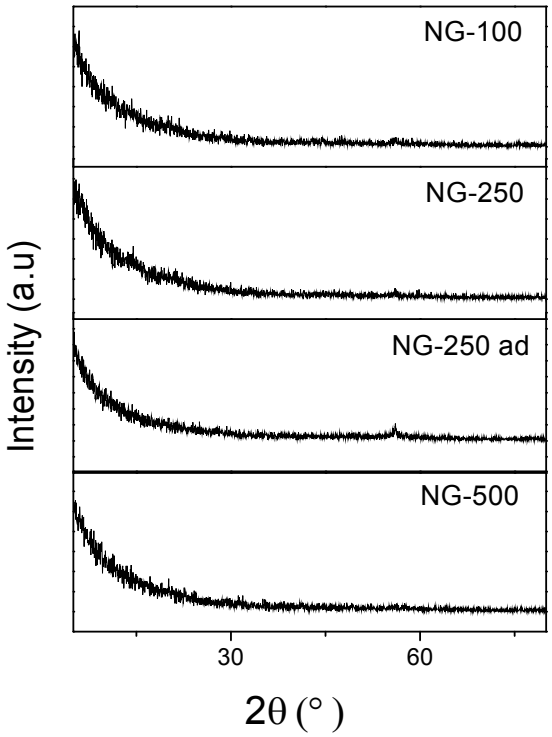

Figure 4.8. X-ray diffraction spectra of graphite oxide and nitrogen doped graphene (NG-100, NG-250, NG-250ad, and NG-500).

Figure 4.9a shows the X-ray diffraction (XRD) patterns of boron doped graphene samples prepared by LVCC processing of graphite oxide in the presence of B_2H_6-He gas mixture. Figure 4.9b presents the X-ray spectra of boron–nitrogen doped graphene samples, which were prepared by laser ablation (LVCC) of graphite oxide in the presence of B_2H_6-NH_3-

He gas mixture. The XRD spectra of both boron and boron–nitrogen doped graphene samples show a peak at 56°. This peak based on reference code 00-023-0073 is plausibly B (1420). It is obvious from the results that there is no peak around 11° in the case of exfoliated graphene indicating that graphite oxide is converted to graphene in the BG and BNG samples. The samples denoted BG-150, BG-300, and BG-400 were prepared under a B_2H_6 partial pressures of 150, 300, and 400 Torr respectively. Similarly, the sample denoted 100B-100N, 100B-200N, and 200B-200N were prepared under partial pressures of 100 B_2H_6/100 NH_3, 100 B_2H_6/200 NH_3, and 200 B_2H_6/200 NH_3 respectively.

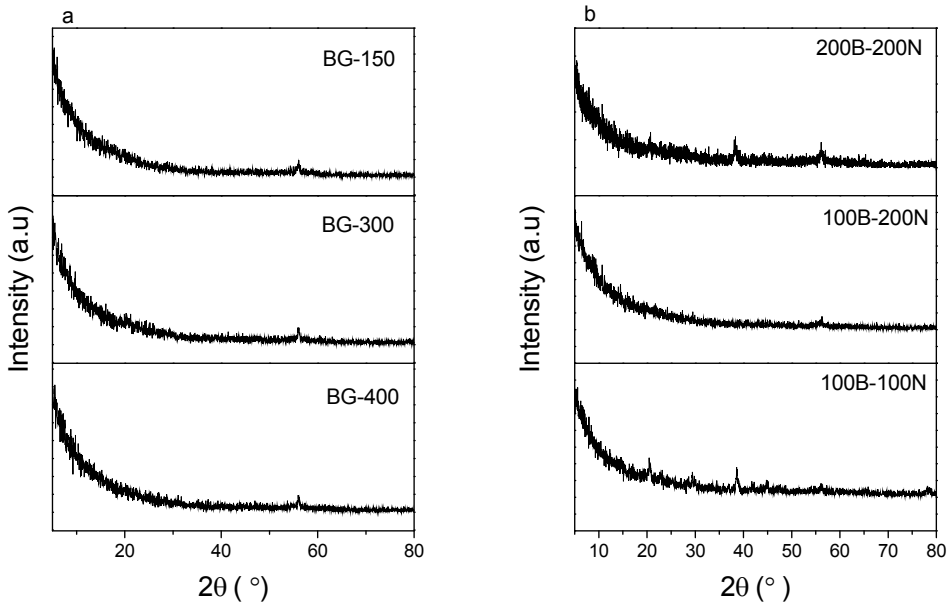

Figure 4.9. X-ray diffraction spectra of (a) boron doped graphene (BG-150, BG-300, and BG-400) and (b) boron-nitrogen doped graphene (BNG: 100B-100N, 100B-200N, and 200B-200N).

Raman spectra of pure as well as nitrogen doped graphene samples prepared by laser exfoliation using LVCC are shown in Figure 4.10. The Raman spectrum of graphene shows three characteristic features including a tangential G-band (~ 1580 cm^{-1}) and a disorder induced D-band (1375 cm^{-1}). The G-band positions of graphene in NG-100, NG-250, NG-250ad, NG-500, and NG-600 samples are at 1579, 1587, 1579, 1581, 1583, and 1583 cm^{-1}, respectively. Raman

results indicate a shift in G-band samples of the nitrogen doped graphene samples comparing to pure graphene, which is consistent with previous work.[148] Panchakarla et al.[148] observed the G-band stiffening in the Raman spectra of N-doped graphene. Many factors can affect this shift in G band including type of doping,[149] number of layers in graphene sample,[150] levels of defects and structural strain. The ratios of I_D/I_G for nitrogen doped graphene samples are lower comparing to that of graphene sample prepared by the same method. This is an indication of a lower level of defects in the nitrogen doped samples prepared by LVCC method. The Raman band positions as well as I_D/I_G ratios of nitrogen doped samples prepared by LVCC are given in Table 4.2.

The Raman spectra of boron doped graphene prepared by laser exfoliation using LVCC are shown in Figure 4.11. All samples show two bands one around 1375 cm^{-1} and another at 1580 cm^{-1}. It has been observed by Panchakarla et al.[148] that G-band of boron-doped graphene shows stiffness, which is consistent with the G-band positions of BG-150, BG-300, and BG-400 at 1579, 1584, and 1586 cm^{-1}, respectively. Like nitrogen doped samples, results indicate shifts in G-band for boron doped graphene samples. There is a blue shift in BG-300 and BG-400 samples that can be explained by the size of the C-C ring, change in the electronic structure, level of boron, and sign of atomic insertions.[142] The peak intensity in the doped samples increased respect to graphite meaning that the defects in boron doped samples could include bonding disorders and vacancies in the graphene lattice that are created by boron doping.[151] The ratios of I_D/I_G in boron doped graphene samples are less than that of graphene indicating a lesser number of defects in the samples. The Raman band positions and I_D/I_G ratios of boron doped samples are given in Table 4.3.

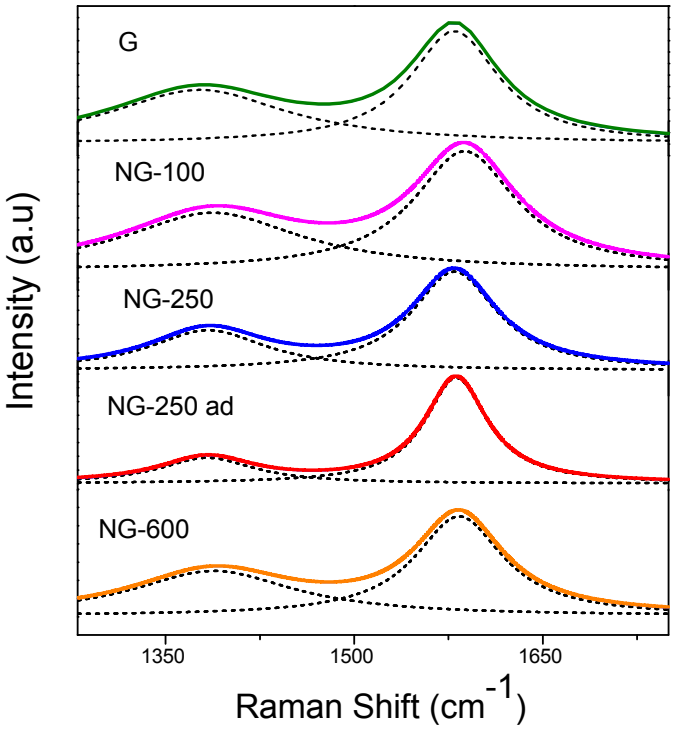

Figure 4.10. Raman spectra of graphene and various nitrogen doped graphene samples identified as NG-100, NG-250, NG-250ad, NG-500, and NG-600 prepared by LVCC methods at an excitation wavelength of 532 nm.

Sample ID	G-band (cm^{-1})	D-band (cm^{-1})	I_D/I_G
Graphene	1579	1377	0.94
NG-100	1587	1387	0.82
NG-250	1579	1383	0.56
NG-250ad	1581	1383	0.37
NG-500	1583	1386	0.41
NG-600	1583	1388	0.82

Table 4.2. Comparison of Raman peak positions and I_D/I_G ratios for graphene and nitrogen doped graphene samples.

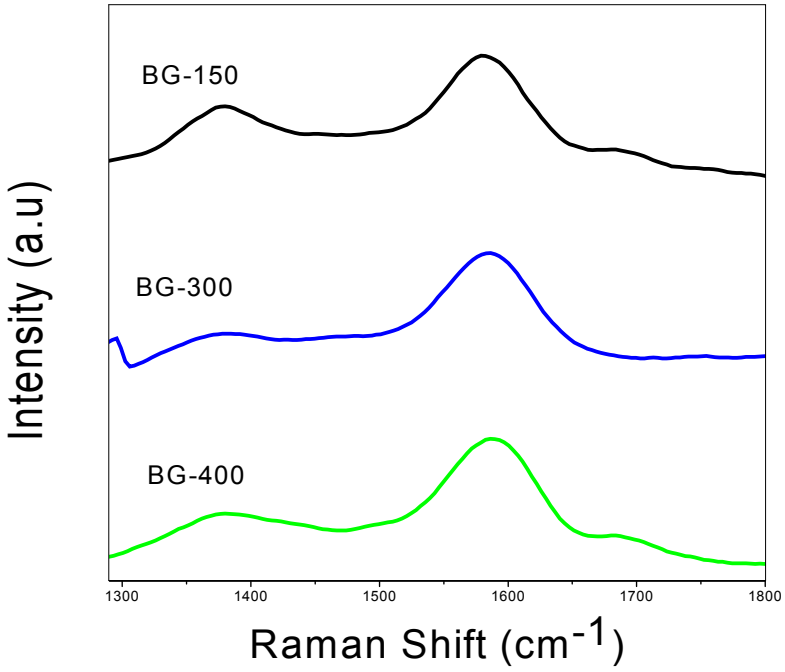

Figure 4.11. Raman spectra of boron doped graphene samples identified as BG-150, BG-300, and BG-400 prepared by LVCC at an excitation wavelength of 532 nm

Sample ID	G-band (cm^{-1})	D-band (cm^{-1})	I_D/I_G
Graphene	1579	1377	0.94
BG-150	1579	1377	0.85
BG-300	1584	1373	0.76
BG-400	1586	1374	0.79

Table 4.3 Comparison of Raman peak positions and I_D/I_G ratios for graphene and boron doped graphene samples.

The Raman spectra of boron-nitrogen doped graphene (BNG) samples prepared by LVCC are shown in Figure 4.12. All samples share two bands: one at around 1340 cm^{-1} and another at around 1580 $cm^{-1}$for the D-band and G-band respectively. The G-bands position of BNG samples, as shown in Table 3.4, are at 1575, 1580, 1580 cm^{-1} for 100B-100N, 100B-200N, and 200B-200N respectively. As can be seen from Figure 4.12 and shown in Table 4.4, there is little to no shift in the G-band and a slight down shift in D-band and 2D-band of boron-nitrogen doped graphene samples , which is consistent with earlier literature.[134] The ratios of I_D/I_G in boron-nitrogen doped samples are higher than that of graphene prepared by the same method. This result indicates that co-doped graphene samples have a higher number of defects than graphene and could possibly be due to the simultaneous introduction of two different elements.

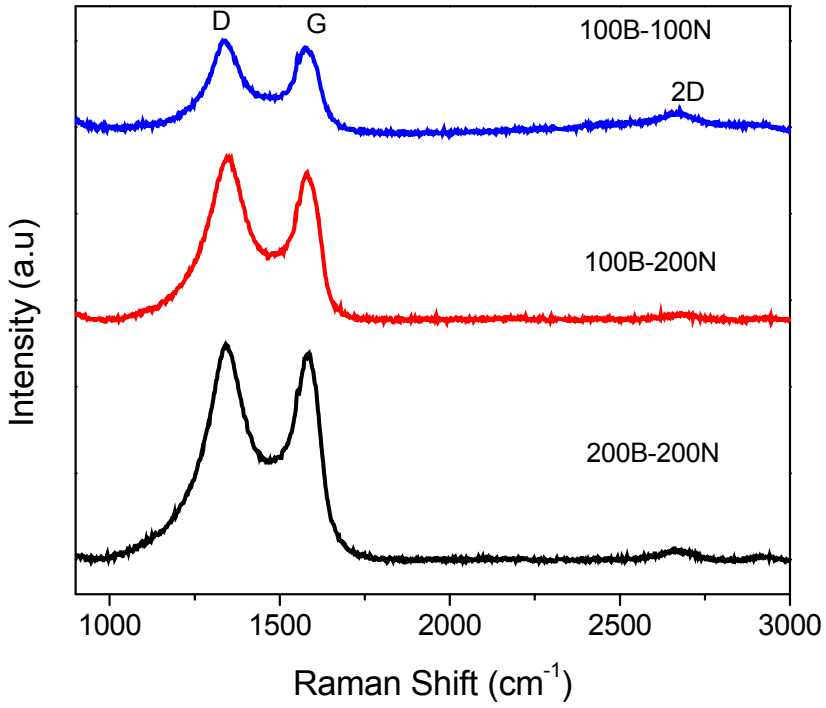

Figure 4.12. Raman spectra of boron-nitrogen doped graphene samples identified as 100B-100N, 100B-200N, and 200B-200N prepared by LVCC at an excitation wavelength of 532 nm.

Samples ID	G-band (cm^{-1})	D-band (cm^{-1})	2D-band (cm^{-1})	I_D/I_G
Graphene	1579	1377	2744	0.94
100B-100N	1575	1341	2668	1.0
100B-200N	1580	1346	2678	1.04
200B-200N	1580	1341	2663	1.03

Table 4.4. Comparison of Raman peak positions and I_D/I_G ratios for graphene and boron-nitrogen doped graphene samples.

Overall, the D and G bands of nitrogen, boron and boron-nitrogen doped graphene nanosheets shift and their I_D/I_G ratio differ from that of graphene nanosheets, which are due to the structural distortion of graphene originated by different bond distances of C-C, C-N, and C-B. It is instructive to remember that the G band arises from the bond stretching of all sp^2 bonded pairs, including C-C, B-C, N-C, and B-N; while the D band is associated with the sp^3 defect sites[145].Thus the above mentioned shifts and ratio changes are further evidence of N and B doping of graphene.

Figure 4.13 shows UV-Vis of boron doped graphene samples prepared by laser exfoliation using LVCC method. In all samples including graphene only one peak around 275 nm can be observed. Thus, this technique hardly provides any differentiation among the samples. The UV-Vis results of boron-nitrogen doped graphene samples are given in Figure 3.14. Similar to boron doped samples, boron-nitrogen samples show only one peak around 275 nm.

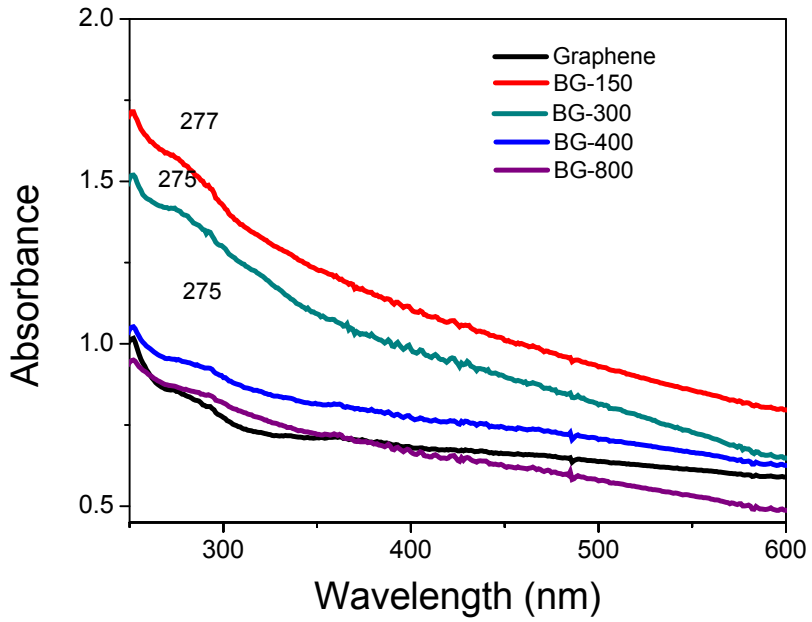

Figure 4.13.UV-Vis spectra of boron doped graphene (BG) prepared at different partial pressure of B_2H_6 using LVCC.

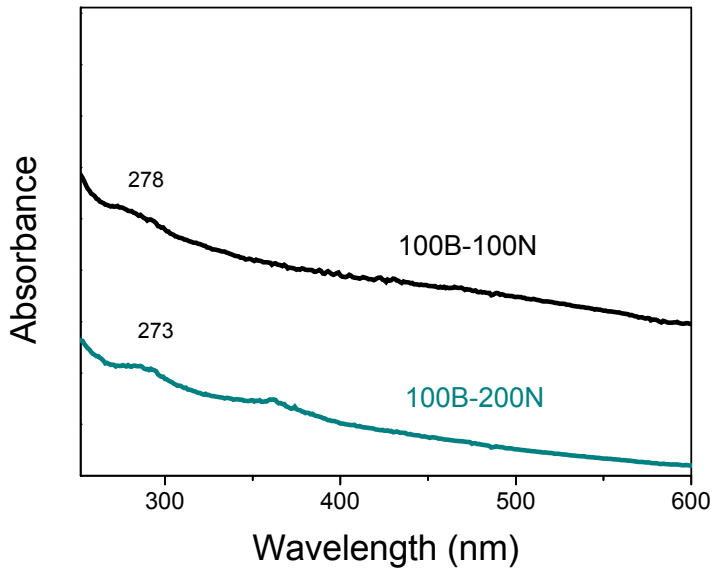

Figure 4.14. UV-Vis of boron-nitrogen doped graphene (BNG) samples prepared at different partial pressures of NH_3 and B_2H_6 using LVCC.

.

The X-ray photoelectron (XPS) spectra of C1s and N1s of nitrogen doped graphene are shown in Figure 4.15. Carbon 1s signal appears at approximately 284.5 eV. The asymmetry of C1s peak conforms to the presence of both C-N and C-O bonding. The higher binding energy peaks at 285.3 and 285.8 eV are attributed to C–N and C–O functional groups, respectively. There are two peaks in N 1s spectra indicating the existence of more than one component. Based on the XPS curve fitting, it becomes clear that there are three peaks centered at around 399.7, 400, and 401.7 eV, which correspond to pyridinic, pyrrolic, and graphitic nitrogen respectively. Based on the XPS data, the atomic percent of nitrogen in the doped samples is 4.0, 5.4, 5.5, and 8.7 for NG100, NG250, NG250ad, and NG600 respectively. It is interesting to note that as the nitrogen content of graphene samples increase so the intensity of the pyridinic component, which is expected to be advantageous over graphitic nitrogen for different applications.[139] The pyridinic nitrogen is thermodynamically more stable compared to graphitic nitrogen and this could be the plausible reason for increasing the intensity of pyridinic component with increasing nitrogen content of graphene sample. A striking observation was that when NH_3 partial pressure was at 250 Torr in the chamber, pyridinic nitrogen doped graphene was the dominant product.

Ammonia adsorbs chemically as well as physically on the graphite oxide structure. The amount of adsorbed NH_3 on graphite oxide increases with time and temperature exhibiting the chemical and physical natures of adsorption. Adsorption also depends on traces of water present in the GO[152] , which in this case, due to multiple vacuuming and purging of the chamber, is expected to be minimal. Rate of adsorption is higher at the beginning where the process is much less diffusion limited for chemisorptions, which seems to be reason for the production of pyridinic component. NH_3 reacts either via Bronsted and Lewis acid containing -COOH groups.[153] The reaction of ammonia with carboxylic acid species leads to the formation of mainly

intermediate amide (Lewis acid route) through nucleophilic substitution. As the temperature locally increases during laser irradiation of graphite oxide, the intramolecular dehydration and decarbonylation take places to form thermally stable heterocyclic aromatic moieties such as pyridine[154] as shown in Figure 4.16. Amide ($C{=}ONH_2$) and quaternary ammonia ($COONH_4$) are expected to be the representative products of Lewis and Bronsted acids reactions with graphene with the respective binding energy of N1s at 399.2 and 401.4 eV. As it can be seen from Figure 4.15, the NG-250 sample shows only the pyridinic component (399.8 eV) and does not contain graphitic component (402 eV) indicating that quaternary nitrogen is driven out of GO and does not contribute to doping. The controlling factors for this unexpected result could be the lack of precise control for bottom plate heating time and laser irradiation time to produce a given amount of product.

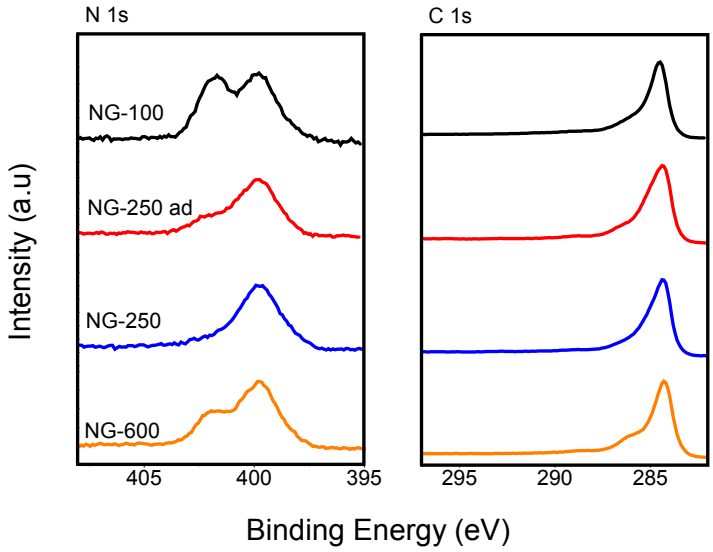

Figure 4.15. XPS N1s and C1s spectra of nitrogen doped graphene prepared under different ammonia partial pressures.

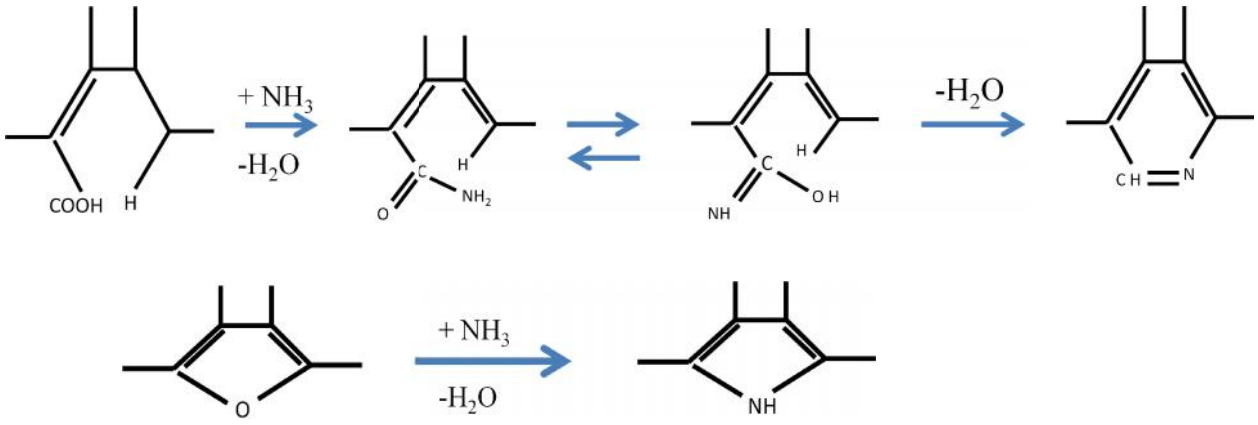

Figure 4.16. Proposed pathways for nitrogen insertion into the graphene lattice.

The X-ray photoelectron spectra of B1s and C1s of boron doped graphene samples are displayed in Figure 4.17a and b. Carbon 1s signal is at approximately 284.0 eV. The asymmetry of C1s peak conforms to the presence of C-C, C-B, and C-O bonds. Based on the XPS curve fitting, four peaks are distinguishable in each spectrum (A, B, C, and D). These four peaks in C1s peak are designated as C-C for A, C-O for B, C=O or C-N for C, and C-C=O or C-B for D. The asymmetric peak of C1s shifts to lower binding energies as B_2H_6 partial pressure in the chamber increases. Results show binding energies of 284.2, 283.9, and 283.8eV for BG-150, BG-300, and BG-400 samples respectively compared to a binding energy of 284.5eV for un-doped graphene. However, the peak intensity of C1s for boron doped graphene is lower than that of un-doped graphene indicating the graphene structure was broken to some extent and the number of sp^2-bonded carbon atoms were decreased.[143]

Based on the XPS data, boron doped graphene (BG) samples contain 1.33, 2.23, and 3.29 atomic % boron in BG-150, BG-300, and BG-400 samples respectively. The B1s spectra has a peak at 192 eV (as shown in Figure 4.17) , which is assigned to the B-C2 bond consistent to Han at al.[155] Any B1s peak that appears at 190 eV and higher binding energy (B1s peak of pure boron

is at 187 eV) indicates that the boron atoms from B_2H_6 vapor should have been incorporated into the carbon sp^2 network. This is clear evidence that graphene nanosheets have been doped by boron atoms and indicative of B-C bond formation in all samples.

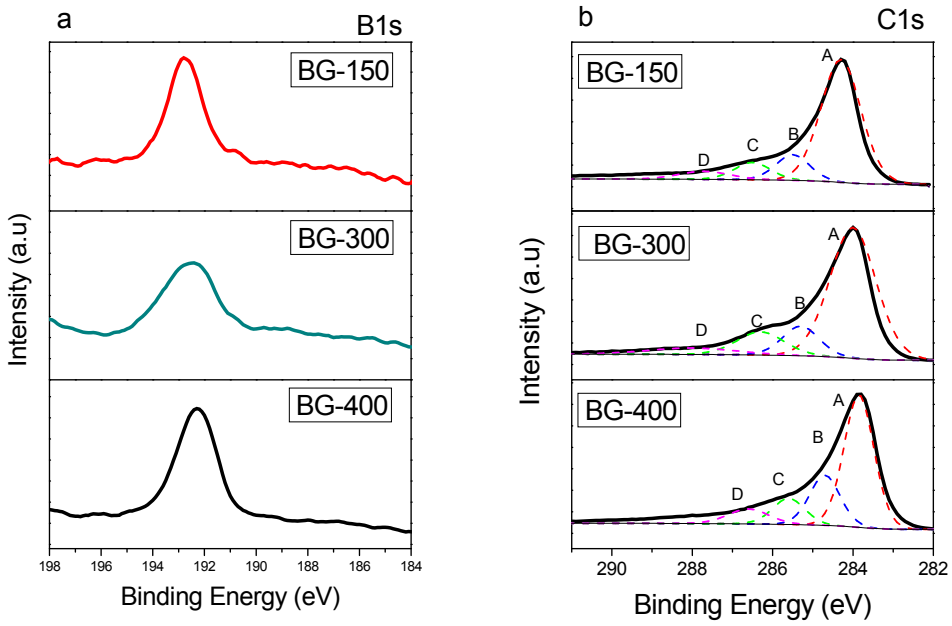

Figure 4.17. XPS spectra of (a) B1s and (b) C1s of boron doped graphene (BG) samples prepared by LVCC under different partial pressure of B_2H_6 gas.

Figure 4.18 shows the XPS spectra of boron- nitrogen doped graphene prepared by laser exfoliation using LVCC and under different partial pressures of B_2H_6 and NH_3 in helium atmosphere. As shown in Fig 4.18a, there are two peaks in N1s spectra indicating the existence of more than one component. Based on the XPS curve fitting of the spectra in Fig 4.18a, two distinct peaks are appeared at 398.7 and 400.9 eV corresponding to pyridinic and graphitic nitrogen respectively. This result is in agreement with nitrogen doped graphene samples reported earlier, which was shown that the intensity of the peak related to pyridinic nitrogen increases with increasing NH_3 partial pressure.

The XPS of spectra of B1s for boron-nitrogen doped sample is displayed in Figure 4.18b. Each spectrum shows two peaks indicative of at least two components. One peak has a very high intensity indicating that the B heteroatoms were bonded to C atoms in the form of a BC3 structure. Another peak with a lower intensity at 189.2 eV is expected to be the representative of BNC bonds. This peak was also seen earlier in the boron doped graphene samples.

The XPS Spectra of C1s, as presented in Figure 4.18c in the range of 284 to 290 eV, illustrates at least three components, which are assigned to C-C, C-O, and C-N bonds. There are generally several carbon groups in the synthesized graphene and are characterized by the appearance of different spectral peaks: C-C at 284.5 eV, C-OH at 285.9 eV, C=O at 287.1 eV, and C-C=O at 289.0 eV. As it is well established, the C=O peak is overlaid with C-N around the binding energy of 287.5 $\pm$ 0.5 eV.[156] Based on these XPS results; the boron-nitrogen doped graphene samples are symbolized by 100B-100N, 100B-200N, and 200B-200N contain 0.8, 0.7, and, 1.2 atomic% boron, and 6.6, 6.8, and 7.2 atomic % nitrogen, respectively.

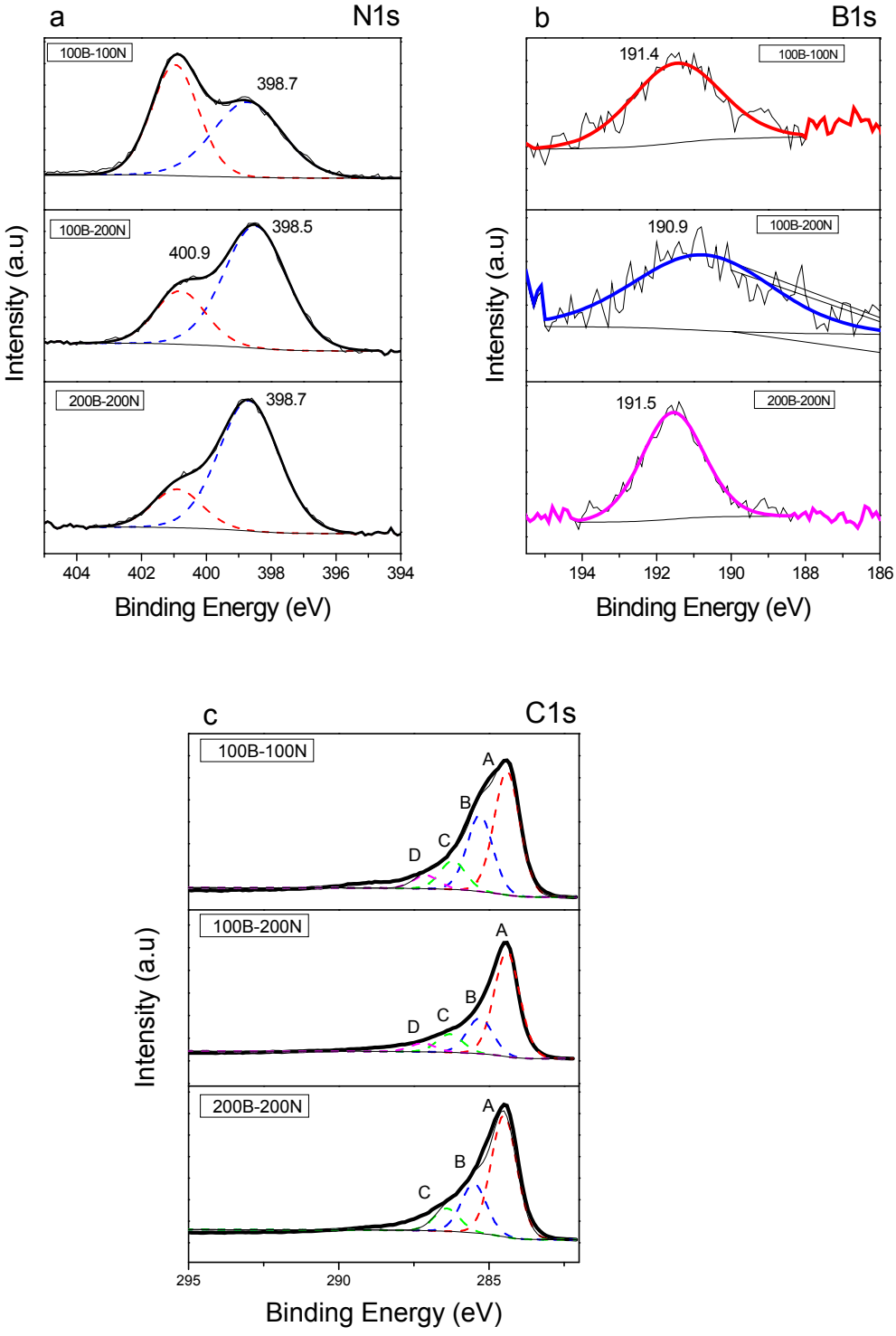

Figure 4.18. XPS spectra of (a) N1s, (b) B1s, and (c) C1s for boron-nitrogen doped graphene (BNG) samples prepared by LVCC under different partial pressures of B_2H_6 and NH_3 in He atmosphere.

Representative TEM images of graphene and nitrogen doped graphene (NG) samples are shown in Figure 4.19, a through d. The folded graphene sheets were observed in many samples with the sheet edges tended to scroll or fold slightly. From these TEM images, transparent micron size graphene sheets can be clearly seen. TEM images of nitrogen doped graphene indicate formation of very thin layer with overlapping graphene sheets with some corrugation on the surface of graphene. In Figure 4.20, representative TEM images of boron doped graphene (BG) and boron-nitrogen doped graphene (BNG) samples are shown. The flattened BG and BNG nanosheets are randomly stacked together, displaying a flake-like structure similar to pristine graphene.

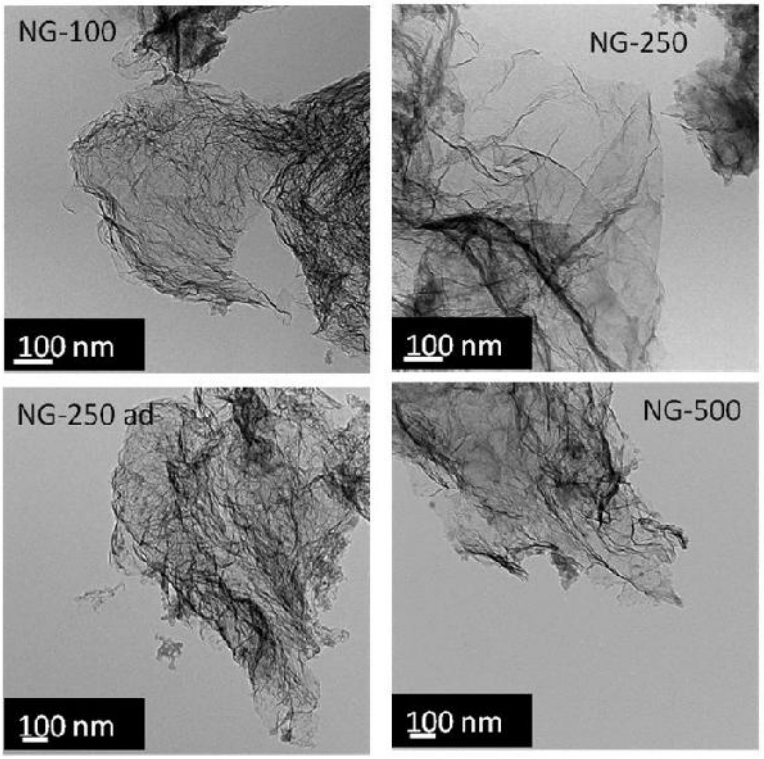

Figure 4.19. Representative TEM images of nitrogen doped graphene (NG) samples.

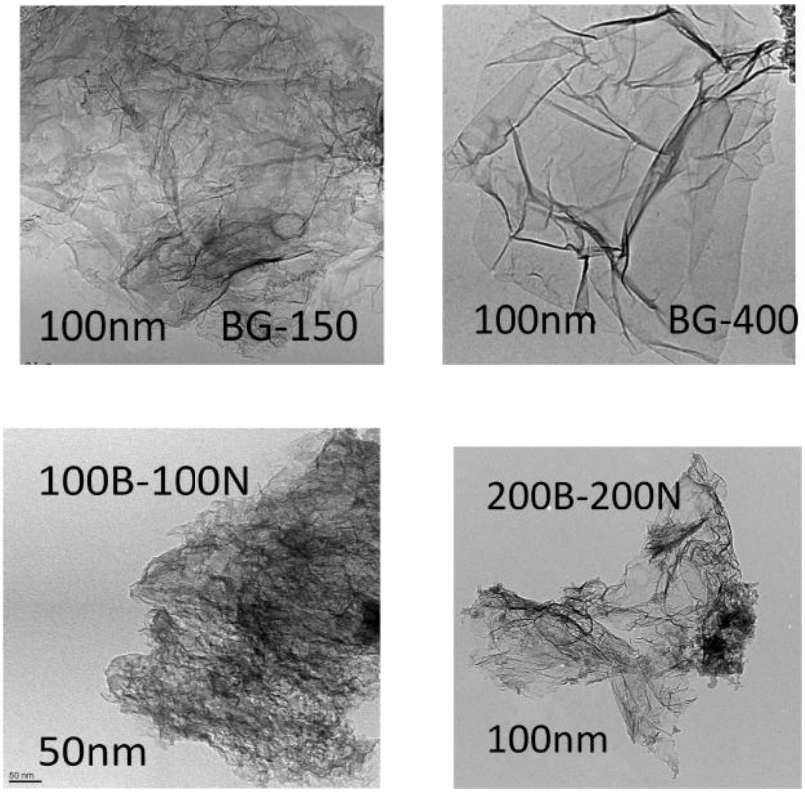

Figure 4.20. Representative TEM images of boron doped graphene (BG) and boron- nitrogen doped graphene (BNG) samples.

The Fourier transform infrared spectra of GO and nitrogen doped graphene samples are shown in Figure 4.21. GO spectrum shows characteristic features of graphite oxide at 1050, 1225, 1390, 1560, 1620, and 1730 cm^{-1} corresponding to C-O stretching, C-O-C, C-OH, aromatic C=C stretching, O-H vibrations, and carbonyl/carboxylic C=O stretching frequencies respectively.[68] GO also shows a broad band in 3000-3500 cm^{-1} region corresponding to O-H stretching. It is expected for ammonia to interact with C=O and C-O-C in GO leading to disappearance of 1730 and 1225 cm^{-1} bands and formation of new N-H bands at 1418, 3019, and 3206 cm^{-1}. The N-H band in sample identified as NG-250 has disappeared, whereas other samples retained some fraction of these bands.

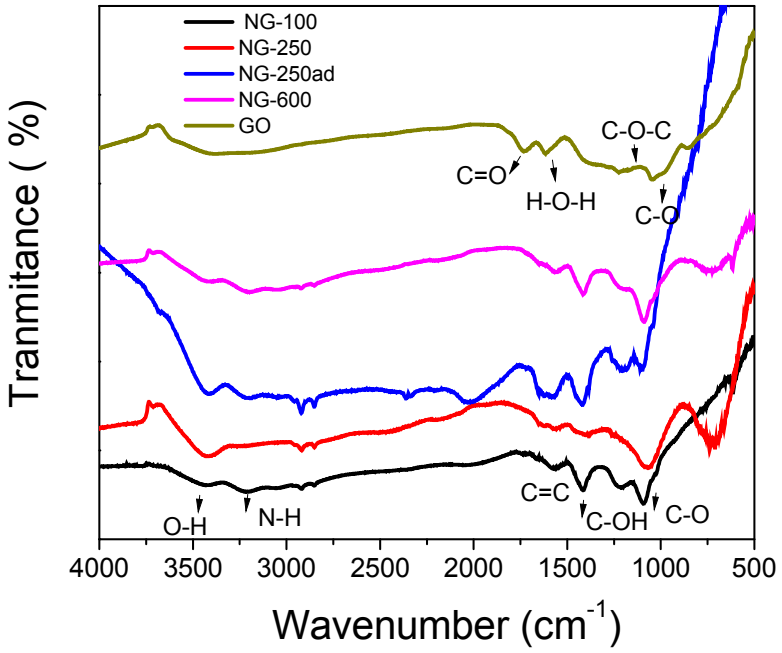

Figure 4.21. FTIR spectra of nitrogen doped graphene (NG) samples prepared by LVCC.

Figure 4.22 shows FTIR spectra of boron doped graphene (BG) and boron-nitrogen doped graphene (BNG) samples. As can be seen from Figure 4.22a for BG samples, the intensity of the C=C stretch relative to the C=O stretch has increased after graphite oxide being doped by boron. In Graphite oxide spectrum, the epoxy and hydroxyl groups are located between 1100 and 1200 cm^{-1} wavelength as shown in Figure 4.22a. The boron doped samples have these functional groups but with lower intensities. This can be attributed to the combination from a single bond stretches between C, O, and B atoms as reported by Han et al.[155] The FTIR spectra of boron-nitrogen doped graphene samples are given in Figure 4.22b. There are three peaks at 1407, 1570, and 1630 cm^{-1}, which are expected to be associated with C-N, C=C, and C=N bonds. The absorption in the 1200-1600 cm^{-1} region can be attributed to the nitrogen atoms bonded into the sp^2 carbon framework. Thus, the peak at 1550 cm^{-1} can be assigned to C-N and the peak at 1662

cm^{-1} to C=N. The peak from 1082 to 1132 cm^{-1} (Figure 4.22a) can be attributed to a B-C bond. The BNG samples do not seem to contain hexagonal boron nitride (h-BN), which is a byproduct of B_2H_6 and NH_3 and identified by two peaks at 1350 and 710-830 cm^{-1}. Nevertheless, the main absorption band centered around 1350 cm^{-1} should be corresponding to the in-plane stretching-vibrations within the fused BCN heterorings, and a minor absorption band at 710–830 cm^{-1} can be ascribed to the corresponding out-of-plane bending modes.[157]

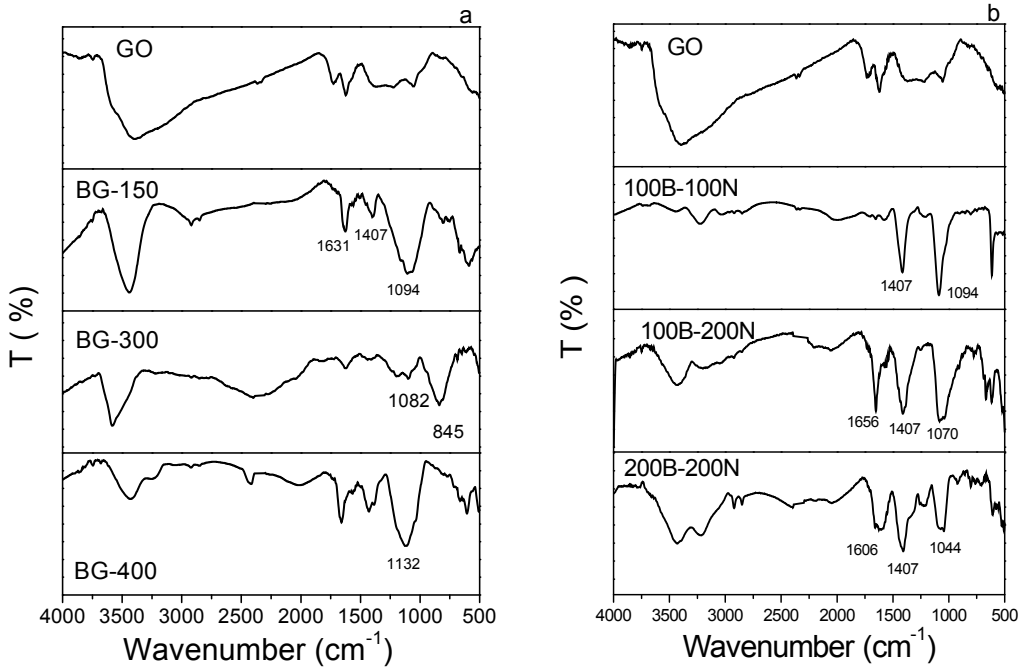

Figure 4.22. FTIR spectra of (a) boron doped graphene (BG) samples, and (b) boron-nitrogen doped graphene (BNG) samples.

Plausible mechanisms for nitrogen and/or born doping of the graphene as a function of the experimental condition are suggested here. The first and more probable mechanism for nitrogen insertion is the reaction of adsorbed NH_3 with –COOH containing sites on graphite oxide upon laser irradiation. The interaction via Lewis acid route leads to the formation of amide. The formed amide group is then converted to pyridinic dopant in graphene (Figure 4.16).

On the other hand, the interaction via Bronsted acid route leads to the formation of quaternary ammonia (-$COONH_4$). The –$COONH_4$ group is released back into the gas phase. The second mechanism is based on the conversion of NH_3 in the chamber upon laser irradiation to H + NH_2 radicals followed by reaction of these radicals with graphite oxide reactive sites. For boron doping of graphite oxide, the adsorption of B_2H_6 is less likely, and thus, the first mechanism is very unlikely. However, formation of B radical upon laser irradiation followed by reaction of B radical with graphite oxide active site such as sp^2 carbon network is more plausible.

4.2.4 Oxygen Reduction Reaction of Doped Graphene Samples

In order to explain the significance of oxygen reduction reaction (ORR) in this work, there is a need to first describe the importance of fuel cells and the major reactions responsible for their operation. A fuel cell is an electrochemical device that can directly convert chemical energy into electric energy with high conversion efficiency, high power density, quiet operation and no major pollution. It oxidizes fuel at the anode and reduces oxygen from air at the cathode to produce electricity. Thus, the major reaction at the cathode is the oxygen reduction reaction (ORR). There are two routes for ORR to proceed. One route is known as the direct four-electron pathway in which O_2 is reduced directly to water without involvement of hydrogen peroxide according to reaction 1:

$$O_2 + 4H^+ + 4e \rightarrow 2H_2O \quad (1)$$

The second and a less efficient route is a two-step two-electron pathway in which hydrogen peroxide is formed as an intermediate according to reaction 2:

$$O_2 + 2H^+ + 2e \rightarrow H_2O_2 \quad (2)$$

To achieve a high efficiency fuel cell, the four-electron pathway is expected to be active. Yu et al. [158] obtained the overall energy profile of the ORR pathway for nitrogen doped graphene in an

alkaline environment. Their study showed that the activation of the first route is achievable by first lowering O_2 dissociation barrier and second making the reaction 3:

$$OOH_{(ads)} \rightarrow O_{(ads)} + OH^- \quad (3)$$

energetically favorable. Because the ORR is principally the four electron pathway and is very slow in nature, catalysts must be employed to facilitate the reaction pathway to increase the efficiency of fuel cells.[159]

Fuel cells are considered to be a promising green energy generation technology. Traditionally Pt nanoparticles supported on carbon composites were used as the catalyst for the ORR at the cathode. Recent work has shown that nitrogen doped CNT displays a higher catalytic activity than Pt/carbon due to the presence of pyridinic and pyrrolic N species. Pyridinic N with one donor pair of electrons in addition to the electron donated to conjugated π bond may facilitate the reductive O_2 adsorption and therefore demonstrate a good catalytic activity[160]. Recently, Wang et al.[161] reported that the graphitic N atoms could facilitate electron transfer from carbon electronic bands to the antibonding orbitals of O_2. To evaluate the performance of the synthesized doped graphene samples as the fuel cell catalysts, their electrocatalytic activities (cyclic voltammograms) were measured. The measurement was carried out in a 0.1 M KOH solution using a conventional three electrode cell system.

The cyclic voltammograms, current as function of applied potential, of several nitrogen doped graphene samples are displayed in Figure 3.23. The value of the reduction current i_p for NG-100, NG-250, and NG-600 were estimated to be about 2.3×10^{-5}, 2.79×10^{-5}, and 1.9×10^{-5} A, respectively. These results indicate that different amount of nitrogen doping could lead to different level of electrical conductivity. According to reported the results,[143,146,160] the current i_p is expected to be higher when the doped nitrogen is predominately pyridinic compared to a

mixed of both graphitic and pyridinic nitrogen. The results of this work however showed a lower electrical conductivity for nitrogen doped samples comparing to graphene sample with no correlation with pyridinic nitrogen, However, Theoretically, doping with electronegative nitrogen atoms reduces the electron density of carbon atoms that bond to nitrogen atoms and polarizes the carbon atoms into C (σ+). This makes the adsorption of O_2 (O–O) molecule easier, which is the first step in the OR process. Subsequent electron transfer between C (σ+) and O–O will result in formation of radical anions.[140] Thus, the introduction of nitrogen into graphene lattice is expected to increase reduction current and justifiable.

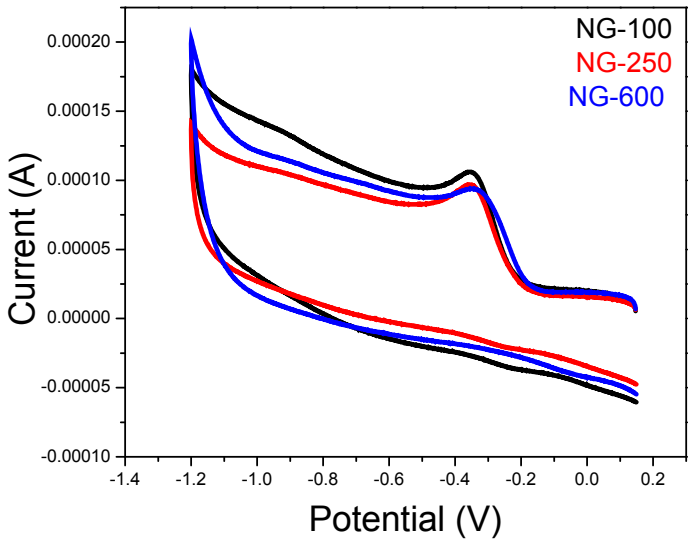

Figure 4.23. Cyclic voltammograms (CV) of nitrogen doped graphene samples.

The cyclic voltammograms of boron doped graphene (BG-150) and graphene samples are shown in Figure 4.24. The estimated ORR peak for BG sample is at -0.34 V. The ORR peaks for bare glassy carbon electrode (GCE) appears at -0.44 V, indicating much faster electron transfer kinetics for ORR in BG. Consistent with voltage results, the reduction current of BG sample at 5.5×10^{-5} is greater than that of graphene at 3.71×10^{-5} A indicating that boron doped graphene possesses a higher electrocatalytic activity towards ORR than pure graphene.

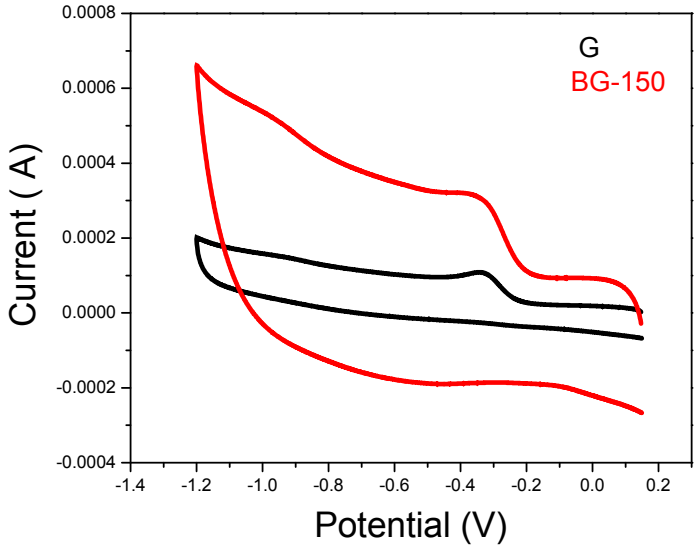

Figure 4.24. Cyclic voltammograms (CV) of graphene and boron doped graphene samples.

The results of cyclic voltammetry for several boron-nitrogen doped graphene (BNG) samples are given in Figure 4.25. The estimated reduction currents (i_p) from Figure 4.25 for 100B-100N, 100B-200N, and 200B-200N samples are 2.85×10^{-5}, 3.04×10^{-5}, and 3.07×10^{-5} A, respectively. The reduction current for these samples are higher than that of observed for nitrogen doped but lower than that of boron doped graphene samples. These results suggest that the reduction current could increase as the amount of boron or nitrogen increases in the doped sample.[146] Moreover, there are one reduction peak for these samples (BG , NG, and BNG) indicating that the electrochemical reduction of oxygen occurs in one step with the production of H_2O as product.[143]

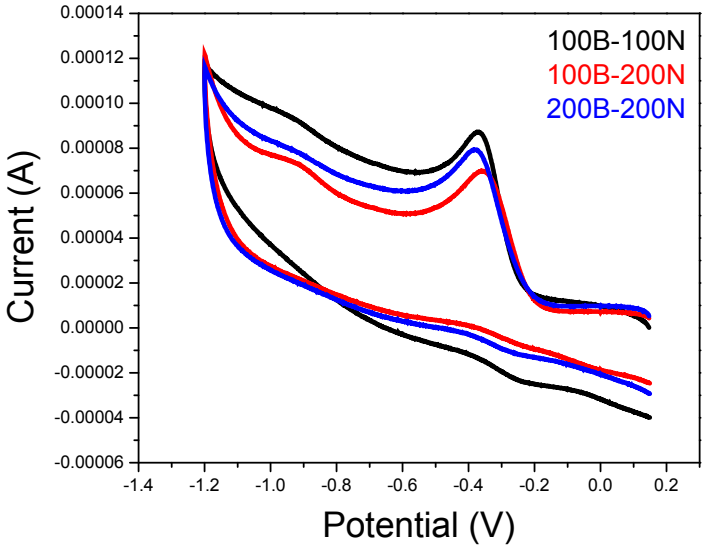

Figure 4.25. Cyclic voltammograms (CV) of boron and nitrogen doped graphene samples.

4.3 Synthesis of Metal Nanoparticle Graphene Composite

As discussed in previous sections, the discovery of graphene opened up a novel field of two dimensional (2D) composites with metal or semiconductor nanoparticles anchored onto one-atom-thick carbon matrix. In comparison to zero dimensional (0D) fullerenes and one dimensional (1-D) CNTs, the 2-D graphene has larger specific surface area and could be obtained more easily and less expensively. Graphene is a good candidate as a support material for a host of nanoparticles due to its large contact area provided by its planar structure and high thermal and electrical conductivities. Therefore, metal nanoparticle/graphene hybrid composites have a great number of applications and potential utilizations in catalysts,[56-85] fuel cells,[162] sensors,[163] biosensors,[164] supercapacitors,[165] hydrogen storage,[166] spectroscopic probes,[167] surface-enhanced Raman scattering substrates[168] and optoelectronic devices.[57] This is mainly due to the synergistic effects between the inherent function of metal nanoparticles and the merits of graphene. The optoelectronic properties of the graphene sheets can thus be tuned over several

orders of magnitude, potentially making them useful for flexible and transparent semiconductors or semimetals.[169] Graphene supported noble metals such as Au,[57] Pt,[162] Pd[170], and Ag nanoparticles were recently synthesized. Graphene supported transitional metal nanoparticles typically including Fe, Co , Ni,[171] and Cu[172] are also a class of novel hybrid materials that possess important features for magnetism, sensors and catalysis.

Graphite oxide (GO) is now well known as a promising precursor to graphene. It not only possesses larger theoretical specific surface area (a range of 400–1500 $m^2 g^{-1}$) than CNTs,[173] but also exhibits higher efficient utilization of surface area because both sides of the nanosheets are accessible. Moreover, the functionalities such as the residual oxygen-containing functional groups, holes,[174] oxygen,[175] carbon vacancies and defects , which are generated during partial oxidation with graphitic domains,[176] facilitate the nanoparticles immobilization.[177] As a result, this may efficiently introduce chemically active sites for use in catalytic reactions and also act as anchoring sites for deposition of metal nanoparticles. It is easy to anchor metal nanoparticles onto graphene sheets by simultaneously reducing GO and metal ions employing an appropriate reducing approach such as chemical,[173] thermal treatment[176] and UV-irradiation.[178] Furthermore, reduced graphene oxide (RGO) decorated with metal nanoparticles could efficiently prevent the aggregation arisen from the stacking and interaction among the graphene sheets after being dried.[170] Using graphite oxide is also known to be beneficial in preventing the metal nanocluster from coalescing and thus leading to form highly dispersed, high density, ultra small size metal nanocluster.[179] Finally, GO is a lower cost carbon material compared to graphene and other carbon nano-scale materials.

Like heteroatom doped graphene, metal nanoparticle graphene composites are synthesized using various approaches of chemical, thermal and irradiation. For instance, silver-

graphene was prepared by first deposition of silver nanoparticles on graphite oxides in the presence of aqueous potassium hydroxide to produce silver ions and next subjected to hydrazine to reduce graphite oxide.[169] Reduced graphite oxide supported platinum (Pt) was prepared by simple ethylene glycol (EG) reduction.[180] Ag, Au, and Cu nanoparticles supported on graphene were prepared by simultaneous reduction of GO and appropriate metal salt using oleylamine as a reducing agent under microwave irradiation.[181] Alternatively, Ag, Au, and Pd nanoparticles graphene composite were prepared by first reducing graphene oxide via photocatalytic approach using phosphotungstate and UV irradiation and then injecting metal precursors into a well dispersed solution of reduced graphene oxide in N,N, dimethylformamide.[182] Platinum nanoparticles supported on reduced graphene oxide was also reported as a catalyst for hydrogenation of nitroarenes.[180] Highly active and stable Pt/reduced graphene oxide (RGO) was reported as an electrocatalyst for the application of proton exchange membrane fuel cells.[183] Since reduced graphene oxide has good electron storage/ accepting properties, it was reported that it may serve as an excellent 2-dimensional matrix to anchor metal nanoparticles in the process of polyoxometalates (POM) assisted reduction of metal ions.[182] Wang et al.[184] reported deposition of gold films with different thicknesses on a single graphene sheet as surface enhanced Raman scattering for characterization of rhodamine molecules. Highly loaded Pd (e.g., 80 wt.%) graphene nanosheets (GNS) as an electrocatalyst was synthesized by colloidal method to alleviate the degradation rate of Pd catalysts in formic acid oxidation.[185]

In this work, metal nanoparticles supported on graphene were synthesized for the first time using LVCC system. In this section, the synthesis, characterization and performance of metals nanoparticles graphene nanocomposites are reported. First, the targets containing 5% of metal and 95% graphite oxide were prepared. These targets were then placed in LVCC system

and irradiated by laser to form metal nanoparticles supported on graphene. The approach for the synthesis of composite is based on the use of laser to simultaneously exfoliate graphite oxide and vaporize metals. Upon condensation from the vapor phase, the formed metal nanoparticles are deposited on reduced graphene oxide surfaces. The method used to synthesize metal nanoparticles supported on graphene was fully described in Chapter 2.

4.3.1 Results and Discussion

As displayed in Figure 4.26, the XRD patterns confirm the reduction of graphite oxide (GO) and formation of metal nanoparticles on graphene sheet using LVCC. The peak at 11.7° (2θ) in GO spectrum indicates the existence of graphite oxide phase. This peak disappears in metals nanoparticles containing samples indicating reduction of GO during the laser irradiation of metal/graphite oxide containing targets and evaporation of metals by LVCC process. The metal nanoparticles on graphene sheets show their own diffraction patterns. For instance, the diffraction peaks of (111), (200), and (220) planes in XRD patterns of gold/graphene sample are representative of gold face-centered cubic crystal structure based on reference code JCPDS 03-065-8601. The diffraction patterns of Pd appears at 2θ = 39.9° (111), 46.4° (200), and 67.7° (220) with a cubic crystal structure based on reference code JCPDS 01-087-0643.

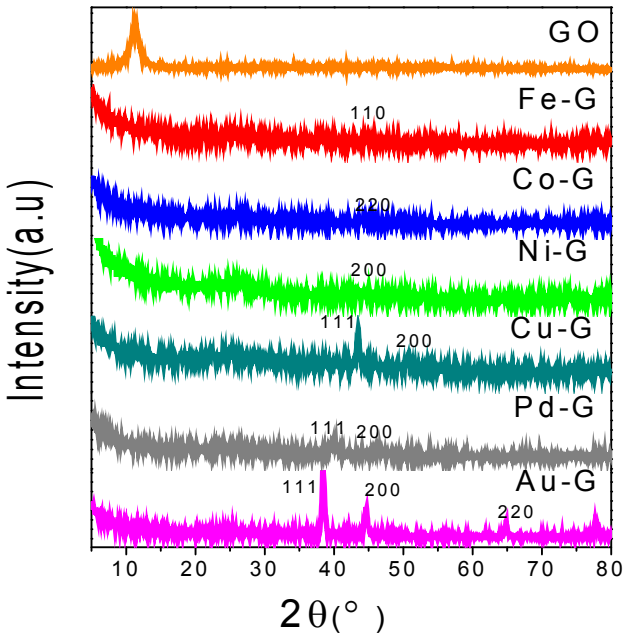

Figure 4.26. XRD patterns of graphite oxide and reduced graphene oxide containing different metal nanoparticles.

A key factor to comprehend the charge transfer between the metal nanoparticles and graphene is the knowledge of relative work function (WF) between the metal and graphene sheets, which can be found from XPS data. Graphene is p-doped (or n-doped) if the metal's WF is larger (or smaller) than that of graphene.[186] XPS data provides insight on the oxidation state of the elements and useful information on the nature and content of the bond between the elements in the graphene sheets. The C1s XPS spectrum of graphite oxide as displayed in Figure 4.27.a shows two distinct bands at 284.7 and 286.9 eV, which are attributed to graphitic (C=C) and different oxygenated functional groups (e.g., C–O) , which are located at the basal planes of the graphite oxide sheet. However, after simultaneous laser exfoliation of graphite oxide and deposition of metal nanoparticles using LVCC, the peak at 286.9 eV decreases significantly (or totally removed) indicating deoxygenation of graphite oxide and formation of graphene sheets. These results also confirm the successful removal of epoxy, hydroxyl and carboxyl functional groups as was explained in Figure 4.4. All the samples containing metal nanoparticles on

graphene, as presented in Figure 4.27a, show a similar pattern to that of graphene sample. This result indicates the formation of reduced graphite oxide after processing of the mixture of graphite oxide and metal powder with LVCC.

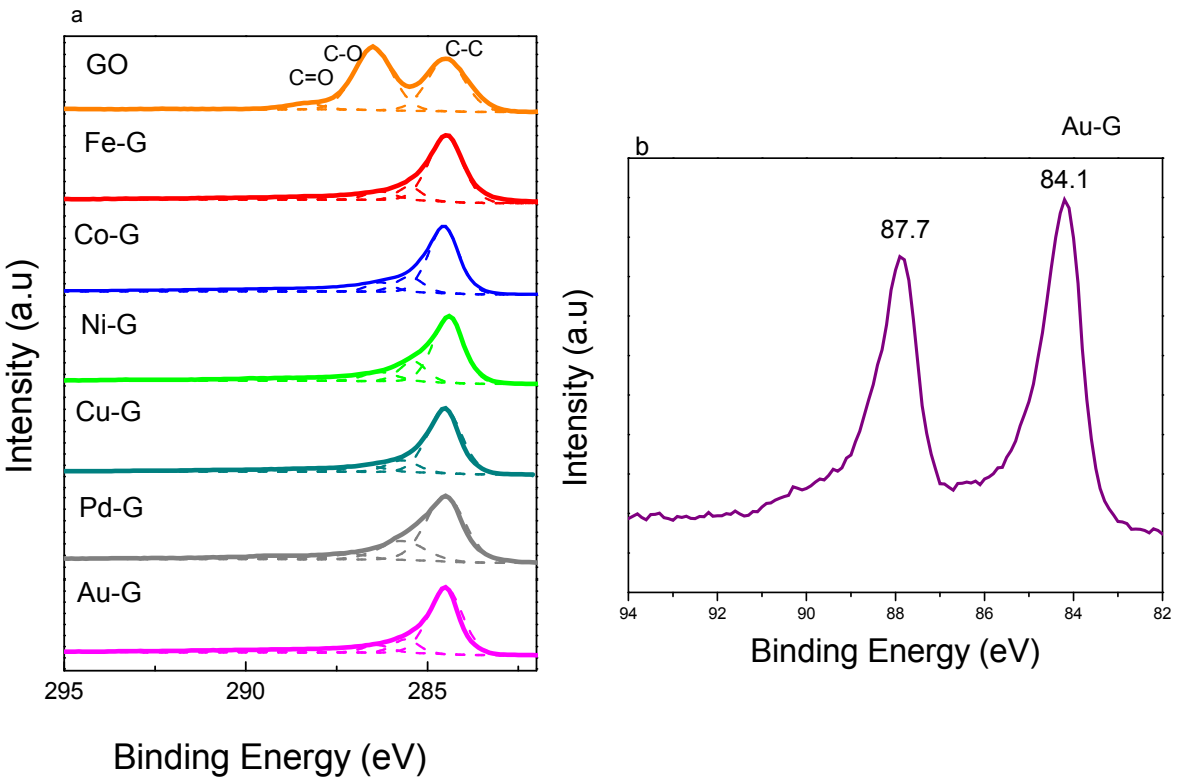

Figure 4.27. (a) XPS C1s spectra of graphite oxide and metal nanoparticle containing garphene samples prepared by LVCC, and (b) XPS of Au 4f deposited on graphene.

Li et al.[187] investigated the electronic properties of Ag nanoparticles supported on graphene sheets by studying Ag $3d_{5/2}$ XPS. They reported a binding energy of 368.1 eV for Ag $3d_{5/2}$ at pure state and a value of 367.5 eV (-0.6 eV) for Ag/G structure; and, concluded a shift to lower energy as a result of electron transfer from metallic Ag to graphene sheets. A discussion of the work functions for pure Ag and G should also lead to the same conclusion. The XPS of Au $4f_{5/2}$ and Au $4f_{7/2}$ for pure Au and Au/G hetero-structure were investigated in this work. The binding energies were estimated to be about 87.71 eV for Au $4f_{5/2}$ and 84.04 eV for Au $4f_{7/2}$

when Au is pure with corresponding values of 87.7 eV and 84.19 eV for Au/G system (Figure 4.27b). Though the binding energies for Au $4f_{5/2}$ are not that different (-0.01 eV), it is quite different for Au $4f_{7/2}$ (+0.15 eV); and as a results, there is an electron transfer from graphene to Au in Au/G sample. The XPS data as presented in Table 3.5 also shows the calculated atomic percentages, C-O/C-C and C=O/C-C atomic ratios for graphite oxide and graphene samples containing metal nanoparticles. The atomic percent of C-C and C=O increased and the C-O atomic percentage decreases for all metal nanoparticle containing samples compared to graphite oxide. The C=O data for Co-G nanocomposite seems to be an anomaly.

Sample ID	Sample Description	C-C (at.%)	C-O (at.%)	C=O (at.%)	C-O/C-C (at. ratio)	C=O/C-C (at. ratio)
1	GO	42.87	53.38	3.75	1.25	0.09
2	Fe-G	79.51	11.59	8.9	0.15	0.11
3	Co-G	75.38	15.55	0.19	0.21	0.12
4	Ni-G	70.64	18.85	10.52	0.26	0.15
5	Cu-G	79.1	13.14	7.75	0.17	0.09
6	Pd-G	70.94	23.95	5.11	0.34	0.07
7	Au-G	80.09	12.35	7.57	0.15	0.09

Table 4.5. Calculated atomic percentages and ratios for C-C, C-O and C=O for GO and metal-graphene samples.

The Raman spectra of metal nanoparticles graphene nanocomposites are shown in Figure 4.28. All samples contained 5% by weight loading of different metals, which prepared under a similar condition. As discussed in previous sections, the two characteristic bands for graphene are the G band (sp^2 bonded carbon atoms in a hexagonal lattice) and the D-band (vibration of sp^3 carbons atoms of defect and disorder), which appear around 1590 and 1370 cm^{-1} respectively. A sample of graphite oxide is included in Figure 4.28 for comparison. As is obvious from Figure 4.28, the G-band around 1578 cm^{-1} is attributed to graphene and a G-band around 1592 cm^{-1} corresponds to graphite oxide. This shift in G-band strongly suggests the reduction of graphene oxide to graphene. All graphene samples containing metal nanoparticles show a G-band around 1578 cm^{-1} and the D-band around 1370 cm^{-1}, which are similar to that of reduced graphene oxide. The G-band of all metal nanoparticle containing graphene samples, as can be seen from Figure 4.28, is red shifted with respect to graphite oxide sample. For instance, Pd-G sample shows a strong G-band at around 1576 cm^{-1}, which is almost similar to that of graphene at 1578 cm^{-1}. This shift could be attributed to the introduction of some defects into the structure, causing its phonon modes particularly at the G band to soften. By increasing the defects, the number of ordered

rings decreases, and D-band intensity (I_D) starts to increase. This shift in the D-band intensity of nanoparticle containing samples could be due to the level of amorphous carbon that is potentially produced as a result of small amount of carbon vaporization and condensation during the LVCC processing of metal/GO samples. A small shift in the G-band from sample to sample is attributed to differences in the electron transfer from graphene to different metals or vice versa. Different G-band intensities for different metal nanoparticles are potentially indicative of the extent of conversion of graphene oxide to graphene. With the results presented here, one may conclude

that the reduction of graphene oxide to graphene and deposition of metal nanoparticles on the resultant graphene sheets are complete. The calculated intensity ratios (I_D/I_G) and the peak positions for both G and D bands are shown in Table 4.6. As shown in Table 4.6, the intensity ratios (I_D/I_G) were decreased in metal-graphene samples in comparison to graphite oxide sample indicating more graphitic domains but smaller in size,[188] and a lower defect after GO was reduced by laser exfoliation using LVCC process.

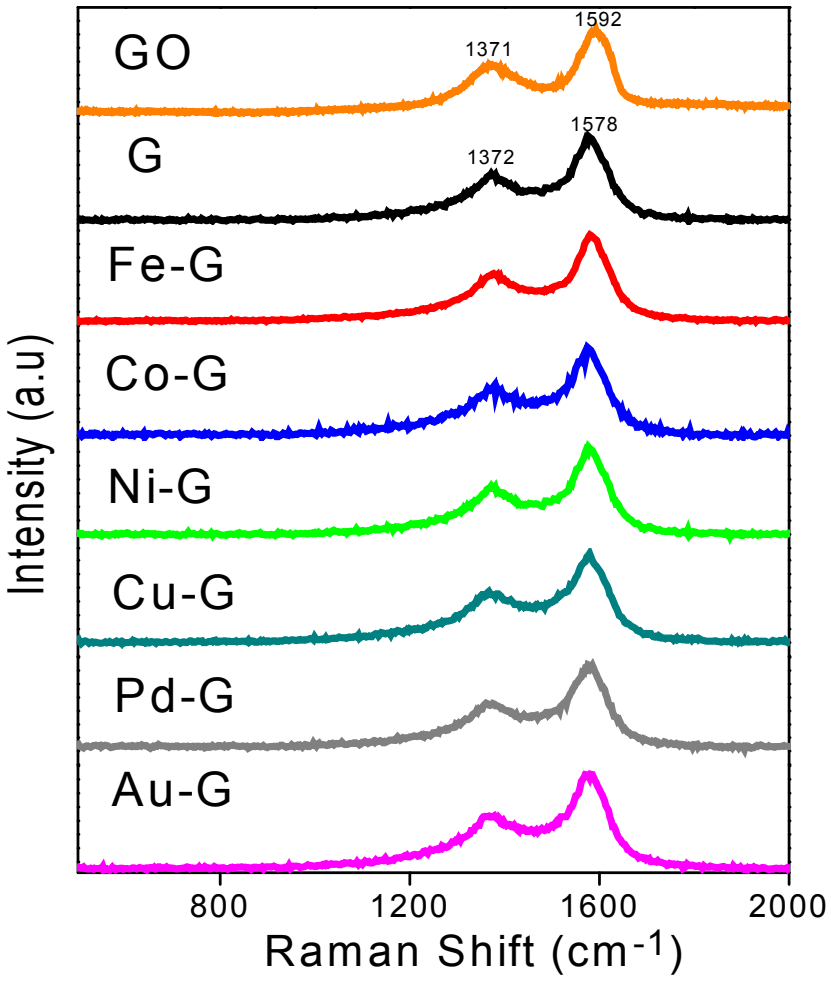

Figure 4.28. Raman spectra of graphite oxide and graphene samples containing metal nanoparticles produced by LVCC process at an excitation wavelength of 406.7 nm.

Samples	D band position (cm^{-1})	G band position (cm^{-1})	I_D/I_G
GO	1371	1592	0.67
G	1372	1578	0.65
Fe-G	1375	1579	0.63
Co-G	1376	1576	0.63
Ni-G	1370	1579	0.64
Cu-G	1366	1578	0.63
Pd-G	1368	1576	0.61
Au-G	1366	1578	0.64

Table 4.6. Position of D-band, G-band and calculated I_D/I_G for graphite oxide, graphene and graphene containing metal-nanoparticle samples.

Representative TEM images of graphene-metal nanoparticles are shown in Figure 3.29. The metal nanoparticles appear as dark spots, which are decorated on the surface of graphene sheets. The average particle size of Fe, Co, Ni, Cu, Pd, and Au nanoparticles deposited on the surface of resulting graphene sheet were estimated to be in the range of 5-10 nm. The dispersion of nanoparticles and their particle size distributions, however, were not very uniform indicating room for improvements. The morphology of reduced graphite oxide surface remains similar to that of reduced graphene oxide without metal nanoparticles. As presented earlier, LVCC produces wrinkled and partially folded sheets with a lateral dimension of up to a few microns in length. It was also demonstrated that the LVCC process exfoliates the GO sheets from the GO

target where they undergo deoxygenation and reduction without any hard evidence for the destruction of their layer structures or atomization to produce carbon nanoparticles.

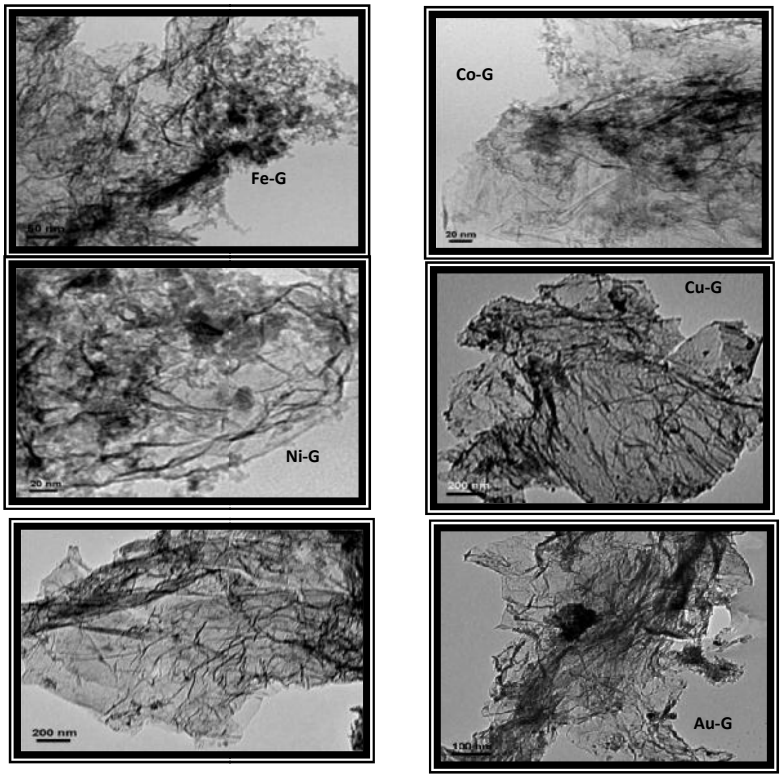

Figure 4.29. Representative TEM images of reduced graphene oxide as a support for metal nanoparticles.

Representative SEM images of selected reduced GO containing metal nanoparticles samples are displayed in Figure 4.30. Contrary to TEM images, these images indicate a uniform distribution of metal nanoparticles on the graphene sheets surface appearing as discrete bright spots. To understand the differences between the TEM and SEM results, one should realize that the SEM results are from a single surface (2D) while the TEM results come from multiple surfaces (3D).

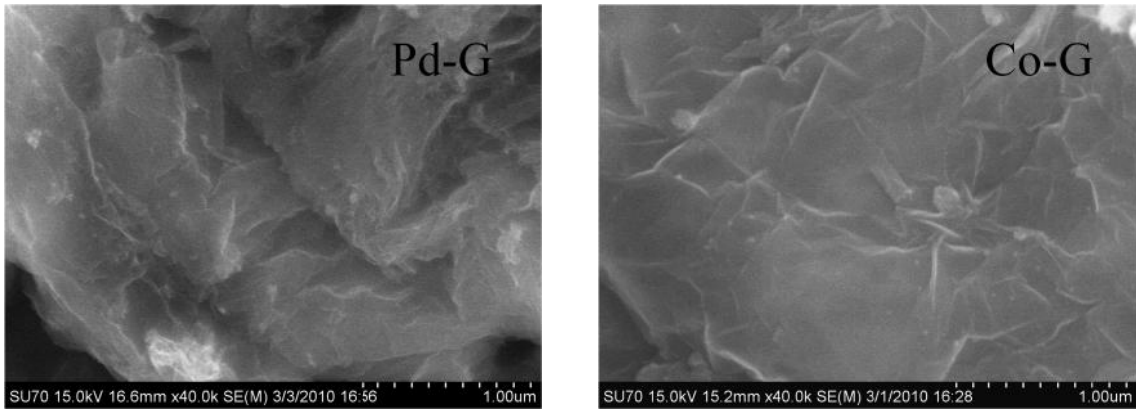

Figure 4.30. Representative SEM images of reduced graphene oxide samples containing Pd and Co.

4.3.4 Suzuki Reaction Catalyzed by Metal Nanoparticle-Graphene

The metal nanoparticles graphene samples containing different weight percent of metals and prepared by LVCC were used for the evaluation of samples catalytic activities in Suzuki reaction. Among all the tested samples, only Pd/graphene sample containing about 5% of Pd and prepared under 20% H_2 atmosphere showed 100% of reactant conversion when the reaction was carried out in a microwave for 5min at 80 °C. This sample showed an identical conversion in the subsequent tests meaning that it has a stable activity and good recyclability. Pure Pd nanoparticles showed a good conversion during the first test, however, the conversion was much lower in the sunsequest tests. This result is suggestive of some kind of agglomeration of particles for pure Pd sample, which was prevented when graphene sheets were present. The unique hexagonal planar structure of graphene and presence of C=C bonds within the graphene structure may play an important role as an electron-rich support system for Pd nanoparticles.

The XPS spectrum of Pd 3d for the Pd/G catalysts is shown in Fgiure 4.31. It can be seen that the Pd 3d XPS spectrum can be deconvoluted into two distinct peaks. The relatively lower binding energy set of double peaks (335.03 eV and 340.2 eV) are due to the metallic Pd and the other set of double peaks (337 eV and 342 eV) belongs to the +2 oxidation state of Pd. Based on

these XPS data, a charge transfer takes place between Pd nanoparticles and graphene, which is due to a lower binding energy of Pd/G system comparing to pure Pd nanoparticles. The data show that most of the Pd nanoparticles are present as Pd (0) consistent with the observed binding energies of 335 eV for Pd $3d_{5/2}$ and 341.1 eV for Pd ($3d_{3/2}$) [NIST].

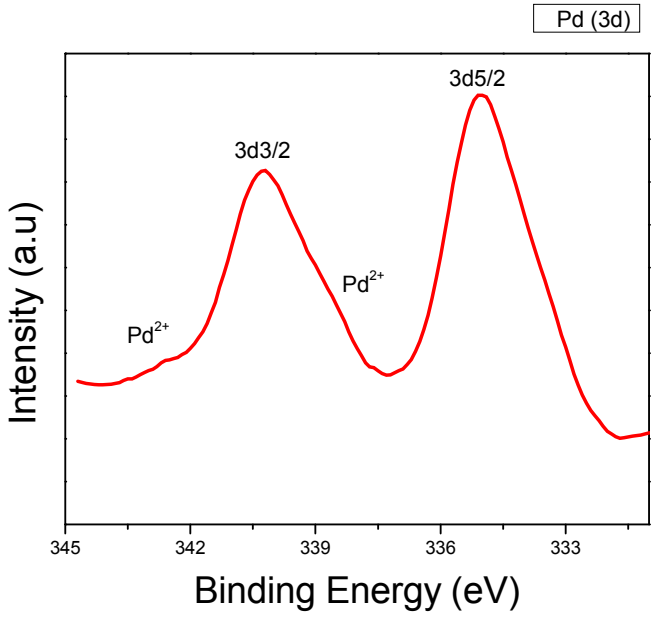

Figure 4.31. XPS (Pd-3d) binding energy of the Pd/G catalyst.

In the Suzuki reaction, bromophenyl and phenylboronic acid were used as the reactants and the product was biphenyl (diphenyl or phenylbenzene) as shown in Figure 4.32. The GC-MS analyses of the final solutions containing Pd-G and Au-G catalysts were carried out and the gas chromatograms of the solutions are shown in Figures 4.33 and 4.34. The peak for bromophenyl (reactant) has totally disappeared in the solution containing Pd-G catalyst and the only appearing peak is that of biphenyl (product) indicating a complete conversion of reactant to final product (Figure 4.33). On the other hand, the solution containing Au-G catalyst does not show any conversion activity by only showing a peak for bromophenyl (Figure 4.34).

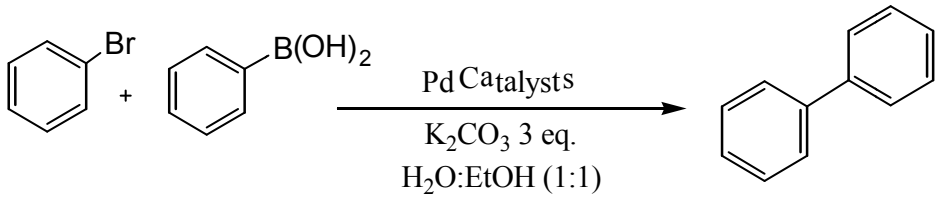

Figure 4.32. Suzuki reaction of bromobenzene (bromophenyl) with phenylboronic acid.

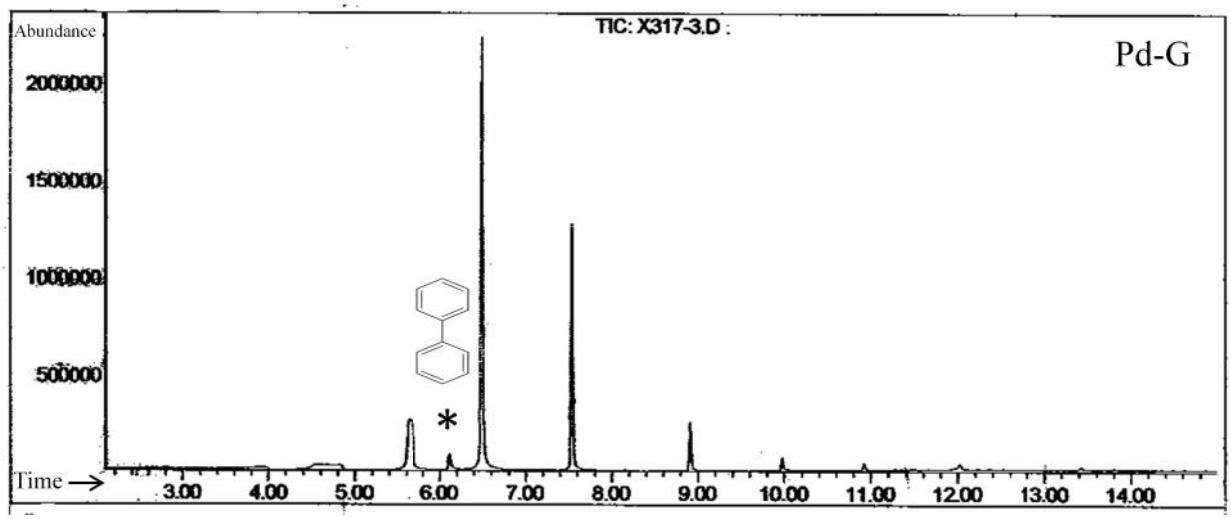

Figure 4.33.Gas chromatogram of Pd-G as catalyst and bromobenzene mixture after heating at 80 °C for 5 min.

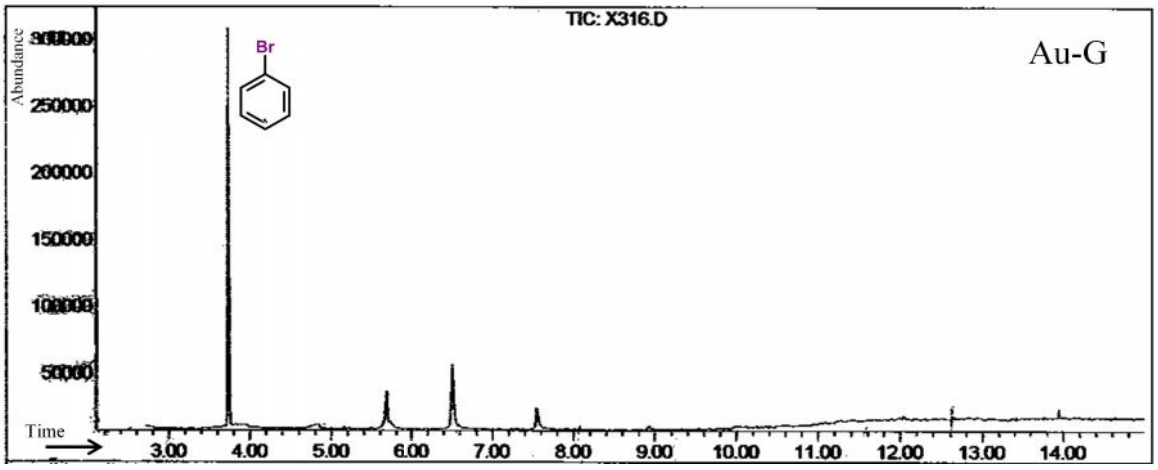

Figure 4.34.Gas chromatogram of Au-G as catalyst and bromobenzene mixture after heating at 80 °C for 5 min.

4.4: Graphene Quantum Dots (GQDs)

4.1.4 Introduction

Semiconductor nanoparticles of sizes in the quantum-confined region were originally referred to as quantum dots (QDs). Their sizes are less than that of exciton Bohr radius typically a few nanometers, namely, those excitons in the small particles are confined in the spatial dimensions with quantized energy states. Typical QD semiconductors are nanoparticles of inorganic compounds based on the elements of group II-VI in the periodic table. These semiconductors have proven themselves to be powerful inorganic fluorescent probes. Quantum dots based on carbon referred to as C-dots are superior to conventional quantum dots in terms of their chemical inertness, low toxicity and exceptional biocompatibility.[189]

C-dots (CDs) represent an interesting class of recently discovered nanostructure carbon materials that comprise discrete and relatively spherical nanoparticles with sizes less than 10 nm. They possess several encouraging attributes such as resistance to photo-bleaching, size- and wavelength-dependent luminescence emission, ease of production and abundance.[189] Graphene quantum dots (GQDs) are one type of C-dots that carry similar properties. Graphene has a perfect π–conjugated single sheet with no electronic band gap and is not photoluminescent, which makes graphene a better candidate for quantum dots as its band gap and photoluminescence properties can be manipulated. The application of 2D graphene sheets is limited by its aggregation and poor dispersion in solvents. To enhance the application of graphene in nanodevices and effectively adjust its band gap, a promising approach is to convert the 2D graphene sheets into 0D GQDs.

In order to transform 2D graphene sheets into 0D GQDs, graphene sheets are sliced into very small pieces and its π electronic network must be manipulated to form quantum confined

sp^2 "island," which requires the formation or exploitation of structural defects. Structural defects are the major cause of creating band gap and make the resultant graphene to be photoluminescent. Similar to C-dots, graphene quantum dots exhibit new characteristics due to quantum confinement and edge effects. Some limitations of C-dots are their size effects and quasi-spherical nanoparticles for sizes below 10 nm. Due to these drawbacks, GQDs and their chemical derivatives have received more attention, as their diameters are mainly distributed in an appropriate size range of 3–20 nm.[189] Typically, GQDs contain carboxylic acid moieties on the edges, similar to graphene, thus providing them with an excellent water solubility and suitability for subsequent functionalization with various organic, inorganic or biological species. In addition, GQDs have some exceptional characteristics including high surface area, larger size and superior surface grafting using the π-π conjugated network due to the graphene chemical structure. As a consequence of a simple structure and the health concerns, GQDs are at the center of significant research efforts to develop low toxicity, eco-friendly alternatives that have the desirable performance characteristics of QDs.

Figure 4.35 illustratively displays the mechanisms of GQDs operations. The PL spectrum can be considered as a transition from the lowest unoccupied molecular orbital (LUMO) to the highest occupied molecular orbital (HOMO) as demonstrated in Figure 4.35a and b. The energy gap depends on the size of graphene and the biggest gap was found to be 4.9 eV. Since the gap decreases gradually as the size of GQDs increase, the sample mixture of different particle sized GQDs have different excitation and emission spectra. The upconverted PL spectrum can be regarded as an anti-Stokes transition as demonstrated in Figures 4.35c and d. The energy levels of π and σ orbitals were provided by the carbene ground-state multiplicity. The carbene ground-state multiplicity is related to the energy difference (δE) between the π and σ orbitals. Most

scholars indicated the upconverted PL property of GQDs should be attributed to the multi-photon active process or the anti-Stoke photoluminescence (ASPL). When some low-energy photons excite, the electrons of the π orbital, the π electrons would transition to a high-energy state such as the LUMO, and then the electrons transition back to a low-energy state. Thus, an upconverted PL is emitted when the electrons are transition back to the σ orbital. Although the electrons of the σ orbital can also be transitioned, it only can emit normal PL (Figure 4.35).[190]

Graphene quantum dots have many applications. Photovoltaic devices are one area of GQDs application due to their size-tuned optical response and efficient multiple carrier generation.[191] Organic light-emitting diodes (OLEDs) can also benefit from the high electron mobility and the strong luminescence of GQDs.[192] The GQDs are also promising for biological applications including bioimaging, biosensors and cell isolations due to their low toxicity.[193] Doped GQDs carry similar or even improved properties comparing to standard GQDs. For instance, nitrogen-doped GQDs show a well defined cathodic peak and good stability as catalyst for the oxygen reduction reaction in fuel cell.[194] Zhuo et al.[195] prepared TiO_2/GQDs as a photo-catalyst for decontaminating wastewaters.

There are various methods to synthesize GQDs with specific properties and geometries. In general these methods may be grouped into two approaches of slicing graphene sheets by electro-mechanical and chemical means and synthesis through pyrolyzing appropriate precursors. The first approach includes cutting graphene sheet using methods such as electron beam lithography (EBL),[196] hydrothermal and solvothermal cutting,[197] chemical exfoliation of graphite,[198] diamond-edge induced nanotomy (nanoscale-cutting) with subsequent exfoliation by super-acid,[199] ultrasonic shearing of graphene sheets,[195] and electrochemically cutting a large

graphene film. The second approach is directly pyrolyzing a proper precursor, such as citric acid[200] and decomposition of fullerene molecules.[201]

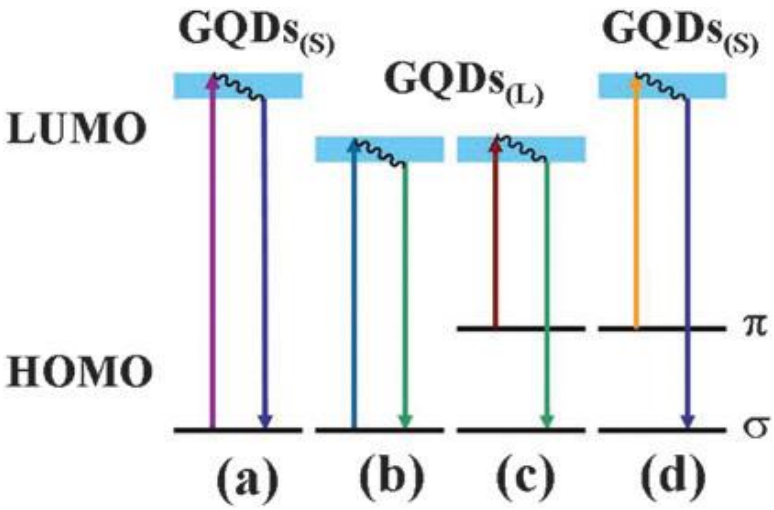

Figure 4.35. A schematic illustration of various typical electronic transitions processes of GQDs. (a and b) Normal PL mechanisms in GQDs for small (S) and large (L) sizes, and (c and d) upconverted PL mechanisms in GQDs for large size and small sizes.[190]

Qian et al.[202] prepared nitrogen-doped graphene quantum dots (N-GQDs) by slicing nitrogen-doped carbon nanotubes. Li et al.[194] recently presented an electrochemical approach by using N–containing tetrabutyl-ammonium perchlorate (TBAP) in acetonitrile as the electrolyte to effectively introduce N atoms into the resultant GQDs. The result was nitrogen doped graphene quantum dots with an average size of 2.5 nm. Another approach to synthesize N-GQDs was hydrothermal approach by cutting pre-oxidized NG into N-GQDs in the size range of 1-7 nm.[203]

In light of the remarkable quantum confinement and edge effect of 0D GQDs, doping GQDs with chemically-bonded N atoms could drastically alter their electronic characteristics and offer new phenomena and surprising properties. As explained in details in section 4.2 of Chapter 4, substitutional nitrogen atoms can modify the electronic structures of the graphene providing a

promising way to modify the transport and electronic properties of graphene for electronic applications. However, N-doping and slicing of N-doped graphenes has inevitably shown requirement of a harsh condition such as high temperature or strong electrical fields. As a result, it is very difficult to control the distribution and bonding configurations of the N-doped graphene in the π-conjugated framework. In this study graphene quantum dots (GQDs) and nitrogen-doped graphene quantum dots (N-GQDs) were synthesized using cutting and nitrogen doping of functionalized graphene using hydrothermal method. A larger amount of synthesized needed for characterization and ease of processing were the major reasons for choosing the hydrothermal method in this work. Experimental procedures will be presented in the next section.

4.2.4 Materials and Preparation Procedures

The starting material is reduced graphene oxide (RGO) or simply graphene, which could be prepared using laser exfoliation such as LVCC, thermal deoxidization in a tubular furnace under argon or by microwave plasma. These methods were explained in Chapter 2 or elsewhere by El-Shall group.[204] In this work, the modified method of Pan et.al.[197] were employed to produce GQDs or N-GQDs from RGO. A schematic of the experimental set-up is shown in Figure 4.36.

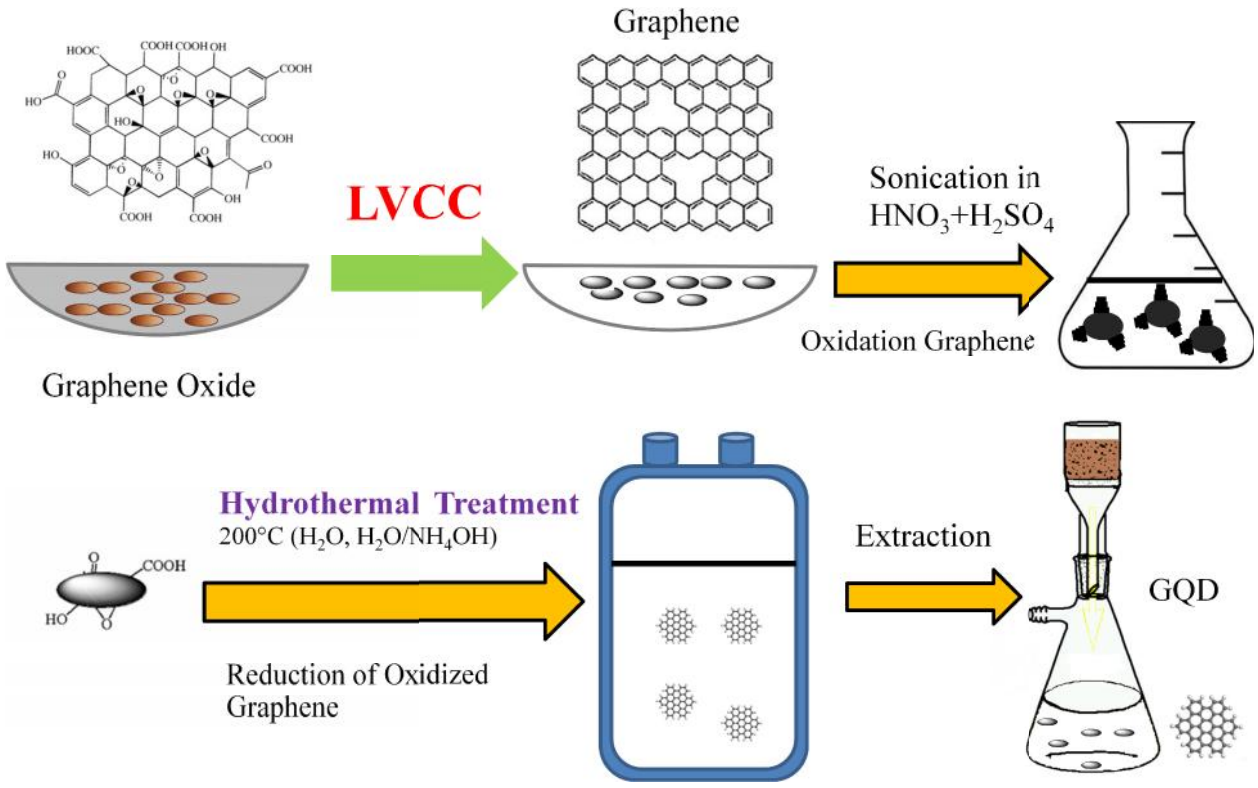

Figure 4.36. A schematic of the experimental set-up used to synthesize graphene and nitrogen-doped graphene quantum dots.

Briefly, a concentrated solution of acids comprising of H_2SO_4 (15 mL) and HNO_3 (45 mL) was prepared in a glass flask. Then, 150 mg of RGO, which was prepared according to one of the methods mentioned above, was added to this acid solution. The mixture was sonicated at room temperature for 20 hours to functionalize RGO to fully oxidized graphene. The mixture was then filtered using a 0.22 μm microporous membrane and was washed a numerous times with de-ionized (DI) water until a pH of 7 was reached. The residual solid from filtration was dried in an oven at 80 °C for 2 hours and saved for the next step hydrothermal processing.

Hydrothermal processing is a technique that is generally used to synthesize graphene. This process was used in this work to cut the functionalized graphene oxide to smaller sizes and then reduce it to graphene. Hydrothermal processing has the capability of making doped

graphene by selecting a right fluid. The operation was carried out under a reducing atmosphere, relatively high pressure and moderate temperatures (200-250 °C). The reactants and a solvent were added to a container (hydrothermal bomb) and then sealed. The sealed container was heated to above boiling point of the solvent. This heating and the solvent vaporization creates a high pressure in the hydrothermal bomb. The generated atmosphere in the container is almost supercritical condition, which is needed for the solvent to behave as a reducing agent to reduce the functionalized graphene oxide to graphene. Zhou et al. showed that hydrothermal treatment by water could remove some of the graphene functional groups and rebuild the aromatic structures in the carbon lattice.[205] In this experiment, 100 mg of functionalized reduced graphene oxide (FRGO) and 70 ml of DI water were added to a hydrothermal bomb. The hydrothermal bomb was sealed and heated at 200 °C for 24 hours to assure reaching the best reduction and highest quality GQDs. Nitrogen doped GQDs were produced using the same procedure but splitting the 70 ml of water between water and ammonium hydroxide. Three separate hydrothermal tests for N-GQDs synthesis were carried out having ratios of 20 ml/50 ml, 40 ml/30 ml and 60 ml/10 ml for NH_4OH to H_2O. After cooling the hydrothermal bomb to room temperature, the resulting black suspension was filtered through a 0.22 μm microporous membrane. The filtrate colloidal solution, which contains GQDs was retained for further processing. This solution still contained some large graphene nanoparticles that emitted weak blue fluorescence through the container. Thus, it was further dialyzed in a dialysis bag (retained molecular weights of up to 3500 Dalton) overnight and GQDs that were strongly fluorescent through the bag were retained for analysis.

4.3.4 Results and Discussion

The starting material for GQDs synthesis was micrometer-sized rippled reduced graphene oxide sheets prepared by reduction of graphene oxide sheets using different techniques such as laser exfoliation by LVCC, microwave plasma or thermal exfoliation under argon atmosphere. The graphene sheets were then functionalized in a concentrated solution of H_2SO_4 and HNO_3 acids. During the oxidation, oxygen-containing functional groups, including C=O/COOH, OH, and C-O-C, were introduced at the edge and on the basal plane of the starting graphene sheets. The presence of these groups makes the graphene sheets soluble in water; thus, water was employed as a solvent for further processing of this material as well as obtaining its UV-Vis and PL spectra. Hydrothermal treatment of the functionalized graphene sheets reduces it to graphene and slices its physical size to ultra-fine graphene nanoparticles. This operation leads to changes in UV-Vis absorption and PL of produced GQDs.

Figure 4.37 shows UV-Vis spectra of nitrogen doped graphene quantum dots, which prepared at different concentration of ammonium hydroxide. The spectra of the products show a peak around 320 nm. The new adsorption band at 320 nm for synthesized GQDs samples was also observed by Pan et al.,[197] which is in addition to the typical strong π-π^* absorption peak at 270 nm due to the π –π^* transition of aromatic sp^2 domains.[104] Zhu et al.[206] have suggested that the shoulder absorption peak centered at a wavelength between 270 and 390 nm may be associated with the n –π^* transition of C=O. The peak position was shown to be more dependent on the synthesis method than anything else. For instance, the GQDs from solvothermal synthesis with 5.3 nm size showed a peak at 320 nm,[197] while the GQDs prepared by hydrothermal approach with a size of 3 nm showed a peak at 360 nm.[207] The main reason for lack of agreement between these results is due to the differences in the details of hydrothermal methodology used

in various studies that have led to different particle sizes in the produced graphene quantum dots. Particle size is known to be a critical factor in adsorption and emission properties of the particles.

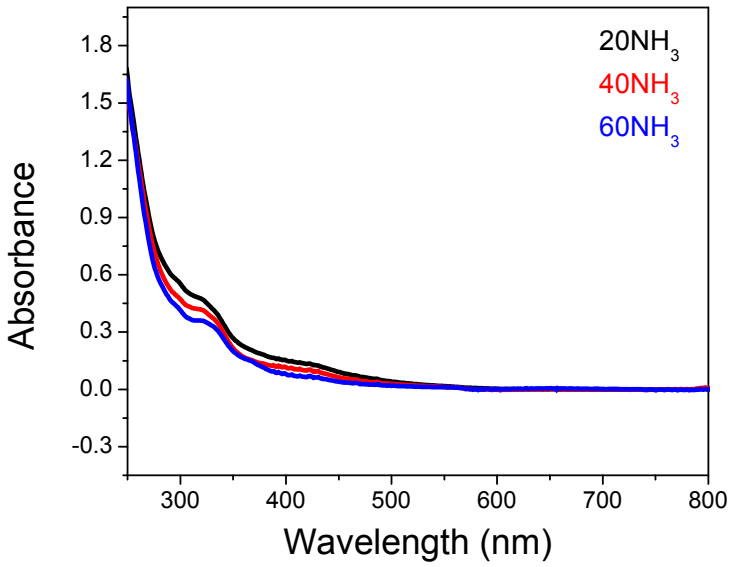

Figure 4.37. UV-Vis of graphene quantum dots containing different amounts of nitrogen.

Figure 4.38a through d displays the photoluminescence spectra of graphene quantum dots and nitrogen-doped graphene quantum dots at different excitation wavelength ranging from 275 to 400 nm. As expected, the reduced graphene oxide does not emit any luminescence, e.g. gives no PL spectrum. In contrast, the GQDs emit bright blue luminescence even in neutral media, which is similar to C-dots. As the spectrum of GQDs illustrates in Figure 4.38a, the intensity and peak location change with the excitation wavelength. For example, upon excitation at an absorption band of 325 nm, the PL spectrum shows a strong peak around 450-480 nm. As the excitation wavelength increases, the location of the peak moves to a higher wavelength. The most interesting finding is the observation of a new PL behavior. According to Tang et al.[208] the GQDs prepared by different methods could emit deep UV and blue, green, yellow, red or white PL. There are some factors that may affect the PL spectrum of GQDs including size, pH, and

solvent and excitation wavelength. The effect of excitation wavelength is clearly shown in Figure 4.38a as it was changed from 275 to 400 nm. As also stated by Qian et al.,[202] PL color may change from blue and green to yellow as particle size increases. Prepared GQDs by hydrothermal exfoliation, according to Pan et al.[197] showed a strong PL under alkaline conditions while under acidic conditions the PL was quenched. The PL of GQDs showed sensitivity with solvent and peak shifted from 475 to 515 nm in THF, acetone, DMF (Dimethylformamide) and water. Changing the excitation wavelength from 320 to 420 nm shifted the PL peak to longer wavelengths.[197]

Usually the observed PL emission could be divided into two classes. One is due to band gap transitions corresponding to conjugated π-domains, and the other with more complex origin that are more or less associated with defects in the graphene structures.[209] Consistent with this division, investigators have suggested the photoluminescence of GQDs is related to emissive traps, electronic conjugate structures, and free zigzag sites having a carbene-like triplet ground state as well as the surface state. It is possible that a combination of all these factors might be at play, as both the edge structure and the defects as well as the surface states can significantly change the electronic properties of GQDs.[210]

The PL spectra of synthesized N-GQDs with 20 ml/50 ml, 40 ml/30 ml, and 60 ml/10 ml NH_4OH/H_2O ratios are shown in Figure 4.38b through d respectively. Though the effect of excitation wavelength is obvious here, the shapes of the spectra are very different from that of GQDs presented in Figure 4.38a. There are two peaks in the spectra of N-GQDs samples; one appears at around 410 and the other at around 480 nm. There seems to be no effects of level of nitrogen substitution on the shape of spectra, peak intensities and locations of the peaks. Depending on the excitation wavelength, there are two peaks that can be seen at all excitation

wavelengths tested here except at 375 nm, which only one peak is seen. The shapes of the spectra changes with excitation wavelength; and as the intensity of the first peak decreases, the intensity of the second peak increases. The differences in the shape of the spectra between GQDs and N-GQDs are clearly the impact of nitrogen atoms in the carbon structure. One reason is the existence of the $n \rightarrow \pi^*$ transitions for the N-substituted aromatic heterocyclic. The large size of particles explains the diminishing oscillator strengths of the $n \rightarrow \pi^*$ transitions, because of the decreasing orbital overlap between the increasingly delocalized π^* electrons and the nonbonding electrons localized on the nitrogen atoms. This causes to show a peak at longer wavelength, while the lowest-energy transition from small size GQDs is $\pi \rightarrow \pi^*$, which is responsible for the emission; and, according to Li et al.[211] have less size-dependent oscillator strength. It has been reported that isolated sp^2 clusters of about 3 nm within the carbon–oxygen matrix could yield band gaps consistent with blue emission due to the localization of electron- hole pairs.[212] This finding along with previous observation of blue PL from nanosized graphene oxides[213] suggests an important role of the O-rich groups, in addition to the size and surface effects, to the observed blue-shift in the PL emissions from N-GQDs. Furthermore, the quantum mechanics calculations have proven the strong electron-withdrawing ability of the N atoms within the carbon conjugated plane[214], which may restrict the electron delocalization and therefore induce the blue shift in N–GQDs.

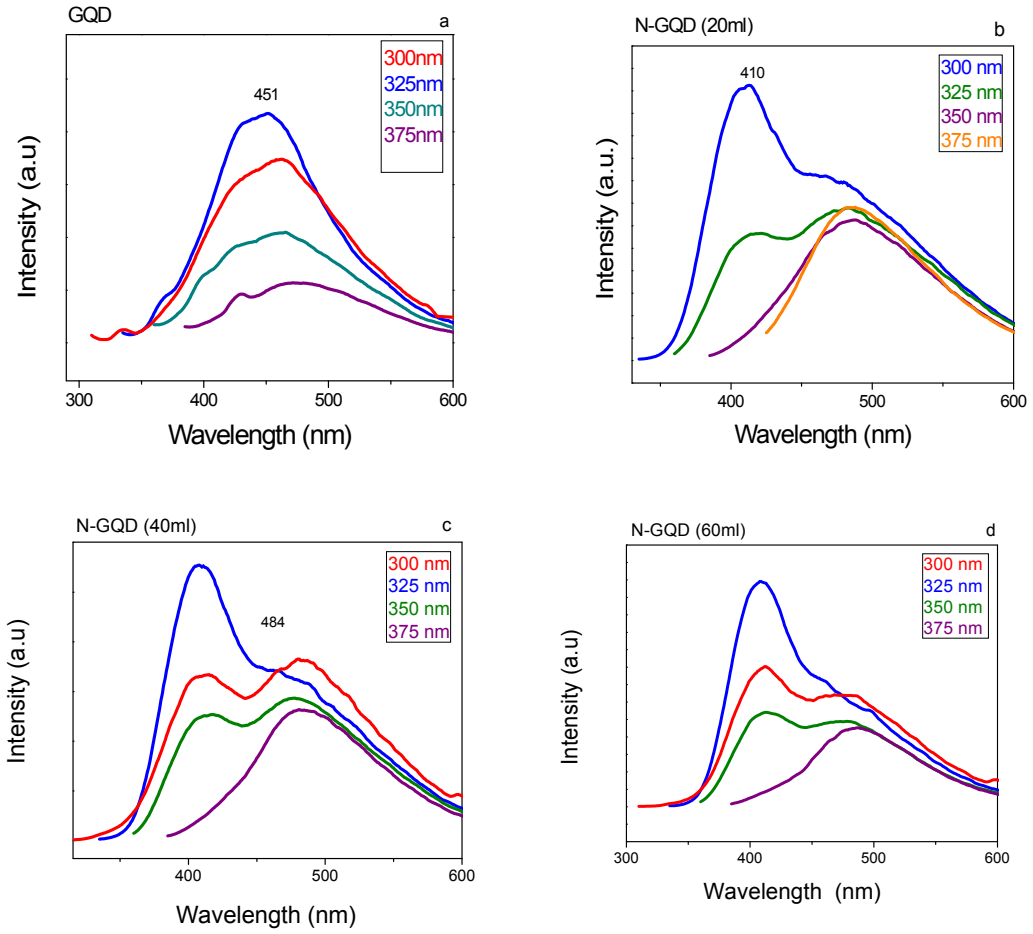

Figure 4.38 Photoluminescence of (a) graphene quantum dots (GQD) and (b, c and d) nitrogen-doped graphene quantum dots (N-GQDs).

The photoluminescence spectra of GQDs and N-GQDs at excitation wavelength of 325 nm are compared in Figure 4.39. The nitrogen doped graphene quantum dots exhibit a red shift of about 20 nm in PL emission (from about 450 to 475 nm) compared to graphene quantum dots with no nitrogen implying that the graphitic nitrogen helps charge transfer through the conjugated system of graphene quantum dots.

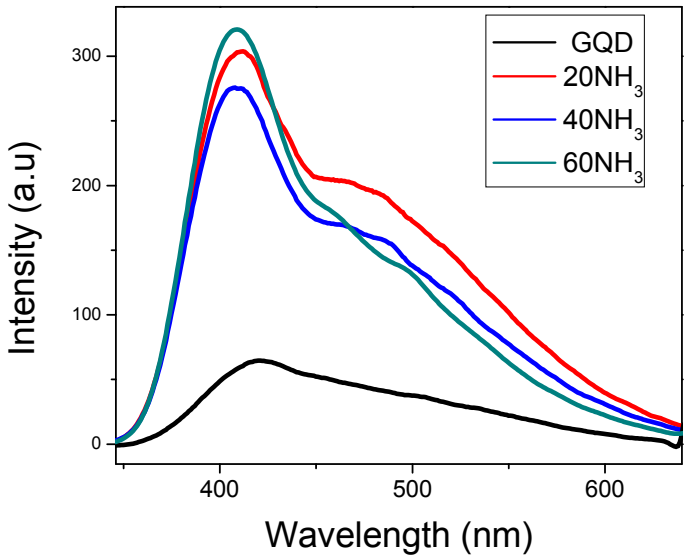

Figure 4.39. Photoluminescence spectra of graphene quantum dots (GQDs) and nitrogen-doped graphene quantum dots (N-GQDs) at excitation wavelength of 325 nm.

Figures 4.40a and 4.40b show representative TEM images of graphene quantum dots and nitrogen graphene quantum dots. The estimated size of graphene quantum dots are in the range of 4-10 nm, which decreases to about 2-6 nm after being dialyzed. For the nitrogen doped GQDs the average size is between 5 to 10 nm, which is qualitatively similar to un-doped graphene quantum dots.

Figure 4.41a shows The XPS C1s spectra of GQDs and N-GQDs where GQDs and N-GQDs were prepared by hydrothermal processing. The XPS C1s spectra show peaks at 284.5, 285, and 287.6 eV for GQDs and at 284.5, 286, and 288.4 eV for N-GQDs. Figure 4.41b presents the XPS survey spectra of G, GQDs and N-GQDs. The data are indicative of an increase in O intensity for both GQDs and N-GQDs demonstrating that GQDs and N-GQDs were functionalized with hydroxyl, carbonyl, and carboxylic acid groups. It is clear that the hydrothermal treatment of oxidized graphene employed in this work has not been able to totally remove all types of oxygen functional groups in GQDs and N-GQDs.

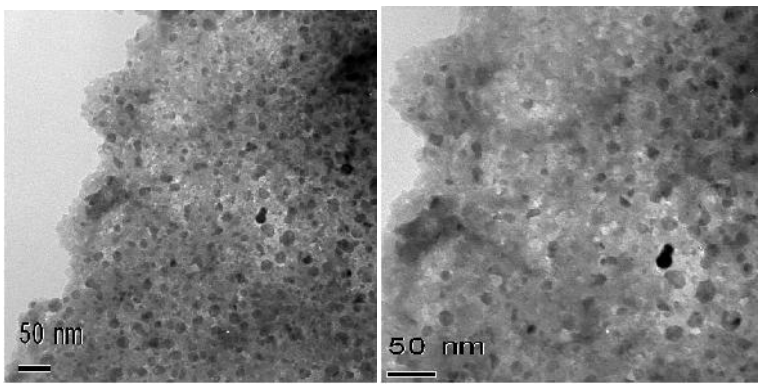

Figure 4.40a. Representative TEM images of graphene quantum dots before dialysis.

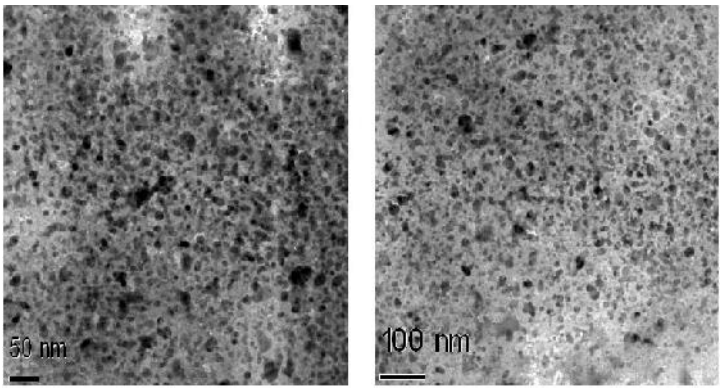

Figure 4.40b. Representative TEM images of nitrogen doped graphene quantum dots.

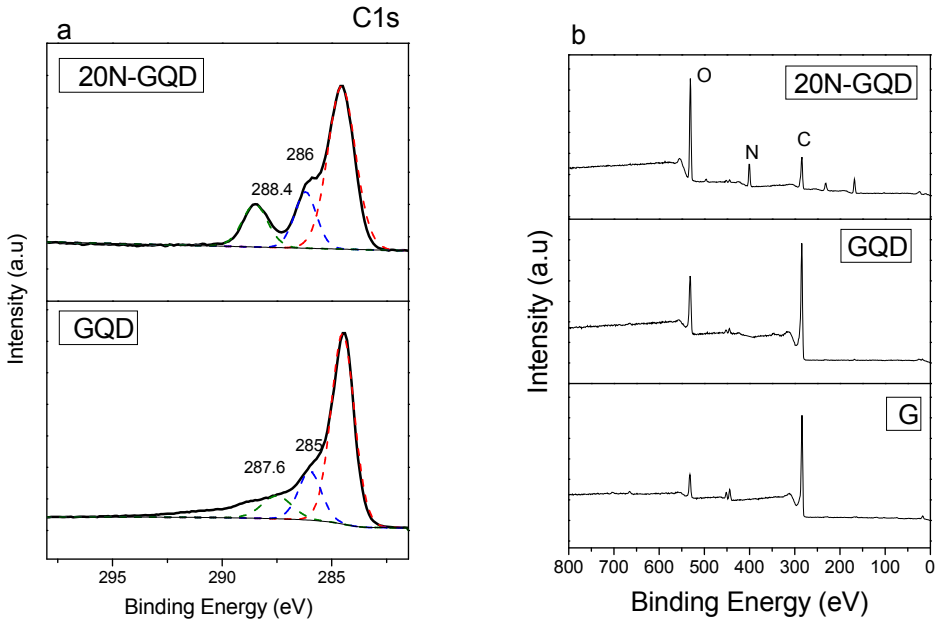

Figure 4.41(a) XPS C1s spectra of GQDs and N-GQDs samples and (b) XPS survey spectrum of G, GQD and N-GQDs.

Figure 4.42 compares the X-ray diffraction patterns of GQDs, graphene prepared thermally at 550 °C under an argon atmosphere, and oxidized graphene. Graphene has a peak at 2θ = 25.3° with d-spacing of 3.6 Å, oxidized graphene has a peak at 2θ = 24.5° with a d-spacing of 3.7 °A and GQDs with no nitrogen has a peak at 2θ = 26.7° with d-spacing of 3.4 Å. As expected the interlayer spacing of graphene at 3.6 Å is greater than that of bulk graphite at 3.34 Å. After the oxidation treatment of graphene and due to the insertion of oxygen functional groups into the structure the spacing increases to 3.7 Å. Hydrothermal treatment of oxidized graphene reduces the spacing to 3.4 Å, which is close to that of graphite indicating the effectiveness of deoxygenation during the hydrothermal processing. All the results are consistent with reported data in literature.[197] Since there were no critical changes in the lateral structure of G, the crystallinity of the final GQDs remained the same as dictated by the starting material.

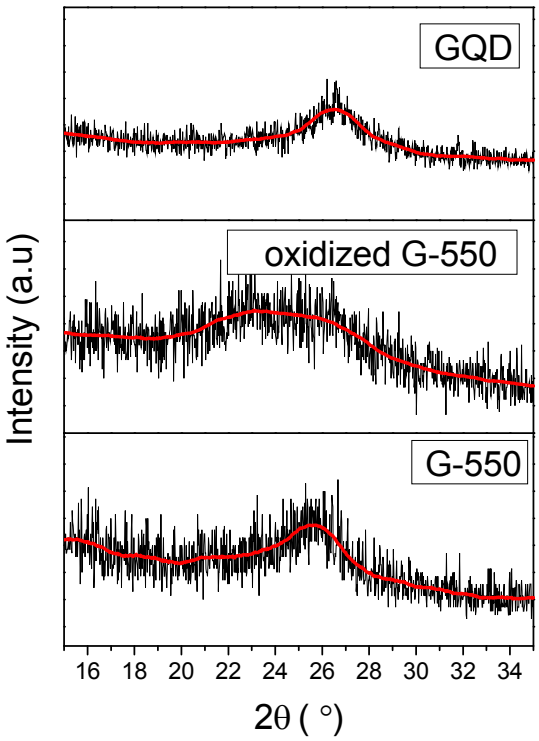

Figure 4.42. X-ray diffraction patterns of graphene (G-550) prepared at 550 °C under argon atmosphere, graphene oxide (oxidized G-550) and quantum graphene dots (GQDs).

Figure 4.43a displays the FTIR spectra of GQDs and 20N-GQDs. The peak at 1556 cm^{-1} corresponds to C=C bonds, which its intensity is reduced in 20N-GQDs sample indicating nitrogen insertion into the aromatic carbon skeleton as graphitic and pyridinic nitrogen. This result is further illustrated by XPS N1s spectra of 20N-GQD and 60N-GQD samples in Figure 4.43b. In Figure 4.43b, the XPS N1s spectra shows two components at 399 and 410 eV corresponding to pyridinic and graphitic nitrogen component respectively with the intensity of graphitic component is greater than that of pyridinic component. During acid oxidization, epoxy groups tend to form a line on a carbon lattice and the cooperative alignment induces a rupture of the underlying C-C bonds. Once an epoxy chain appears, it is energetically preferable for it to be further oxidized into epoxy pairs that converted to more stable carbonyl pairs at room

temperature. Nevertheless, FTIR spectrum of the oxidized graphene shows a strong carbonyl signal at 1712 cm^{-1} and a very weak epoxy signal at 1230 cm^{-1} (Figure 4.3a). As a result, one may suggest the existence of mixed epoxy chains composed of fewer epoxy groups and more carbonyl groups in the oxidized graphene. The presence of these linear defects makes the graphene structure fragile and susceptible to external attacks. Thus, some ultrafine pieces surrounded by the mixed epoxy lines and/ or edges may further break up during the hydrothermal deoxidization process, by, which the bridging O atoms in the epoxy lines are removed leading to the formation of GQDs.[197] After deoxygenation by hydrothermal treatment, the vibration band of C=O/COOH at 1730 cm^{-1} becomes weak and vibration band of epoxy groups at 1052 cm^{-1} disappear as shown in Figure 4.43a.

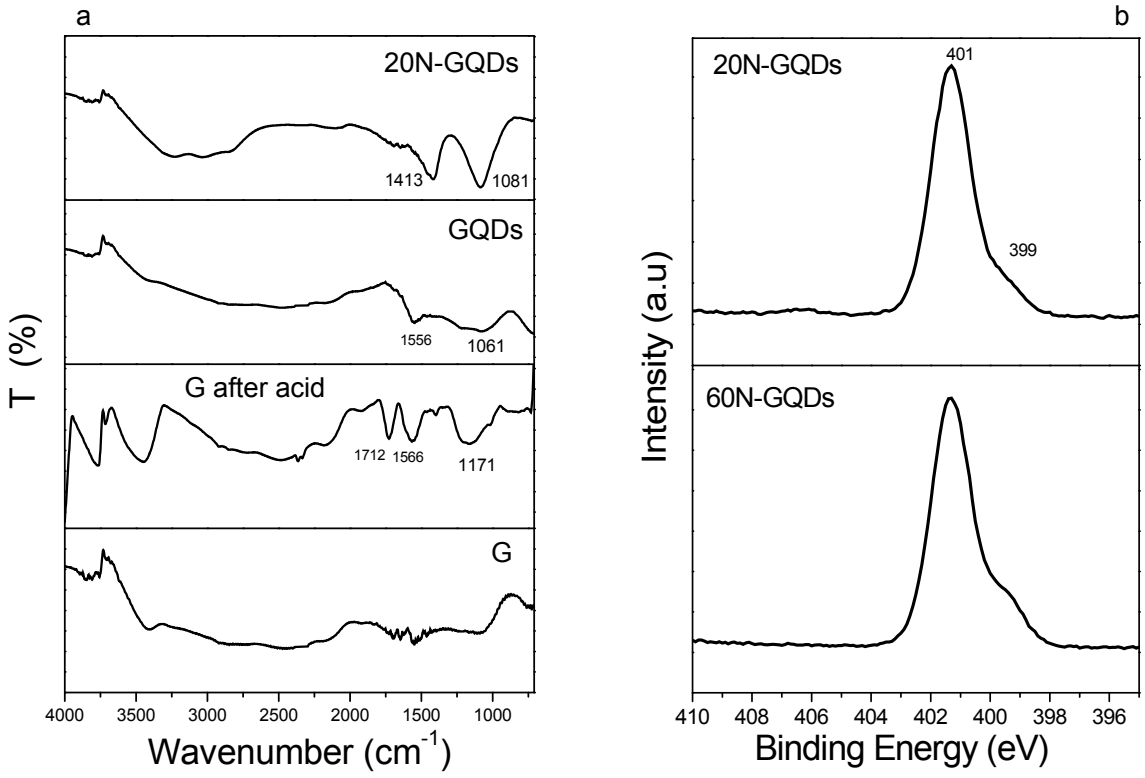

Figure 4.43 (a) FTIR spectra of 20N-GQD and GQD samples prepared by hydrothermal treatment, oxidized graphene (G after acid treatment), and G prepared by LVCC. (b) XPS N1s of 20N-GQD and 60N-GQD samples.

Raman spectra of graphene and graphene quantum dots prepared by hydrothermal treatment are shown in Figure 4.44. There are two bands one at 1371 and another at 1605 cm^{-1} for graphene and two bands at 1368 and 1603 cm^{-1} for GQD , which first one is assigned to D-band and second to for G-band. The calculated I_D/I_G ratio for GQD decreases to 0.87 relative to that of graphene at about 0.92 indicating more repaired conjugated system in graphene sheets.

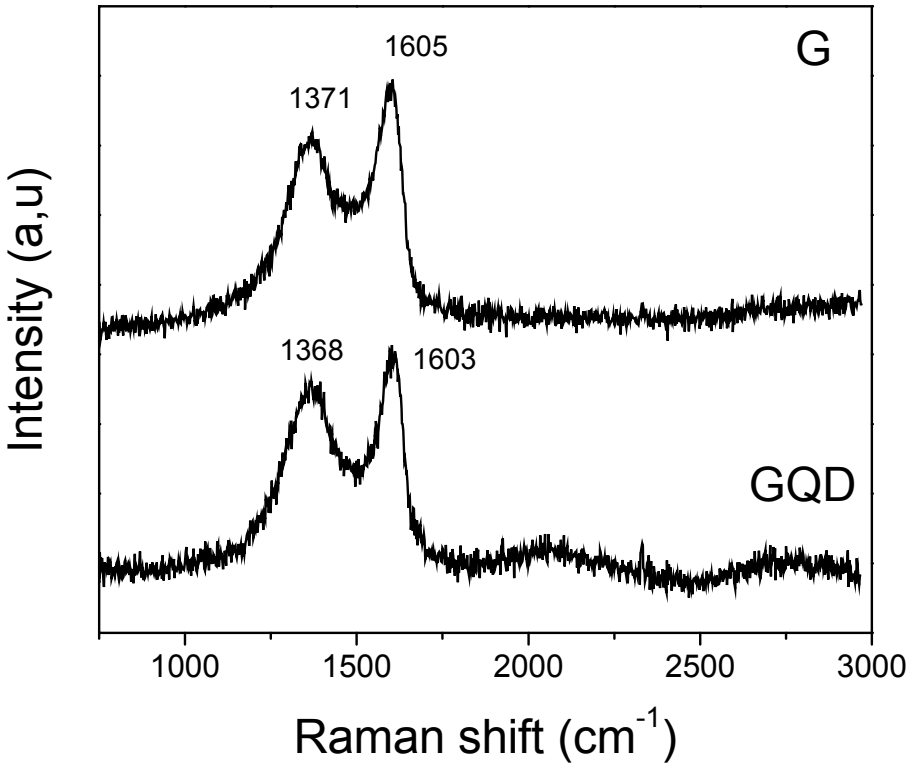

Figure 4.44. Raman spectra of graphene (G) and graphene quantum dots (GQDs) prepared by hydrothermal treatment at an excitation wavelength of 406.7 nm.

Chapter 5: Synthesis and Characterization of Vanadium, Molybdenum and Tungsten Nanoparticles, Their Oxides and Nanocomposite with Graphene in Different Media

Transition metal oxides are fascinating materials due to their structural variability and redox activity. In recent years, oxides of transition metals particularly oxides of vanadium, molybdenum and tungsten were used in numerous applications including electronic devices, batteries, sensors and catalysts. For instance, vanadium oxides and vanadium-based oxides were shown to be worthy host materials for the reversible inter-chelation and extraction of lithium, and therefore have been widely studied as suitable materials for electrode. In addition, the wide range of oxidation states of vanadium from +2 to +5 allows vanadium to potentially transfer more than one electron; hence, these materials have potential to provide higher capacities than the common one-electron-transfer materials.

The oxides of molybdenum and tungsten, on the other hand, are attractive for their photochromic[215-216] properties. Molybdenum oxide (MoO_3) is of special interest because of its multifaceted structural and functional properties. Molybdenum trioxide (MoO_3) have three forms, a thermodynamically stable α-phase,[217] a metastable β-phase,[216] and a h-MoO_3 phase.[218] Molybdenum trioxide exhibits optical absorption bands when it is irradiated with UV light.[219] As a result, molybdenum trioxide turns from white to blue in color. This photochromic effect has

resulted in numerous applications.[220] Molybdenum trioxide has thermo-chromic[221] properties and has widely been used as an electro-chromic material.[222]

Tungsten oxide is a n-type semiconductor , which its behavior is due to oxygen vacancies acting as donor sites.[223] Tungsten oxide has many properties including electronic,[224] photo-electrochemical,[225] photocatalytic activities,[226] and gas sensing effects, which makes it an excellent choice in various applications. Tungsten atom in tungsten oxide similar to other transition metal oxides assumes a lower valence (W^{4+} instead of W^{6+}).[227] In order to maintain the charge neutrality in the structure, oxygen vacancies is induced by removing oxygen from the lattice.[228] Changes in oxygen stoichiometry are responsible for the WO_3 response to ambient gases by varying its electrical conductivity. Surface reactions of tungsten oxide with reducing and oxidizing gases (e.g., H_2 or O_2) causes the formation and extinction of oxygen vacancies related to the transfer of electrons to or from the absorbed gases.[229]

These oxides have been produced in several different nano- and micro-structural morphologies including particles, rods, belts and tubes[230] using numerous techniques. Vanadium oxide (V_2O_5) nanoparticles were produced using various physical and chemical methods,[231-236] including pulsed laser deposition (PLD).[237] Formation of a thin film of vanadium oxide has been reported by an ultra-short pulsed laser deposition of vanadium oxide using a frequency doubled Nd:YAG laser.[238] Vanadium oxide nanoparticles were synthesized using different capping aliphatic amines, e.g. oleylamine and ethanol, acting as medium agents.[239] Molybdenum oxide (MoO_3) has also been synthesized using a number of techniques [240-243] including pulsed laser deposition.[240] Tungsten oxide nanoparticles (WO_3) were prepared by various methods,[244-247] including microwave plasma[244] and laser vaporization of metal.[248]

Among all vanadium oxides (V_2O_5, V_2O_3, V_3O_5, VO_2, and VO), vanadium pentoxide (V_2O_5) is the most stable form with various applications including potential application as catalyst, sensor and electrode. As a catalyst, it can be used for the mild oxidation of hydrocarbons and alcohols[249] or oxidation of sulfur dioxide to sulfur trioxide.[250] Vanadium oxide (V_2O_5) nanotube has lower diffusion distance and higher surface area,[251] , which could be used as electrode materials for energy storage devices[252] and cathode materials in lithium batteries. Molybdenum oxides are particularly found in applications such as supported catalysts, bolometric detectors, sensors and spintronic devices.[253] To name just a few, MoO_3 has been demonstrated to be applied in generating enhanced electric field emission[254] in batteries,[255] as a catalyst,[256] and in gas sensors.[257] Tungsten oxide nanoparticles have also many application such as solar control filters in car[258] and electrocatalytic hydrogen evolution in a sulfuric acid medium[259] and gas sensor devices. For instance, these nanoparticles can detect small concentrations in the ppm ranges of gases such as NO_x, H_2S, NH_3, O_3, O_2, H_2, and ethanol.[260-264]

The objectives of this chapter are first to synthesize the nanoparticles of metal (V, Mo, and W) and metal oxide (V_xO_y, Mo_xO_y, and W_xO_y) using LVCC. Then the capped nanoparticles of these metal and their oxides with certain organic solvents were prepared using LVSC. Finally, the nanocomposites comprising capped metal oxide by acetonitrile supported on graphene are produced by LVSC and MW treatment. All these techniques are fully described in Chapter 2. The synthesized samples for all cases are chemically and physically characterized using PL, UV-Vis, TEM, SEM, Raman, and XPS.

5.1 Nanoparticles of Vanadium, Molybdenum, and Tungsten and Their Oxides Using LVCC

The nanoparticles of metal (V, Mo, and W) and metal oxide (V_xO_y, Mo_xO_y, and W_xO_y) were synthesized using LVCC in He and O_2/He atmospheres. The characterization of synthesized nanoparticles was carried out by a number of spectroscopic techniques as will be shown in the next section.The LVCC, LVSC, and characterization methodologies were fully described in Chapter 2.

5.1.1 Results and Discussion

The X-ray diffraction patterns of vanadium and vanadium oxide nanoparticles prepared under pure He and O_2/He atmospheres are shown in Figure 5.1. Peaks at $2\theta = 42°$ (110), 60.9° (200), and 76.7° (211) correspond to vanadium nanoparticles with cubic crystal structure. Peaks at $2\theta = 26.9°$ (110), 38.5° (210), and 44.7° (310) correspond to vanadium oxide (V_2O_5) crystal. The XRD spectra in Figure 5.1 verify the formation of crystalline vanadium nanoparticle by LVCC under helium atmosphere with little to no surface oxides. Under O_2/He atmosphere, the formed structure is free of vanadium and is fully vanadium oxide. These results are in accordance with the data given for vanadium and its oxides in reference code JCPDS 03-065-4776.

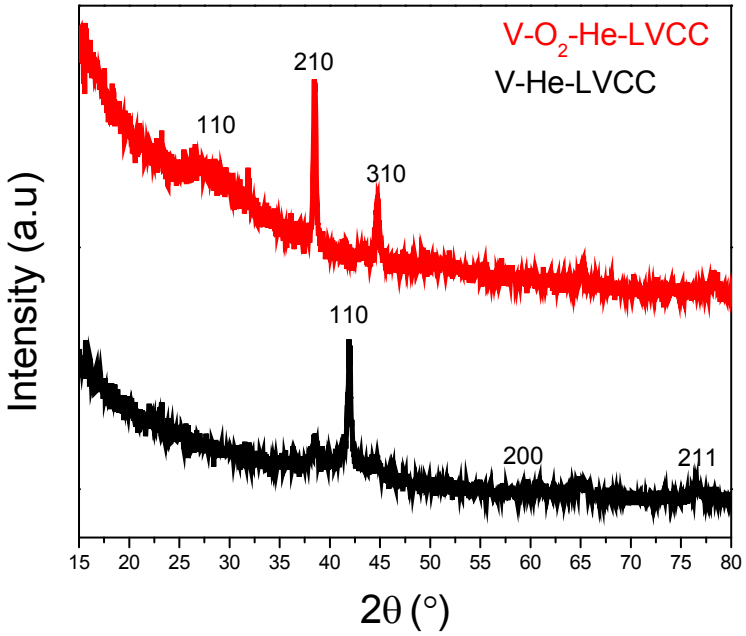

Figure 5.1. X-ray diffraction patterns of vanadium and vanadium oxide nanoparticles prepared by LVCC under pure He and O_2-He atmospheres.

The XRD patterns of molybdenum and molybdenum oxide samples prepared in pure He, and in 20, 50, and 100% O_2 using LVCC are shown in Figure 5.2. According to reference code JCPDS 01-088-2331, peaks at 2θ = 38.4° (111) and 40.6° (110) are assigned to cubic molybdenum nanoparticles. Peaks at 2θ = 23.8° (110), 26.2° (040), 38.4° (111), 40.4° (110), and 44.7° (200) represent MoO_3 nanoparticles structure formed under oxygen atmospheres.[265]

The XRD patterns for tungsten and tungsten oxide nanoparticles are given in Figure 5.3. For tungsten (W) nanoparticles prepared under helium atmosphere, the spectra has peaks at 2θ = 35.3° (200), 39.8° (210), 43.6° (211), 63.3° (222), 66.5° (320), and 69.5° (321). Based on the spectra given for tungsten in reference JCPDS 03-065-6453, tungsten nanoparticles prepared by LVCC should have cubic crystal structure and could be β-W. For tungsten oxides (WO_3) nanoparticles prepared under different partial pressures of O_2 atmospheres, the identified peaks are at 2θ = 23.9° (110), 33.2° (200), 41.3° (201), 44.8-44.9° (211), 54.6° (221), and 60.5° (311)

are in good agreement with reference JCPDS 01-085-0808 for tungsten oxide (WO_3) nanoparticles with tetragonal crystal.

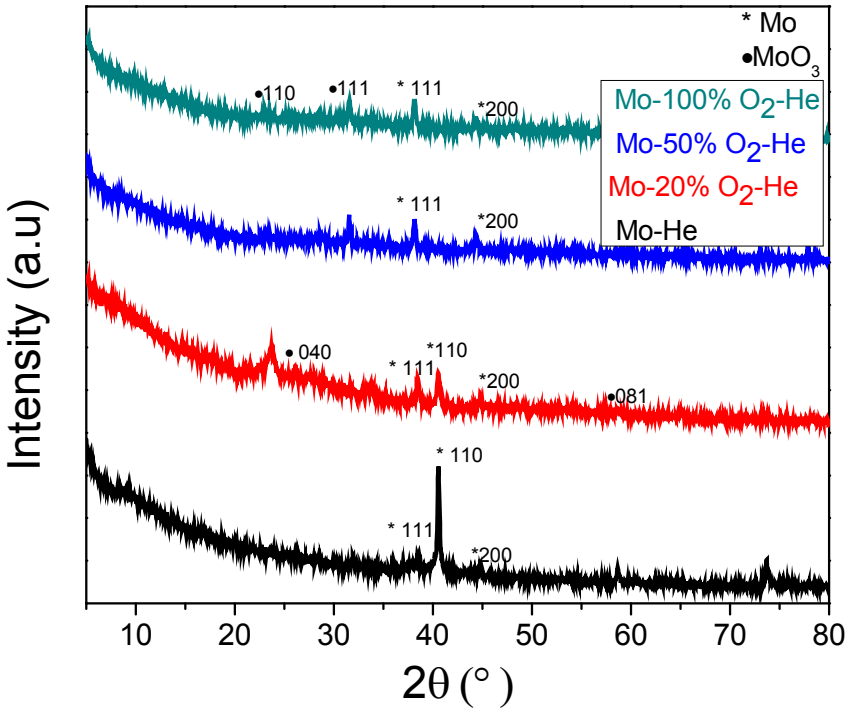

Figure 5.2. X-ray diffraction patterns of molybdenum and molybdenum oxide nanoparticles prepared under pure He and O_2/He atmospheres using LVCC.

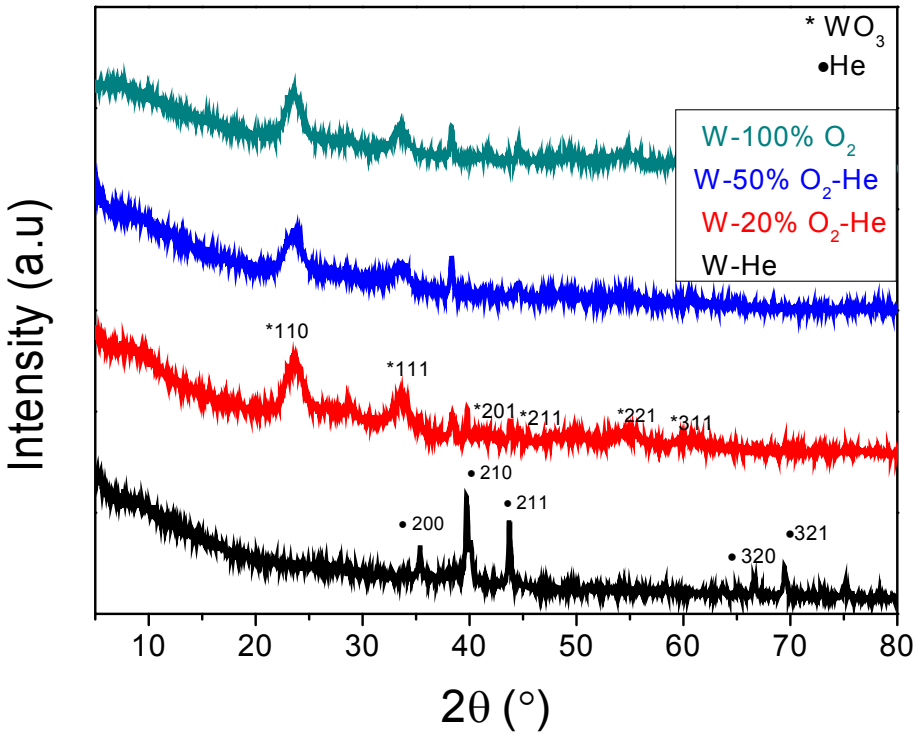

Figure 5.3. X-ray diffraction patterns of tungsten and tungsten oxide nanoparticles prepared by LVCC under He and O_2/He atmospheres.

Samples of vanadium and vanadium oxide were characterized by Raman spectroscopy and the results are displayed in Figure 5.4. Raman analysis of vanadium nanoparticle presents bands at 94, 140.5, 191.6, 282.4, 407, 691, and 989 cm^{-1}, which is similar to the Raman spectrum of vanadium oxide nanoparticles and according to Pol et al.,[266] correspond to V_2O_5. These results are in agreement with XPS data (discussed later in this section), but somewhat different from the XRD results for vanadium nanoparticles. This can be explained by remembering that the Raman is a surface analysis technique and X-ray provides information for the bulk. According to Zhang et al.,[267] the bands observed in the Raman spectrum of V_2O_5 at 989 cm^{-1} and 691 cm^{-1} are for V=O and V-O stretching from doubly coordinated edge-shared oxygen atoms common to two VO_5. Peaks at 407 and 282 cm^{-1} are attributed to V=O bending.

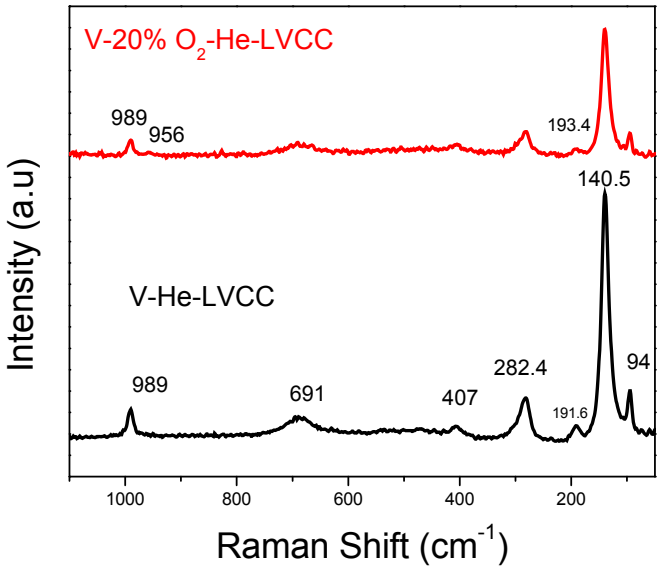

Figure 5.4. Raman spectra of vanadium and vanadium oxide nanoparticles prepared by LVCC at an excitation wavelength of 780 nm.

Raman spectrum of molybdenum nanoparticles prepared in a helium atmosphere displays peaks at 375, 523, 893, 1035, 1095, 1123, and 1603 cm^{-1} as shown in Figure 5.5. The main features of the spectra are located in the region of 800-1000 cm^{-1}, which are due to Mo=O (sym/asym) at higher frequencies and to Mo-O-Mo (sym) at lower frequencies and are consistent with the results presented by Miras et al.[268] The Raman spectra of synthesized MoO_3 nanoparticles in 20% O_2/He were collected using an excitation wavelength of 780 nm and presented in Figure 5.6. According to Klinbumrung et al.[269], the O-Mo-O bending scissoring, O-Mo-O bending, Rc modes and O=Mo=O twisting modes appear at 375, 336, and 213 cm^{-1} respectively. The peak at 280 cm^{-1} is assigned to the wagging mode for the double bond O=Mo=O and is evidence of partial oxidation. The peak at 661 cm^{-1} represents the triply coordinated oxygen (Mo_3–O) stretching mode resulting from corner-shared oxygen atoms common to three octahedral. The 820 cm^{-1} peak is for the doubly coordinated oxygen (Mo_2–O)

stretching mode, which results from corner-sharing oxygen atoms common to two MoO_3 octahedrons. The peak at 991 cm^{-1} according to Kalantar-zadeh et al.[270] is assigned to the terminal oxygen (Mo^{6+}=O) stretching mode resulting from an unshared oxygen.

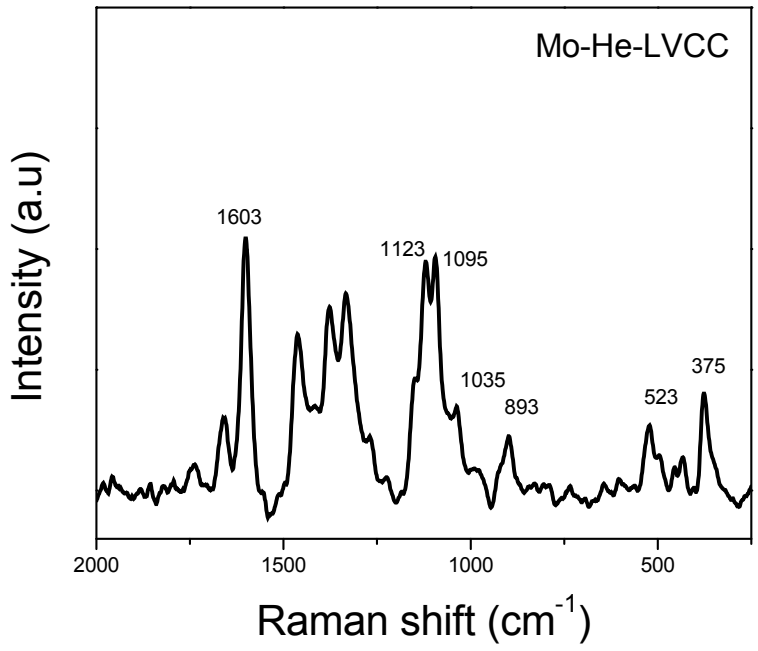

Figure 5.5. Raman spectrum of molybdenum prepared by LVCC under pure He atmosphere at an excitation wavelength of 780 nm.

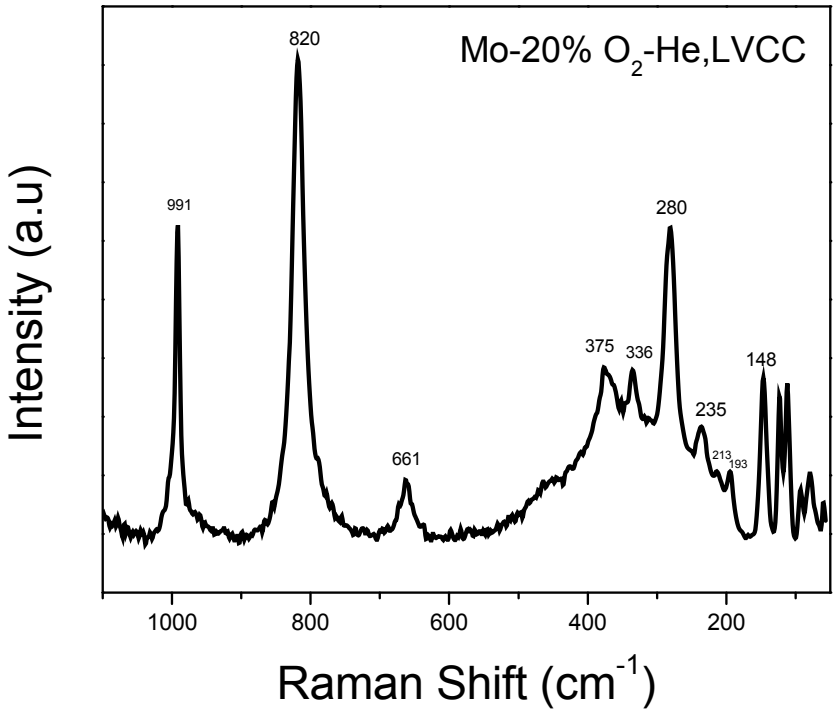

Figure 5.6. Raman spectrum of molybdenum oxide prepared by LVCC under O_2/He atmosphere at an excitation wavelength of 780 nm.

Figure 5.7 displays Raman spectra for tungsten and tungsten oxide nanoparticles prepared under different gaseous conditions of pure He and O_2/He by LVCC. The Raman spectrum of the tungsten oxide nanoparticles shows bands at 256.5, 323, 524, 698, and 802 cm^{-1}. Bands at 698 and 802 cm^{-1} could be attributed to W-O-W stretching modes, and bands at 256.5 and 323 cm^{-1} are expected to be due to W-O-W bending mode. The bands between 250 and 450 cm^{-1} correspond to the bending of O-W-O. The bands between 630 and 900 cm^{-1} according to Li et al. [271] are attributed to either the anti-symmetric stretch of M-O-M or the symmetric stretch of O-M-O bonds. The weak shoulder at 631 cm^{-1} can be logically assigned to the O–W–O stretching vibration, which is in good agreement with Xiao et al.'s [272] suggestions. Peaks at 273, 327, 715 and, 807 cm^{-1}, according to Horsley et al.[273] can be assigned to crystal tungsten oxide (WO_3). The intense peaks in the range of 715 to 807 cm^{-1} are typical Raman peaks of crystalline WO_3

(m-phase). These peaks correspond to the stretching vibrations of the oxygen bridges and can be assigned to W-O stretching, W-O bending and O-W-O deformation modes respectively. The Raman spectra, however, do not clearly indicate peaks that may be attributed to crystalline WO_2 presence in the samples synthesized in this study. The major bands for WO_2 should occur at around 286, 617, and 781 cm^{-1}, which are almost absent in the oxide samples from this study. The sample prepared by Frey et al.[274] showed these peaks but with very low intensity. Again the spectrum of tungsten nanoparticles has similar feature as tungsten oxide nanoparticles indicating an oxide surface coating, which is typical of most metal nanoparticles exposed to air.

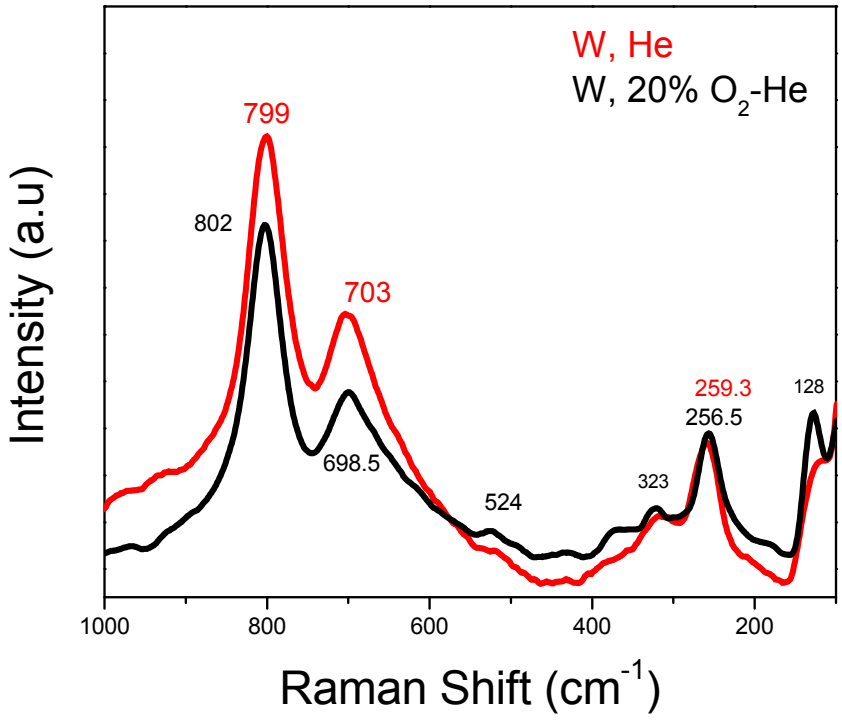

Figure 5.7. Raman spectra of tungsten and tungsten oxide nanoparticle prepared under He and O_2/He atmosphere by LVCC at an excitation wavelength of 780 nm.

The XPS spectra of molybdenum and molybdenum oxide nanoparticles prepared by LVCC are displayed in Figure 5.8. The Mo 3d XPS spectrum of MoO_3 shows the characteristic

of doublet ($3d_{5/2}$ at 232.5 eV and $3d_{3/2}$ at 235.7 eV) caused by spin-orbit coupling , which is in agreement with He et al. [216] results. Peaks for 3d (5/2 and 3/2) at around 228 and 228.8 eV for molybdenum nanoparticles are indicative of some surface oxidation on Mo nanoparticles [NIST].

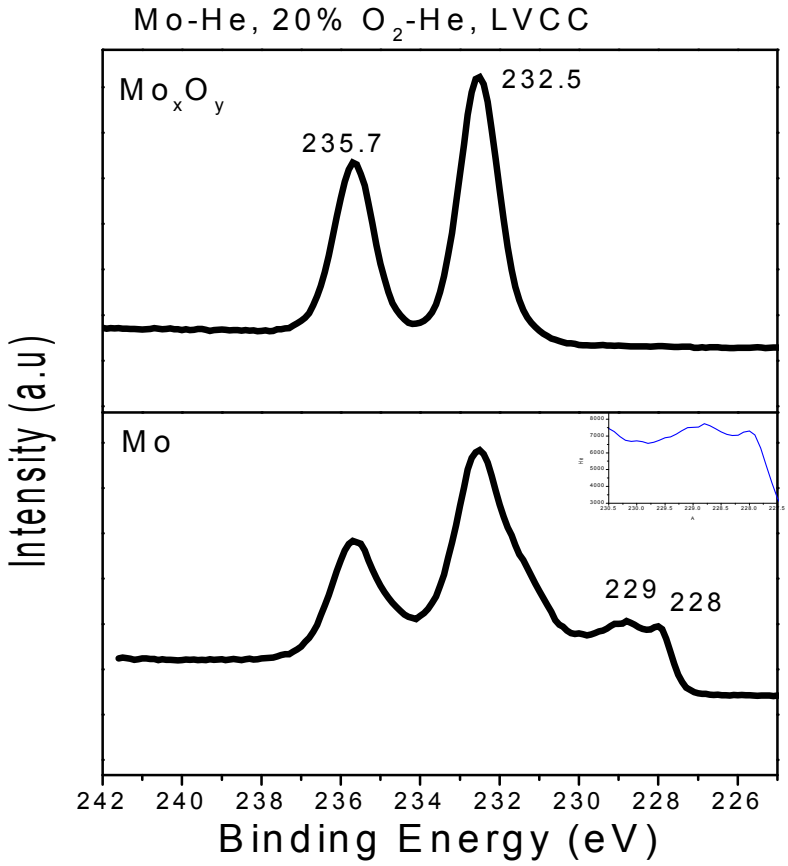

Figure 5.8. XPS spectra of molybdenum and molybdenum oxide nanoparticles prepared by LVCC under He and O_2/He atmospheres.

Figure 5.9 presents the XPS results for tungsten and tungsten oxide nanoparticles prepared by LVCC. The spectra in Figure 5.9 demonstrates the results for tungsten 4f (5/2 and 7/2) and 5p ($_{3/2}$), and for tungsten oxide 4f (5/2 and 7/2) and $5p_{3/2}$ components. The binding

energies of W $4f_{7/2}$ and W $4f_{5/2}$ with representative peaks at 30.4 eV and 32.5 eV are indicative of metallic tungsten. There are two main peaks at 35.1 and 37.2 eV, which correspond to $4f_{7/2}$ and $4f_{5/2}$ of WO_3 respectively. The small peak at 40.8 eV could be assigned to $5p_{3/2}$ of WO_3. As these results suggest the surface of tungsten nanoparticles carries a large amount of WO_3. Figure 5.9 also presents the XPS spectra of tungsten oxide nanoparticles. There are W 4f doublet peaks at 35.2, and 37.4 eV and a small peak at 41.1 eV, which are due to W $4f_{7/2}$, $4f_{5/2}$, and $5p_{3/2}$ respectively. The peak at 35.2 eV is assigned to W^{6+} of the stoichiometric WO_3. All the binding energies are indicative of the WO_3 chemical state on the surface. In tungsten oxide there is 0.5 eV shift toward higher energy relative to the metal state. To explain this higher energy in the oxide state, one can say that the six valence electrons of the tungsten atom are transferred into the oxygen p-like bands, which are completely filled in WO_3 nanoparticles. So 5d valence electrons have no part of their wave function near tungsten atom and remaining electrons in the tungsten atom experience a stronger Coulomb interaction with the nucleus than in the case of tungsten atom in metallic form. Therefore the binding energy of the W 4f level is higher in WO_3 than in metallic tungsten.

Figure 5.10 displays typical TEM images of vanadium, molybdenum and tungsten nanoparticles and their oxides nanoparticles prepared by LVCC. The average size of the nanoparticles is in the range of 1.5 to 6 nm for Mo, W, and V nanoparticles prepared by LVCC in a He gas atmosphere.

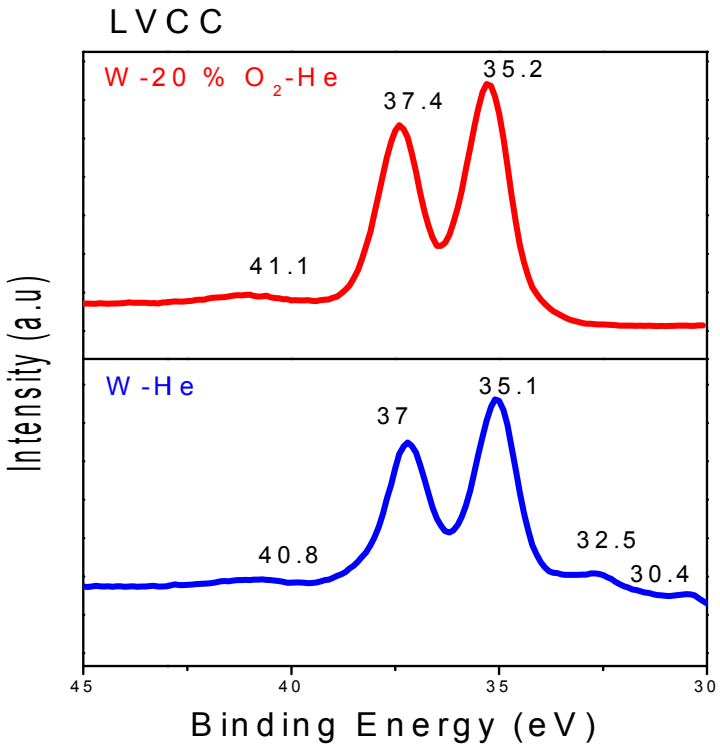

Figure 5.9. XPS spectra of tungsten and tungsten oxide prepared by LVCC.

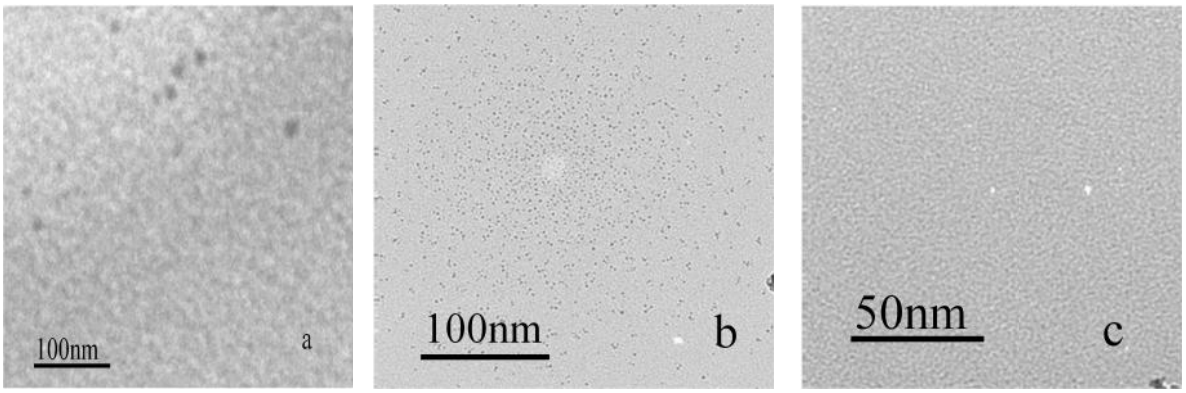

Figure 5.10. Representative TEM images of (a) Mo, (b) W, and (c) V nanoparticles prepared by LVCC under He gas.

5.2 Nanoparticles of Vanadium, Molybdenum and Tungsten and Their Oxides Capped with Different Organic Molecules Using LVSC

In this section, LVSC was employed to produce nanoparticles of V, Mo, and W and their oxides capped with different organic molecule such as acetonitrile (AN), methanol (Met), and tetrahydrofuran (THF). LVSC method was fully described in Chapter 2. This method also provides several advantages over LVCC method, including (a) combining gas phase and wet chemistry for nanoparticle synthesis, (b) utilization of different solvents during the synthesis, (c) capturing of nanoparticles by polar solvent upon their formation, (d) stability of the suspension compared to dispersion of pre-formed nanoparticles in a solvent, (e) achieving smaller size nanoparticles due to hindrance of particle growth, and (f) preparation in short time with little to no contamination due to the limited number of steps, comparing to other techniques.

5.2.1 Results and Discussion

While presenting the results for the nanoparticles prepared by LVSC in this section, from time to time comparisons are made with the results of nanoparticles obtained by LVCC. In LVSC, the formed nanoparticles were collected in an organic solvent as they are formed; while in LVCC, the solvent was only used as a media for dispersing the already synthesized nanoparticles.

Figure 5.11 compares the FTIR spectra of two vanadium oxide samples, one prepared by LVCC and the other by LVSC in acetonitrile. The sample prepared by LVSC in acetonitrile displays peaks at 553, 768, and 992 cm^{-1}, which indicate some shift from the corresponding peaks of the sample prepared by LVCC with no acetonitrile. The sample by LVCC shows peaks at 582, 782, and 982 cm^{-1}. The absorption bands between 500 and 1,000 cm^{-1} could be indexed to various vibrations of vanadium-oxygen bonds. According to Sediri et al.[235] there are two bands for V=O and V–O–V in V_2O_5 nanoparticles, which appear at 982 and 582 cm^{-1} respectively.

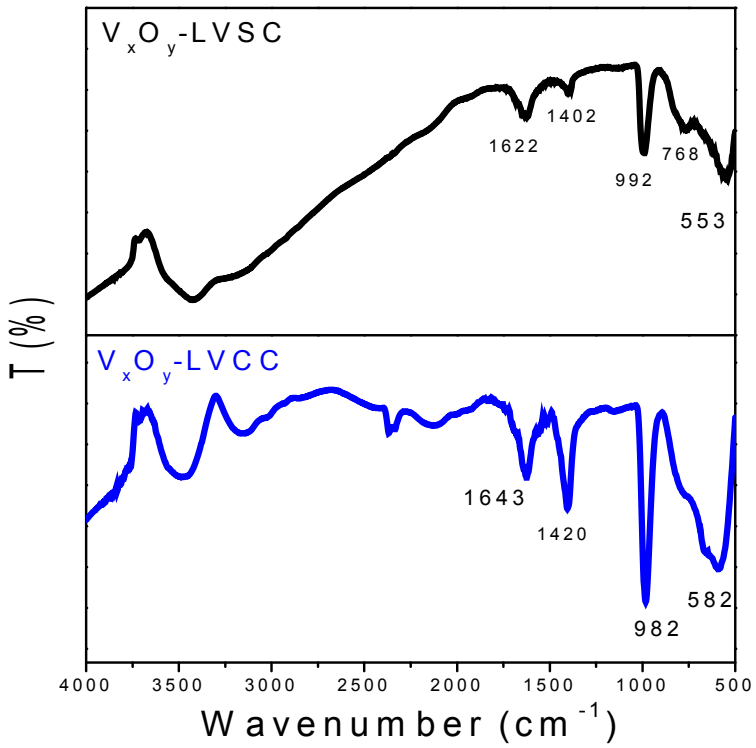

Figure 5.11. FTIR spectra of vanadium oxide nanoparticles prepared by two methods of LVCC and LVSC.

Absorption (UV-Vis) and photoluminescence (PL) results of vanadium oxide nanoparticles prepared by LVSC in various solvents as capping agents are shown in Figures 6.25a and b. The UV-Vis spectra of the vanadium oxide nanoparticles as shown in Figure 5.12a indicate a broad and strong absorbance around 280 – 350 nm. The absorption peak is at a higher wavelength (343 nm) for vanadium oxide nanoparticles prepared under O_2/He using LVSC and AN solvent than those of two other solvent namely THF and CH_3OH. All three nanoparticle prepared with THF, AN, and CH_3OH were expected to form bonds with solvents. An indication of such bonding is evident in Figure 5.12b as the capped nanoparticles exhibited an intense and broad photoluminescence from 420 – 440 nm.

As presented in Figure 5.12b the nanoparticles of vanadium oxide coated with THF and AN show a strong PL from 420 to 440 nm. Nanoparticles prepared in methanol did not display a PL, thus, the effects of excitation wavelength were investigated further with only THF and AN, and the results are presented in Figure 5.13. A broad photoluminescence from 350 to 430 nm for the excitation wavelengths ranging from 320 to 400 nm can be observed. The white light emission has been observed for vanadium oxide samples , which is consistent with the results reported by Ard et al.[275] The emission seems to be coming from vanadium oxide for both samples of V_2O_5-THF and V_2O_5-AN.

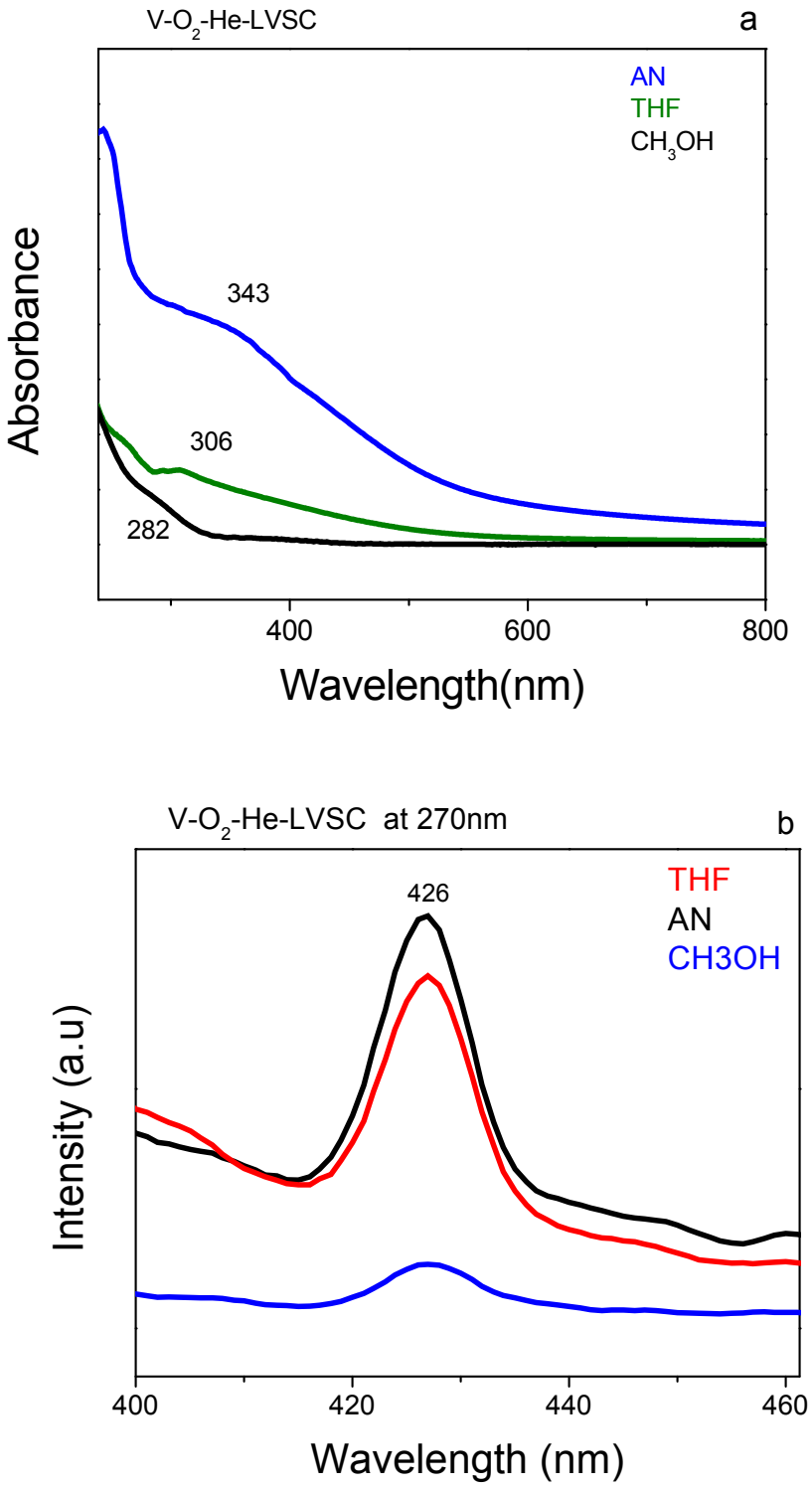

Figure 5.12. (a) UV-Vis and (b) Photoluminescence of vanadium oxide nanoparticles coated with different solvents (THF, AN, and CH_3OH) prepared by LVSC.

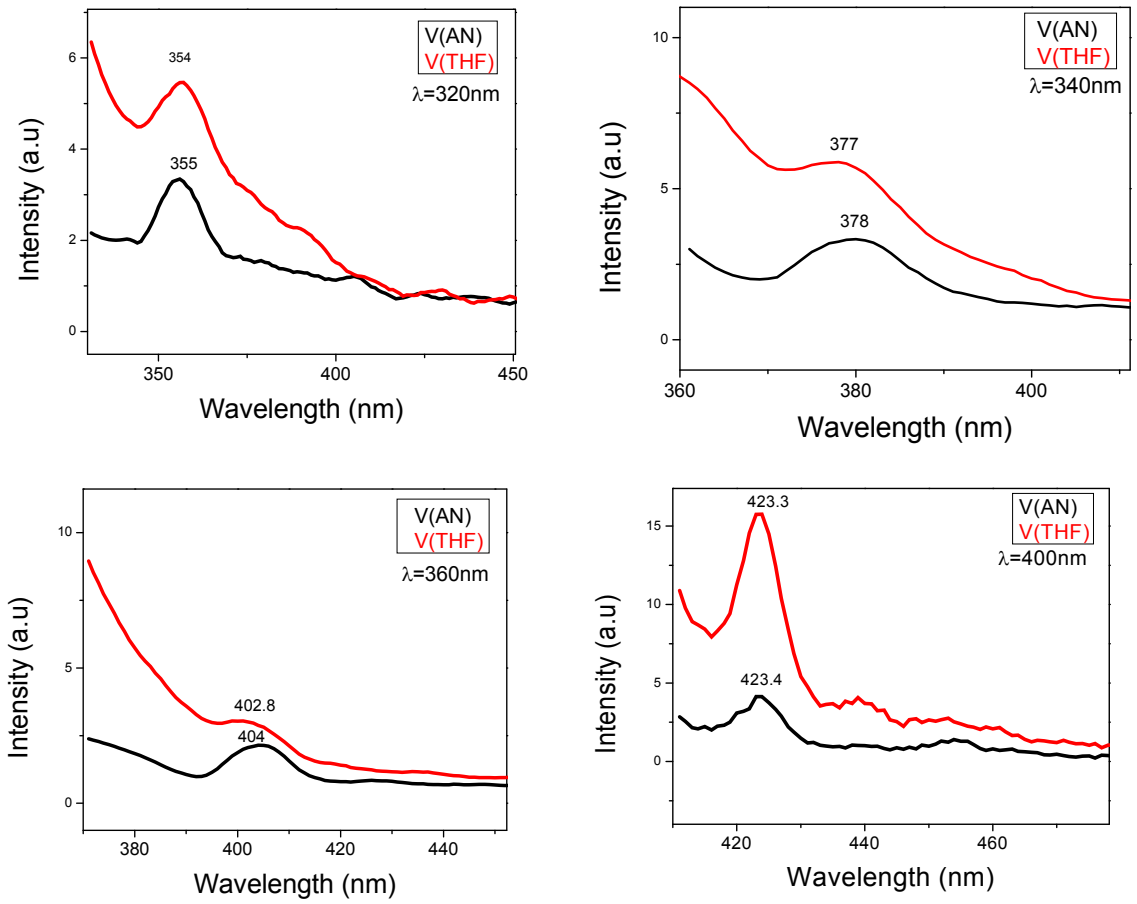

Figure 5.13. Photoluminescence as a function of excitation wavelength for vanadium oxide nanoparticles capped with THF and AN using LVSC method.

Figure 5.14 (a and b) compares the UV-Vis and photoluminescence of vanadium oxide nanoparticle samples prepared by two methods of LVCC and LVSC using acetonitrile (AN). As shown in Figure 5.14a, the nanoparticles prepared by LVCC display an absorbance around 432 nm, which is blue shifted to 340 nm for the nanoparticles prepared using LVSC. This blue shift is attributed to the smaller size of nanoparticles as well as the capping of nanoparticles by acetonitrile during preparation in LVSC. The capping of nanoparticles by the acetonitrile is expected to be absent in the sample preparation by LVCC. This absorption band (340 nm) according to Ghabi et al. [276] could be responsible for the charge-transfer bands (π - d) between oxygen and vanadium. Similarly in the photoluminescence spectra as shown in Figure 5.14.b, the

nanoparticles prepared by LVSC show peaks at 311, 361, and 383.4 nm, which are clearly shifted compared to 305, 359, and 382 nm for the sample prepared by LVCC.

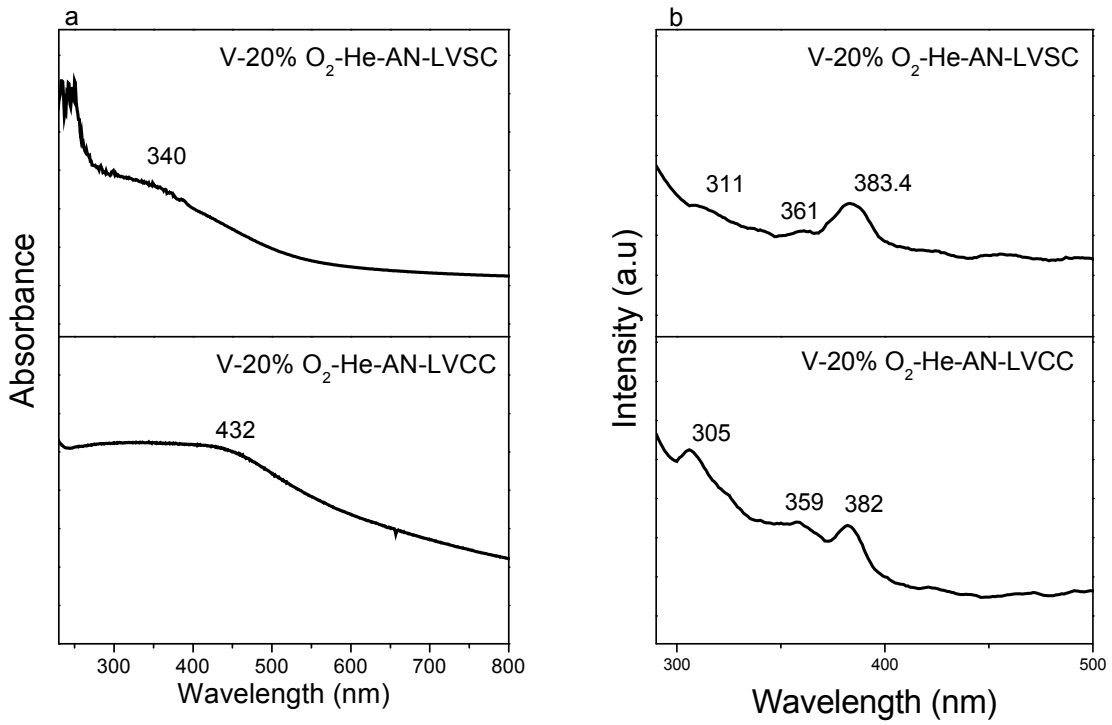

Figure 5.14. (a) UV-Vis absorption and (b) photoluminescence spectra of vanadium oxide nanoparticles prepared by two methods of LVCC and LVSC.

Figures 5.15a and b shows, respectively, the UV-Vis absorption and photoluminescence spectra of molybdenum and molybdenum oxide samples prepared by LVCC and LVSC in acetonitrile. The UV-Vis spectrum of the nanoparticles synthesized by LVSC shows a blue shift in comparison to the samples prepared by LVCC, which acetonitrile was only used as a dispersing agent. This blue shift could be attributed to a smaller size of nanoparticles as well as surface coverage by acetonitrile during LVSC process. As can be seen in Figure 5.15a, samples prepared by both methods show a strong absorbance in UV with an extensive low-energy tail. The samples prepared by LVSC show peaks around 324.7 and 303 nm for molybdenum and molybdenum oxide respectively. These peaks were not observed in samples prepared by LVCC.

Photoluminescence of all samples prepared by both methods and under inert (He) or oxidative atmospheres show two peaks one around 360 nm and the other around 430 nm (Figure 5.15b). These results are in overall agreement with prior work published by Song et al.[277] and Klinbumrung et al.[269] Thermodynamically stable α-MoO_3 phase shows a strong emission centered around 430–440 nm. This emission is expected to be caused by the band-to-band transition. Furthermore, according to Navas et al.[278] the PL spectra of molybdenum oxide samples could show two emission bands, namely a UV luminescence (343–389 nm) and a UV-visible (blue at 450 nm and bluish green at 470 nm). The UV luminescence band (343-389 nm) can be attributed to the strong near-band edge emission caused by the free-excitation recombination in each film. The visible light emission can be originated from transitions of excited optical centers in the deep levels. This deep level emission is usually caused by the presence of impurities, molybdenum interstitials, and surface as well as structural defects.

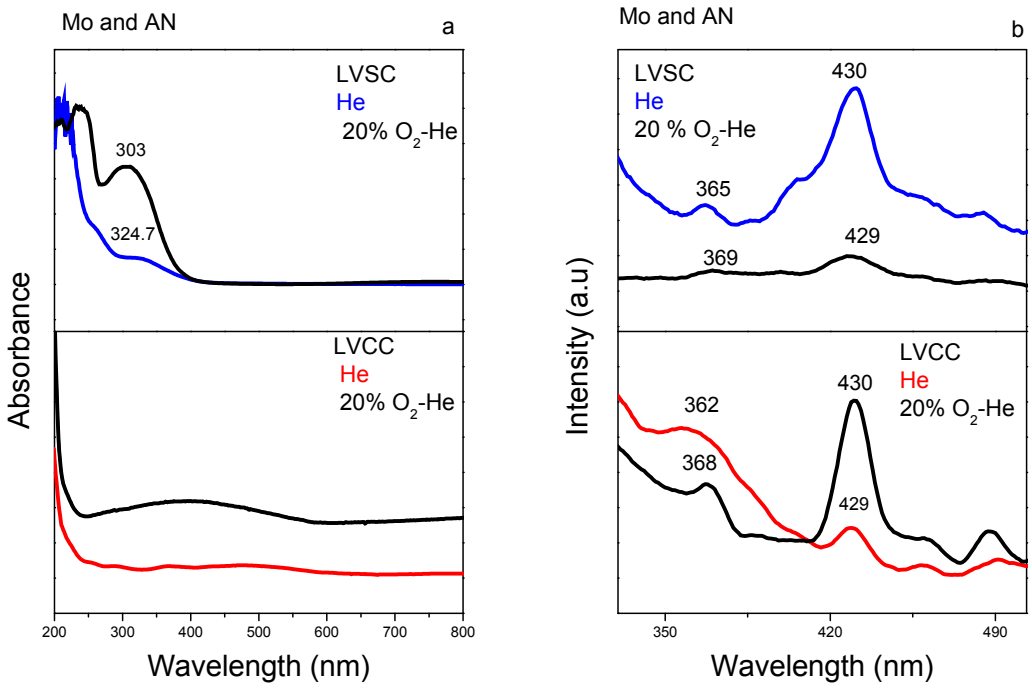

Figure 5.15. (a) UV-Vis absorption and (b) photoluminescence spectra of molybdenum and molybdenum oxide nanoparticles prepared by two methods of LVCC and LVSC.

Figure 5.16 through 5.18 shows UV-Vis and the photoluminescence spectra of tungsten and tungsten oxide nanoparticle samples prepared using LVCC and LVSC methods. Figures 5.16a, 5.17a, and 5.18a show the UV-Vis spectra of tungsten and tungsten oxide samples prepared by LVCC (no solvent) and LVSC using three capping solvents, namely acetonitrile, tetrahydrofuran and methanol. The tungsten nanoparticles, regardless of the preparation methods, do not show any absorption while tungsten oxide nanoparticles present a peak at around 280-300 nm. Pure colloidal WO_3, according to Su et al.,[279] is expected to have an absorption at around 360 nm. Tungsten oxide sample prepared in this study is not purely colloidal and this could be the reason for being different from Su et al.[279] Another study has shown the oxygen vacancies or

defects could be responsible for the red shift phenomenon from 394 to 417 nm.[280] This later proposition can be verified by decreasing oxygen partial pressure in the system.

The PL spectra of similar samples using an excitation wavelength of 270 nm are presented in Figures 5.16b, 5.17b, and 5.18b. Similar to UV-Vis results, none of the tungsten nanoparticle samples show any peak at around 430 nm indicating insignificant level of surface oxides in the sample. The tungsten oxide and tungsten nanoparticles prepared by LVSC show a clear peak at around 430 nm. The oxide samples prepared using capping agents show an additional peak between 366-370 nm. These results are consistent with the prior literature such as the work by Jayatissa et al.[281] They presented two peaks for the tungsten oxide samples; a UV emission peak at 355 nm caused by band-to-band transitions, and another peak at 435 nm for blue emission caused by defects like oxygen deficiencies or other impurities. The pure WO_3 do not exhibit the blue emission because it contains minor oxygen vacancies.[282]

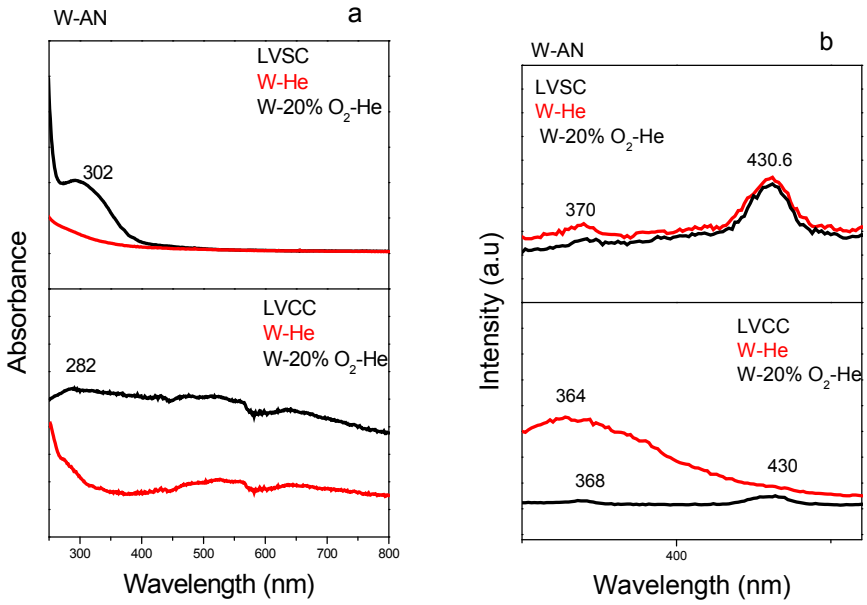

Figure 5.16. (a) UV-Vis absorption and (b) the photoluminescence spectra of tungsten and tungsten oxide nanoparticles prepared under He or O_2-He atmospheres by two methods of LVCC and LVSC using acetonitrile (AN).

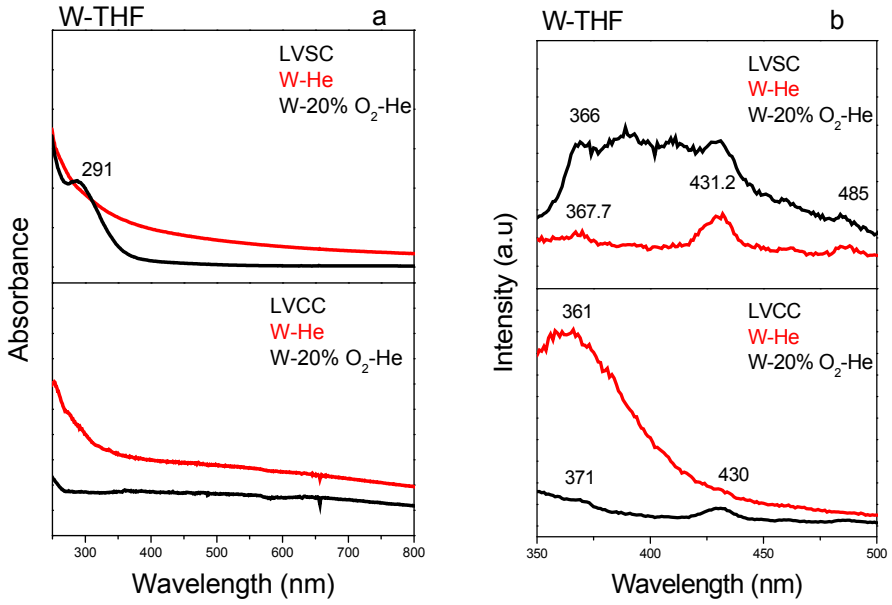

Figure 5.17. (a) UV-Vis absorption and (b) the photoluminescence spectra of tungsten and tungsten oxide nanoparticles prepared under He or O_2-He atmospheres by two methods of LVCC and LVSC using tetrahydrofuran (THF).

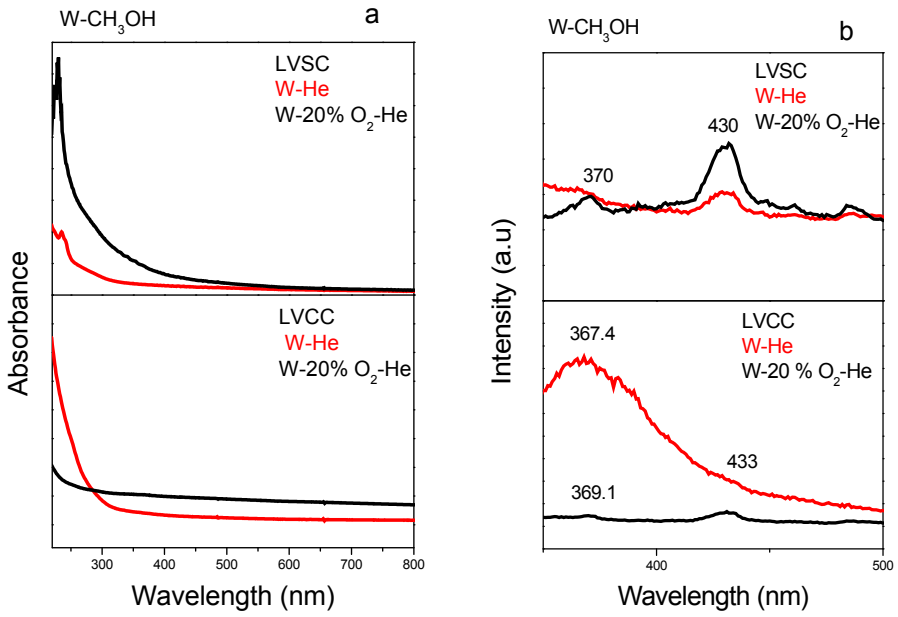

Figure 5.18. (a) UV-Vis absorption and (b) the photoluminescence spectra of tungsten and tungsten oxide nanoparticles prepared under He or O_2-He atmospheres by two methods of LVCC and LVSC using CH_3OH.

Figure 5.19 shows the XPS V2p spectra of vanadium oxide nanoparticles capped by tetrahydrofuran (THF) and acetonitrile (AN). In these spectra the doublets at binding energies (BE) of 517.3 eV and 524 eV for V_xO_y-THF sample and 516.3 eV and 523.8 eV for V_xO_y-AN sample (V^{+5} $2p_{3/2}$ and V^{+5} $2p_{1/2}$) are assigned to oxygen bonded vanadium. Teghil et al.[238] assigned the peaks at binding energies of 530.7 and 532.4 eV to oxygen bonded vanadium and contamination respectively. Generally speaking, the photoelectron peaks of O1s could be resolved into two components as shown in Figure 5.20. The results would be a peak around 530 eV and the other between 531 eV to 532 eV. Consistent with Teghil et al.[238], the dominant peak at about 529.9 eV is the characteristic of metallic oxides. The O1s peaks at around 531.4 eV to 532.2 eV correspond to the surface hydroxyl and adsorbed oxygen respectively, which come mainly from adsorbed water molecules. Peak at 516 to 517 eV could be assigned to V^{4+} , which is consistent with the result reported by Le et al.[283] It can be argued that the oxidation state of vanadium on the surface of vanadium nanoparticles is between +4 and +5. As a result, the sample of V_xO_y-AN could have both V_2O_5 and V_2O_4 while V_xO_y-THF sample has only V_2O_5.

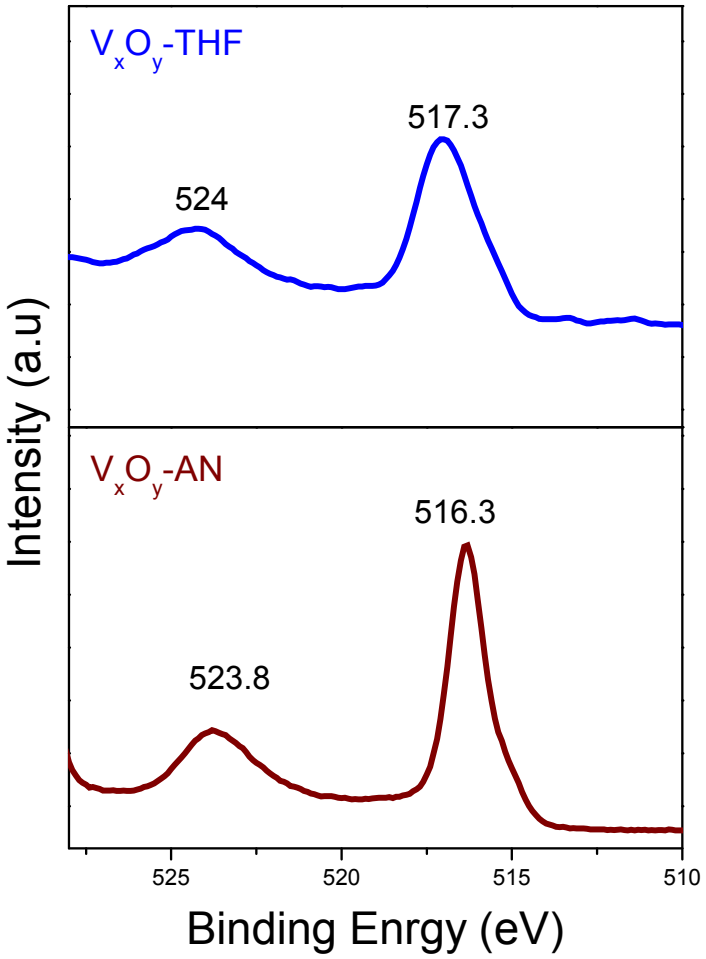

Figure 5.19. XPS V2p spectra of vanadium oxide capped with THF and AN samples prepared by LVSC under O_2/He atmosphere.

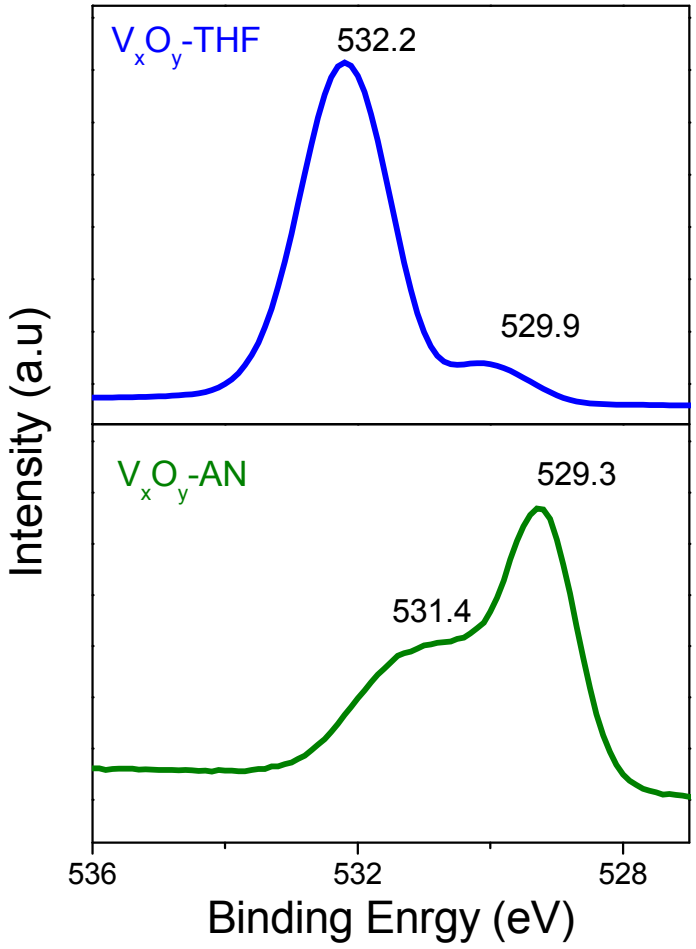

Figure 5.20 XPS O1s spectra of V_xO_y-THF and V_xO_y-AN samples prepared by LVSC under O_2/He atmosphere.

The XPS spectra of molybdenum and molybdenum oxide nanoparticles capped by AN is given in Figure 5.21. Peaks at around 232 and 236 are indicative of surface oxide dominant effects in both cases of molybdenum and molybdenum oxide nanoparticles.

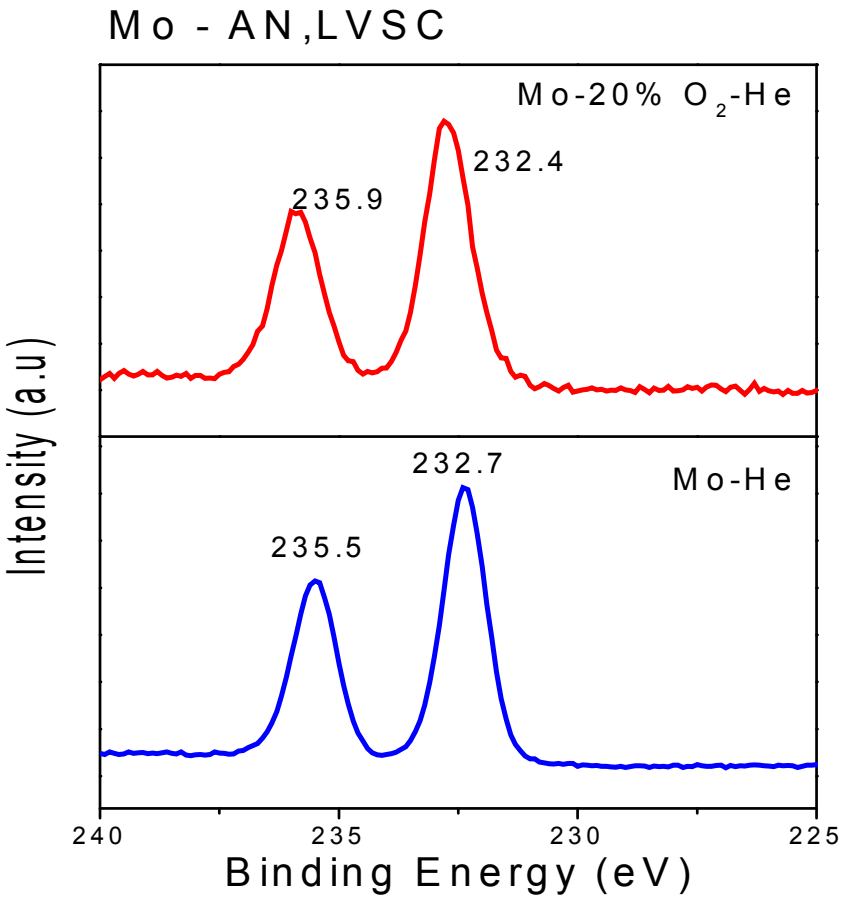

Figure 5.21. XPS spectra of molybdenum and molybdenum oxide capped by AN under He and O_2/He atmospheres using LVSC.

Figure 5.22 shows the XPS results for tungsten and tungsten oxide nanoparticles prepared by LVSC. The spectra in Figure 5.22 display the XPS results for tungsten $4f_{5/2}$, $4f_{7/2}$, and $5p_{3/2}$, and for tungsten oxide $4f_{5/2}$, $4f_{7/2}$, and $5p_{3/2}$ components. There are two main peaks at 35.25 and 37.39 eV , which correspond to $4f_{7/2}$ and $4f_{5/2}$ of WO_3 respectively.[284] The small peak at 41eV could be assigned to $5p_{3/2}$ component of WO_3. As these results suggest the surface of tungsten nanoparticles carries a large amount of WO_3. Figure 5.22 also present the XPS spectra of tungsten oxide nanoparticles. There are W 4f doublet peaks at 35.13, and 37.22 eV and a small

peak at 41.09 eV, which are due to W $4f_{7/2}$, $4f_{5/2}$, and $5p_{3/2}$ respectively. The peak at 35.13 eV is assigned to W^{6+} of the stoichiometric WO_3.

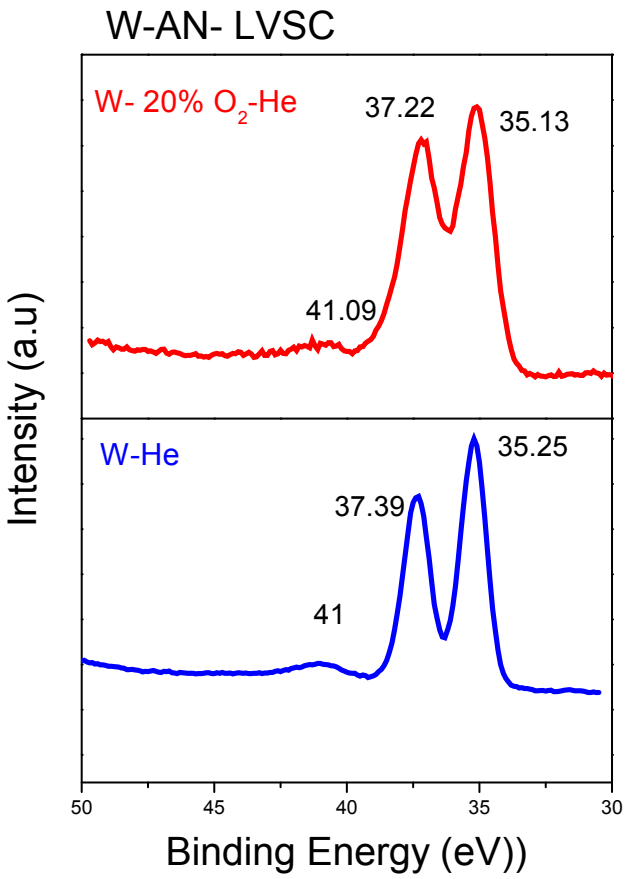

Figure 5.22. XPS spectra of tungsten and tungsten oxide nanoparticles capped by acetonitrile using LVSC.

Figure 5.23 displays some representative TEM images of vanadium oxide, molybdenum oxide, and tungsten oxide nanoparticles capped by acetonitrile. Tungsten oxide nanoparticles display several types of particle shape, a spherical shape with a size in the range of 1 to 5 nm and various forms of wire like structures with a width of 3 to 6 nm and a length of 10 to 15 nm. Molybdenum oxide and vanadium oxide nanoparticles show various wire and star shapes. Each nanostar is composed of a few nanowalls crossing each other.

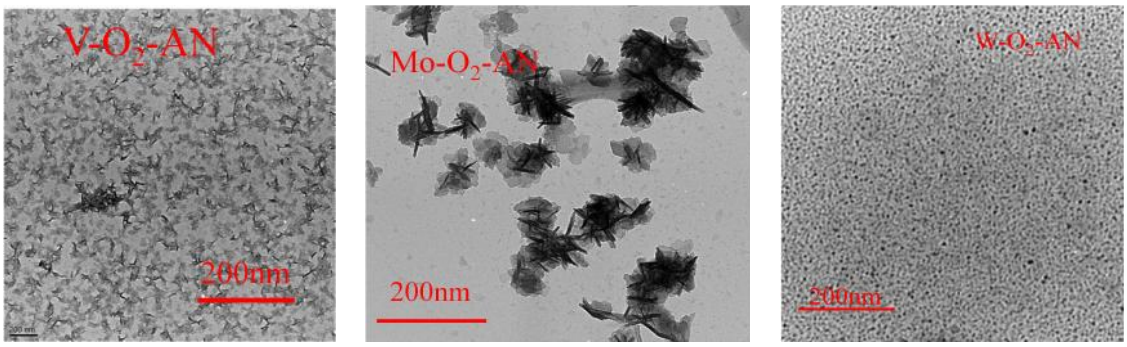

Figure 5.23. Representative TEM images of vanadium, molybdenum and tungsten oxide nanoparticles capped with acetonitrile using LVSC process.

Figure 5.24 (a and b) presents mass spectra of vanadium oxide and molybdenum oxide nanoparticles, both capped with AN using LVSC. These spectra were obtained using a laser desorption time of flight (LD-TOF) mass spectrometer. Figure 5.24a displays mass spectrum for V_xO_y nanoparticle containing sample with masses at 184, 207, 297, 357, 372, 410, 426, 437, and 545 amu. The mass at 207 amu is assigned to V_2O_4AN, which is one V_2O_4 attached to one AN ligand. Masses at 357, 372, 437, and 545 amu are assigned to V_4O_7AN, $V_3O_6AN_3$, $V_4O_{12}AN$, and $V_5O_{13}AN_2$ respectively. A positive assignment to other masses was not possible at this time and their identities require further investigations. Figure 5.24b shows mass spectrum for molybdenum oxide nanoparticles containing sample with peaks at 361, 377, 642, 714, and 785 amu, which are assigned to Mo_2O_8AN, Mo_2O_9AN, $Mo_4O_{11}AN_2$, $Mo_4O_{13}AN_3$ or $Mo_5O_7AN_3$, and $Mo_5O_{14}AN_2$ respectively. These results confirm that vanadium oxide and molybdenum oxide nanoparticles are attached to 1, 2 or 3 acetonitrile molecules.

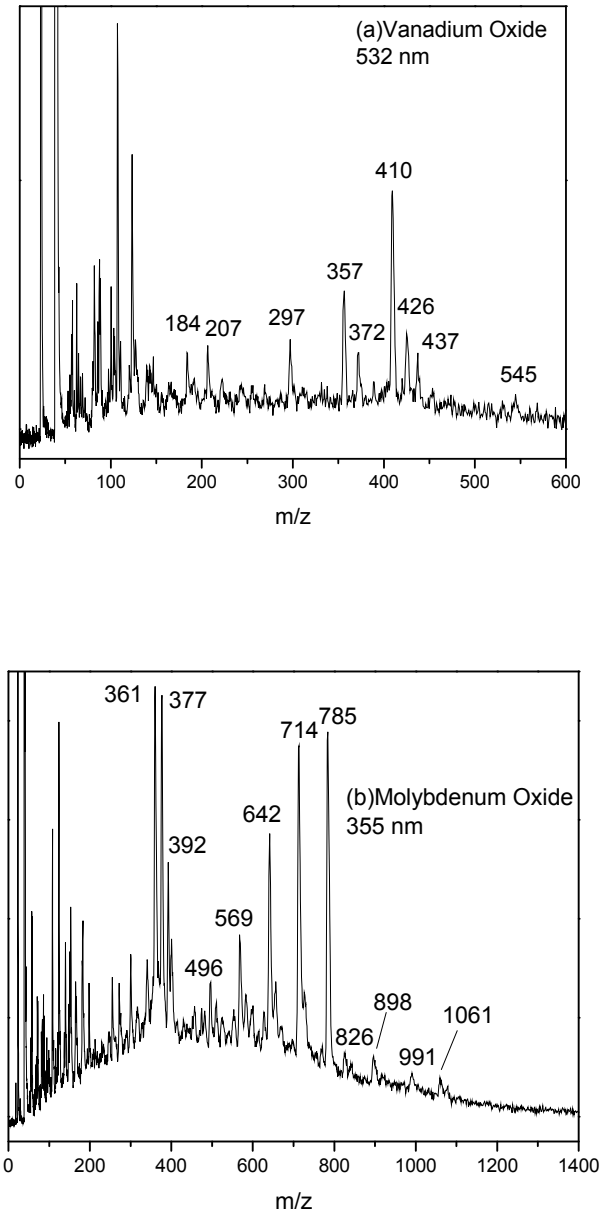

Figure 5.24. (a) Mass spectra of vanadum oxide nanoparticles and (b) molybdenium oxide nanoparticles both capped with AN using LVSC.

5.3 Nanocomposites of Graphene with Capped V_xO_y, Mo_xO_y, or W_xO_y Nanoparticles by Acetonitrile

Graphene-semiconductor nanocomposites are becoming a popular and fascinating topic for research due to their unique optical and electrical properties. Due to the graphene large conjugated π electron system, it has high intrinsic carrier mobility, which makes it an excellent conductor. Graphene structure also makes it one of the strongest materials. And lastly, its large surface area makes it ideal for the formation of nanocomposites with semiconductors nanoparticles.

Vanadium, tungsten and molybdenum oxides have also been considered as possible materials for nanoelectronics. These oxides have stable structures as well as high capacitance. Tungsten oxide also has strong photocatalytic activity making it a potential solar cell material. However, V, W, Mo oxides suffer from low charge mobility. In order for use in electronics, their conductivities must be increased.[285-286] One approach to improve their conductivities is addition of a carbon source, such as graphene. Graphene also increases the strength of the nanocomposites. Vanadium oxide nanowire-graphene for electrodes in supercapacitors was synthesized hydrothermally at 120 °C.[287] By using solvothermal approach, vanadium oxide spheres on graphene sheets was synthesized to be used as support in Li-ion batteries.[288] MoO_2/G nanocomposites can also be used as anode for Li-ion batteries.[289] Graphene–wrapped tungsten oxide nanoparticles have been also shown an improved gas sensing capability toward alcohols.[290] An et al.[291] reported a NO_2 gas sensing capability using tungsten oxide nanorods/graphene nanocomposites. Tungsten oxide (WO_3) nanoparticles were synthesized and supported on the surface of graphene for photo-dissociating of water under visible light.[286]

In this section, the nanocomposites of capped metal oxide nanoparticles by acetonitrile supported on graphene (V_xO_y/G, Mo_xO_y/G, and W_xO_y/G) is synthesized and characterized. The

approach to synthesize these composites was LVSC process complimented by chemical (hydrazine hydrate) treatment and microwave irradiation. After preparation, samples were characterized using techniques such as XRD, FT-IR, UV-Vis, PL, XPS, TEM, and Raman.

5.3.1 Results and Discussion

The PL spectrum of V_xO_y/G nanocomposite, as shown in Figure 5.25a, displays a strong emission peak around 520 nm whereas there is no emission at around this wavelength from V_xO_y nanoparticles. Furthermore, V_xO_y/G nanocomposite (NCs) gives a yellow-green emission that is not seen in V_xO_y NPs after exited with UV light at 254 nm (Figure 5.25b). As a result, it can be stated that the addition of the graphene nanosheets lowers the band gap of the V_xO_y/G nanocomposite (NCs) and increases its emission.

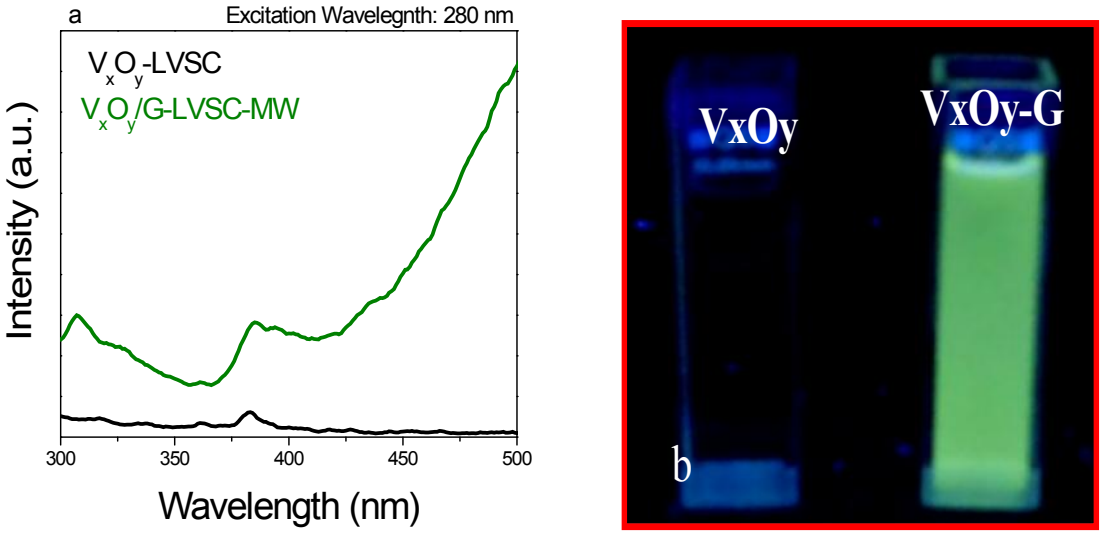

Figure 5.25. (a) Photoluminescence of vanadium oxide NPs and V_xO_y/G NCs capped with acetonitrile. (b) UV excitation of V_xO_y, and V_xO_y/G samples at a wavelength of 254 nm.

Figure 5.26a compares the XRD spectra of GO sheets and V_xO_y/G nanocomposite. It is evident from the spectra that GO has been greatly reduced to form graphene. The XRD spectra for V_xO_y NPs and V_xO_y/G nanocomposite are shown in Figure 5.26b. Both samples contain

primarily cubic V_xO_y crystals according to reference JCPDS 03-065-4054. Peaks at 38°, 44°, and 64° represent the scattering angles of 111, 200, and 220 respectively. Figure 5.26c displays the XPS C1s data for V_xO_y/G nanocomposite, which clearly indicate the reduction of C-O and C=O groups in V_xO_y/G. Figure 5.26d shows the XPS V 2p spectra of Vanadium oxide nanoparticles capped by acetonitrile (AN). In this spectrum the doublets at binding energies (BE) of 517.3 eV and 524.6 eV for V_xO_y-AN sample (V^{+5} $2p_{3/2}$ and V^{+5} $2p_{1/2}$) are assigned to oxygen bonded vanadium.

The UV absorbance of V_xO_y nanoparticles and V_xO_y/G nanocomposite is shown in Figure 5.27a. V_xO_y NPs display an absorbance peak at 339 nm , which is assigned to O-V charge transfer[292]. In the V_xO_y/G spectrum the absorbance is blue shifted to 292 nm. Figure 5.27b compares the FTIR spectra of V_xO_y and V_xO_y/G samples. FTIR spectra of both samples display peaks for V-O bond at 768 cm^{-1} and 952 cm^{-1}. The V_xO_y NPs shows a peak at 992 cm^{-1} that corresponds to V=O bond.[293] The corresponding peak for V=O bond in V_xO_y/G nanocomposite is seen at 1072 cm^{-1}. The peaks at 1402 cm^{-1} and 1357 cm^{-1} are likely due to metal-solvent interaction, possibly with the nitrogen of the acetonitrile group. It is also evident that various oxygen functionalities, reminiscence of GO functional groups, have greatly been reduced in the V_xO_y/G when compared to GO.

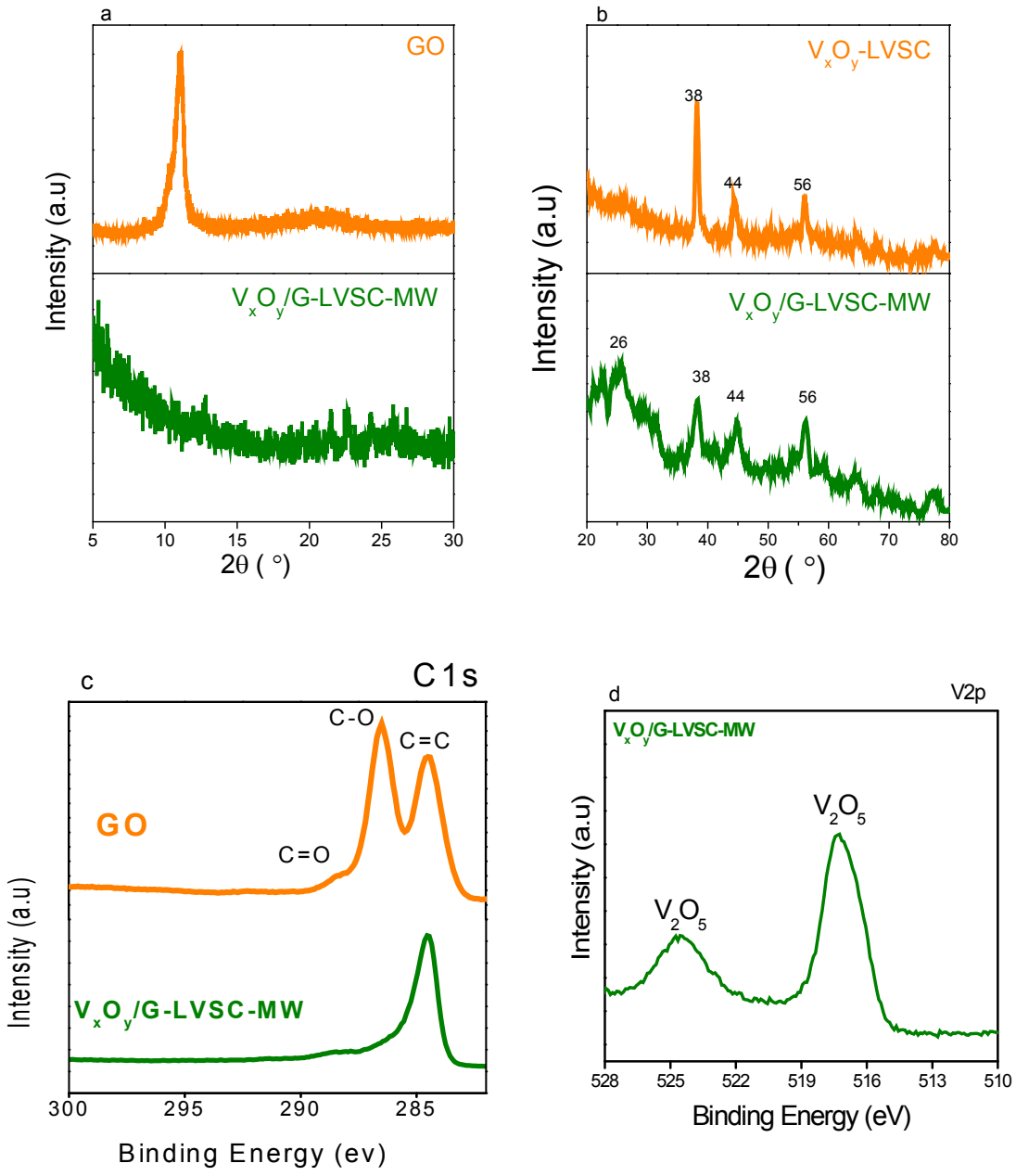

Figure 5.26. (a-b) X-ray diffraction spectra of GO, V_xO_y NPs and V_xO_y/G NCs, and (c-d) XPS spectra of V_xO_y NPs and V_xO_y/G NCs.

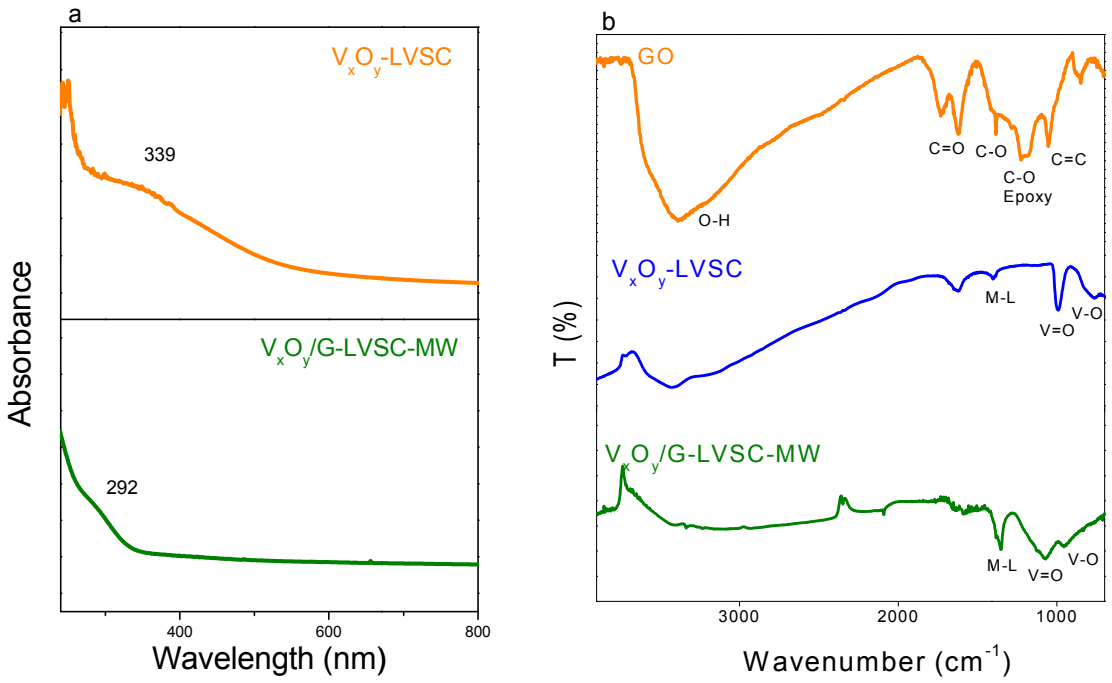

Figure 5.27. (a) UV-Vis and (b) FTIR spectra of V_xO_y NPs and V_xO_y/G nanocomposite.

A typical TEM image of V_xO_y/G sample is shown in Figure 5.28. The photomicrograph indicates the existence of vanadium oxide nanoparticles along with nanowires on the graphene nanosheets surfaces. The vast majority of the vanadium oxides NPs are under 2 nm in diameter.

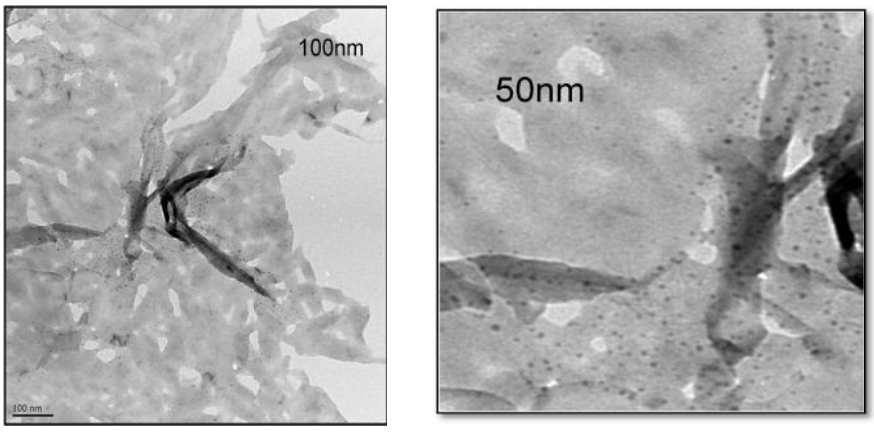

Figure 5.28. A typical TEM image of V_xO_y/G nanocomposite prepared by LVSC/MW.

Figure 5.29 displays the Raman spectra of V_xO_y NPs and V_xO_y/G nanocomposite. V-O-V stretch is seen at 517 cm^{-1} in the V_xO_y spectrum, which is shifted down to 510 cm^{-1} in the V_xO_y/G. Triple V coordinated oxygen is seen at 789 cm^{-1} in V_xO_y spectrum. This peak is not clearly seen in V_xO_y/G spectrum. Terminal V=O stretch is seen at 982 cm^{-1} and 929 cm^{-1} for the V_xO_y and V_xO_y/G samples respectively.[285] In the V_xO_y/G samples, D and G bands of the graphene are easily seen at 1384 cm^{-1} and 1591 cm^{-1} respectively. The I_D/I_G ratio for V_xO_y/G is 0.83. Electrical resistance of a V_xO_y/G pellet (2 mm thickness) was measured using a Fluke 73III multimeter, it was found to be about 1.2 kΩ. This number is significantly lower compared to a V_xO_y pellet of similar size with a resistance of greater than 2 MΩ.

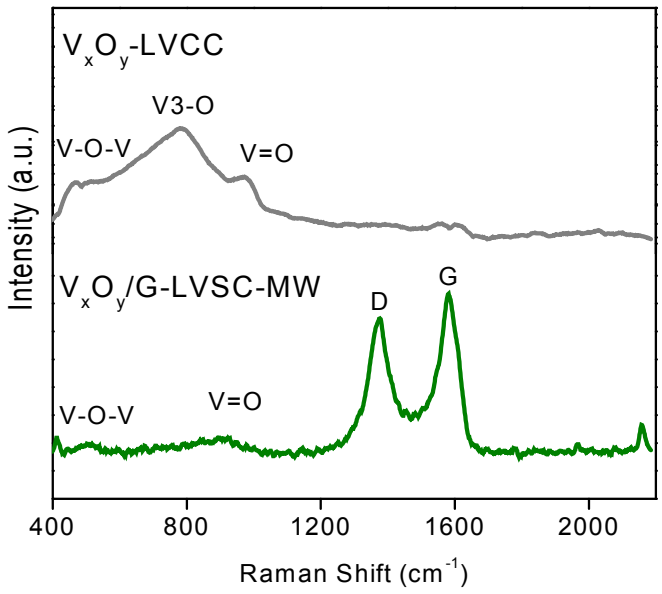

Figure 5.29. Raman spectra of V_xO_y and V_xO_y/G samples at an excitation wavelength of 406.7 nm.

The XRD patterns of W_xO_y/G and Mo_xO_y/G nanocomposites are given in Figure 5.30. As expected, due to their proximity in the periodic table, Tungsten and molybdenum oxides nanoparticles composited similarly with graphene to produce comparable nanocomposites. The XRD spectra of W_xO_y/G and Mo_xO_y/G systems along with GO for 2θ ranging from 5 to 30 are shown in Figure 5.30a. From the spectra it is evident that the majority of GO oxygen functional groups were reduced and graphene was formed as a result of hydrazine hydrates (HH) and microwave irradiation (MW) treatment of the mixture prepared by LVSC. Figure 5.30b presents XRD patterns of acetonitrile capped tungsten oxide and molybdenum oxide nanoparticles along with their composites with graphene nanosheets. The closely spaced peaks in spectra presented in Figure 5.30b are characteristic of transition metal oxides.

For tungsten oxide nanoparticles capped with AN, the spectrum shows peaks at 2θ = 25.7° (110), 33.7° (200),40 °(211), and 43.5° (113) that are in good agreement with reference JCPDS 01-087-2393 standard card for tungsten oxide (WO_3) nanoparticles with monoclinic crystal. Peaks at 40°, 44°, and 70° represent the scattering angles of 210, 211, and 321 respectively in tungsten according to JCPDS 03-065-6453 standard card. The peak at 12.7° is consistent with highly ordered tungsten oxide. Peaks at 36° (100), and 75° (200) could be assigned to W-N with a hexagonal structure according to JCPDS 01-089-4754. From the data in Figure 5.30b, the structure of W_xO_y can be deduced. Both W_xO_y and W_xO_y/G samples are comprised of a combination of cubic tungsten and tungsten oxides. In Mo_xO_y and Mo_xO_y/G, the NPs are a combination of cubic Mo and monoclinic MoO_3. Peaks at 40° and 73° represent the scattering angles of 110 and 211 of cubic Mo according to JCPDS 03-065-7442. Peaks at 12°, 26°, and 39° represent the scattering angles of 001, 002, and 102 for MoO_3.

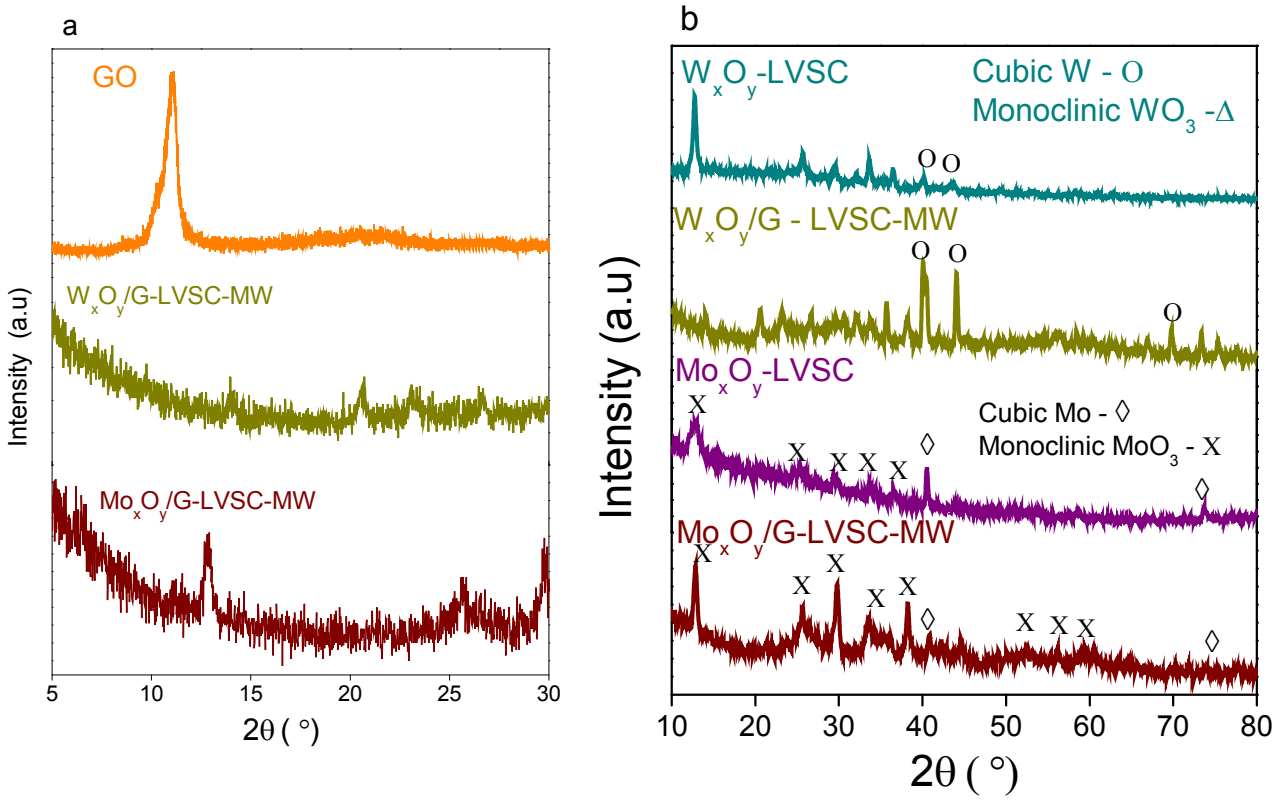

Figure 5.30.X-ray diffraction spectra of W_xO_y and Mo_xO_y nanoparticles, and W_xO_y/G and Mo_xO_y/G nanocomposites prepared by LVSC and MW processing.

The XPS C1s spectra of W_xO_y/G, Mo_xO_y/G, and GO are shown in Figure 5.31a. Consistent with previous results, the XPS data shows that GO in W_xO_y/G and Mo_xO_y/G were significantly reduced by hydrazine hydrate and microwave treatment. The XPS 4f of W_xO_y/G, as given in Figure 5.31b, shows two peaks for W $4f_{7/2}$ and W $4f_{5/2}$ at 35.3 and 37.5 eV with shift to lower binding energies compared to WO_3. This indicates a higher electron density for tungsten atoms in tungsten oxide/G nanocomposites.[290] The spectrum clearly shows that the surface of W_xO_y NPs contains primarily WO_3. The XPS 3d of Mo_xO_y/G is shown in Figure 5.31c. The Mo 3d spectrum of MoO_3 shows the characteristic of doublet ($3d_{5/2}$ at 232.6 eV and $3d_{3/2}$ at 235.7 eV) caused by spin-orbit coupling, which is in agreement with He et al.[216] results.

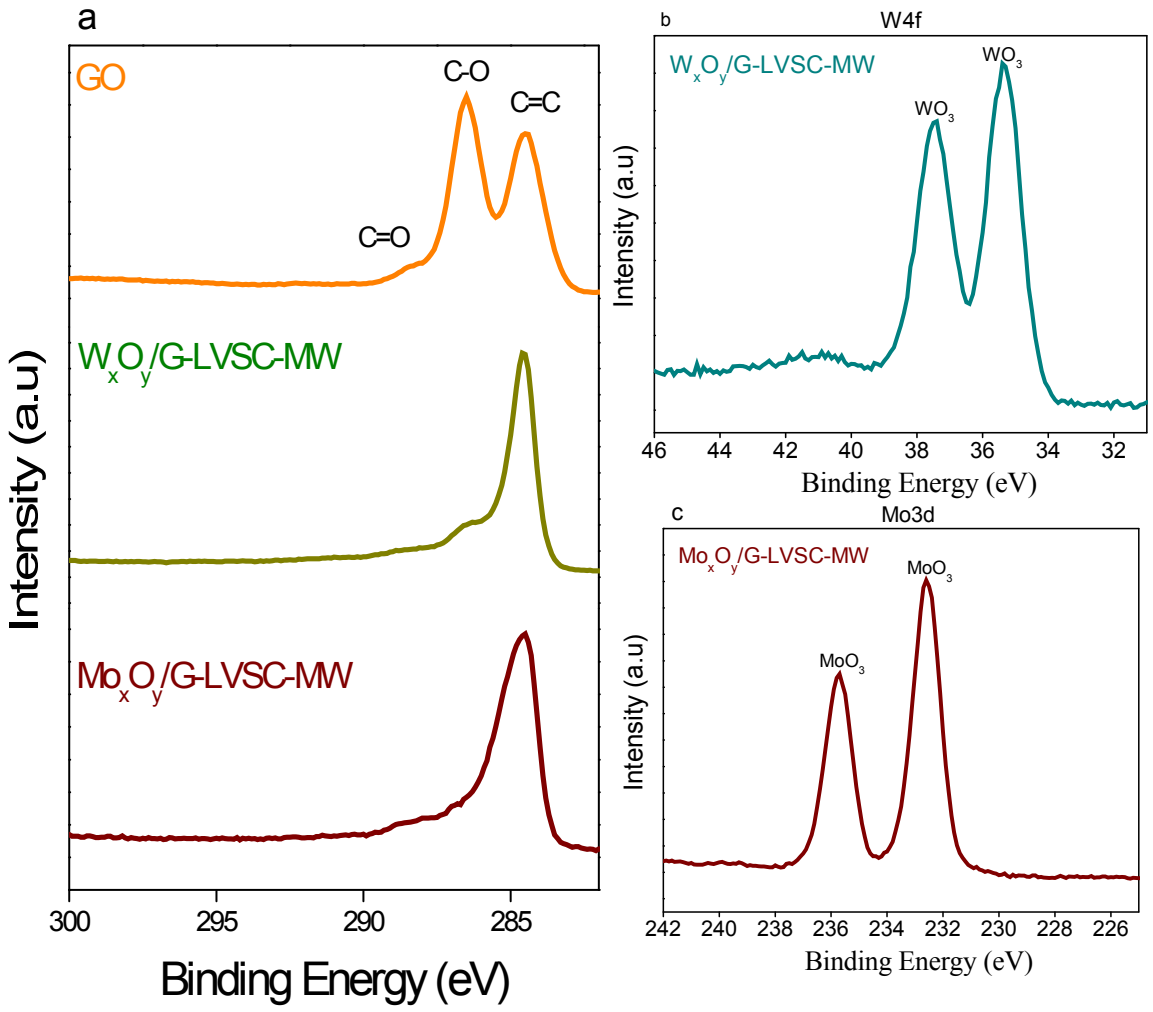

Figure 5.31. (a) C1s XPS spectra for GO, W_xO_y/G and Mo_xO_y/G, (b) W4f XPS spectra for W_xO_y/G and (c) Mo3d XPS spectra for Mo_xO_y/G.

Figure 5.32 shows UV-Vis and FTIR spectra of W_xO_y NPs and W_xO_y/G nanocomposite samples. The UV-Vis spectra (Figure 5.32a) show an absorbance at 308 nm and 311 nm for W_xO_y, and W_xO_y/G samples respectively. It is understood that this absorbance corresponds to W to O charge transfer. In the FTIR spectra (Figure 5.32b) W-O-W stretch is seen at 877 cm^{-1} and 824 cm^{-1} for W_xO_y and W_xO_y/G samples respectively. Peaks at 1037 cm^{-1} in W_xO_y spectra and at 1147 cm^{-1} and 1190 cm^{-1} in W_xO_y/G spectra are assigned to W=O terminal stretching. Both

spectra have a strong asymmetric absorbance at around 1390 cm^{-1}, which is assigned to acetonitrile-metal oxide interaction.

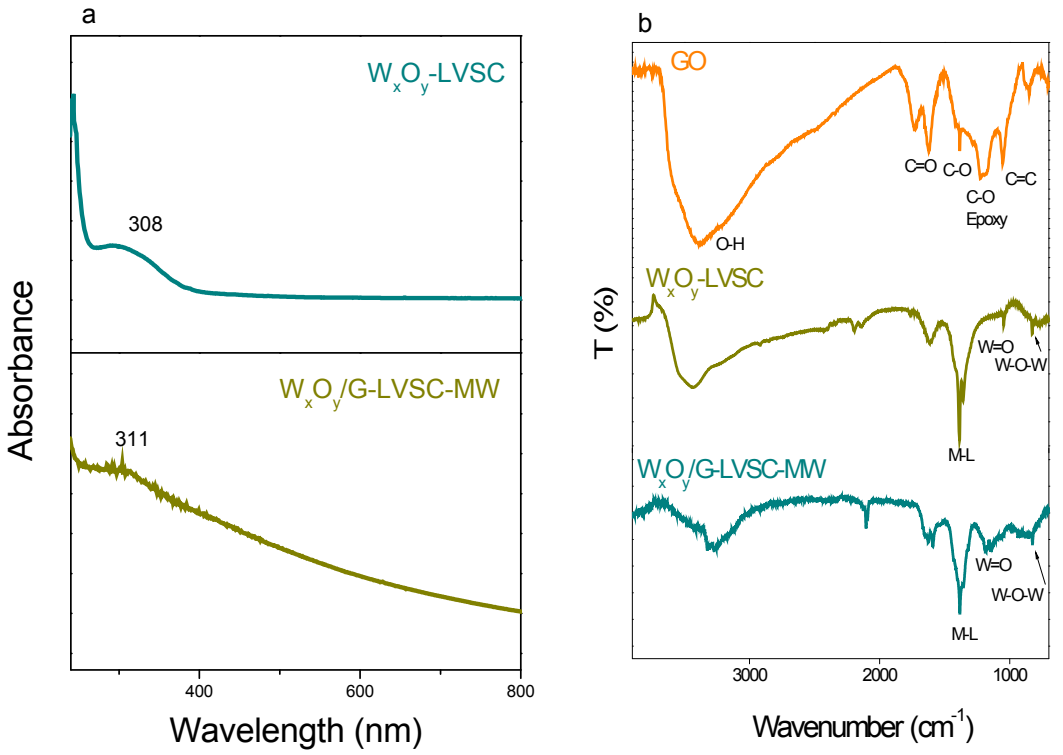

Figure 5.32. (a) UV-Vis and (b) FTIR spectra of tungsten oxide nanoparticles and nanocomposite with graphene and capped with AN.

UV-Vis and FTIR spectra of the samples containing Mo_xO_y are shown in Figure 5.33. As shown in Figure 5.33a, UV-Vis spectra of Mo_xO_y sample absorbs UV radiation at 327 nm, which is blue shifted to 294 nm for the Mo_xO_y/G sample. This absorbance is assigned to Mo to O charge transfer band. FTIR spectra of Mo_xO_y NPs and Mo_xO_y/G nanocomposite are given in Figure 5.33b. FTIR spectra shows Mo-O-Mo stretch at 837 cm^{-1} for Mo_xO_y and 830 cm^{-1} for Mo_xO_y/G. Mo=O stretch is seen at 1375 cm^{-1} and 1047 cm^{-1} for Mo_xO_y and Mo_xO_y/G respectively.[294] A strong asymmetric absorbance peak is seen at 1375 cm^{-1} for Mo_xO_y and at

1382 cm^{-1} for Mo_xO_y/G. This peak is assigned to metal oxide–acetonitrile interaction. This is expected to be similar to the metal oxide interaction seen in the vanadium and tungsten oxide samples. Nevertheless, this peak does not appear in spectra of vanadium, tungsten and molybdenum and their oxides that were produced by LVCC and in the absence of any solvents to form ligands.

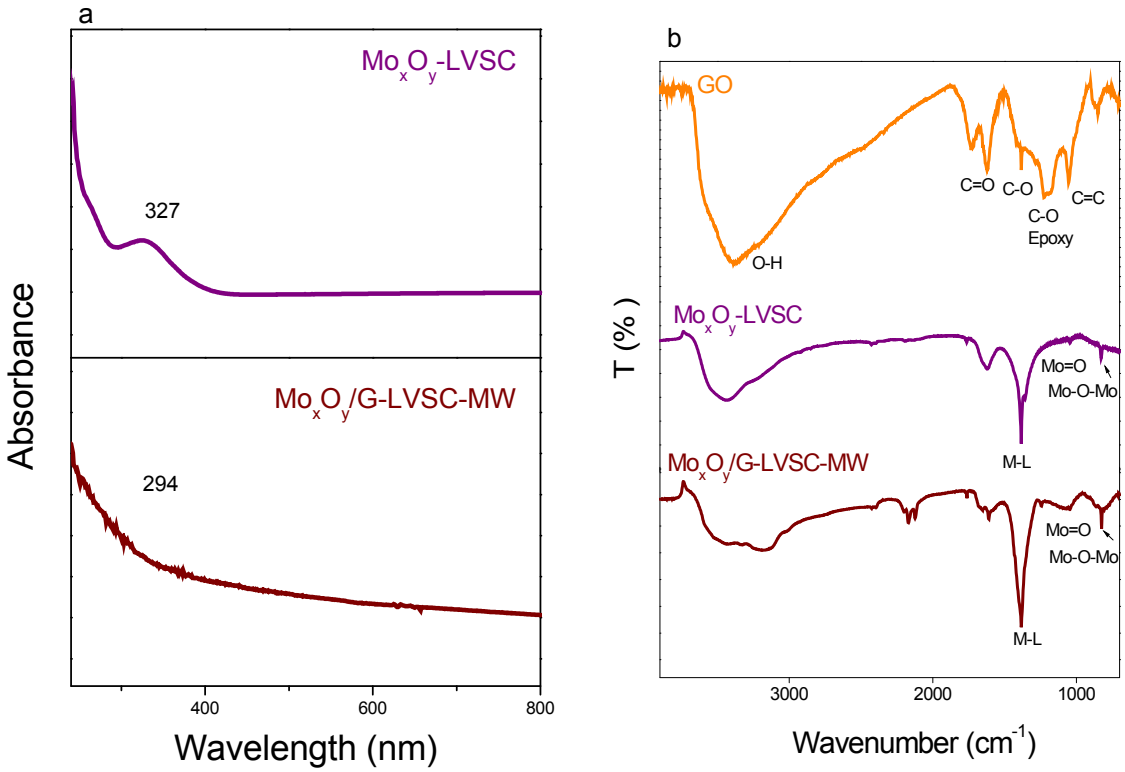

Figure 5.33. (a) UV-Vis and (b) FTIR spectra of molybdenum oxide nanoparticles and nanocomposite with graphene and capped with AN.

Figure 5.34 shows representative TEM images of W_xO_y/G and Mo_xO_y/G nanocomposites prepared by the combination of LVSC, HH and MW processing. In W_xO_y/G sample, cubically shaped nanoparticles and nano-flower shapes are seen, which were dispersed evenly on graphene nanosheets. The cubic shaped nanoparticles are less than 10 nm wide. The Mo_xO_y/G sample

show some ultra small spherical nanoparticles dispersed on the graphene surface. The majority of these NPs are less than 2 nm in diameter.

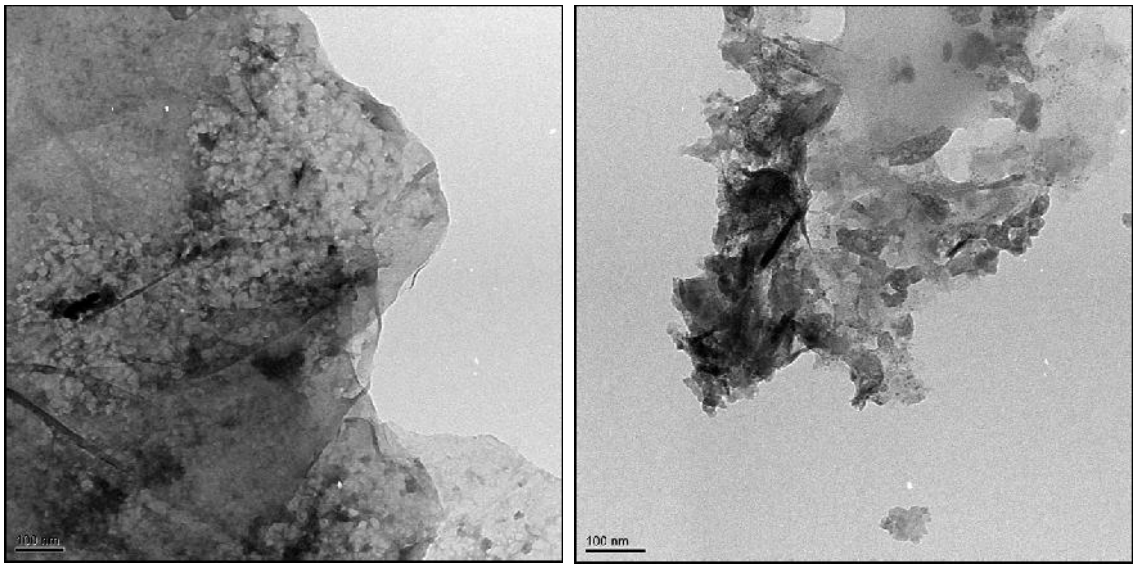

Figure 5.34. Representative TEM images of W_xO_y/G and Mo_xO_y/G nanocomposites prepared by LVSC/MW processing.

Figure 5.35a shows emission of W_xO_y and W_xO_y/G and Figure 5.35b exhibits the emission of Mo_xO_y and Mo_xO_y/G samples. The oxide nanoparticle samples without graphene show a peak at around 430 nm whereas nanocomposites of W_xO_y/G and Mo_xO_y/G have an emission at around 500 nm and higher wavelengths. As can be seen in Figure 5.36, the emission is easily observed when the samples are irradiated by UV lamp at an excitation wavelength of 254 nm. Both W_xO_y/G and Mo_xO_y/G samples give off a bright yellowish emission. This emission is expected to be coming as a result of electron transfer from graphene to metal oxides. No emission is visible from W_xO_y and Mo_xO_y nanoparticle.

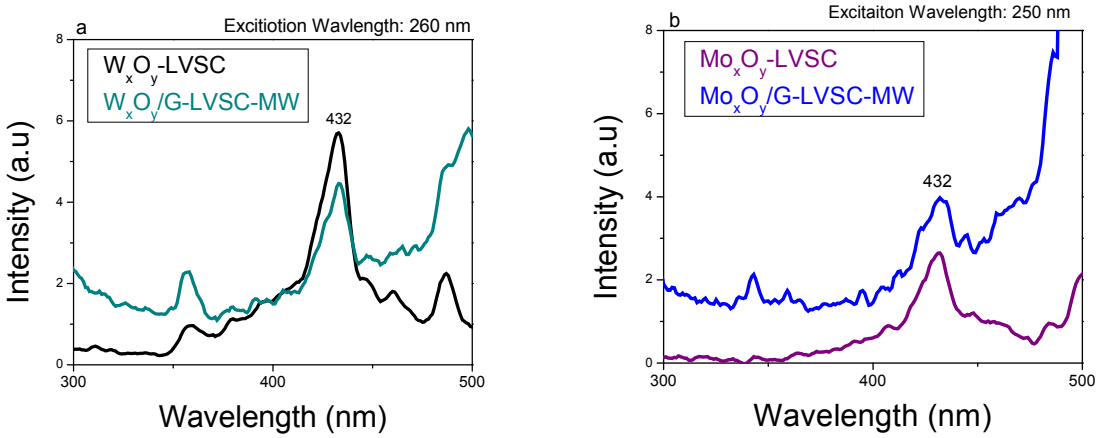

Figure 5.35. Photoluminescence of (a) W_xO_y and W_xO_y/G at 260 nm, (b) Mo_xO_y and Mo_xO_y/G at 250 nm excitation wavelength.

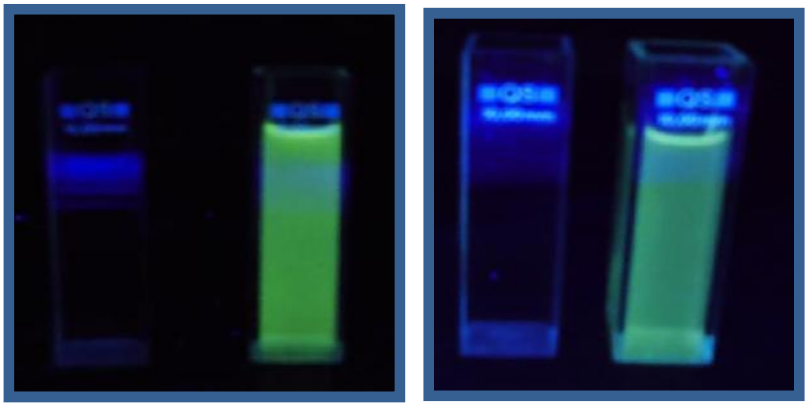

Figure5.36. UV Excitation of (a) W_xO_y and W_xO_y/G (b) Mo_xO_y and Mo_xO_y/G samples at a wavelength of 254 nm.

The Raman spectra of W_xO_y and W_xO_y/G samples, as demonstrated in Figure 5.37 (a and b), confirm the presence of tungsten oxide. The peaks observed at 802 cm^{-1} and 704 cm^{-1}on the spectra for W_xO_y and W_xO_y/G are assigned to W-O-W stretch. Whereas peaks at 964 cm^{-1} on W_xO_y spectrum and 1042 cm^{-1} on W_xO_y/G spectrum are due to W=O terminal bonds, which shift

to higher frequency as a results of graphene effects. The D and G bands of the graphene are seen in W_xO_y/G spectra at 1378 cm^{-1} and 1596 cm^{-1} respectively. W_xO_y/G has an I_D/I_G ratio of 0.69. Figure 5.37 displays the Raman spectra of Mo_xO_y nanoparticles and Mo_xO_y/G nanocomposite samples. Mo_xO_y has Mo_2-O and Mo_3-O stretches that appear at 704 cm^{-1} and 809 cm^{-1}. The terminal Mo=O stretch appears in Mo_xO_y and Mo_xO_y/G at 957 cm^{-1} and 901 cm^{-1} respectively, which has shifted to lower frequency as a results of graphene. The D and G bands of graphene oxide in Mo_xO_y/G spectra are at 1378cm^{-1} and 1596 cm^{-1} respectively. Mo_xO_y/G shows an I_D/I_G ratio of 0.84. Electrical resistances of WxOy/G and MoxOy/G nanocomposites (2 mm thickness) were measured using a Fluke 73III multimeter, and they were found to be 40 kΩ and 1.6 kΩ respectively. Both resistances are considerably lower than the resistances of their respected metal oxides, which are greater than 2 MΩ. The electrical conductivity of W_xO_y/G was expected to be higher than what was measured. It was thought that an unexpectedly higher humidity level in the pellet has caused the higher resistance measurement.

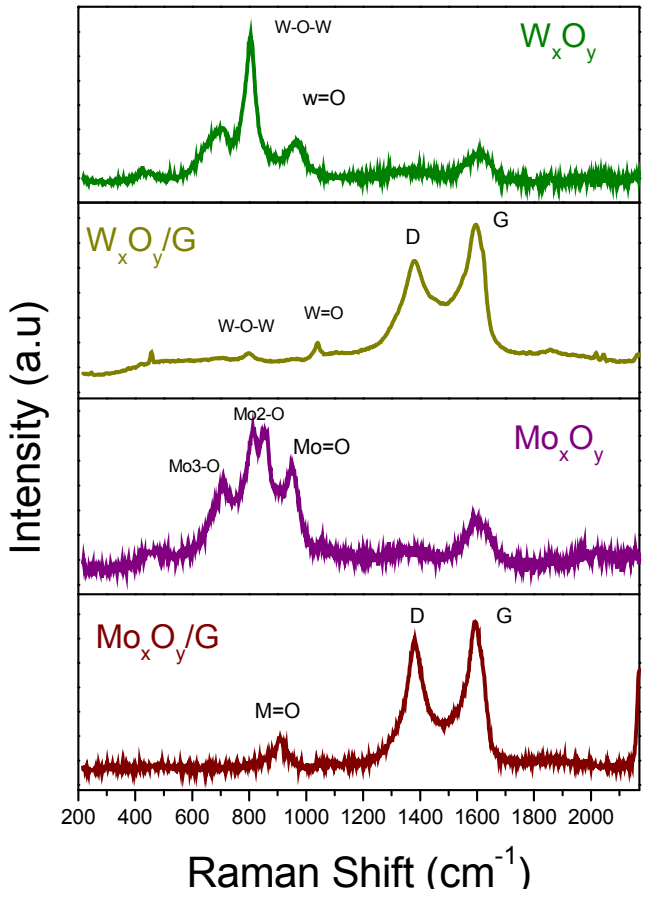

Figure 5.37. Raman spectra of W_xO_y, W_xO_y/G, Mo_xO_y, and Mo_xO_y/G at an excitation wavelength of 406.7 nm.

Chapter 6: Synthesis and Characterization of Silicon Nanoparticles and its Nanocomposites with Graphene in Different Media

Silicon nanoparticles (Si NPs) in general and silicon quantum dots (SiQDs) in particular have attracted enormous attention over the last few years for their potentials use in various applications such as optoelectronic, nonlinear optics, solar energy, and bioimaging.[295] This is mainly due to their exceptional optical properties such as size-dependent tunable light emission,[296] high brightness,[297] and their great stability against photo-bleaching compared to organic dye molecules.[298] Silicon nanoparticles have a lower toxicity, lower cost and higher abundance comparing to for instance heavy metals. Once appropriate capping group chelates Si nanoparticles, a complex between Si as core and ligands are formed, which causes a charge transfer between them. This charge transfer property makes Si quantum dots even a better candidate for numerous applications particularly in cellular and assay labeling or in deep-tissue imaging.

There are a variety of techniques to synthesize Si NPs capped with different organic molecules. Alkyl halide and ester terminated Si nanoparticles were prepared from the reduction of silicon tetrachloride with sodium naphthalide.[299] Pyrolysis of silane by CO_2 laser[300] followed by hydrofluoric acid (HFA) etching were used to produce Si nanoparticles functionalized with carboxyl group.[301] The aminopropenyl-terminated Si quantum dots were synthesized by

microwave-assisted reaction.[302] Pulsed laser ablation in liquid (PLAL) was reported for conjugation of pure Si nanoparticles with oligonucleotide and biomolecules.[303] Allylamine-capped[298] and propionic-acid-capped[304] Si nanoparticles were synthesized as biological sensors. Amine-terminated Si nanoparticles with different alkyl chain lengths between core Si and amine end-groups were synthesized for bioimaging.[305] DNA-biomolecule[306] terminated Si nanoparticles were synthesized as an alternative approach to size controlled generation semiconductors. And, finally colloidal chemistry is an approach to successfully control the size and protect the surface of Si nanoparticles from oxygen.[305]

The objectives of this chapter are the synthesis of silicon nanoparticles using LVCC, silicon nanoparticles capped by organic solvent using LVSC, and silicon nanoparticles capped with acetonitrile and supported on graphene using LVSC and MW treatment. The synthesized materials are then characterized chemically and physically using numerous analytical techniques.

6.1 Silicon Nanoparticles Using LVCC

The effects of gaseous atmospheres and the total chamber pressure on the properties of synthesized silicon nanoparticles were studied in this section using LVCC techniques. The effects of different gases on the formed nanoparticles were studied by filling the LVCC chamber with gases like Ar, He, H_2/He or O_2/He. The effect of total pressure was also studied using a total chamber pressure of 100, 500, and 1000 Torr. To analyze the synthesized silicon nanoparticles by UV-Vis and PL spectroscopy, a small amount of produced nanoparticles with a yellowish color was added to a test tube containing methanol and then irradiated with unfocused laser. A small quantity (1 ml) of this suspension was used in the analysis. The influence of laser irradiation time on the results was verified using an irradiation time of 5, 10, and 30 minutes by

unfocused laser (Nd:YAG). Other spectroscopic characterization of the produced silicon nanoparticles were carried out on the as-produced solid products.

6.1.1 Results and Discussion

Figure 6.1 displays the X-ray diffraction patterns of Si nanoparticles prepared in different gaseous atmospheres of Ar, He, and 10% H_2-He. All samples show peaks at 2θ = 28.5° (111), 47.4° (220), and 56.3° (311), which based on reference code JCPDS 01-078-2500 belongs to silicon nanoparticles with cubic structure. The crystalline lines presented here are not present in the X-ray diffraction pattern of silica (SiO_2) NPs prepared in the presence of O_2 where a completely amorphous material was obtained.

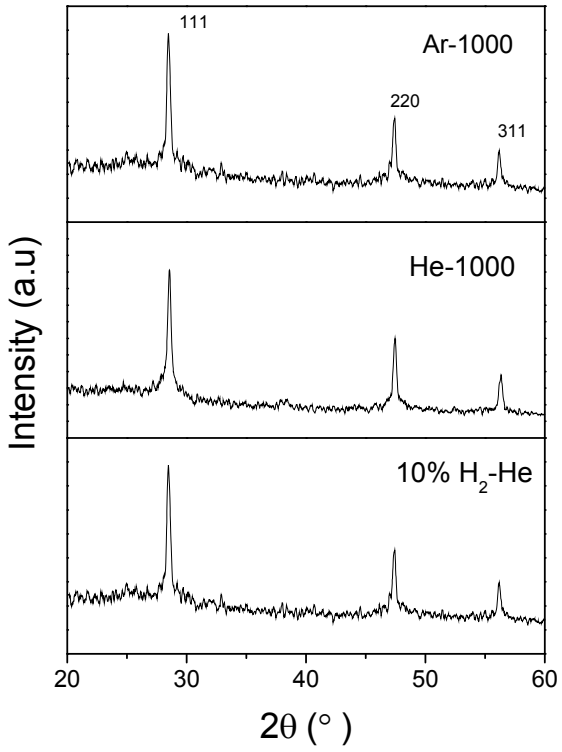

Figure 6.1. X-ray diffraction spectra of silicon nanoparticles prepared in different gases using LVCC process.

Figure 6.2 shows UV absorption of Si NPs prepared in different gases using LVCC. Figure 6.2a and 6.2b displays the effects of total chamber pressure and type of gas on Si NPs. Figure 6.2 (c, d) shows the effects of laser irradiation time (0, 5, 10, and 30min) for the nanoparticles produced under helium at 1000 Torr and argon at 500 Torr. All Si NPs show an absorption band at around 270 nm, which is attributed to direct band gap transition and a long tail absorption around 300 nm, which continues to 400 nm and is assigned for indirect band gap transition.

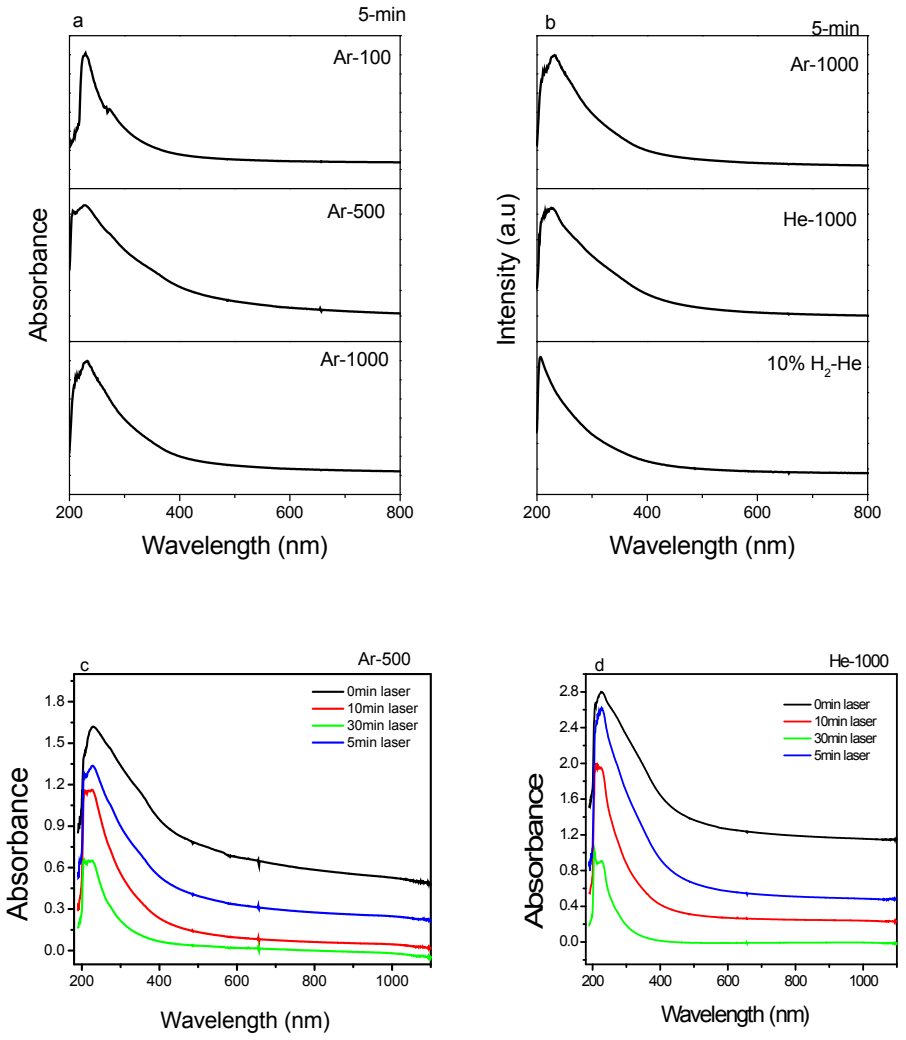

Figure 6.2 UV-Vis spectra of Si NPs prepared under different conditions including total pressure and gas type using LVCC and laser irradiation time for sample analysis.

The PL spectra of Si nanoparticles prepared under different total pressure and gas type are given in Figure 6.3. The effect of sample irradiation time for analysis on the PL spectra is also displayed shown in Figure 6.3. The effects of chamber total pressure using argon, at a fixed sample irradiation time of 5 minute, is shown in Figure 6.3a. The peak at 327 nm disappears and the intensity of the peak at 428 increases as the total pressure increases from 100 to 1000 Torr using argon. The effects of gas type are shown in Figure 6.3b by comparing the results of Ar, He

and 10%H_2/He at a total pressure of 1000 Torr and a sample irradiation time of 5 minutes. The PL spectra of the samples prepared in He and H_2/He have similar peaks at 315, 362, and 429 nm while the sample prepared in Ar does not show any peak at the lower wavelength of 315 nm. These results indicate the formation of smaller size nanoparticles at lower argon pressure and in both He and H_2/He atmospheres and somewhat larger particles at higher pressure in argon. This finding is consistent with the fundamentals of gas phase formation of nanoparticles in systems like LVCC where a heavier gas (argon as compared to helium) and a higher pressure would lead to larger size nanoparticles. In fact, a higher thermal diffusivity and a stronger convective flow of He as compared to Ar facilitate the removal of formed nucleus form the nucleation zone and their cooling thus reducing the particle growth and agglomeration. Figure 6.3 (c and d) also shows the effects of sample irradiation time for nanoparticle synthesized in argon at a total pressure of 500 Torr (6.3c) and in helium at a total pressure of 1000 Torr (Figure 6.3d). The results clearly indicate that as the irradiation time increases the intensity of peak at 429 nm (e.g., larger particle size) decreases, and correspondingly, the intensity of the peaks at bands around 315 and 360 nm increases. This finding is consistent with the expected result for the effect of irradiation time, which as it increases the large agglomerates break down leading to the formation of smaller size nanoparticles.

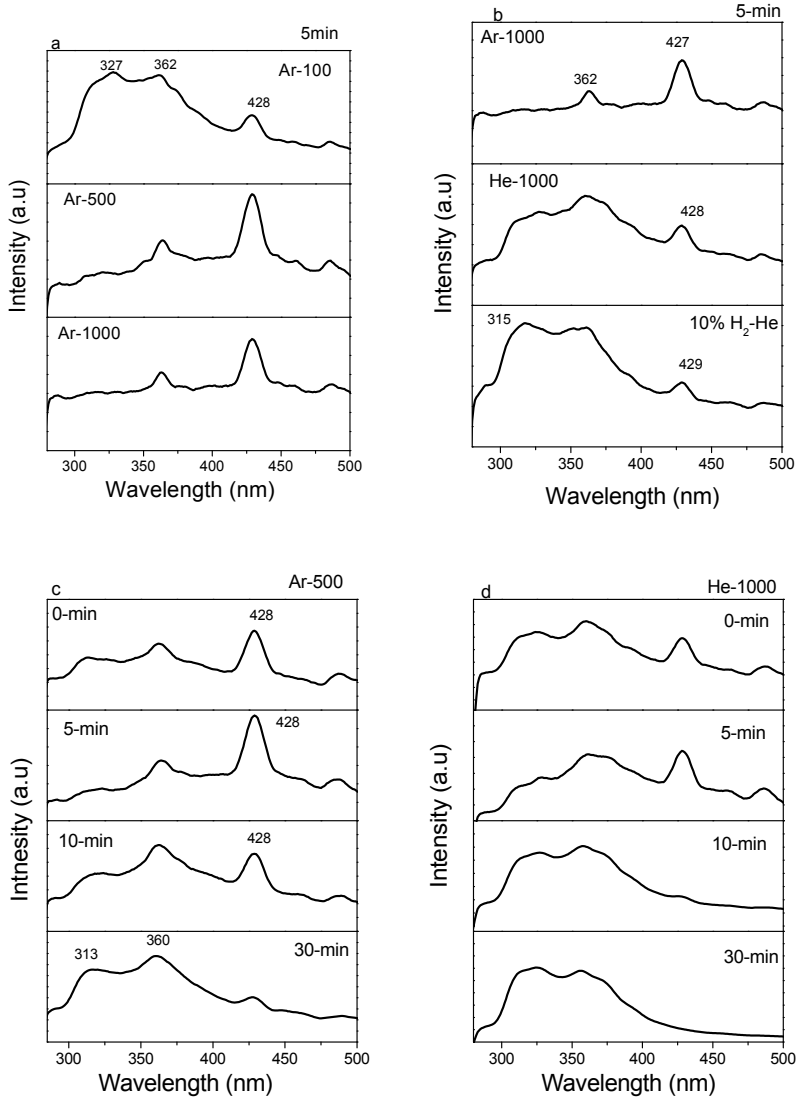

Figure 6.3. PL spectra of Si NPs prepared under different conditions of total pressure and gas type using LVCC and sample irradiation time.

Figure 6.4 represents typical TEM images of Si NPs prepared under different gaseous atmosphere. The average size of Si nanoparticles produced in Ar atmosphere, as shown in Figure 6.4 (a through c), were estimated to be 10, 12.4, and 17 nm for 100, 500, and 1000 Torr total pressure, respectively. The average sizes of Si NPS produced in He gas as shown in Figure 6.4 (d and e) were estimated to be 9.8 nm for 100 Torr and 5.6 nm for 1000 Torr total chamber

pressure. The average size of Si nanoparticles produced under H_2/He at 1000 Torr pressure were estimated to be around 1-8 nm (Figure 6.4f). The average sizes of the formed silicon nanoparticles are smaller in He and 10% H_2-He than in the Ar gas. Similar to the results from UV-Vis and PL spectroscopy, these results also indicate an increase in average particle size with increasing the density of the carrier gas and total chamber pressure. This occurs because the heavier gas are more effective at confining the metal vapors leading to particle growth and eventually to larger size nanoparticle, which is also consistent with the prior work.[307]

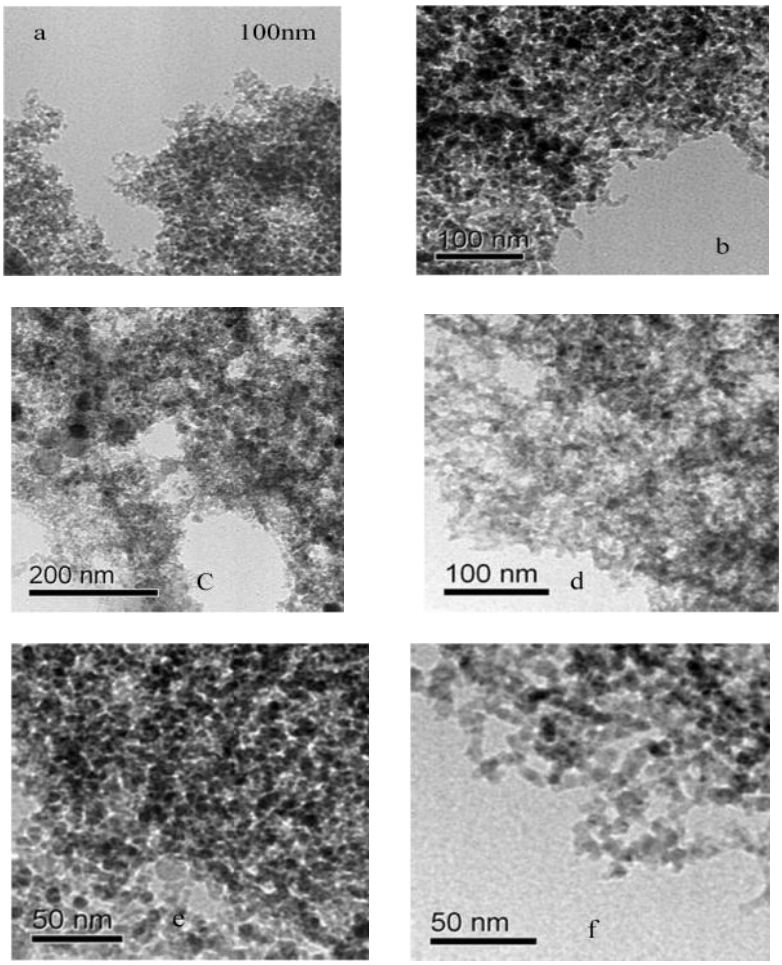

Figure 6.4. Representative TEM images of Si NPs prepared under different gases atmosphere (a) Ar-100 Torr, (b) Ar-500 Torr, (c) Ar-1000 Torr, (d) He-100 Torr, (e) He-1000 Torr, and (f) 10% H_2-He.

The FTIR spectra of Si nanoparticles prepared in H_2/He and O_2/He gaseous atmospheres using LVCC is shown in Figure 6.5a. The FTIR spectrum of Si NPs under H_2/He displays peaks at 1076, 884, and 797 cm^{-1}, which are assigned to Si-O-Si stretching, and amorphous SiO_x films respectively. Si NPs under O_2 atmosphere shows peak at 1635 cm^{-1} for O-H, 1101 cm^{-1} for Si-O, 934 cm^{-1} for Si-O-Si bridge, and 810 cm^{-1} for Si-H cm^{-1}. Figure 6.5b displays XPS Si 2p spectrum of silicon NPs prepared under pure helium. The Si 2p peak in Figure 6.5.b shows two components appearing at 99.2 and 102.5 eV. These peaks are attributed to Si and SiO_2 respectively.

Silicon nanoparticles prepared under He and silicon oxide nanoparticles prepared in O_2/He were irradiated with UV lamp at 254 nm and the results are shown in Figure 6.6. The samples on the left were not irradiated and the samples on the right were irradiated with a UV lamp. The unexpected blue shift from Si NPs that were irradiated could be attributed to the formation of oxide layers on Si nanoparticles during the exposure to air.

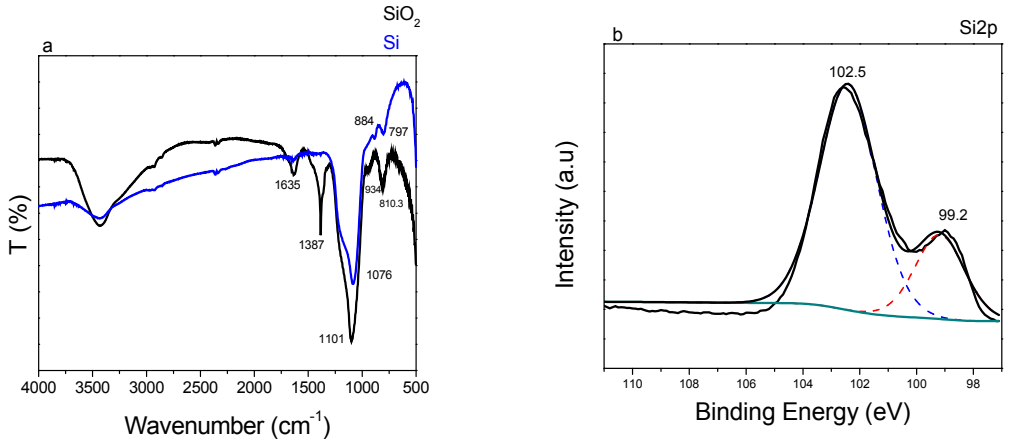

Figure 6.5. (a) FTIR spectra of Si and SiO_2 NPs, and (b) XPS Si 2p spectrum of Si NPs prepared in He gas using LVCC.

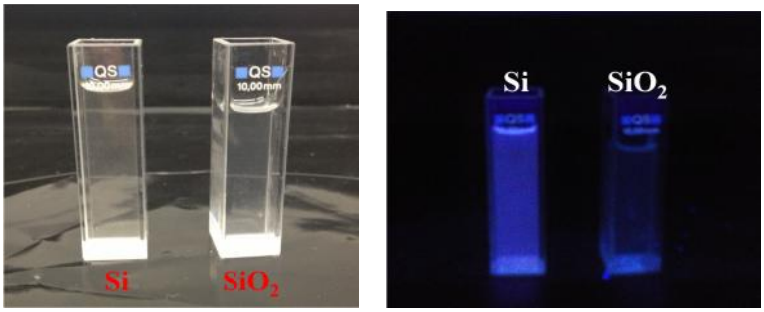

Figure 6.6 UV excitation of Si and SiO_2 nanoparticles at a wavelength of 254 nm before irradiation (left) and after irradiation (right).

6.2 Silicon Quantum Dots Capped by Different Organic Molecules Using LVSC

In this section, LVCC and solution chemistry were simultaneously employed to produce Si NPs (or SiQDs) capped with different organic molecule such as acetonitrile (AN), N-N-dimethylformamide (DMF), Propargylamine (PPA), methanol (Met), and tetrahydrofuran (THF). As discussed earlier, this integrated approach is called laser vaporization solvent capturing (LVSC) and was fully described in Chapter 2.

6.2.1 Results and Discussion

Samples of organic molecules terminated -Si quantum dots that were produced in this work were characterized using a series of microscopic, spectroscopic and mass spectrometric techniques such as TEM, Raman, FTIR, XRD, XPS, UV-Vis, PL and, TOF-MS, and the results are reported here. Figure 6.7a shows a typical transmission electron microscopy image and Figure 6.7b shows a UV-Vis spectrum of Si nanoparticles prepared by LVCC. No solvent was used during the synthesis but to obtain UV-Vis spectrum, Si nanoparticles were dispersed in acetonitrile as a solvent. From the TEM images, the estimated average particles size of Si nanoparticles is 7 nm and they have nearly a spherical shape. The absorption around 270 or 260 nm in UV-Vis spectrum could be attributed to Si nanoparticles with sizes less than 2 nm. The

long tail absorption around 300 nm, which continue to 400 nm is a characteristic of indirect band gap.

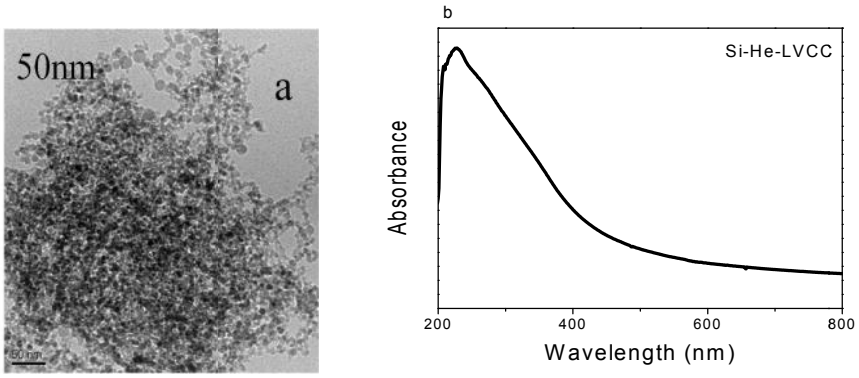

Figure 6.7. (a) A representative TEM image and (b) UV-Vis spectrum of a Si-nanoparticles sample produced in He by LVCC.

The XRD patterns of Si nanoparticles prepared with and without solvents are displayed in Figure 6.8. The crystalline structure of Si nanoparticles was verified by X-ray diffraction, which shows the Si crystalline planes of 111, 220, and 311 at scattering angles of 28°, 47°, and 56°, respectively. The XRD of Si nanoparticles capped with acetonitrile (AN) and produced by LVSC is also shown in Figure 6.2. This XRD pattern shows a few additional peaks, marked with star at 38°, 44°, and 64°, which are indicative of Si-N bond according to JCPDS: 00-051-1334. For Si-THF nanoparticles prepared by LVSC, the crystalline line (110) marked with a small circle, , which is indicative of Si-O bond with a hexagonal crystal structure according to JCPDS: 01-086-1563). Such crystalline lines are not present in the X-ray diffraction pattern of silica nanoparticles prepared in the presence of O_2 where a completely amorphous oxidized material was obtained.[308]

Figure 6.9 shows schematic of two possible pathways for capping Si nanoparticle. One possible pathway is the formation of an oxide layer around the Si nanoparticles before they bond

to any molecules (a); and, the alternative pathway is a direct bond of a ligand (capping agent) to Si nanoparticles (b).

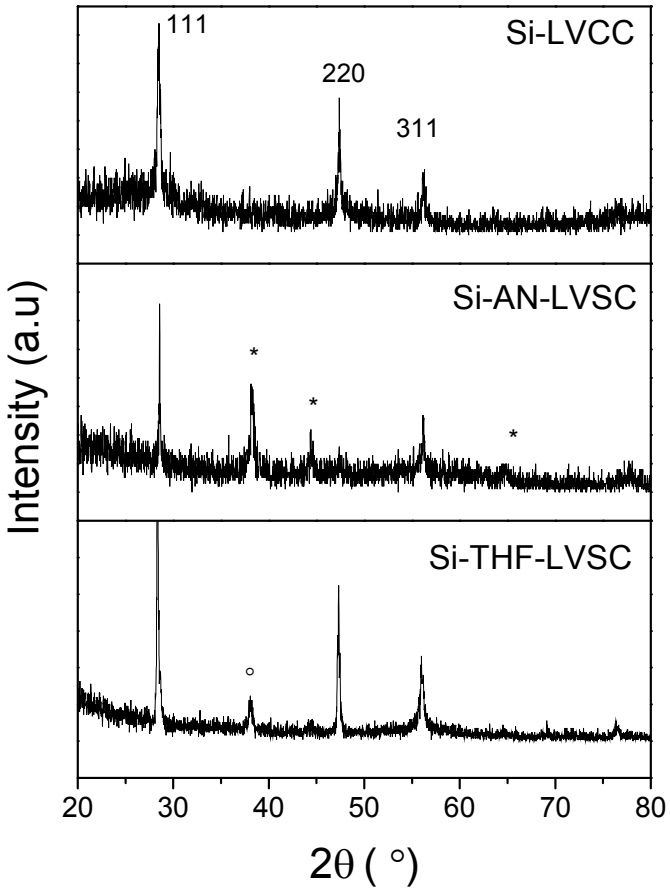

Figure 6.8. X-ray diffraction patterns of Si nanoparticles prepared by LVCC and Si nanoparticles capped with THF and AN prepared by LVSC.

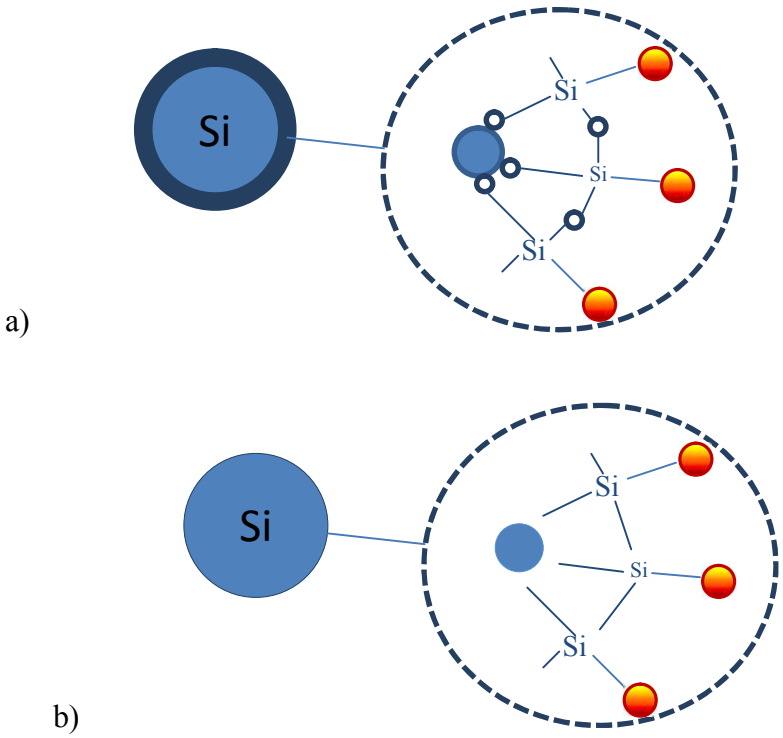

Figure 6.9. Schematic of Si nanoparticles with different ligands through two possible mechanisms: (a) through a surface oxide layer or (b) direct attachment to Si nanoparticles.

The FTIR spectra of three samples of Si nanoparticles, one prepared by LVCC and two others one capped with tetrahydrofuran and the other with acetonitrile, are given in Figure 6.10. FTIR spectrum of THF capped silicon quantum dots exhibits several peaks. There are two small peaks at 2125 and 2383 cm^{-1}, which are assigned to Si-H and O-Si-H stretching, respectively. The peak at around 657 cm^{-1} is for the stretching mode of $Si-O_2$ and the peak at 1069 cm^{-1} is due to Si-O-Si. A broad band at around 3425 cm^{-1} could have been caused by Si-O-H group as has also been reported by Wang et al.[309] FTIR spectrum of AN terminated silicon quantum dots is also presented in Figure 6.10. As can be seen, there are two peaks at 1266 and 1448 cm^{-1}, which are due to the symmetric bending and vibration scissoring of $Si-CH_2$ bonds. This finding is

consistent with the reported results by Warner.[298] The peak at 2916 cm^{-1} indicates the vibration of CH_3 stretching. A strong peak at 1632 cm^{-1} corresponds to a C=N group. Another strong band at about 1070-1080 cm^{-1} is typically due to a Si-O stretching-bending mode. The peak at 1032 cm^{-1} could be attributed to either Si-O or Si-N bonds. The peak at 857 cm^{-1} could also be attributed to Si-N stretching mode , which is in agreement with data reported by Zaitseva.[310] To shed light on Si-N bond in acetonitrile capped Si, a discussion on the role of nitriles would be helpful. Nitriles have a very rich chemical behavior due to the polarization of their CN bonds (withdrawal of electron density towards the N atom). Nitriles can form charge transfer complexes, and their strong polarization allow them to react through both nucleophilic (N) and electrophilic (C) atoms. Thus, N-atom of acetonitrile donates electron to Si , which create a dative-bonded configuration.[311] Figure 6.11 demonstrates a possible pathway of chelating acetonitrile groups toward Si nanoparticles. The appearance of vibration at 1032 cm^{-1} for Si-AN and Si-THF might be due to the surface oxidation layer on Si core. Therefore, these results suggest a potential chemical bond directly between the ligands and Si nanoparticles or through an oxide layer. However, XPS data (presented later) shows a low intensity for oxygen meaning that the surface oxide layer of Si nanoparticles probably plays a less significant role.

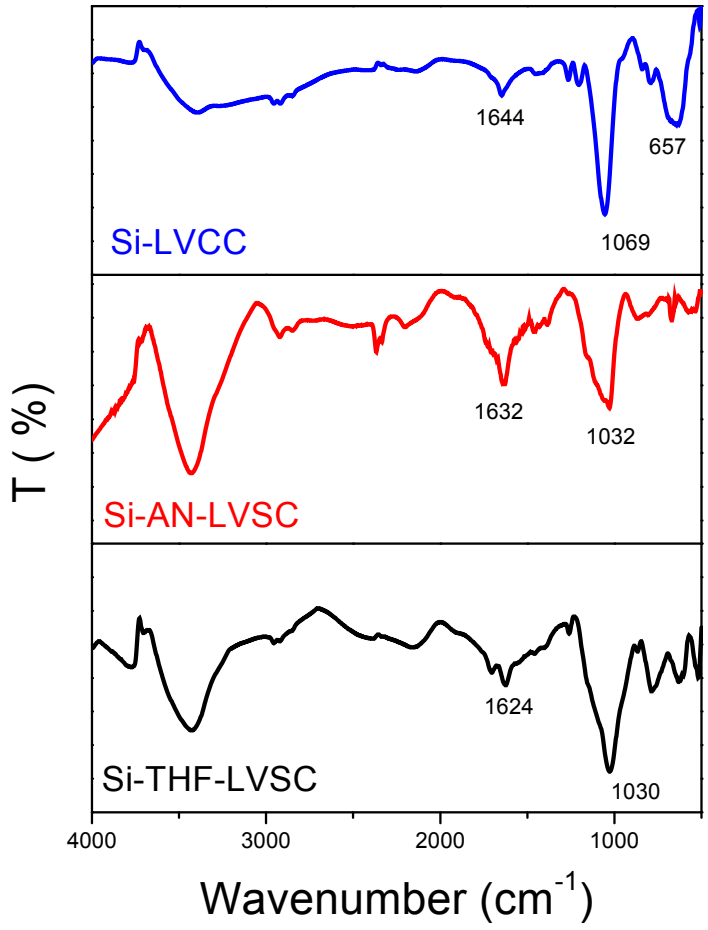

Figure 6.10. FTIR spectra of Si nanoparticles prepared by LVCC and Si nanoparticles capped with THF and AN prepared by LVSC under He atmosphere.

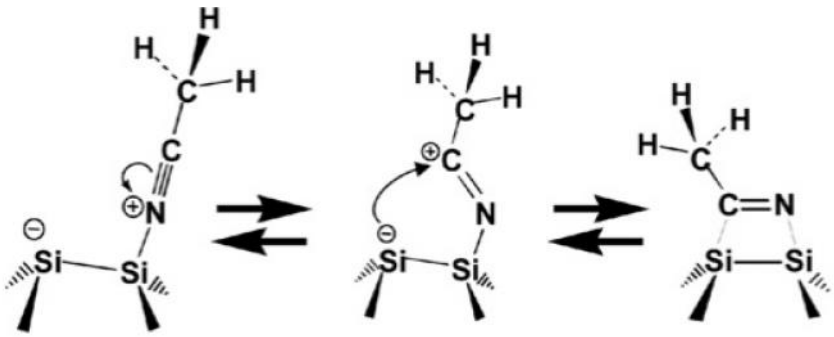

Figure 6.11. Possible mechanism of electron donation from N to Si and charge transfer from Si to C[311].

Figures 6.12a and 6.13 show the UV-Vis absorption spectra for Si nanoparticles capped with acetonitrile (Si-AN) and propargylamine (Si-PPA) prepared by LVSC. The spectra exhibit a shoulder around 250-350 nm for both acetonitrile and propargylamine samples. This is attributed to the absorption from Γ-Γ direct band gap transition and is consistent with the results reported by Tilley et al.[312] Figure 6.12b shows a representative TEM image of Si nanoparticles capped with acetonitrile indicating an average particle size of about 2-3 nm.

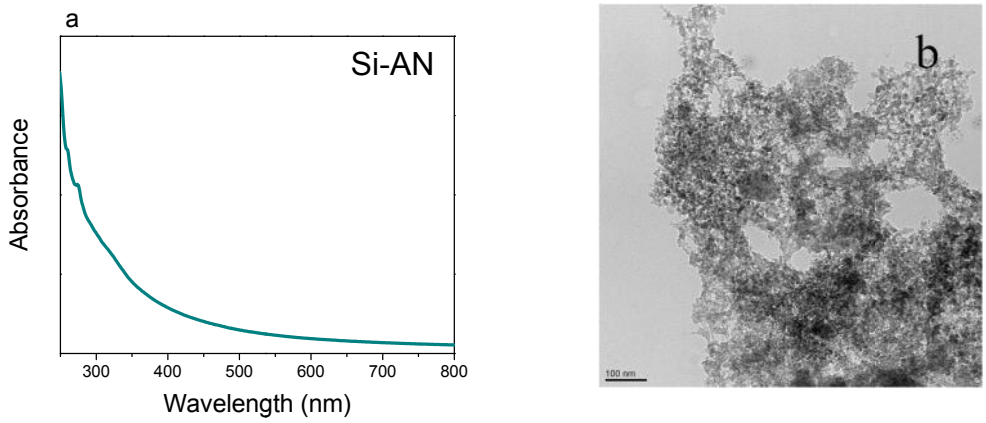

Figure 6.12. (a) UV-Vis spectrum and (b) a representative TEM image of Si-AN prepared by LVSC.

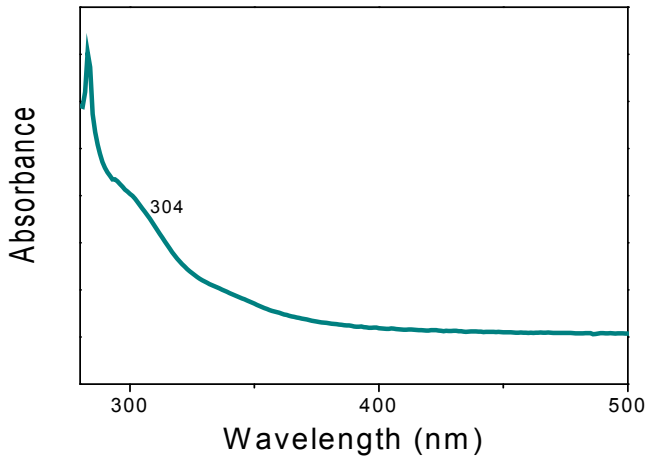

Figure 6.13. UV-Vis spectrum of Si nanoparticles capped with propargylamine using LVSC.

Figures 6.14, 6.15, and 6.16 show photoluminescence (PL) spectra of acetonitrile (AN) terminated silicon nanoparticles, dimethylformamide (DMF) capped Si nanoparticles and propargylamine (PPA) capped Si nanoparticles, respectively. Photoluminescence spectra were obtained using excitation wavelengths ranging from 250 to 400 nm in 10 nm intervals. The photoluminescence of Si capped with amines is expected to have a broad peak at around 470 nm with an excitation wavelength of 400 nm. Some of these amines have slightly red or blue shift. This shift could be attributed to the effect of surface-capping molecules. The photoluminescence of AN terminated Si (Figure 6.14) shows a peak at 471 and 474.5 nm for excitation wavelengths of 350 and 400 nm, respectively. This gives only about 4 nm blue shift in PL peak position. There is also a 4 nm blue shift for DMF capped Si (Figure 6.15) while PPA capped Si (Figure 6.16) gives a 63 nm red shift in PL peak position. Si NPs were also capped using additional solvents without N atoms like tetrahydrofuran (THF) and Methanol (Met). The photoluminescence of Si nanoparticles with these solvents (methanol and tetrahydrofuran) along with acetonitrile are given in Figure 6.17. The spectra show a similar peak around 430 nm with an excitation wavelength of 270 nm. Intensity of PL peak for Si-THF is lower than other two

samples (Si-AN and Si-Met). This difference could be due to the different radiative pathways resulting from the polarity of the ligands on Si nanoparticles surface, which as a result, the Si capped organic molecules attain different emission intensity. According to Werner et al.,[298] emission at 600 nm is typically associated with the defects and types of Si-O surface bonds, which all the samples from this study show an extremely low emission at this wavelength. This result indicates the potentials of achieving low defects and relatively capped Si nanoparticles for the samples prepared by LVSC.

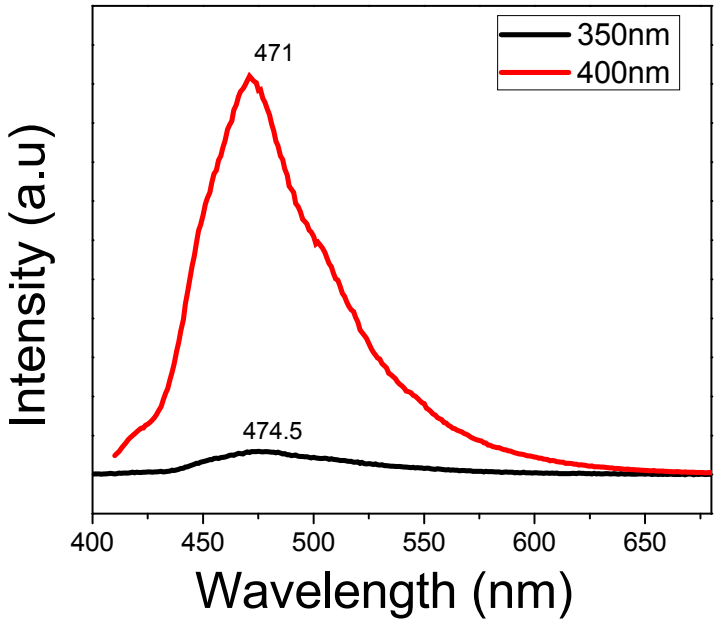

Figure 6.14. Photoluminescence of colloidal suspension of Si nanoparticles capped with acetonitrile at two different excitation wavelengths of 350 nm and 400 nm. Sample was prepared by LVSC.

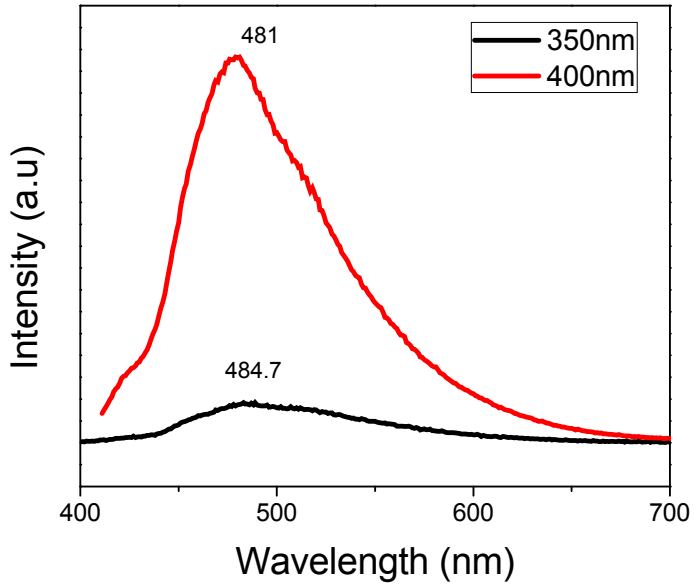

Figure 6.15. Photoluminescence of colloidal suspension of Si capped by DMF at two different excitation wavelengths of 350 nm and 400 nm. Sample was prepared by LVSC.

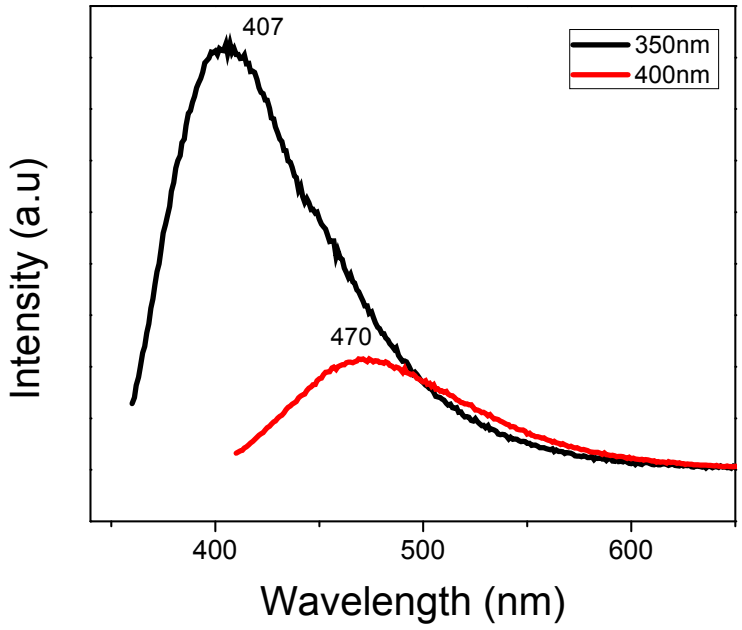

Figure 6.16. Photoluminescence of colloidal solution of Si nanoparticles capped with Propargylamine at two different excitation wavelengths of 350 and 400 nm. Sample was prepared by LVSC.

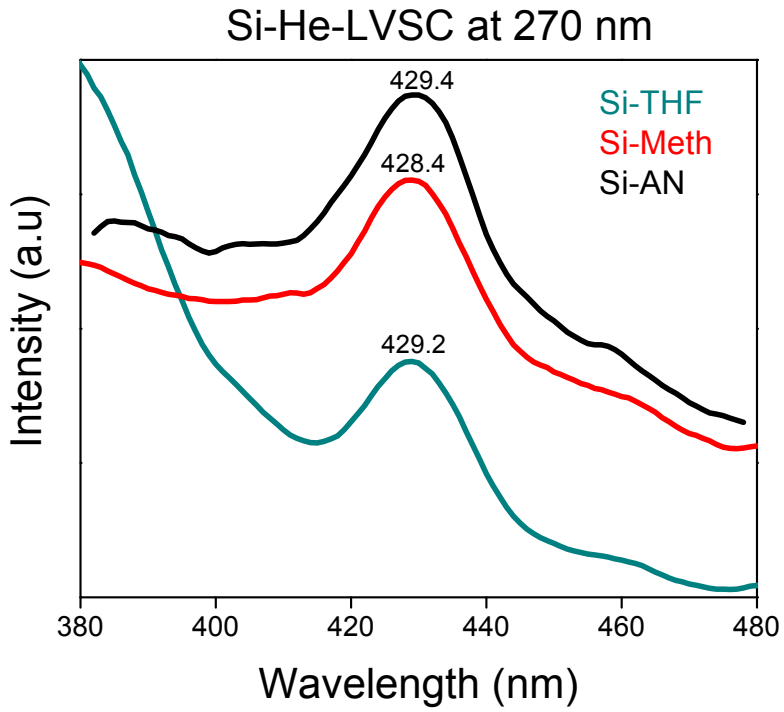

Figure 6.17. Photoluminescence of Si nanoparticles capped with tetrahydrofuran (THF), methanol (Met) and acetonitrile (AN) at an excitation wavelength of 270 nm.

The XPS spectra of Si 2p capped with THF and AN are shown in Figure 6.18. The Si 2p line of Si-AN is asymmetric and could be deconvoluted by curve fitting into two components. The more intense component, which is centered at around 102.5 eV corresponds to Si-N bond, and the second one at about 100.3 eV signifies Si-Si or Si-C bonds. The XPS spectra of Si 2p of Si capped with THF shows again two peaks, one at about 102.7 eV and the other at about 99.2 eV. The peak at 99.2 eV is indicative of a Si-C bond and the peak at 102.7eV is attributed to a Si-O bond.

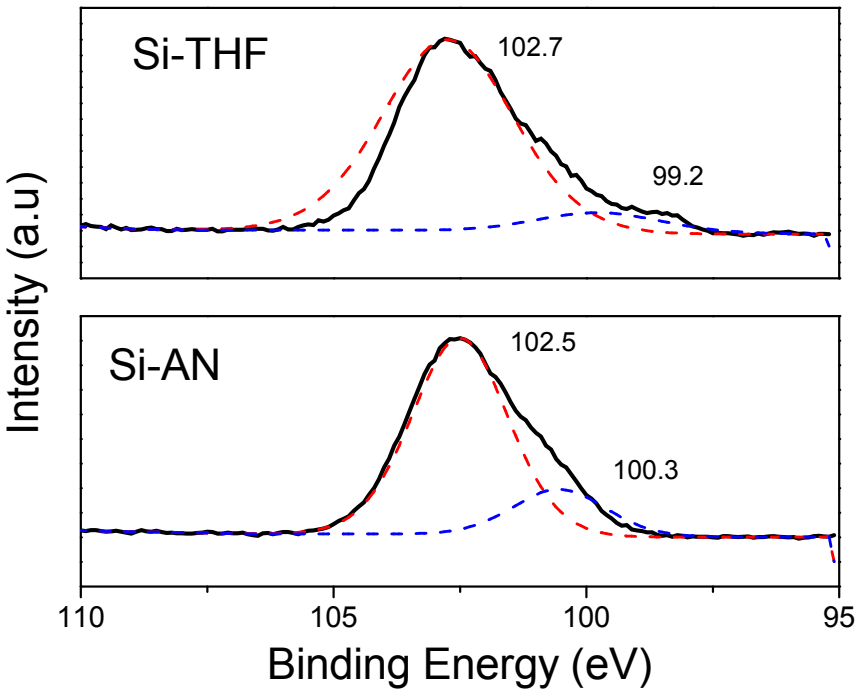

Figure 6.18. XPS Si 2p spectra of Si nanoparticles capped with (a) THF and (b) AN.

The XPS spectra of Si NPs capped with acetonitrile is given in Figure 6.19. According to Figure 6.19a, N1s peak of Si nanoparticles capped with acetonitrile appears at about 399.8 eV indicating a C=N group in the structure of amine terminated Si nanoparticles.[311] The O1s spectra given in Figure 6.19b shows a peak at 532 eV confirming the existence of Si-O group around the Si surface , which might also be indicative of lack of full Si surface coverage by amine groups.[313] The C1s spectrum presented in Figure 6.19c, for Si capped with AN, was deconvoluted by curve fitting to three components, which are located at 284.5, 286.8, and 288.5 eV. The first C1s peak at binding energy of 284.5 eV is assigned to C-Si bond, the second one at 286.8 eV is attributed to C-C or C-H and last peak at 288.5 eV could be the result of Si-N bond. These XPS results clearly suggest the existence of amine ligands around the surface of the Si nanoparticles.

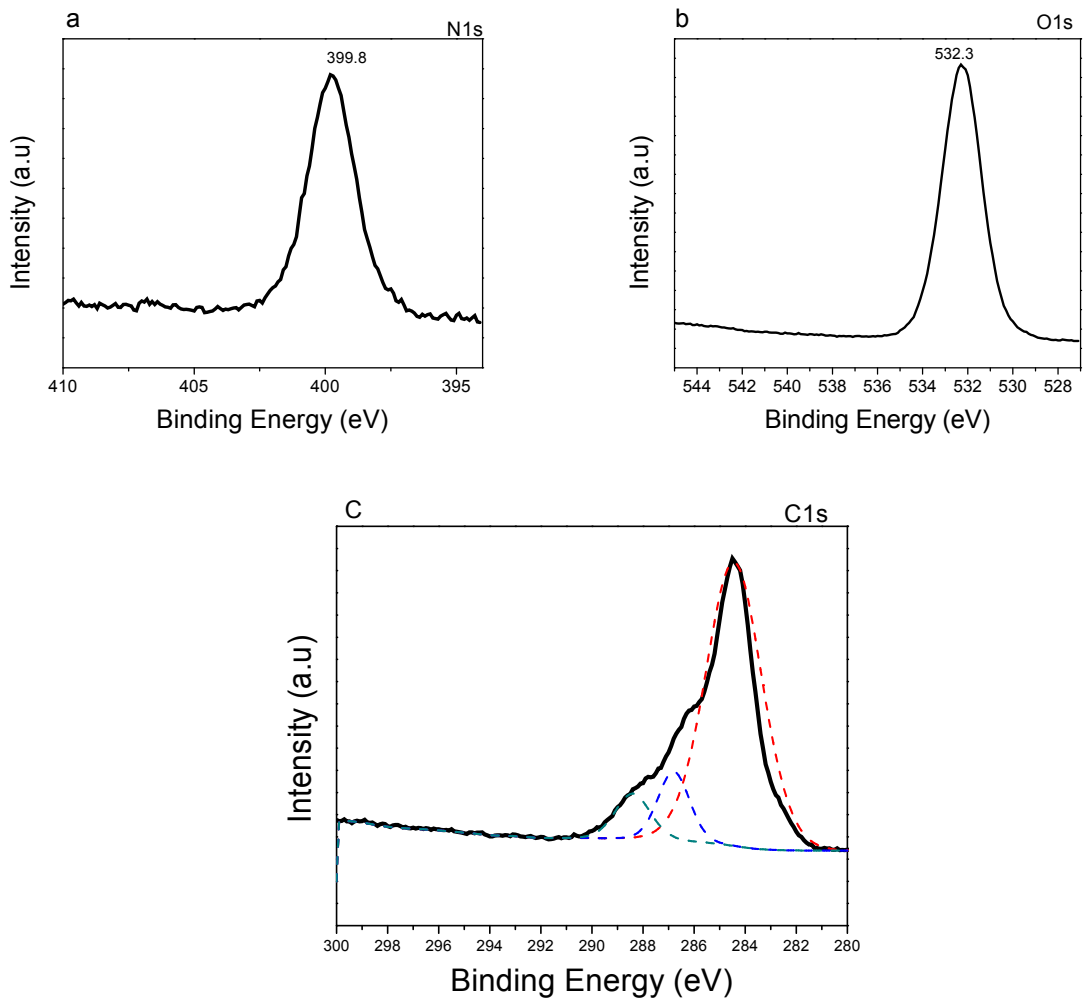

Figure 6.19. XPS spectra of (a) N1s, (b) O1s, and (c) C1s of Si nanoparticles capped with acetonitrile.

The XPS spectra of Si NPs capped with THF is presented in Figure 6.20. The C1s spectrum presented in Figure 6.20a was deconvoluted to three components, which are located at 282.4, 284.6, and 286.8 eV. The first C1s peak at binding energy of 282.4 eV is assigned to C-Si bond, the second one at 284.6 eV is attributed to C-C bond, and the last peak at 286.8 eV could be the result of C-O bond. The O1s spectrum that is given in Figure 6.20b shows a peak at 532.5 eV, which confirms the existence of Si-O group around the Si surface.

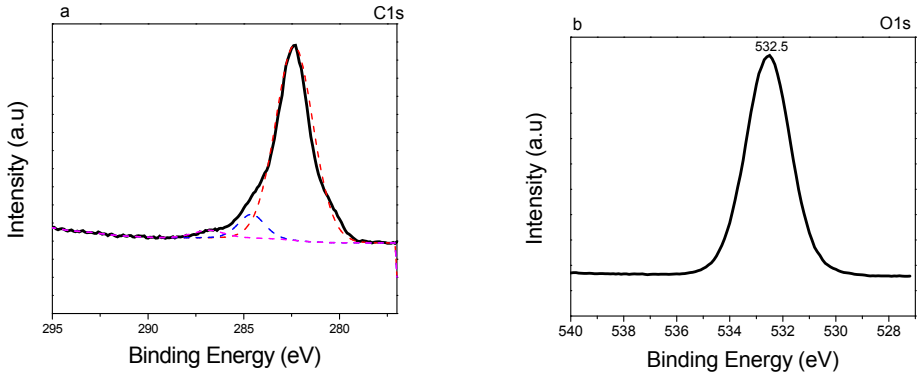

Figure 6.20 . XPS of (a) C1s and (b) O1s of Si nanoparticles capped with tetrahydrofuran (THF).

Figure 6.21 compares the Raman spectra of Si nanoparticles prepared by LVCC with Si nanoparticles capped with AN and THF using LVSC. There is a peak at 510 cm^{-1} for Si capped and 514.5 cm^{-1} for Si using LVCC, which are due to Si-Si bond vibration indicting the dominance of Si nanoparticles rather than surface oxidation layer in the sample. The Raman spectrum of Si nanoparticles prepared in the absence of oxygen by LVCC also shows a sharp peak at 514.5 cm^{-1}.[308] According to Okada et al.,[314] this Raman shift is close to the Raman allowed optical phonon, a characteristic of microcrystalline silicon at 520 cm^{-1}. This shift to a higher frequency can be attributed to the oxygen atoms added to nanoparticle during the sample synthesis. The downshift of this band is attributed to the size and strain effects.[315] The work done by Tsu et al.[315] on porous Si samples prepared under various etching conditions show Raman shifts, which are well correlated with the size of nanoparticles. For instance, Raman shifts of 501 cm^{-1}, 507 cm^{-1}, 515 cm^{-1}, and 517 cm^{-1} belongs to particle sizes of 1.6 nm, 2.5 nm, 4.8 nm, and 7 nm, respectively. Based on these Raman shift, the average particle size of Si nanoparticles capped with organic molecules in this study is estimated to be about 4 nm, which is close to the estimated particle size of 2-3 nm from TEM images.

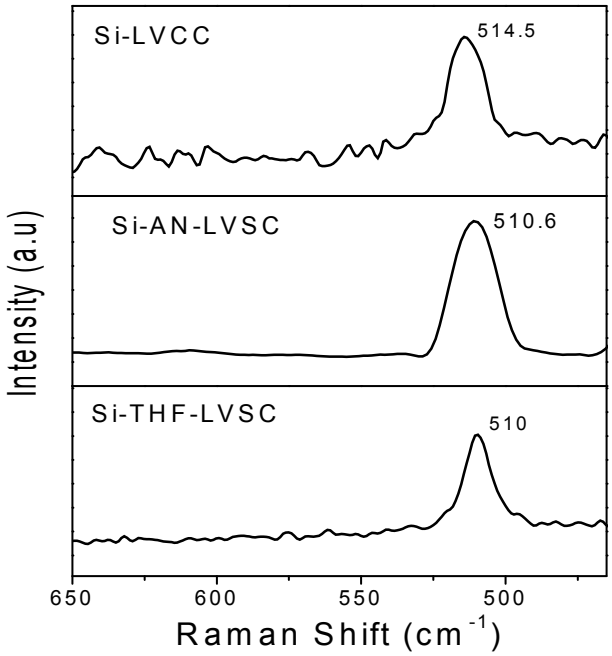

Figure 6.21 Raman spectra of Si nanoparticles prepared by LVCC and Si nanoparticles capped with AN and THF using LVSC method at an excitation wavelength of 532 nm.

Figure 6.22 presents the mass spectrum of Si nanoparticles sample capped with AN using LVSC technique. This mass spectrum was prepared by a laser desorption time of flight (LD-TOF) mass spectrometer. Graph presents masses at 168, 184, 260, 496, 733, 970, and 1206 amu. The mass at 168 amu is supposed to be a Si_8 cluster and mass at 184 amu could be attributed to Si_8O. The mass at 260 amu is assigned to Si_2AN_5 and mass at 496 amu would be $[Si_2AN_5]$ Si_4AN_3. Masses at 733, 970, and 1206 amu are attributed to structures such as $[Si_2AN_5]$ $(Si_4AN_3)_2$, $[Si_2AN_5]$ $(Si_4AN_3)_3$, and $[Si_2AN_5]$ $(Si_4AN_3)_4$ respectively. Consistent with the data presented earlier, this result is a strong evidence for the formation of Si nanoparticles capped with acetonitrile.

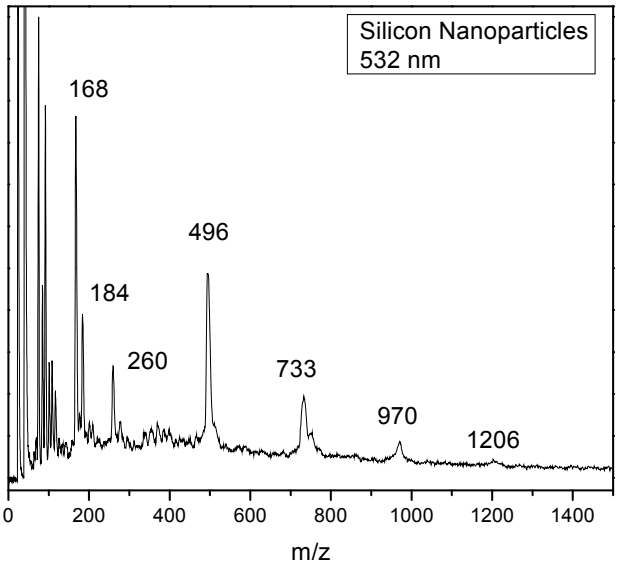

Figure 6.22 Mass spectra of Si nanoparticles capped with AN obtained by an excitation wavelength laser of 532 nm.

6.3 Nanocomposite of Graphene with capped Silicon Nanoparticles by Acetonitrile

Graphene-semiconductor nanocomposites are becoming a popular and fascinating topic for research due to their unique optical and electrical properties. Due to the graphene large conjugated π electron system, it has high intrinsic carrier mobility making it an excellent conductor. Graphene structure also makes it one of the strongest materials, and its large surface area makes it ideal for the formation of nanocomposites.

Silicon is one of the most common materials used in electronics. Since Si is an indirect band gap semiconductor, bulk Si is unable to emit light. Only Si nanoparticles (Si NPs) with a diameter under 4 nm have a strong photoemission. Silicon on the other hand has a drawback that expands by 300% during charging when used as the anode for Li ion batteries, which this property makes it unstable for particularly this application. Combining Si NPs with graphene sheets to form Si-G nanocomposites increases their physical strength. Graphene structure is also

capable of supporting Si expansion during charging.[316] Si nanoparticles on graphene sheets were synthesized by a sono-chemical and magnesiothermic reduction processes for application in Li-ion batteries.[316]

The capped silicon nanoparticles by acetonitrile supported on graphene are discussed in this section. The approach to synthesize these nanocomposites was LVSC process complimented by chemical (hydrazine hydrate) treatment and microwave irradiation. The details of the processing steps and procedures were given in Chapter 2. Once samples prepared, they were characterized using techniques such as XRD, FT-IR, UV-Vis, PL, XPS, TEM, and Raman.

6.3.1 Results and Discussion

Figure 6.23a shows PL spectra of Si nanoparticles capped by acetonitrile (AN) with and without graphene support. For Si NPs without graphene support, there is a strong emission centered at around 428-433 nm, which is assigned to Γ to Γ band. This emission is much weaker for the Si/GO and Si/G samples. This is a clear evidence for the interaction between Si and graphene, as graphene has effectively quenched Si nanoparticles emission. The visible evidence of this emission can be seen when the samples were irradiated with a UV lamp at 254 nm as the results are presented in Figure 6.23b.

Figure 6.24a displays the XPS spectrum of Si 2p for Si nanoparticles capped by AN and supported on graphene. There are two peaks at 99.4 and 103 eV, which are attributed to Si nanoparticles and its surface oxides. Figure 6.24b presents a representative TEM image of Si NPs capped with AN supported on graphene. The photomicrograph shows a spherical shape for Si nanoparticles deposited on graphene with an average particle size of 1-7 nm.

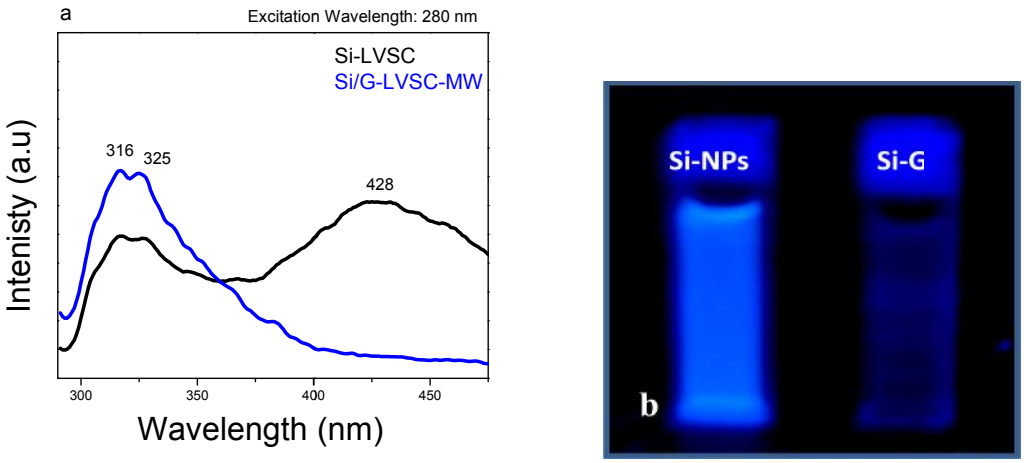

Figure 6.23. (a) Photoluminescence of colloidal suspension of Si nanoparticles capped with acetonitrile at an excitation wavelength of 280 nm. (b) UV excitation of Si and Si/G samples at a wavelength of 254 nm.

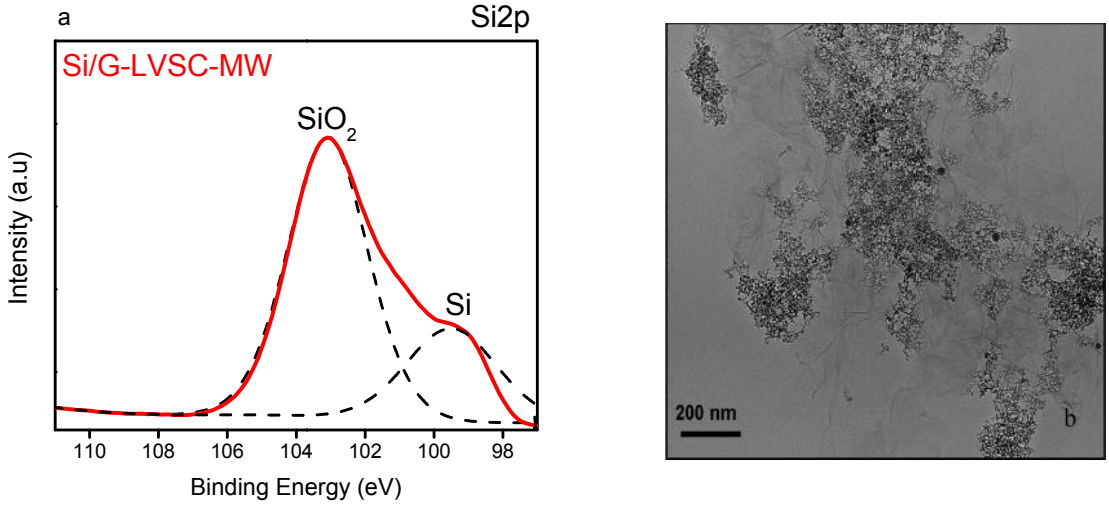

Figure 6.24. (a) XPS spectrum of S2p of Si nanoparticles capped with acetonitrile and supported on graphene. (b) A representative TEM image of Si/G.

Figure 6.25a compares the XRD patterns of GO with Si/G. There is no evidence of GO in Si/G nanocomposite, indicating the complete reduction of GO during LVSC/HH/MW processing of the sample. Figure 6.25b displays the XRD patterns of Si NPs and Si/G both capped by AN. The Si/G nanocomposite shows cubic structure for Si nanoparticles. The 2θ peaks at 28°, 47°,

and 56° represent the 110, 220, 312 scattering angles respectively according to reference JCPDS 01-077-2109. Along with cubic Si there are SiN_x crystals, which has scattering angles at 38°, 44°, and 64°according to reference JCPDS 00-051-1334.

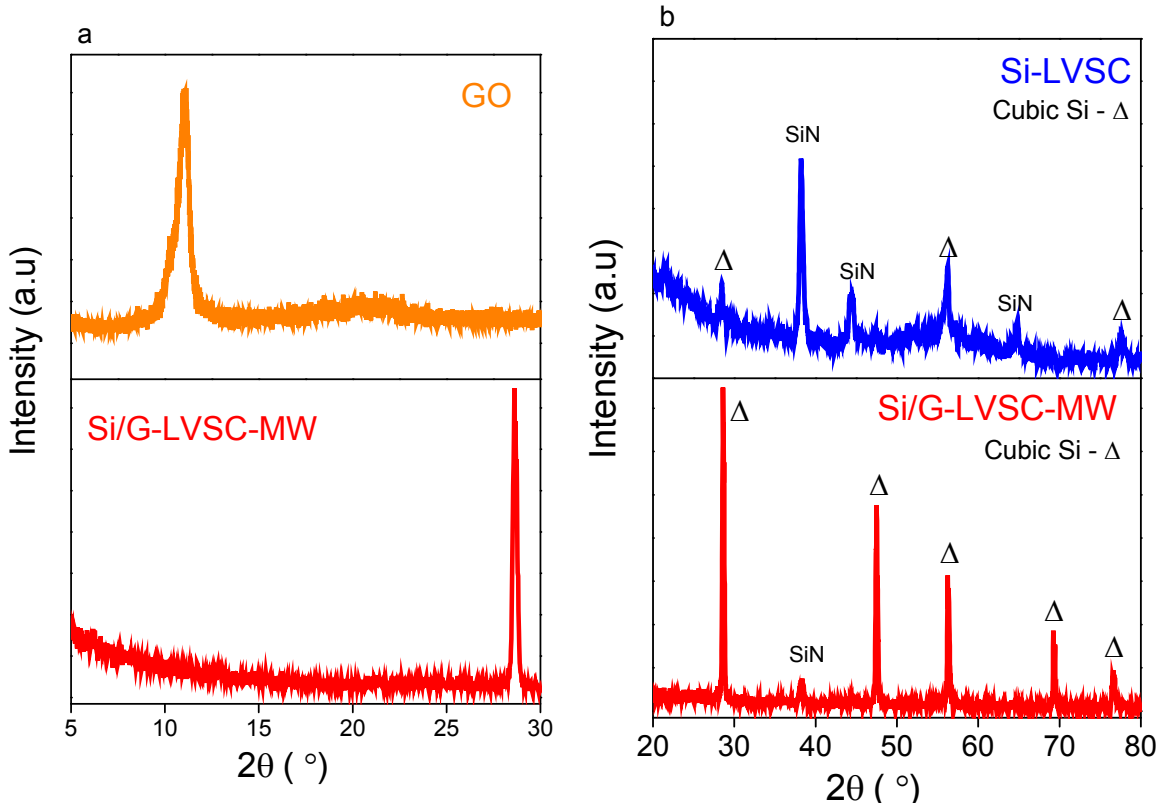

Figure 6.25. X-ray diffraction spectra of (a) GO and Si/G, and (b) Si NPs and Si/G prepared by LVSC/MW.

The UV absorptions of Si NPs and Si/G capped by AN are shown in Figure 6.26a. The long wavelength absorption tail is an evidence of an indirect band gap , which is commonly observed for Si NPs.[317] Evidence of Γ to Γ direct band gap absorption can also be seen at 245 nm for Si NPs prepared by LVSC. The absorbance at 284 nm in the Si/G nanocomposite can be attributed to $\pi \rightarrow \pi^*$ transition of graphene. The FTIR spectra of GO, Si NPs and Si/G nanocomposite are compared in Figure 6.26b. The Spectrum of Si/G nanocomposite clearly

indicates the disappearance of GO characteristic peaks from the sample. It is attributed to the microwave treatment of the composite using hydrazine hydrate that has converted GO to graphene. As can be seen from Figure 6.26.b, the C=O stretch at 1740 cm^{-1}, CO-H deformations at 1350-1390 cm^{-1}, C-O stretch at 1060-1100 cm^{-1} and epoxy group at 1230 cm^{-1} were either greatly reduced or disappeared in Si NPs and Si/G spectra. The Si-O stretch at 1058 cm^{-1} and 1074 cm^{-1} are observed for both Si NPs and Si/G samples.[318] Evidence of AN coordination can also been seen at 886 cm^{-1} and 905 cm^{-1}. These peaks are assigned to Si-N stretch.

Representative TEM images of reduced graphite oxide and Si/G nanocomposite are shown in Figure 6.27 (a and b). A relatively even dispersion of Si NPs on graphene nanosheets is evident from the images in Figure 6.27b. The majority of Si NPs were found to have a particle size of around 7 nm or less.

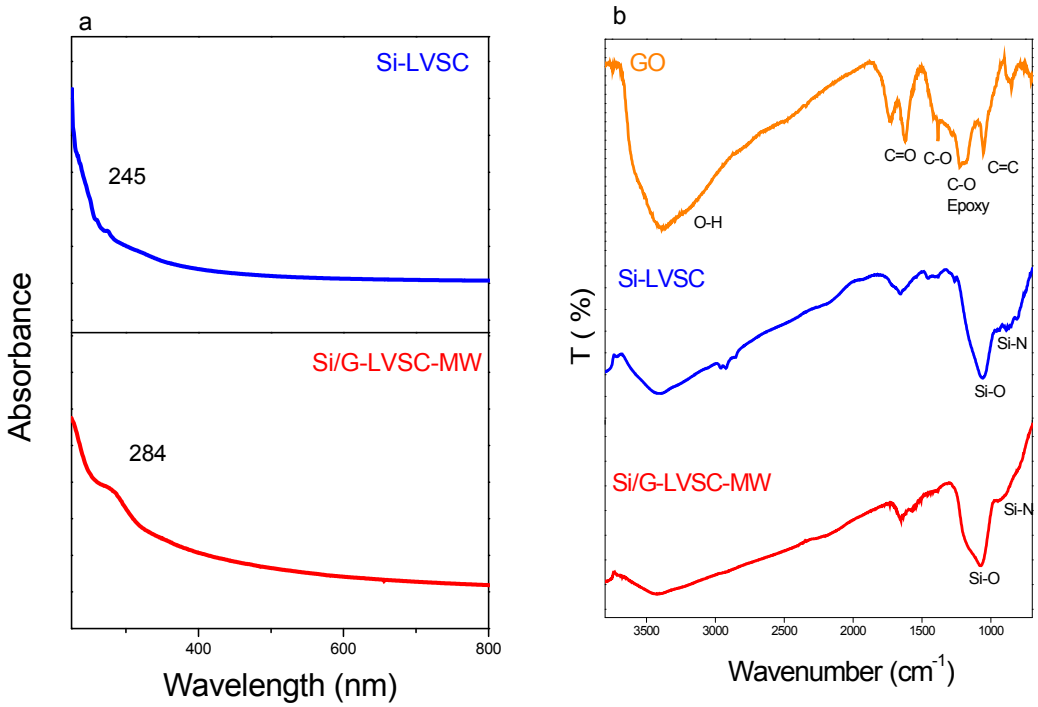

Figure 6.26. (a) UV absorption and (b) FTIR spectra of Si NPs, and Si/G prepared by LVSC/MW method.

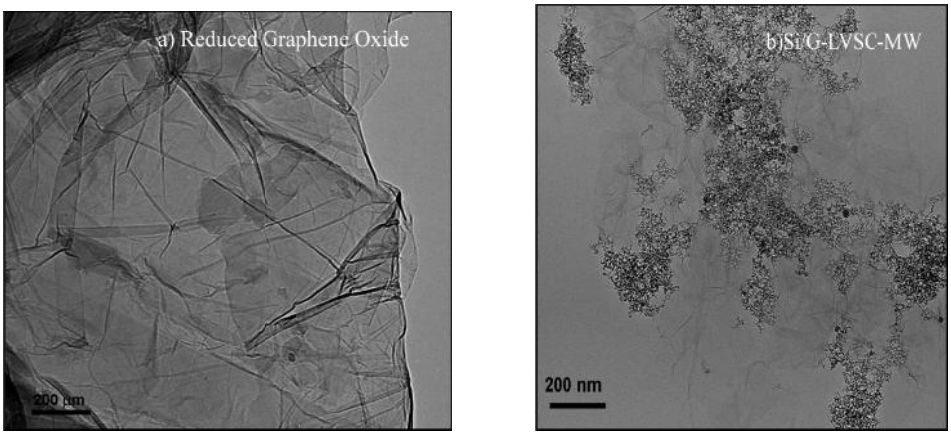

Figure 6.27. Representative TEM images of (a) reduced graphene oxide (b) and Si/G nanocomposite.

The Raman spectra of Si NPs and Si/G nanocomposite are compared in Figure 6.28. Peaks at 519 cm^{-1} in Si NPs and 516 cm^{-1} in Si/G nanocomposite represent the Si-Si vibration. Broad peaks at 1382 cm^{-1} and 1590 cm^{-1} represent the D and G bands of the graphene, respectively. The I_D/I_G ratio for Si/G nanocomposite is 0.84. Electrical resistance of a Si/G pellet (2 mm thickness) was measured using a Fluke 73III multimeter. The Si/G resistance was measured to be 150 kΩ, which is considerably less than that of the same size Si wafer at 3.5 MΩ.

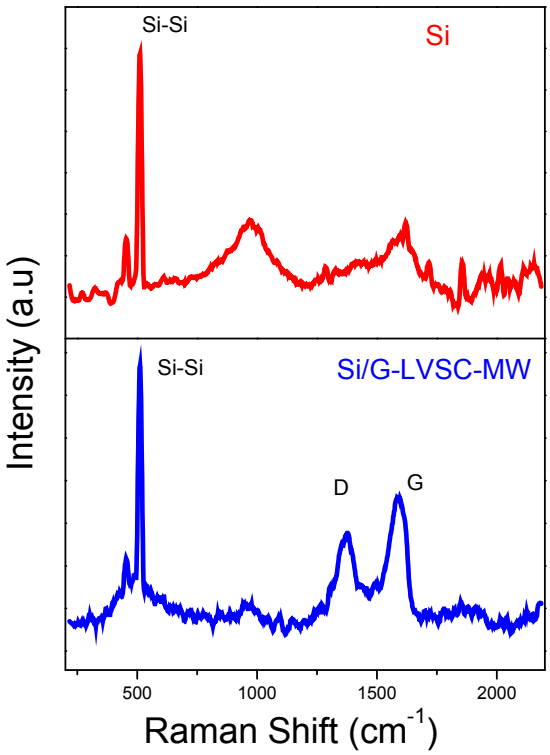

Figure 6.28. Raman spectra of Si NPs and Si/G at an excitation wavelength of 406.7 nm.

Chapter 7: Conclusions

The major objective of the research described in this dissertation was the development of new laser vaporization methods for the synthesis of metal and semiconductor nanoparticles, graphene, B- and N-doped graphene, and metal and semiconductor nanoparticles supported on graphene. These methods included the Laser Vaporization Controlled Condensation (LVCC) approach, which was used this work for the synthesis of: (1) gold nanoparticles supported on ceria and zirconia nanoparticles for the low temperature oxidation of carbon monoxide, and (2) graphene, boron- and nitrogen-doped graphene, hydrogen-terminated graphene (HTG), metal nanoparticles supported on graphene, and graphene quantum dots.

The second method used in the research described in this dissertation was the Laser Vaporization Solvent Capturing (LVSC), which was introduced and developed, for the first time, during this research for the synthesis of solvent-capped semiconductor and metal oxide nanoparticles.

It was demonstrated throughout this work that LVCC and LVSC are two flexible methods for producing graphene (hydrogen terminated graphene, reduced graphite oxide, etc.) with different heteroatoms and nanoparticles inclusion from graphite oxide. The quantities of synthesized products were in the orders of tens of milligrams, large enough for most of the characterization work. When a larger sample quantity, e.g. in the order of 100 mg, was required,

the above mentioned methods were augmented by methods such as thermal and hydrothermal treatment for quantum dots formation or combined chemical (hydrazine hydrate) and microwave irradiation methods for the formation of metal/metal oxide nanoparticles composited with graphene and capped with different organic molecules.

In Chapter 3, gold (Au) nanoparticles supported on two different oxide nanoparticles: ceria (CeO_2) and zirconia (ZrO_2) were synthesized, in one step, using the LVCC method and applied as CO oxidation catalysts. XRD, Raman, IR, and XPS measurements of the prepared supported catalysts indicated formation of small Au nanoparticles and confirmed their homogeneous distribution within the oxide nanoparticle matrix. TEM images of the Au/CeO_2 and Au/ZrO_2 showed that most of Au nanoparticles were in the size range of 2 to 6 nm and well dispersed on the surface of support material with almost no large aggregates of Au nanoparticles. Gold/ceria catalysts with 5% by weight loading of gold showed the highest activity for CO oxidation with a 100% oxidation of CO at about 60 °C. Stability and reproducibility under typical reaction condition were tested and the result showed a complete CO oxidation (100% conversion) at 86 °C for 5% Au/CeO_2 catalyst after one week use.

In Chapter 4, the LVCC method was used, for the first time, for the synthesis of graphene and HTG. The synthesized graphene samples by LVCC under different atmospheres showed a relatively good removal of oxygen functional groups from the starting graphite oxide. The method allows rapid deoxygenation of bulk graphite oxide in an atmosphere of helium or a helium-hydrogen mixture to produce hydrogen-terminated graphene nanosheets without the need for any chemical reducing agents or solvents. Different atmospheres affected the extent of reduction differently with 20% H_2-He atmosphere the most effective one. The FTIR confirms that the LVCC method of bulk GO produces HTG nanosheets. A combination of different

techniques including laser vaporization/ionization time-of-flight (LVI-TOF) mass spectrometry was used to characterize the formation of graphene by the LVCC of bulk GO. These experiments established the formation of abundant hydrogen-capped linear carbon chains containing $-(C\equiv C)_n-$ units with n at least up to 15 from the LVI of GO in vacuum.[123] In contrast, LVI of bulk graphite under identical experimental conditions generates mainly the carbon cluster series C_n without any significant hydrogenation in both the positive and negative ion modes. The observation of hydrogen-capped carbon chains C_nH^-, C_nH^- and $C_nH_2^+$ with n = 2-30 confirms that the LVCC method of bulk GO produces HTG nanosheets, which can be ionized and dissociated in vacuum to produce the observed hydrogen-capped polyyne chains. These species could be deposited from the gas phase to form one-dimensional conducting molecular wires for a variety of potential applications in nanoelectronics, sensors and devices.

In Chapter 4, the LVCC method was used for the synthesis of boron- and nitrogen-doped graphene by including diborane (B_2H_6) and ammonia (NH_3), respectively within the carrier gas mixture during the LVCC process. The X-ray data showed that in all experiments the reduction of graphite oxide was achieved. From the Raman data, the D and G bands of nitrogen-, boron- and boron-nitrogen- doped graphene nanosheets show significant spectral shifts and their corresponding I_D/I_G ratios vary from that of graphene nanosheets due to the interaction of heteroatom with graphene, and the structural distortion of graphene originated by the different bond lengths of C-C, C-N, and C-B bonds. The XPS data clearly indicated the incorporation of nitrogen and boron into the graphene structure with the formation of different nitrogen-carbon and boron-carbon bonds in the synthesized graphene structure. The FTIR data also demonstrated the removal or reduction of various oxygen functional groups from graphite oxide with the formation of new C-N and C-B bonds in the graphene structure. Among the most important

results of this work is the demonstration that the partial pressure of NH_3 in the carrier gas mixture of the LVCC process can selectively control the type and concentration of the different N-doped structures in graphene such as graphitic, pyridininc, and pyrollic N-substitutions. Based on the results, a two pathways mechanism for nitrogen and boron doping of the graphene were suggested. The first and more probable pathway for nitrogen insertion is the reaction of adsorbed ammonia with –COOH containing sites upon laser irradiation. The interaction via Lewis acid route leads to the formation of amide and via Bronsted acid route to quaternary ammonia. The formed amide group is converted to pyridinic dopant and the -$COONH_4$ group is released back into the gas phase. The second mechanism is based on the conversion of NH_3 during the plasma laser vaporization process to H + NH_2 radicals followed by reaction of these radicals with active sites of graphite oxide. For boron doping of graphite oxide, the adsorption of B_2H_6 is less likely, and thus, the first mechanism for boron inclusion is very unlikely. However, formation of B radical upon laser irradiation followed by reaction of B radical with graphite oxide active site such as sp^2 carbon network is more plausible.

Incorporation of metal (Ni, Co, Fe, Cu, Pd, and Au) nanoparticles into graphene sheets was successfully demonstrated by the simultaneous LVCC processing of metal and graphite oxide mixtures. This was achieved by laser vaporization of a target containing a mixture of selected metal powder and graphite oxide. XRD, Raman, IR, and XPS results of the samples indicated that graphite oxide was reduced to graphene and metal nanoparticles were deposited on graphene surface. The G-band of most samples was red shifted with respect to graphene indicating an interaction between metal nanoparticle and graphene nanosheets. The calculated intensity ratio (I_D/I_G) based on Raman data indicated a more graphitic domain but smaller in size, and less density of defects compared to graphite oxide. The average size of Fe, Co, Ni, Cu, Pd,

and Au nanoparticles were estimated from TEM images of the samples to be in the range of 5-10 nm. Amongst the metal nanoparticles graphene nanocomposite, only Pd-graphene nanocomposite showed a good activity as a catalyst for the Suzuki carbon-carbon cross-coupling reaction.

Graphene quantum dots (GQDs) and nitrogen-doped graphene quantum dots (N-GQDs) were successfully synthesized from reduced graphene oxide prepared using different techniques such as laser exfoliation by LVCC, microwave plasma or thermal exfoliation under argon atmosphere. The graphene sheets were then functionalized in a concentrated solution of H_2SO_4 and HNO_3 acids. Hydrothermal treatment of the functionalized graphene sheets in H_2O or H_2O/NH_3OH generated ultra-fine graphene nanoparticles (GQDs) and N-GQDs, which led to changes in UV-Vis absorption and PL of produced samples. The nitrogen doped graphene quantum dots exhibited a red shift of about 20 nm in PL emission (from about 450 to 475 nm) compared to graphene quantum dots without nitrogen implying that the graphitic nitrogen helps charge transfer through the conjugated system of graphene quantum dots. Raman spectra of graphene and graphene quantum dots prepared by hydrothermal treatment indicated a decrease in I_D/I_G ratio from G to GQDs suggesting the presence of an extended conjugated system in GQDs nanosheets. The estimated size of the graphene quantum dots was in the range of 4-10 nm, which was decreased to about 2-6 nm after dialysis. For the nitrogen doped GQDs the average size was between 5 to 10 nm, which was qualitatively similar to the un-doped graphene quantum dots.

The second objective of the research described in this dissertation was the development of the Laser Vaporization Solvent Capturing (LVSC) approach for the synthesis of solvent-capped semiconductor and metal oxide nanoparticles. The method has been demonstrated for the synthesis of V, Mo, and W oxide nanoparticles capped by different solvent molecules such as

acetonitrile and methanol. The LVSC method has also been applied for the synthesis of Si nanocrystals capped by acetonitrile clusters. The Si and the metal oxide nanoparticles prepared by the LVSC method have been incorporated into graphene in order to synthesize graphene nanosheets with tunable properties depending on graphene-nanoparticle interactions.

In Chapter 5, V, Mo, and W metal nanoparticles and their oxides (V_xO_y, Mo_xO_y, and W_xO_y) capped with different organic solvents were successfully produced using a combination of the LVCC and LVSC processes. The synthesized samples were analyzed using PL, UV-Vis, TEM, Raman, XPS, and TOF-MS. The results indicated that almost all the nanoparticles have a thin (1 nm) surface oxide layer even if they were prepared under pure helium atmosphere. This oxide layer is formed upon the exposure of the nanoparticles to air following the LVCC synthesis in inert atmospheres. Furthermore, XPS, Raman, and PL spectra indicated the formation of ligand bonds between nanoparticles and the organic solvent molecules used in the study. The strongest evidence for the formation of ligand-capped nanoparticles was obtained using laser desorption time of flight (LD-TOF) mass spectrometry of the metal oxide nanoparticles prepared by the LVSC method. The mass spectra indicated the formation of complexes presumably with a core metal oxide and acetonitrile ligands surrounding the core. These results confirmed that vanadium and molybdenum oxide nanoparticles are attached to 1, 2 or 3 acetonitrile molecules. The extent of bonding and surface coverage depended on the type of solvent and the nature of metal oxide core. The photomicrographs of metal oxide nanoparticles display different types of shapes. For tungsten oxide nanoparticles, the most stable spherical shape with a size range of 1 to 5 nm and various forms of wire-like shapes with a width of 3 to 6 nm and a length of 10 to 15 nm were observed. Molybdenum oxide and vanadium oxide

nanoparticles show various wire-like and star-like shapes, each nanostar is composed of a few nanowalls crossing each other.

In Chapter 6, Silicon nanoparticles and silicon quantum dots capped by different organic solvents were successfully prepared by the LVCC and LVSC methods. The organic molecules used in this study included acetonitrile (AN), N-N- dimethylformamide (DMF), and propargylamine. Other organic molecules containing only oxygen functional groups such as methanol and tetrahydrofuran (THF) were also used. The synthesized samples were characterized with multiple analytical instrument including X-ray, PL, UV-Vis, FTIR, Raman, XPS, TEM, and TOF-MS. The results indicated that the formation of Si capped ligands has indeed been achieved. The results further indicated that the nanoparticles have an average size of about 4 nm with very little or no surface oxide layers present. The mass spectra of the Si nanoparticles capped with acetonitrile molecules obtained by laser desorption time of flight (LD-TOF) mass spectrometry confirmed that the capped clusters contain a combination of Si atoms and acetonitrile molecules. Model structures have been suggested to explain the formation of a size-specific Si core surrounded by a certain number of acetonitrile molecules. Graphene nanocomposites containing the acetonitrile-capped silicon clusters were successfully prepared using a combination of the LVSC method and the chemical reduction of graphene oxide using hydrazine hydrate under microwave irradiation. A relatively even dispersion of Si nanoparticles within the graphene nanosheets is evident from the TEM images of the Si-graphene nanocomposites. The majority of the Si nanoparticles were found to have a particle size of about 7 nm or less. Evidence of the presence of acetonitrile is also obtained from FTIR data, which show absorptions bands due to Si-N stretching vibrations. The acetonitrile-capped Si nanoclusters exhibit strong blue emission where Si-graphene nanocomposites show much weaker

emission. This is a clear evidence for the interaction between Si nanoparticles and graphene sheets since graphene can effectively quench the blue emission from the Si nanoparticles. Electrical resistance of the Si-graphene nanocomposite pellet (2 mm thick) was measured to be 150 kΩ, which is considerably less than the 3.5 MΩ measured for the same size Si wafer.

References:

1. El-Shall, M. S., Laser-Vaporization-Controlled Conensation for the synthesis of Semiconductor, Metallic, and Bimetallic Nanocrystals and Nanoparticles catalysts. In *nanomaterials Processing and Characterization with Lasers*, Subhash Chandra Singh, H. Z., Chunlei Guo, and Weiping Cai, Ed. WILEY-VCH: 2013.
2. Liu, Y. W.; Men, Y. M.; Zhang, X. R., How nanoscale seed particles affect vapor-liquid nucleation. *Journal of Chemical Physics* **2011,** *135* (18).
3. Swihart, M. T., Vapor-phase synthesis of nanoparticles. *Current Opinion in Colloid & Interface Science* **2003,** *8* (1), 127-133.
4. Wegner, K.; Walker, B.; Tsantilis, S.; Pratsinis, S. E., Design of metal nanoparticle synthesis by vapor flow condensation. *Chemical Engineering Science* **2002,** *57* (10), 1753-1762.
5. Weber, A. P.; Seipenbusch, M.; Kasper, G., Application of aerosol techniques to study the catalytic formation of methane on gasborne nickel nanoparticles. *Journal of Physical Chemistry A* **2001,** *105* (39), 8958-8963.
6. Urban, F. K.; Hosseini-Tehrani, A.; Griffiths, P.; Khabari, A.; Kim, Y. W.; Petrov, I., Nanophase films deposited from a high-rate, nanoparticle beam. *Journal of Vacuum Science & Technology B* **2002,** *20* (3), 995-999.
7. Kim, J. H.; Germer, T. A.; Mulholland, G. W.; Ehrman, S. H., Size-monodisperse metal nanoparticles via hydrogen-free spray pyrolysis. *Advanced Materials* **2002,** *14* (7), 518-+.
8. Ledoux, G.; Gong, J.; Huisken, F.; Guillois, O.; Reynaud, C., Photoluminescence of size-separated silicon nanocrystals: Confirmation of quantum confinement. *Applied Physics Letters* **2002,** *80* (25), 4834-4836.
9. Heberlein, J.; Postel, O.; Girshick, S.; McMurry, P.; Gerberich, W.; Iordanoglou, D.; Di Fonzo, F.; Neumann, D.; Gidwani, A.; Fan, M.; Tymiak, N., Thermal plasma deposition of nanophase hard coatings. *Surface & Coatings Technology* **2001,** *142*, 265-271.
10. Janzen, C.; Roth, P., Formation and characteristics of Fe2O3 nano-particles in doped low pressure H-2/O-2/Ar flames. *Combustion and Flame* **2001,** *125* (3), 1150-1161.
11. Madler, L.; Kammler, H. K.; Mueller, R.; Pratsinis, S. E., Controlled synthesis of nanostructured particles by flame spray pyrolysis. *Journal of Aerosol Science* **2002,** *33* (2), 369-389.
12. Sarigiannis, D.; Peck, J. D.; Kioseoglou, G.; Petrou, A.; Mountziaris, T. J., Characterization of vapor-phase-grown ZnSe nanoparticles. *Applied Physics Letters* **2002,** *80* (21), 4024-4026.
13. El-shall, M. S. a. L., S, Advances in Metal and Semiconductor Clusters. M.A.Duncan, Ed. Jar Press, Ltd,London: 1998; p 115.
14. Abdelsayed, V.; El-Shall, M. S.; Seto, T., Differential mobility analysis of nanoparticles generated by laser vaporization and controlled condensation (LVCC). *Journal of Nanoparticle Research* **2006,** *8* (3-4), 361-369.
15. Abdelsayed, V.; Glaspell, G.; Nguyen, M.; Howe, J. M.; Samy El-Shall, M., Laser synthesis of bimetallic nanoalloys in the vapor and liquid phases and the magnetic

properties of PdM and PtM nanoparticles (M = Fe, Co and Ni). *Faraday Discussions* **2008,** *138* (0), 163-180.
16. Abdelsayed, V.; Saoud, K. M.; El-Shall, M. S., Vapor phase synthesis and characterization of bimetallic alloy and supported nanoparticle catalysts. *Journal of Nanoparticle Research* **2006,** *8* (3-4), 519-531.
17. Abdelsayed, V. M. S. E.-S., Vapor phase nucleation on neutral and charged nanoparticles: Condensation of supersaturated trifluoroethanol on Mg nanoparticles *J. Chem. Phys.* **2007,** *126*, 024706.
18. Baraton, M. I.; El-Shall, M. S., Synthesis and characterization of nanoscale metal oxides and carbides: II. Micro-raman and FT-IR surface studies of a silicon carbide powder. *Nanostructured Materials* **1995,** *6* (1–4), 301-304.
19. El-Shall, M. S., Shoutian Li, Synthesis of nanoparticles by a laser-vaporization-controlled condensation technique *SPIE* **1997,** *3123*, 98.
20. El-Shall, M. S.; Abdelsayed, V.; Pithawalla, Y. B.; Alsharaeh, E.; Deevi, S. C., Vapor Phase Growth and Assembly of Metallic, Intermetallic, Carbon, and Silicon Nanoparticle Filaments. *The Journal of Physical Chemistry B* **2003,** *107* (13), 2882-2886.
21. El-Shall, M. S.; Graiver, D.; Pernisz, U.; Baraton, M. I., Synthesis and characterization of nanoscale zinc oxide particles: I. laser vaporization / condensation technique. *Nanostructured Materials* **1995,** *6* (1–4), 297-300.
22. El-Shall, M. S.; Li, S.; Turkki, T.; Graiver, D.; Pernisz, U. C.; Baraton, M. I., Synthesis and Photoluminescence of Weblike Agglomeration of Silica Nanoparticles. *The Journal of Physical Chemistry* **1995,** *99* (51), 17805-17809.
23. El-Shall, M. S.; Slack, W.; Vann, W.; Kane, D.; Hanley, D., Synthesis of Nanoscale Metal Oxide Particles Using Laser Vaporization/Condensation in a Diffusion Cloud Chamber. *The Journal of Physical Chemistry* **1994,** *98* (12), 3067-3070.
24. Germanenko, I. N.; Li, S.; El-Shall, M. S., Decay Dynamics and Quenching of Photoluminescence from Silicon Nanocrystals by Aromatic Nitro Compounds. *The Journal of Physical Chemistry B* **2000,** *105* (1), 59-66.
25. Germanenko, I. N.; Li, S.; Silvers, S. J.; El-Shall, M. S., Characterization of silicon nanocrystals and photoluminescence quenching in solution. *Nanostructured Materials* **1999,** *12* (5–8), 731-736.
26. Germanenko, I. N. M. D. Y. B. P.; Carlisle, M. S. E.-S. a. J. A., Effect of atmospheric oxidation on the electronic and photoluminescence properties of silicon nanocrystals *Pure Appl. Chem* **2000,** *72*, 245-255.
27. Glaspell, G.; Anderson, J.; Wilkins, J. R.; El-Shall, M. S., Vapor Phase Synthesis of Upconverting Y 2O 3 Nanocrystals Doped with Yb 3+, Er 3+, Ho 3+, and Tm 3+ to Generate Red, Green, Blue, and White Light. *The Journal of Physical Chemistry C* **2008,** *112* (30), 11527-11531.
28. Glaspell, G. P.; Jagodzinski, P. W.; Manivannan, A., Formation of Cobalt Nitrate Hydrate, Cobalt Oxide, and Cobalt Nanoparticles Using Laser Vaporization Controlled Condensation. *The Journal of Physical Chemistry B* **2004,** *108* (28), 9604-9607.
29. Glaspell, G. V. A., Khaled M. Saoud, and; El-Shall, M. S., Vapor-phase synthesis of metallic and intermetallic nanoparticles and nanowires: Magnetic and catalytic properties *Pure Appl. Chem* **2006,** *78*, 1667-1689.

30. Li, S.; El-Shall, M. S., Synthesis of nanoparticles by reactive laser vaporization: silicon nanocrystals in polymers and properties of gallium and tungsten oxides. *Applied Surface Science* **1998,** *127–129* (0), 330-338.
31. Li, S.; Germanenko, I.; El-Shall, M. S., Nanoparticles from the Vapor Phase: Synthesis and Characterization of Si, Ge, MoO3, and WO3Nanocrystals. *Journal of Cluster Science* **1999,** *10* (4), 533-547.
32. Li, S.; Germanenko, I. N.; El-Shall, M. S., Semiconductor Nanoparticles in Contact: Quenching of the Photoluminescence from Silicon Nanocrystals by WO3 Nanoparticles Suspended in Solution. *The Journal of Physical Chemistry B* **1998,** *102* (38), 7319-7322.
33. Li, S.; Samy El-Shall, M., Synthesis and characterization of photochromic molybdenum and tungsten oxide nanoparticles. *Nanostructured Materials* **1999,** *12* (1–4), 215-219.
34. Li, S.; Silvers, S. J.; El-Shall, M. S., Surface Oxidation and Luminescence Properties of Weblike Agglomeration of Silicon Nanocrystals Produced by a Laser Vaporization−Controlled Condensation Technique. *The Journal of Physical Chemistry B* **1997,** *101* (10), 1794-1802.
35. Mautner, M. N.; Abdelsayed, V.; El-Shall, M. S.; Thrower, J. D.; Green, S. D.; Collings, M. P.; McCoustra, M. R. S., Meteorite nanoparticles as models for interstellar grains: Synthesis and preliminary characterisation. *Faraday Discussions* **2006,** *133* (0), 103-112.
36. Pithawalla, Y. B.; Deevi, S. C.; El-Shall, M. S., Preparation of ultrafine and nanocrystalline FeAl powders. *Materials Science and Engineering: A* **2002,** *329–331* (0), 92-98.
37. Pithawalla, Y. B.; El Shall, M. S.; Deevi, S. C., Synthesis and characterization of nanocrystalline iron aluminide particles. *Intermetallics* **2000,** *8* (9–11), 1225-1231.
38. Pithawalla, Y. B.; El-Shall, M. S.; Deevi, S., Laser based synthesis of intermetallic Cu–Zn nanoparticles and filaments. *Scripta Materialia* **2003,** *48* (6), 671-676.
39. Pithawalla, Y. B.; El-Shall, M. S.; Deevi, S. C.; Ström, V.; Rao, K. V., Synthesis of Magnetic Intermetallic FeAl Nanoparticles from a Non-Magnetic Bulk Alloy. *The Journal of Physical Chemistry B* **2001,** *105* (11), 2085-2090.
40. Radwan, N. R. E.; El-Shall, M. S.; Hassan, H. M. A., Synthesis and characterization of nanoparticle Co3O4, CuO and NiO catalysts prepared by physical and chemical methods to minimize air pollution. *Applied Catalysis A: General* **2007,** *331* (0), 8-18.
41. El-Shall, M. S., Laser vaporization for the synthesis of nanoparticles and polymers containing metal particulates. *Applied Surface Science* **1996,** *106* (0), 347-355.
42. Yang, Y.; Saoud, K. M.; Abdelsayed, V.; Glaspell, G.; Deevi, S.; El-Shall, M. S., Vapor phase synthesis of supported Pd, Au, and unsupported bimetallic nanoparticle catalysts for CO oxidation. *Catalysis Communications* **2006,** *7* (5), 281-284.
43. Abraham, F., F, *Homogeneous Nucleation Theory*. New York:Academic: 1974.
44. Zeltlemoyer, A., C, *Nucleation phenomena*. New York :dekker: 1969.
45. Lamer, V. K. D., R.H, Theory, production and mechanism of formation of monodispersed hydrosols. *J Am chem Soc* **1950,** *72*, 4847-4854.
46. Yasuoka, K.; Matsumoto, M., Molecular dynamics of homogeneous nucleation in the vapor phase. I. Lennard-Jones fluid. *Journal of Chemical Physics* **1998,** *109* (19), 8451-8462.
47. Fletcher.N.H, Size Effect in Heterogeneous Nucleation *Chemical Physics Letters* **1958,** *29*, 572.

48. Gorbunov, B., Free energy of embryo formation for heterogeneous multicomponent nucleation. *Journal of Chemical Physics* **1999,** *110* (20), 10035-10045.
49. Steer, B.; Gorbunov, B.; Rowles, J.; Green, D., Surface area controlled heterogeneous nucleation. *Journal of Chemical Physics* **2012,** *136* (5).
50. Hass, J.; de Heer, W. A.; Conrad, E. H., The growth and morphology of epitaxial multilayer graphene. *Journal of Physics-Condensed Matter* **2008,** *20* (32).
51. El-shall, M. S., Heterogeneous Catalysis by Metal nanoparticles Supported on Graphene. In *Graphene, Synthesis, Properties, and Phenomena*, A.K.Soad, C. N. R. R. a., Ed. Wiley-VCH VerlagGmbH&Co.KGaA: 2013; pp 303-338.
52. Lang, B., LEED STUDY OF DEPOSITION OF CARBON ON PLATINUM CRYSTAL-SURFACES. *Surface Science* **1975,** *53* (DEC), 317-329.
53. Novoselov, K. S. G., A. K.Morozov, S. V.Jiang, D.Katsnelson, M. I.Grigorieva, I. V.Dubonos, S. V.Firsov, A. A., Two-dimensional gas of massless Dirac fermions in graphene. *Nature* **2005,** *438* (7065), 197-200.
54. Kim, B.; Sigmund, W. M., Functionalized multiwall carbon nanotube/gold nanoparticle composites. *Langmuir* **2004,** *20* (19), 8239-8242.
55. Wang, X. R.; Tabakman, S. M.; Dai, H. J., Atomic layer deposition of metal oxides on pristine and functionalized graphene. *Journal of the American Chemical Society* **2008,** *130* (26), 8152-+.
56. Seger, B.; Kamat, P. V., Electrocatalytically Active Graphene-Platinum Nanocomposites. Role of 2-D Carbon Support in PEM Fuel Cells. *Journal of Physical Chemistry C* **2009,** *113* (19), 7990-7995.
57. Muszynski, R.; Seger, B.; Kamat, P. V., Decorating graphene sheets with gold nanoparticles. *Journal of Physical Chemistry C* **2008,** *112* (14), 5263-5266.
58. Liu, H. T.; Liu, Y. Q.; Zhu, D. B., Chemical doping of graphene. *Journal of Materials Chemistry* **2011,** *21* (10), 3335-3345.
59. Park, S.; Ruoff, R. S., Chemical methods for the production of graphenes. *Nature Nanotechnology* **2009,** *4* (4), 217-224.
60. Subrahmanyam, K. S. P., L. S.Govindaraj, A.Rao, C. N. R., Simple Method of Preparing Graphene Flakes by an Arc-Discharge Method. *Journal of Physical Chemistry C* **2009,** *113* (11), 4257-4259.
61. Kim, K. S. Z., Y.Jang, H.Lee, S. Y.Kim, J. M.Ahn, J. H.Kim, P.Choi, J. Y.Hong, B. H., Large-scale pattern growth of graphene films for stretchable transparent electrodes. ***Nature*** **2009,** *457* (7230), 706-710.
62. Berger, C. S., Z. M.Li, X. B.Wu, X. S.Brown, N.Naud, C.Mayou, D.Li, T. B.Hass, J.Marchenkov, A. N.Conrad, E. H.First, P. N.de Heer, W. A., Electronic confinement and coherence in patterned epitaxial graphene. *Science* **2006,** *312* (5777), 1191-1196.
63. Abdelsayed, V. M., S.Hassan, H. M.Aluri, H. S.Collinson, M. M.El-Shall, M. S., Photothermal Deoxygenation of Graphite Oxide with Laser Excitation in Solution and Graphene-Aided Increase in Water Temperature. *Journal of Physical Chemistry Letters* **2010,** *1* (19), 2804-2809.
64. Choucair, M.; Thordarson, P.; Stride, J. A., Gram-scale production of graphene based on solvothermal synthesis and sonication. *Nature Nanotechnology* **2009,** *4* (1), 30-33.
65. Stankovich, S. D., D. A.Piner, R. D.Kohlhaas, K. A.Kleinhammes, A.Jia, Y.Wu, Y.Nguyen, S. T.Ruoff, R. S., Synthesis of graphene-based nanosheets via chemical reduction of exfoliated graphite oxide. *Carbon* **2007,** *45* (7), 1558-1565.

66. Tung, V. C. A., M. J.Yang, Y.Kaner, R. B., High-throughput solution processing of large-scale graphene. *Nature Nanotechnology* **2009,** *4* (1), 25-29.
67. Wang, G. X. Y., J.Park, J.Gou, X. L.Wang, B.Liu, H.Yao, J., Facile synthesis and characterization of graphene nanosheets. *Journal of Physical Chemistry C* **2008,** *112* (22), 8192-8195.
68. Si, Y.; Samulski, E. T., Synthesis of water soluble graphene. *Nano Letters* **2008,** *8* (6), 1679-1682.
69. Fan, X. B. P., W. C.Li, Y.Li, X. Y.Wang, S. L.Zhang, G. L.Zhang, F. B., Deoxygenation of Exfoliated Graphite Oxide under Alkaline Conditions: A Green Route to Graphene Preparation. *Advanced Materials* **2008,** *20* (23), 4490-4493.
70. Williams, G.; Seger, B.; Kamat, P. V., TiO2-graphene nanocomposites. UV-assisted photocatalytic reduction of graphene oxide. *Acs Nano* **2008,** *2* (7), 1487-1491.
71. McAllister, M. J. L., J. L.Adamson, D. H.Schniepp, H. C.Abdala, A. A.Liu, J.Herrera-Alonso, M.Milius, D. L.Car, R.Prud'homme, R. K.Aksay, I. A., Single sheet functionalized graphene by oxidation and thermal expansion of graphite. *Chemistry of Materials* **2007,** *19* (18), 4396-4404.
72. Hassan, H. M. A. A., V.Khder, AersAbouZeid, K. M.Terner, J.El-Shall, M. S.Al-Resayes, S. I.El-Azhary, A. A., Microwave synthesis of graphene sheets supporting metal nanocrystals in aqueous and organic media. *Journal of Materials Chemistry* **2009,** *19* (23), 3832-3837.
73. Schniepp, H. C. L., J. L.McAllister, M. J.Sai, H.Herrera-Alonso, M.Adamson, D. H.Prud'homme, R. K.Car, R.Saville, D. A.Aksay, I. A., Functionalized single graphene sheets derived from splitting graphite oxide. *Journal of Physical Chemistry B* **2006,** *110* (17), 8535-8539.
74. Li, X. L. Z., G. Y.Bai, X. D.Sun, X. M.Wang, X. R.Wang, E.Dai, H. J., Highly conducting graphene sheets and Langmuir-Blodgett films. *Nature Nanotechnology* **2008,** *3* (9), 538-542.
75. Fozooni, S.; Tikdari, A. M., Microwave-assisted graphite-support synthesis of imidazolones. *Catalysis Letters* **2008,** *120* (3-4), 303-306.
76. Mattevi, C.; Eda, G.; Agnoli, S.; Miller, S.; Mkhoyan, K. A.; Celik, O.; Mostrogiovanni, D.; Granozzi, G.; Garfunkel, E.; Chhowalla, M., Evolution of Electrical, Chemical, and Structural Properties of Transparent and Conducting Chemically Derived Graphene Thin Films. *Advanced Functional Materials* **2009,** *19* (16), 2577-2583.
77. Cote, L. J.; Cruz-Silva, R.; Huang, J. X., Flash Reduction and Patterning of Graphite Oxide and Its Polymer Composite. *Journal of the American Chemical Society* **2009,** *131* (31), 11027-11032.
78. Lee, S. W.; Mattevi, C.; Chhowalla, M.; Sankaran, R. M., Plasma-Assisted Reduction of Graphene Oxide at Low Temperature and Atmospheric Pressure for Flexible Conductor Applications. *Journal of Physical Chemistry Letters* **2012,** *3* (6), 772-777.
79. Qian, M.; Zhou, Y. S.; Gao, Y.; Park, J. B.; Feng, T.; Huang, S. M.; Sun, Z.; Jiang, L.; Lu, Y. F., Formation of graphene sheets through laser exfoliation of highly ordered pyrolytic graphite. *Applied Physics Letters* **2011,** *98* (17).
80. Hummers, W. S.; Offeman, R. E., Preparation of Graphitic Oxide. *Journal of the American Chemical Society* **1958,** *80* (6), 1339-1339.

81. Dervishi, E.; Li, Z. R.; Watanabe, F.; Biswas, A.; Xu, Y.; Biris, A. R.; Saini, V.; Biris, A. S., Large-scale graphene production by RF-cCVD method. *Chemical Communications* **2009,** (27), 4061-4063.
82. Ei-Shobaky, G. A.; Radwan, N. R. E.; Ei-Shall, M. S.; Turky, A. M.; Hassan, H. M. A., Synthesis and characterization of pure and ZrO2-doped nanocrystalline CuO-NiO system. *Applied Surface Science* **2008,** *254* (6), 1651-1660.
83. Chang, L. H.; Sasirekha, N.; Rajesh, B.; Chen, Y. W., CO oxidation on ceria- and manganese oxide-supported gold catalysts. *Separation and Purification Technology* **2007,** *58* (1), 211-218.
84. Lipshutz, B. H.; Sclafani, J. A.; Blomgren, P. A., Biaryls via Suzuki cross-couplings catalyzed by nickel on charcoal. *Tetrahedron* **2000,** *56* (15), 2139-2144.
85. Li, Y.; Fan, X. B.; Qi, J. J.; Ji, J. Y.; Wang, S. L.; Zhang, G. L.; Zhang, F. B., Palladium nanoparticle-graphene hybrids as active catalysts for the Suzuki reaction. *Nano Research* **2010,** *3* (6), 429-437.
86. Li, Y.; Fan, X. B.; Qi, J. J.; Ji, J. Y.; Wang, S. L.; Zhang, G. L.; Zhang, F. B., Gold nanoparticles-graphene hybrids as active catalysts for Suzuki reaction. *Materials Research Bulletin* **2010,** *45* (10), 1413-1418.
87. Deschamps, B.; Le Goff, X.; Ricard, L.; Le Floch, P., Phosphaalkenes palladium(II) complexes in the Suzuki and Sonogashira cross-coupling reactions. *Heteroatom Chemistry* **2007,** *18* (4), 363-371.
88. Tschope, A.; Liu, W.; Flytzani-Stephanopoulos, M.; Ying, J. Y., REDOX ACTIVITY OF NONSTOICHIOMETRIC CERIUM OXIDE-BASED NANOCRYSTALLINE CATALYSTS. *Journal of Catalysis* **1995,** *157* (1), 42-50.
89. Varon, J.; Marik, P. E.; Fromm, R. E.; Gueler, A., Carbon monoxide poisoning: A review for clinicians. *Journal of Emergency Medicine* **1999,** *17* (1), 87-93.
90. Sanchez, R. M. T.; Ueda, A.; Tanaka, K.; Haruta, M., Selective oxidation of CO in hydrogen over gold supported on manganese oxides. *Journal of Catalysis* **1997,** *168* (1), 125-127.
91. Bunluesin, T.; Gorte, R. J.; Graham, G. W., Studies of the water-gas-shift reaction on ceria-supported Pt, Pd, and Rh: implications for oxygen-storage properties. *Applied Catalysis B-Environmental* **1998,** *15* (1-2), 107-114.
92. Venezia, A. M.; Pantaleo, G.; Longo, A.; Di Carlo, G.; Casaletto, M. P.; Liotta, F. L.; Deganello, G., Relationship between structure and CO oxidation activity of ceria-supported gold catalysts. *Journal of Physical Chemistry B* **2005,** *109* (7), 2821-2827.
93. Shen, Y. N.; Yang, X. Z.; Wang, Y. Z.; Zhang, Y. B.; Zhu, H. Y.; Gao, L.; Jia, M. L., The states of gold species in CeO2 supported gold catalyst for formaldehyde oxidation. *Applied Catalysis B-Environmental* **2008,** *79* (2), 142-148.
94. Miao, S. D.; Liu, Z. M.; Miao, Z. J.; Han, B. X.; Ding, K. L.; An, G. M.; Xie, Y., Ionic liquid-mediated synthesis of crystalline CeO2 mesoporous films and their application in aerobic oxidation of benzyl alcohol. *Microporous and Mesoporous Materials* **2009,** *117* (1-2), 386-390.
95. Huang, X. S.; Sun, H.; Wang, L. C.; Liu, Y. M.; Fan, K. N.; Cao, Y., Morphology effects of nanoscale ceria on the activity of Au/CeO2 catalysts for low-temperature CO oxidation. *Applied Catalysis B-Environmental* **2009,** *90* (1-2), 224-232.
96. Pan, Y. H.; Gao, Y.; Kong, D. D.; Wang, G. D.; Hou, J. B.; Hu, S. W.; Pan, H. B.; Zhu, J. F., Interaction of Au with Thin ZrO2 Films: Influence of ZrO2 Morphology on the

Adsorption and Thermal Stability of Au Nanoparticles. *Langmuir* **2012,** *28* (14), 6045-6051.
97. Aslan, K.; Perez-Luna, V. H., Surface modification of colloidal gold by chemisorption of alkanethiols in the presence of a nonionic surfactant. *Langmuir* **2002,** *18* (16), 6059-6065.
98. Mayya, K. S.; Patil, V.; Sastry, M., On the stability of carboxylic acid derivatized gold colloidal particles: The role of colloidal solution pH studied by optical absorption spectroscopy. *Langmuir* **1997,** *13* (15), 3944-3947.
99. Karwacki, C. J.; Ganesh, P.; Kent, P. R. C.; Gordon, W. O.; Peterson, G. W.; Niu, J. J.; Gogotsi, Y., Structure-activity relationship of Au/ZrO2 catalyst on formation of hydroxyl groups and its influence on CO oxidation. *Journal of Materials Chemistry A* **2013,** *1* (19), 6051-6062.
100. Radnik, R.; Mohr, C.; Claus, P., On the origin of binding energy shifts of core levels of supported gold nanoparticles and dependence of pretreatment and material synthesis. *Physical Chemistry Chemical Physics* **2003,** *5* (1), 172-177.
101. Epling, W. S.; Hoflund, G. B.; Weaver, J. F.; Tsubota, S.; Haruta, M., Surface characterization study of Au/alpha-Fe2O3 and Au/Co3O4 low-temperature CO oxidation catalysts. *Journal of Physical Chemistry* **1996,** *100* (23), 9929-9934.
102. Ying, J. Y.; Tschope, A., Synthesis and characteristics of non-stoichiometric nanocrystalline cerium oxide-based catalysts. *Chemical Engineering Journal* **1996,** *64* (2), 225-237.
103. Kuzmenko, A. B.; van Heumen, E.; Carbone, F.; van der Marel, D., Universal optical conductance of graphite. *Physical Review Letters* **2008,** *100* (11).
104. Novoselov, K. S.; Geim, A. K.; Morozov, S. V.; Jiang, D.; Zhang, Y.; Dubonos, S. V.; Grigorieva, I. V.; Firsov, A. A., Electric field effect in atomically thin carbon films. *Science* **2004,** *306* (5696), 666-669.
105. Geim, A. K.; Novoselov, K. S., The rise of graphene. *Nature Materials* **2007,** *6* (3), 183-191.
106. Han, M. Y.; Ozyilmaz, B.; Zhang, Y. B.; Kim, P., Energy band-gap engineering of graphene nanoribbons. *Physical Review Letters* **2007,** *98* (20).
107. Lee, C.; Wei, X. D.; Kysar, J. W.; Hone, J., Measurement of the elastic properties and intrinsic strength of monolayer graphene. *Science* **2008,** *321* (5887), 385-388.
108. Balandin, A. A.; Ghosh, S.; Bao, W. Z.; Calizo, I.; Teweldebrhan, D.; Miao, F.; Lau, C. N., Superior thermal conductivity of single-layer graphene. *Nano Letters* **2008,** *8* (3), 902-907.
109. Chen, J. H.; Jang, C.; Xiao, S. D.; Ishigami, M.; Fuhrer, M. S., Intrinsic and extrinsic performance limits of graphene devices on SiO2. *Nature Nanotechnology* **2008,** *3* (4), 206-209.
110. Stoller, M. D.; Park, S. J.; Zhu, Y. W.; An, J. H.; Ruoff, R. S., Graphene-Based Ultracapacitors. *Nano Letters* **2008,** *8* (10), 3498-3502.
111. Novoselov, K. S.; Jiang, D.; Schedin, F.; Booth, T. J.; Khotkevich, V. V.; Morozov, S. V.; Geim, A. K., Two-dimensional atomic crystals. *Proceedings of the National Academy of Sciences of the United States of America* **2005,** *102* (30), 10451-10453.
112. Ramanathan, T.; Abdala, A. A.; Stankovich, S.; Dikin, D. A.; Herrera-Alonso, M.; Piner, R. D.; Adamson, D. H.; Schniepp, H. C.; Chen, X.; Ruoff, R. S.; Nguyen, S. T.; Aksay, I. A.; Prud'homme, R. K.; Brinson, L. C., Functionalized graphene sheets for polymer nanocomposites. *Nature Nanotechnology* **2008,** *3* (6), 327-331.

113. Wang, Y.; Shi, Z. Q.; Huang, Y.; Ma, Y. F.; Wang, C. Y.; Chen, M. M.; Chen, Y. S., Supercapacitor Devices Based on Graphene Materials. *Journal of Physical Chemistry C* **2009,** *113* (30), 13103-13107.
114. Yoo, E.; Kim, J.; Hosono, E.; Zhou, H.; Kudo, T.; Honma, I., Large reversible Li storage of graphene nanosheet families for use in rechargeable lithium ion batteries. *Nano Letters* **2008,** *8* (8), 2277-2282.
115. Wang, X.; Zhi, L. J.; Tsao, N.; Tomovic, Z.; Li, J. L.; Mullen, K., Transparent carbon films as electrodes in organic solar cells. *Angewandte Chemie-International Edition* **2008,** *47* (16), 2990-2992.
116. Kamat, P. V., Graphene-Based Nanoarchitectures. Anchoring Semiconductor and Metal Nanoparticles on a Two-Dimensional Carbon Support. *The Journal of Physical Chemistry Letters* **2009,** *1* (2), 520-527.
117. Gierz, I.; Riedl, C.; Starke, U.; Ast, C. R.; Kern, K., Atomic Hole Doping of Graphene. *Nano Letters* **2008,** *8* (12), 4603-4607.
118. Maier, F.; Riedel, M.; Mantel, B.; Ristein, J.; Ley, L., Origin of surface conductivity in diamond. *Physical Review Letters* **2000,** *85* (16), 3472-3475.
119. Stankovich, S.; Dikin, D. A.; Piner, R. D.; Kohlhaas, K. A.; Kleinhammes, A.; Jia, Y.; Wu, Y.; Nguyen, S. T.; Ruoff, R. S., Synthesis of graphene-based nanosheets via chemical reduction of exfoliated graphite oxide. *Carbon* **2007,** *45* (7), 1558-1565.
120. Moussa, S.; Siamaki, A. R.; Gupton, B. F.; El-Shall, M. S., Pd-Partially Reduced Graphene Oxide Catalysts (Pd/PRGO): Laser Synthesis of Pd Nanoparticles Supported on PRGO Nanosheets for Carbon–Carbon Cross Coupling Reactions. *Acs Catalysis* **2011,** *2* (1), 145-154.
121. Siamaki, A. R.; Khder, A. E. R. S.; Abdelsayed, V.; El-Shall, M. S.; Gupton, B. F., Microwave-assisted synthesis of palladium nanoparticles supported on graphene: A highly active and recyclable catalyst for carbon–carbon cross-coupling reactions. *Journal of Catalysis* **2011,** *279* (1), 1-11.
122. Abdelsayed, V.; Aljarash, A.; El-Shall, M. S.; Al Othman, Z. A.; Alghamdi, A. H., Microwave Synthesis of Bimetallic Nanoalloys and CO Oxidation on Ceria-Supported Nanoalloys. *Chemistry of Materials* **2009,** *21* (13), 2825-2834.
123. Afshani, P.; Attah, I.; Moussa, S.; Terner, J.; El-Shall, M. S., Hydrogen-Terminated Graphene by Laser Vaporization-Controlled Condensation of Graphite Oxide. Observation of Hydrogen-Capped Carbon Chains CnH–, CnH+, and CnH2+ (n = 2–30) in the Gas Phase. *The Journal of Physical Chemistry C* **2013,** *117* (18), 9485-9495.
124. Sokolov, D. A.; Shepperd, K. R.; Orlando, T. M., Formation of Graphene Features from Direct Laser-Induced Reduction of Graphite Oxide. *Journal of Physical Chemistry Letters* **2010,** *1* (18), 2633-2636.
125. Dresselhaus, M. S.; Jorio, A.; Hofmann, M.; Dresselhaus, G.; Saito, R., Perspectives on Carbon Nanotubes and Graphene Raman Spectroscopy. *Nano Letters* **2010,** *10* (3), 751-758.
126. Ferrari, A. C., Raman spectroscopy of graphene and graphite: Disorder, electron-phonon coupling, doping and nonadiabatic effects. *Solid State Communications* **2007,** *143* (1-2), 47-57.
127. Chen, W. F.; Yan, L. F.; Bangal, P. R., Preparation of graphene by the rapid and mild thermal reduction of graphene oxide induced by microwaves. *Carbon* **2010,** *48* (4), 1146-1152.

128. Shen, J. F.; Shi, M.; Li, N.; Yan, B.; Ma, H. W.; Hu, Y. Z.; Ye, M. X., Facile Synthesis and Application of Ag-Chemically Converted Graphene Nanocomposite. *Nano Research* **2010,** *3* (5), 339-349.
129. Li, Z.; Yao, Y. G.; Lin, Z. Y.; Moon, K. S.; Lin, W.; Wong, C. P., Ultrafast, dry microwave synthesis of graphene sheets. *Journal of Materials Chemistry* **2010,** *20* (23), 4781-4783.
130. Wang, H. B.; Maiyalagan, T.; Wang, X., Review on Recent Progress in Nitrogen-Doped Graphene: Synthesis, Characterization, and Its Potential Applications. *Acs Catalysis* **2012,** *2* (5), 781-794.
131. Shiraishi, S.; Kibe, M.; Yokoyama, T.; Kurihara, H.; Patel, N.; Oya, A.; Kaburagi, Y.; Hishiyama, Y., Electric double layer capacitance of multi-walled carbon nanotubes and B-doping effect. *Applied Physics a-Materials Science & Processing* **2006,** *82* (4), 585-591.
132. Yi, J. Y.; Bernholc, J., ATOMIC-STRUCTURE AND DOPING OF MICROTUBULES. *Physical Review B* **1993,** *47* (3), 1708-1711.
133. Miwa, R. H.; Martins, T. B.; Fazzio, A., Hydrogen adsorption on boron doped graphene: an ab initio study. *Nanotechnology* **2008,** *19* (15).
134. Wu, Z. S.; Winter, A.; Chen, L.; Sun, Y.; Turchanin, A.; Feng, X. L.; Mullen, K., Three-Dimensional Nitrogen and Boron Co-doped Graphene for High-Performance All-Solid-State Supercapacitors. *Advanced Materials* **2012,** *24* (37), 5130-5135.
135. Wang, X. R.; Li, X. L.; Zhang, L.; Yoon, Y.; Weber, P. K.; Wang, H. L.; Guo, J.; Dai, H. J., N-Doping of Graphene Through Electrothermal Reactions with Ammonia. *Science* **2009,** *324* (5928), 768-771.
136. Kang, H. S.; Jeong, S., Nitrogen doping and chirality of carbon nanotubes. *Physical Review B* **2004,** *70* (23).
137. Wang, S. Y.; Iyyamperumal, E.; Roy, A.; Xue, Y. H.; Yu, D. S.; Dai, L. M., Vertically Aligned BCN Nanotubes as Efficient Metal-Free Electrocatalysts for the Oxygen Reduction Reaction: A Synergetic Effect by Co-Doping with Boron and Nitrogen. *Angewandte Chemie-International Edition* **2011,** *50* (49), 11756-11760.
138. Li, X. L.; Wang, H. L.; Robinson, J. T.; Sanchez, H.; Diankov, G.; Dai, H. J., Simultaneous Nitrogen Doping and Reduction of Graphene Oxide. *Journal of the American Chemical Society* **2009,** *131* (43), 15939-15944.
139. Sheng, Z. H.; Shao, L.; Chen, J. J.; Bao, W. J.; Wang, F. B.; Xia, X. H., Catalyst-Free Synthesis of Nitrogen-Doped Graphene via Thermal Annealing Graphite Oxide with Melamine and Its Excellent Electrocatalysis. *Acs Nano* **2011,** *5* (6), 4350-4358.
140. Luo, Z. Q.; Lim, S. H.; Tian, Z. Q.; Shang, J. Z.; Lai, L. F.; MacDonald, B.; Fu, C.; Shen, Z. X.; Yu, T.; Lin, J. Y., Pyridinic N doped graphene: synthesis, electronic structure, and electrocatalytic property. *Journal of Materials Chemistry* **2011,** *21* (22), 8038-8044.
141. Lin, T. Q.; Huang, F. Q.; Liang, J.; Wang, Y. X., A facile preparation route for boron-doped graphene, and its CdTe solar cell application. *Energy & Environmental Science* **2011,** *4* (3), 862-865.
142. Wu, T. R.; Shen, H. L.; Sun, L.; Cheng, B.; Liu, B.; Shen, J. C., Nitrogen and boron doped monolayer graphene by chemical vapor deposition using polystyrene, urea and boric acid. *New Journal of Chemistry* **2012,** *36* (6), 1385-1391.

143. Sheng, Z. H.; Gao, H. L.; Bao, W. J.; Wang, F. B.; Xia, X. H., Synthesis of boron doped graphene for oxygen reduction reaction in fuel cells. *Journal of Materials Chemistry* **2012,** *22* (2), 390-395.
144. Qu, L. T.; Liu, Y.; Baek, J. B.; Dai, L. M., Nitrogen-Doped Graphene as Efficient Metal-Free Electrocatalyst for Oxygen Reduction in Fuel Cells. *Acs Nano* **2010,** *4* (3), 1321-1326.
145. Wang, S. Y.; Zhang, L. P.; Xia, Z. H.; Roy, A.; Chang, D. W.; Baek, J. B.; Dai, L. M., BCN Graphene as Efficient Metal-Free Electrocatalyst for the Oxygen Reduction Reaction. *Angewandte Chemie-International Edition* **2012,** *51* (17), 4209-4212.
146. Zheng, Y.; Jiao, Y.; Ge, L.; Jaroniec, M.; Qiao, S. Z., Two-Step Boron and Nitrogen Doping in Graphene for Enhanced Synergistic Catalysis. *Angewandte Chemie-International Edition* **2013,** *52* (11), 3110-3116.
147. Reddy, A. L. M.; Srivastava, A.; Gowda, S. R.; Gullapalli, H.; Dubey, M.; Ajayan, P. M., Synthesis Of Nitrogen-Doped Graphene Films For Lithium Battery Application. *Acs Nano* **2010,** *4* (11), 6337-6342.
148. Panchokarla, L. S.; Subrahmanyam, K. S.; Saha, S. K.; Govindaraj, A.; Krishnamurthy, H. R.; Waghmare, U. V.; Rao, C. N. R., Synthesis, Structure, and Properties of Boron- and Nitrogen-Doped Graphene. *Advanced Materials* **2009,** *21* (46), 4726-+.
149. Das, A.; Pisana, S.; Chakraborty, B.; Piscanec, S.; Saha, S. K.; Waghmare, U. V.; Novoselov, K. S.; Krishnamurthy, H. R.; Geim, A. K.; Ferrari, A. C.; Sood, A. K., Monitoring dopants by Raman scattering in an electrochemically top-gated graphene transistor. *Nature Nanotechnology* **2008,** *3* (4), 210-215.
150. Graf, D.; Molitor, F.; Ensslin, K.; Stampfer, C.; Jungen, A.; Hierold, C.; Wirtz, L., Spatially resolved raman spectroscopy of single- and few-layer graphene. *Nano Letters* **2007,** *7* (2), 238-242.
151. Guo, B. D.; Liu, Q. A.; Chen, E. D.; Zhu, H. W.; Fang, L. A.; Gong, J. R., Controllable N-Doping of Graphene. *Nano Letters* **2010,** *10* (12), 4975-4980.
152. Seredych, M.; Bandosz, T. J., Combined Role of Water and Surface Chemistry in Reactive Adsorption of Ammonia on Graphite Oxides. *Langmuir* **2010,** *26* (8), 5491-5498.
153. Seredych, M.; Bandosz, T. J., Mechanism of ammonia retention on graphite oxides: Role of surface chemistry and structure. *Journal of Physical Chemistry C* **2007,** *111* (43), 15596-15604.
154. Chen, C. M.; Zhang, Q.; Zhao, X. C.; Zhang, B. S.; Kong, Q. Q.; Yang, M. G.; Yang, Q. H.; Wang, M. Z.; Yang, Y. G.; Schlogl, R.; Su, D. S., Hierarchically aminated graphene honeycombs for electrochemical capacitive energy storage. *Journal of Materials Chemistry* **2012,** *22* (28), 14076-14084.
155. Han, J.; Zhang, L. L.; Lee, S.; Oh, J.; Lee, K. S.; Potts, J. R.; Ji, J. Y.; Zhao, X.; Ruoff, R. S.; Park, S., Generation of B-Doped Graphene Nanoplatelets Using a Solution Process and Their Supercapacitor Applications. *Acs Nano* **2013,** *7* (1), 19-26.
156. Wang, Y.; Shao, Y. Y.; Matson, D. W.; Li, J. H.; Lin, Y. H., Nitrogen-Doped Graphene and Its Application in Electrochemical Biosensing. *Acs Nano* **2010,** *4* (4), 1790-1798.
157. Wang, W. L.; Bai, X. D.; Liu, K. H.; Xu, Z.; Golberg, D.; Bando, Y.; Wang, E. G., Direct synthesis of B-C-N single-walled nanotubes by bias-assisted hot filament chemical vapor deposition. *Journal of the American Chemical Society* **2006,** *128* (20), 6530-6531.

158. Yu, L.; Pan, X. L.; Cao, X. M.; Hu, P.; Bao, X. H., Oxygen reduction reaction mechanism on nitrogen-doped graphene: A density functional theory study. *Journal of Catalysis* **2011,** *282* (1), 183-190.
159. Zhang, L. P.; Xia, Z. H., Mechanisms of Oxygen Reduction Reaction on Nitrogen-Doped Graphene for Fuel Cells. *Journal of Physical Chemistry C* **2011,** *115* (22), 11170-11176.
160. Lai, L. F.; Potts, J. R.; Zhan, D.; Wang, L.; Poh, C. K.; Tang, C. H.; Gong, H.; Shen, Z. X.; Jianyi, L. Y.; Ruoff, R. S., Exploration of the active center structure of nitrogen-doped graphene-based catalysts for oxygen reduction reaction. *Energy & Environmental Science* **2012,** *5* (7), 7936-7942.
161. Wang, P.; Wang, Z. K.; Jia, L. X.; Xiao, Z. L., Origin of the catalytic activity of graphite nitride for the electrochemical reduction of oxygen: geometric factors vs. electronic factors. *Physical Chemistry Chemical Physics* **2009,** *11* (15), 2730-2740.
162. Xu, C.; Wang, X.; Zhu, J. W., Graphene-Metal Particle Nanocomposites. *Journal of Physical Chemistry C* **2008,** *112* (50), 19841-19845.
163. Dey, R. S.; Raj, C. R., Development of an Amperometric Cholesterol Biosensor Based on Graphene-Pt Nanoparticle Hybrid Material. *Journal of Physical Chemistry C* **2010,** *114* (49), 21427-21433.
164. Kong, B. S.; Geng, J. X.; Jung, H. T., Layer-by-layer assembly of graphene and gold nanoparticles by vacuum filtration and spontaneous reduction of gold ions. *Chemical Communications* **2009,** (16), 2174-2176.
165. Wang, H. L.; Casalongue, H. S.; Liang, Y. Y.; Dai, H. J., Ni(OH)(2) Nanoplates Grown on Graphene as Advanced Electrochemical Pseudocapacitor Materials. *Journal of the American Chemical Society* **2010,** *132* (21), 7472-7477.
166. Singh, A. K.; Ribas, M. A.; Yakobson, B. I., H-Spillover through the Catalyst Saturation: An Ab Initio Thermodynamics Study. *Acs Nano* **2009,** *3* (7), 1657-1662.
167. Goncalves, G.; Marques, P.; Granadeiro, C. M.; Nogueira, H. I. S.; Singh, M. K.; Gracio, J., Surface Modification of Graphene Nanosheets with Gold Nanoparticles: The Role of Oxygen Moieties at Graphene Surface on Gold Nucleation and Growth. *Chemistry of Materials* **2009,** *21* (20), 4796-4802.
168. Xu, C.; Wang, X., Fabrication of Flexible Metal-Nanoparticte Film Using Graphene Oxide Sheets as Substrates. *Small* **2009,** *5* (19), 2212-2217.
169. Pasricha, R.; Gupta, S.; Srivastava, A. K., A Facile and Novel Synthesis of Ag-Graphene-Based Nanocomposites. *Small* **2009,** *5* (20), 2253-2259.
170. Si, Y. C.; Samulski, E. T., Exfoliated Graphene Separated by Platinum Nanoparticles. *Chemistry of Materials* **2008,** *20* (21), 6792-6797.
171. Bian, J.; Xiao, M.; Wang, S. J.; Lu, Y. X.; Meng, Y. Z., Graphite oxide as a novel host material of catalytically active Cu-Ni bimetallic nanoparticles. *Catalysis Communications* **2009,** *10* (11), 1529-1533.
172. Luechinger, N. A.; Athanassiou, E. K.; Stark, W. J., Graphene-stabilized copper nanoparticles as an air-stable substitute for silver and gold in low-cost ink-jet printable electronics. *Nanotechnology* **2008,** *19* (44).
173. Scheuermann, G. M.; Rumi, L.; Steurer, P.; Bannwarth, W.; Mulhaupt, R., Palladium Nanoparticles on Graphite Oxide and Its Functionalized Graphene Derivatives as Highly Active Catalysts for the Suzuki-Miyaura Coupling Reaction. *Journal of the American Chemical Society* **2009,** *131* (23), 8262-8270.

174. Erickson, K.; Erni, R.; Lee, Z.; Alem, N.; Gannett, W.; Zettl, A., Determination of the Local Chemical Structure of Graphene Oxide and Reduced Graphene Oxide. *Advanced Materials* **2010,** *22* (40), 4467-4472.
175. Jafri, R. I.; Rajalakshmi, N.; Ramaprabhu, S., Nitrogen doped graphene nanoplatelets as catalyst support for oxygen reduction reaction in proton exchange membrane fuel cell. *Journal of Materials Chemistry* **2010,** *20* (34), 7114-7117.
176. Yoo, E.; Okata, T.; Akita, T.; Kohyama, M.; Nakamura, J.; Honma, I., Enhanced Electrocatalytic Activity of Pt Subnanoclusters on Graphene Nanosheet Surface. *Nano Letters* **2009,** *9* (6), 2255-2259.
177. Kamat, P. V., Graphene-Based Nanoarchitectures. Anchoring Semiconductor and Metal Nanoparticles on a Two-Dimensional Carbon Support. *Journal of Physical Chemistry Letters* **2010,** *1* (2), 520-527.
178. Lightcap, I. V.; Kosel, T. H.; Kamat, P. V., Anchoring Semiconductor and Metal Nanoparticles on a Two-Dimensional Catalyst Mat. Storing and Shuttling Electrons with Reduced Graphene Oxide. *Nano Letters* **2010,** *10* (2), 577-583.
179. Shang, N. G.; Papakonstantinou, P.; Wang, P.; Ravi, S.; Silva, P., Platinum Integrated Graphene for Methanol Fuel Cells. *Journal of Physical Chemistry C* **2010,** *114* (37), 15837-15841.
180. Nie, R. F.; Wang, J. H.; Wang, L. N.; Qin, Y.; Chen, P.; Hou, Z. Y., Platinum supported on reduced graphene oxide as a catalyst for hydrogenation of nitroarenes. *Carbon* **2012,** *50* (2), 586-596.
181. Hassan, H. M. A.; Abdelsayed, V.; Khder, A.; AbouZeid, K. M.; Terner, J.; El-Shall, M. S.; Al-Resayes, S. I.; El-Azhary, A. A., Microwave synthesis of graphene sheets supporting metal nanocrystals in aqueous and organic media. *Journal of Materials Chemistry* **2009,** *19* (23), 3832-3837.
182. Moon, G. H.; Park, Y.; Kim, W.; Choi, W., Photochemical loading of metal nanoparticles on reduced graphene oxide sheets using phosphotungstate. *Carbon* **2011,** *49* (11), 3454-3462.
183. He, D. P.; Cheng, K.; Peng, T.; Sun, X. L.; Pan, M.; Mu, S. C., Bifunctional effect of reduced graphene oxides to support active metal nanoparticles for oxygen reduction reaction and stability. *Journal of Materials Chemistry* **2012,** *22* (39), 21298-21304.
184. Wang, Y. Y.; Ni, Z. H.; Hu, H. L.; Hao, Y. F.; Wong, C. P.; Yu, T.; Thong, J. T. L.; Shen, Z. X., Gold on graphene as a substrate for surface enhanced Raman scattering study. *Applied Physics Letters* **2010,** *97* (16).
185. Bong, S.; Uhm, S.; Kim, Y. R.; Lee, J.; Kim, H., Graphene Supported Pd Electrocatalysts for Formic Acid Oxidation. *Electrocatalysis* **2010,** *1* (2-3), 139-143.
186. Pi, K.; McCreary, K. M.; Bao, W.; Han, W.; Chiang, Y. F.; Li, Y.; Tsai, S. W.; Lau, C. N.; Kawakami, R. K., Electronic doping and scattering by transition metals on graphene. *Physical Review B* **2009,** *80* (7).
187. Li, J.; Liu, C.-y., Ag/Graphene Heterostructures: Synthesis, Characterization and Optical Properties. *European Journal of Inorganic Chemistry* **2010,** *2010* (8), 1244-1248.
188. Li, F. H.; Song, J. F.; Yang, H. F.; Gan, S. Y.; Zhang, Q. X.; Han, D. X.; Ivaska, A.; Niu, L., One-step synthesis of graphene/SnO2 nanocomposites and its application in electrochemical supercapacitors. *Nanotechnology* **2009,** *20* (45).
189. Baker, S. N.; Baker, G. A., Luminescent Carbon Nanodots: Emergent Nanolights. *Angewandte Chemie-International Edition* **2010,** *49* (38), 6726-6744.

190. Shen, J. H.; Zhu, Y. H.; Chen, C.; Yang, X. L.; Li, C. Z., Facile preparation and upconversion luminescence of graphene quantum dots. *Chemical Communications* **2011,** *47* (9), 2580-2582.
191. Kamat, P. V., Quantum Dot Solar Cells. Semiconductor Nanocrystals as Light Harvesters. *Journal of Physical Chemistry C* **2008,** *112* (48), 18737-18753.
192. Gupta, V.; Chaudhary, N.; Srivastava, R.; Sharma, G. D.; Bhardwaj, R.; Chand, S., Luminscent Graphene Quantum Dots for Organic Photovoltaic Devices. *Journal of the American Chemical Society* **2011,** *133* (26), 9960-9963.
193. Dong, Y. Q.; Chen, C. Q.; Zheng, X. T.; Gao, L. L.; Cui, Z. M.; Yang, H. B.; Guo, C. X.; Chi, Y. W.; Li, C. M., One-step and high yield simultaneous preparation of single- and multi-layer graphene quantum dots from CX-72 carbon black. *Journal of Materials Chemistry* **2012,** *22* (18), 8764-8766.
194. Li, Y.; Zhao, Y.; Cheng, H. H.; Hu, Y.; Shi, G. Q.; Dai, L. M.; Qu, L. T., Nitrogen-Doped Graphene Quantum Dots with Oxygen-Rich Functional Groups. *Journal of the American Chemical Society* **2012,** *134* (1), 15-18.
195. Zhuo, S. J.; Shao, M. W.; Lee, S. T., Upconversion and Downconversion Fluorescent Graphene Quantum Dots: Ultrasonic Preparation and Photocatalysis. *Acs Nano* **2012,** *6* (2), 1059-1064.
196. Ponomarenko, L. A.; Schedin, F.; Katsnelson, M. I.; Yang, R.; Hill, E. W.; Novoselov, K. S.; Geim, A. K., Chaotic dirac billiard in graphene quantum dots. *Science* **2008,** *320* (5874), 356-358.
197. Pan, D. Y.; Zhang, J. C.; Li, Z.; Wu, M. H., Hydrothermal Route for Cutting Graphene Sheets into Blue-Luminescent Graphene Quantum Dots. *Advanced Materials* **2010,** *22* (6), 734.
198. Liu, R. L.; Wu, D. Q.; Feng, X. L.; Mullen, K., Bottom-Up Fabrication of Photoluminescent Graphene Quantum Dots with Uniform Morphology. *Journal of the American Chemical Society* **2011,** *133* (39), 15221-15223.
199. Mohanty, N.; Moore, D.; Xu, Z. P.; Sreeprasad, T. S.; Nagaraja, A.; Rodriguez, A. A.; Berry, V., Nanotomy-based production of transferable and dispersible graphene nanostructures of controlled shape and size. *Nature Communications* **2012,** *3*.
200. Zhou, K. F.; Zhu, Y. H.; Yang, X. L.; Jiang, X.; Li, C. Z., Preparation of graphene-TiO2 composites with enhanced photocatalytic activity. *New Journal of Chemistry* **2011,** *35* (2), 353-359.
201. Lu, J.; Yeo, P. S. E.; Gan, C. K.; Wu, P.; Loh, K. P., Transforming C-60 molecules into graphene quantum dots. *Nature Nanotechnology* **2011,** *6* (4), 247-252.
202. Qian, Z. S.; Zhou, J.; Chen, J. R.; Wang, C.; Chen, C. C.; Feng, H., Nanosized N-doped graphene oxide with visible fluorescence in water for metal ion sensing. *Journal of Materials Chemistry* **2011,** *21* (44), 17635-17637.
203. Li, M.; Wu, W. B.; Ren, W. C.; Cheng, H. M.; Tang, N. J.; Zhong, W.; Du, Y. W., Synthesis and upconversion luminescence of N-doped graphene quantum dots. *Applied Physics Letters* **2012,** *101* (10).
204. ElShall, M. S.; Li, S. T., *Synthesis of nanoparticles by a laser vaporization - Controlled condensation technique*. 1997; Vol. 3123, p 98-109.
205. Zhou, Y.; Bao, Q. L.; Tang, L. A. L.; Zhong, Y. L.; Loh, K. P., Hydrothermal Dehydration for the "Green" Reduction of Exfoliated Graphene Oxide to Graphene and

Demonstration of Tunable Optical Limiting Properties. *Chemistry of Materials* **2009,** *21* (13), 2950-2956.
206. Zhu, S. J.; Tang, S. J.; Zhang, J. H.; Yang, B., Control the size and surface chemistry of graphene for the rising fluorescent materials. *Chemical Communications* **2012,** *48* (38), 4527-4539.
207. Pan, D. Y.; Guo, L.; Zhang, J. C.; Xi, C.; Xue, Q.; Huang, H.; Li, J. H.; Zhang, Z. W.; Yu, W. J.; Chen, Z. W.; Li, Z.; Wu, M. H., Cutting sp(2) clusters in graphene sheets into colloidal graphene quantum dots with strong green fluorescence. *Journal of Materials Chemistry* **2012,** *22* (8), 3314-3318.
208. Tang, L. B.; Ji, R. B.; Cao, X. K.; Lin, J. Y.; Jiang, H. X.; Li, X. M.; Teng, K. S.; Luk, C. M.; Zeng, S. J.; Hao, J. H.; Lau, S. P., Deep Ultraviolet Photoluminescence of Water-Soluble Self-Passivated Graphene Quantum Dots. *Acs Nano* **2012,** *6* (6), 5102-5110.
209. Cao, L.; Meziani, M. J.; Sahu, S.; Sun, Y. P., Photoluminescence Properties of Graphene versus Other Carbon Nanomaterials. *Accounts of Chemical Research* **2013,** *46* (1), 171-180.
210. Shen, J. H.; Zhu, Y. H.; Yang, X. L.; Li, C. Z., Graphene quantum dots: emergent nanolights for bioimaging, sensors, catalysis and photovoltaic devices. *Chemical Communications* **2012,** *48* (31), 3686-3699.
211. Li, Q. Q.; Zhang, S.; Dai, L. M.; Li, L. S., Nitrogen-Doped Colloidal Graphene Quantum Dots and Their Size-Dependent Electrocatalytic Activity for the Oxygen Reduction Reaction. *Journal of the American Chemical Society* **2012,** *134* (46), 18932-18935.
212. Eda, G.; Lin, Y. Y.; Mattevi, C.; Yamaguchi, H.; Chen, H. A.; Chen, I. S.; Chen, C. W.; Chhowalla, M., Blue Photoluminescence from Chemically Derived Graphene Oxide. *Advanced Materials* **2010,** *22* (4), 505.
213. Liu, Z.; Robinson, J. T.; Sun, X. M.; Dai, H. J., PEGylated nanographene oxide for delivery of water-insoluble cancer drugs. *Journal of the American Chemical Society* **2008,** *130* (33), 10876-.
214. Gong, K. P.; Du, F.; Xia, Z. H.; Durstock, M.; Dai, L. M., Nitrogen-Doped Carbon Nanotube Arrays with High Electrocatalytic Activity for Oxygen Reduction. *Science* **2009,** *323* (5915), 760-764.
215. He, T.; Yao, J. N., Photochromic materials based on tungsten oxide. *Journal of Materials Chemistry* **2007,** *17* (43), 4547-4557.
216. He, T.; Yao, J. N., Photochromism of molybdenum oxide. *Journal of Photochemistry and Photobiology C-Photochemistry Reviews* **2003,** *4* (2), 125-143.
217. Mougin, O.; Dubois, J. L.; Mathieu, F.; Roussett, A., Metastable hexagonal vanadium molybdate study. *Journal of Solid State Chemistry* **2000,** *152* (2), 353-360.
218. Komaba, S.; Kumagai, N.; Kumagai, R.; Yashiro, H., Molybdenum oxides synthesized by hydrothermal treatment of A(2)MoO(4) (A=Li, Na, K) and electrochemical lithium intercalation into the oxides. *Solid State Ionics* **2002,** *152*, 319-326.
219. Sian, T. S.; Reddy, G. B., Optical, structural and photoelectron spectroscopic studies on amorphous and crystalline molybdenum oxide thin films. *Solar Energy Materials and Solar Cells* **2004,** *82* (3), 375-386.
220. Ivanova, T.; Szekeres, A.; Gartner, M.; Gogova, D.; Gesheva, K. A., Spectroscopic characterization of CVD-molybdenum oxide films. *Electrochimica Acta* **2001,** *46* (13-14), 2215-2219.

221. Quevedo-Lopez, M. A.; Reidy, R. F.; Orozco-Teran, R. A.; Mendoza-Gonzalez, O.; Ramirez-Bon, R., Enhancement of the photochromic and thermochromic properties of molybdenum oxide thin films by a cadmium sulfide underlayer. *Journal of Materials Science-Materials in Electronics* **2000,** *11* (2), 151-155.
222. Chernova, N. A.; Roppolo, M.; Dillon, A. C.; Whittingham, M. S., Layered vanadium and molybdenum oxides: batteries and electrochromics. *Journal of Materials Chemistry* **2009,** *19* (17), 2526-2552.
223. Hutchins, M. G.; Abu-Alkhair, O.; El-Nahass, M. M.; Abdel-Hady, K., Electrical conduction mechanisms in thermally evaporated tungsten trioxide (WO3) thin films. *Journal of Physics-Condensed Matter* **2006,** *18* (44), 9987-9997.
224. Yoo, S. J.; Jung, Y. H.; Lim, J. W.; Choi, H. G.; Kim, D. K.; Sung, Y. E., Electrochromic properties of one-dimensional tungsten oxide nanobundles. *Solar Energy Materials and Solar Cells* **2008,** *92* (2), 179-183.
225. Monllor-Satoca, D.; Borja, L.; Rodes, A.; Gomez, R.; Salvador, P., Photoelectrochemical behavior of nanostructured WO3 thin-film electrodes: The oxidation of formic acid. *Chemphyschem* **2006,** *7* (12), 2540-2551.
226. Kim, Y. S., Thermal treatment effects on the material and gas-sensing properties of room-temperature tungsten oxide nanorod sensors. *Sensors and Actuators B-Chemical* **2009,** *137* (1), 297-304.
227. Moulzolf, S. C.; Ding, S. A.; Lad, R. J., Stoichiometry and microstructure effects on tungsten oxide chemiresistive films. *Sensors and Actuators B-Chemical* **2001,** *77* (1-2), 375-382.
228. Reyes, L.; Hoel, A.; Saukko, S.; Heszler, P.; Lantto, V.; Granqvist, C. G., Gas sensor response of pure and activated WO3 nanoparticle films made by advanced reactive gas deposition. *Sensors and Actuators B-Chemical* **2006,** *117* (1), 128-134.
229. Gillet, M.; Lemire, C.; Gillet, E.; Aguir, K., The role of surface oxygen vacancies upon WO3 conductivity. *Surface Science* **2003,** *532*, 519-525.
230. Comini, E.; Yubao, L.; Brando, Y.; Sberveglieri, G., Gas sensing properties of MoO3 nanorods to CO and CH3OH. *Chemical Physics Letters* **2005,** *407* (4-6), 368-371.
231. Navone, C.; Baddour-Hadjean, R.; Pereira-Ramos, J. P.; Salot, R., A kinetic study of electrochemical lithium insertion into oriented V2O5 thin films prepared by rf sputtering. *Electrochimica Acta* **2008,** *53* (8), 3329-3336.
232. Ramana, C. V.; Hussain, O. M.; Naidu, B. S.; Reddy, P. J., Spectroscopic characterization of electron-beam evaporated V2O5 thin films. *Thin Solid Films* **1997,** *305* (1-2), 219-226.
233. Barreca, D.; Armelao, L.; Caccavale, F.; Di Noto, V.; Gregori, A.; Rizzi, G. A.; Tondello, E., Highly oriented V2O5 nanocrystalline thin films by plasma-enhanced chemical vapor deposition. *Chemistry of Materials* **2000,** *12* (1), 98-103.
234. Field, M. N.; Parkin, I. P., Atmospheric pressure chemical vapour deposition of vanadium(v) oxide films on glass substrates from reactions of VOCl(3) and VCl(4) with water. *Journal of Materials Chemistry* **2000,** *10* (8), 1863-1866.
235. Sediri, F.; Gharbi, N., From crystalline V2O5 to nanostructured vanadium oxides using aromatic amines as templates. *Journal of Physics and Chemistry of Solids* **2007,** *68* (10), 1821-1829.

236. Shin, D. H.; Bang, C. U.; Hong, Y. C.; Uhm, H. S., Preparation of vanadium pentoxide powders by microwave plasma-torch at atmospheric pressure. *Materials Chemistry and Physics* **2006,** *99* (2-3), 269-275.
237. McGraw, J. M.; Perkins, J. D.; Hasoon, F.; Parilla, P. A.; Warmsingh, C.; Ginley, D. S.; Mateeva, E.; Readey, D. W., Pulsed laser deposition of oriented V2O5-thin films. *Journal of Materials Research* **2000,** *15* (10), 2249-2265.
238. Teghil, R.; D'Alessio, L.; De Bonis, A.; Galasso, A.; Ibris, N.; Salvi, A. M.; Santagata, A.; Villani, P., Nanoparticles and Thin Film Formation in Ultrashort Pulsed Laser Deposition of Vanadium Oxide. *Journal of Physical Chemistry A* **2009,** *113* (52), 14969-14974.
239. Nguyen, T. D.; Do, T. O., Solvo-Hydrothermal Approach for the Shape-Selective Synthesis of Vanadium Oxide Nanocrystals and Their Characterization. *Langmuir* **2009,** *25* (9), 5322-5332.
240. Bhosle, V.; Tiwari, A.; Narayan, J., Epitaxial growth and properties of MoOx($2 < x < 2.75$) films. *Journal of Applied Physics* **2005,** *97* (8).
241. Zhou, J.; Xu, N. S.; Deng, S. Z.; Chen, J.; She, J. C.; Wang, Z. L., Large-area nanowire arrays of molybdenum and molybdenum oxides: synthesis and field emission properties. *Advanced Materials* **2003,** *15* (21), 1835-1840.
242. Navas, I.; Vinodkumar, R.; Lethy, K. J.; Detty, A. P.; Ganesan, V.; Sathe, V.; Pillai, V. P. M., Growth and characterization of molybdenum oxide nanorods by RF magnetron sputtering and subsequent annealing. *Journal of Physics D-Applied Physics* **2009,** *42* (17).
243. Lee, Y. J.; Nichols, W. T.; Kim, D. G.; Do Kim, Y., Chemical vapour transport synthesis and optical characterization of MoO3 thin films. *Journal of Physics D-Applied Physics* **2009,** *42* (11).
244. Sagmeister, M.; Postl, M.; Brossmann, U.; List, E. J. W.; Klug, A.; Letofsky-Papst, I.; Szabo, D. V.; Wurschum, R., Structure and electrical properties of nanoparticulate tungsten oxide prepared by microwave plasma synthesis. *Journal of Physics-Condensed Matter* **2011,** *23* (33).
245. Ashkarran, A. A.; Zad, A. I.; Ahadian, M. M.; Ardakani, S. A. M., Synthesis and photocatalytic activity of WO(3) nanoparticles prepared by the arc discharge method in deionized water. *Nanotechnology* **2008,** *19* (19).
246. Baserga, A.; Russo, V.; Di Fonzo, F.; Bailini, A.; Cattaneo, D.; Casari, C. S.; Bassi, A. L.; Bottani, C. E., Nanostructured tungsten oxide with controlled properties: Synthesis and Raman characterization. *Thin Solid Films* **2007,** *515* (16), 6465-6469.
247. Landstrom, L.; Kokavecz, J.; Lu, J.; Heszler, P., Characterization and modeling of tungsten nanoparticles generated by laser-assisted chemical vapor deposition. *Journal of Applied Physics* **2004,** *95* (8), 4408-4414.
248. Li, S. T.; El-Shall, M. S., Synthesis and characterization of photochromic molybdenum and tungsten oxide nanoparticles. *Nanostructured Materials* **1999,** *12* (1-4), 215-219.
249. Chandrappa, G. T.; Steunou, N.; Cassaignon, S.; Bauvais, C.; Livage, J., Hydrothermal synthesis of vanadium oxide nanotubes from V2O5 gels. *Catalysis Today* **2003,** *78* (1-4), 85-89.
250. Fielicke, A.; Rademann, K., Stability and reactivity patterns of medium-sized vanadium oxide cluster cations VxOy+ ($4 <= x <= 14$). *Physical Chemistry Chemical Physics* **2002,** *4* (12), 2621-2628.

251. Xiong, C. R.; Aliev, A. E.; Gnade, B.; Balkus, K. J., Fabrication of silver vanadium oxide and V2O5 nanowires for electrochromics. *Acs Nano* **2008,** *2* (2), 293-301.
252. Perera, S. D.; Patel, B.; Bonso, J.; Grunewald, M.; Ferraris, J. P.; Balkus, K. J., Vanadium Oxide Nanotube Spherical Clusters Prepared on Carbon Fabrics for Energy Storage Applications. *Acs Applied Materials & Interfaces* **2011,** *3* (11), 4512-4517.
253. de Almeida, L. A. L.; Deep, G. S.; Lima, A. M. N.; Khrebtov, I. A.; Malyarov, V. G.; Neff, H., Modeling and performance of vanadium-oxide transition edge microbolometers. *Applied Physics Letters* **2004,** *85* (16), 3605-3607.
254. Li, Y. B.; Bando, Y.; Golberg, D.; Kurashima, K., Field emission from MoO3 nanobelts. *Applied Physics Letters* **2002,** *81* (26), 5048-5050.
255. Lee, S. H.; Kim, Y. H.; Deshpande, R.; Parilla, P. A.; Whitney, E.; Gillaspie, D. T.; Jones, K. M.; Mahan, A. H.; Zhang, S. B.; Dillon, A. C., Reversible Lithium-Ion Insertion in Molybdenum Oxide Nanoparticles. *Advanced Materials* **2008,** *20* (19), 3627.
256. Bielanski, A.; Najbar, M., V2O5-MoO3 catalysts for benzene oxidation. *Applied Catalysis a-General* **1997,** *157* (1-2), 223-261.
257. Okumu, J.; Koerfer, F.; Salinga, C.; Wuttig, M., In situ measurements of thickness changes and mechanical stress upon gasochromic switching of thin MoOx films. *Journal of Applied Physics* **2004,** *95* (12), 7632-7636.
258. Takeda, H.; Adachi, K., Near infrared absorption of tungsten oxide nanoparticle dispersions. *Journal of the American Ceramic Society* **2007,** *90* (12), 4059-4061.
259. Ganesan, R.; Gedanken, A., Synthesis of WO(3) nanoparticles using a biopolymer as a template for electrocatalytic hydrogen evolution. *Nanotechnology* **2008,** *19* (2).
260. Rout, C. S.; Hegde, M.; Rao, C. N. R., H2S sensors based on tungsten oxide nanostructures. *Sensors and Actuators B-Chemical* **2008,** *128* (2), 488-493.
261. Szilagyi, I. M.; Wang, L. S.; Gouma, P. I.; Balaszsi, C.; Madarasz, J.; Pokol, G., Preparation of hexagonal WO3 from hexagonal ammonium tungsten bronze for sensing NH3. *Materials Research Bulletin* **2009,** *44* (3), 505-508.
262. Cantalini, C.; Wlodarski, W.; Li, Y.; Passacantando, M.; Santucci, S.; Comini, E.; Faglia, G.; Sberveglieri, G., Investigation on the O-3 sensitivity properties of WO3 thin films prepared by sol-gel, thermal evaporation and r.f. sputtering techniques. *Sensors and Actuators B-Chemical* **2000,** *64* (1-3), 182-188.
263. Galatsis, K.; Li, Y. X.; Wlodarski, W.; Kalantar-zadeh, K., Sol-gel prepared MoO3-WO3 thin-films for O-2 gas sensing. *Sensors and Actuators B-Chemical* **2001,** *77* (1-2), 478-483.
264. Chaudhari, G. N.; Bende, A. M.; Bodade, A. B.; Patil, S. S.; Sapkal, V. S., Structural and gas sensing properties of nanocrystalline TiO2 : WO3-based hydrogen sensors. *Sensors and Actuators B-Chemical* **2006,** *115* (1), 297-302.
265. Rahmani, M. B.; Keshmiri, S. H.; Yu, J.; Sadek, A. Z.; Al-Mashat, L.; Moafi, A.; Latham, K.; Li, Y. X.; Wlodarski, W.; Kalantar-zadeh, K., Gas sensing properties of thermally evaporated lamellar MoO3. *Sensors and Actuators B-Chemical* **2010,** *145* (1), 13-19.
266. Pol, V. G.; Pol, S. V.; Calderon-Moreno, J. M.; Gedanken, A., Core-Shell Vanadium Oxide-Carbon Nanoparticles: Synthesis, Characterization, and Luminescence Properties. *Journal of Physical Chemistry C* **2009,** *113* (24), 10500-10504.
267. Zhang, X. L.; Frech, R., Vibrational spectroscopic study of lithium vanadium pentoxides. *Electrochimica Acta* **1997,** *42* (3), 475-482.

268. Miras, H. N.; Richmond, C. J.; Long, D. L.; Cronin, L., Solution-Phase Monitoring of the Structural Evolution of a Molybdenum Blue Nanoring. *Journal of the American Chemical Society* **2012,** *134* (8), 3816-3824.
269. Klinbumrung, A.; Thongtem, T.; Thongtem, S., Characterization of Orthorhombic alpha-MoO3 Microplates Produced by a Microwave Plasma Process. *Journal of Nanomaterials* **2012**.
270. Kalantar-zadeh, K.; Tang, J. S.; Wang, M. S.; Wang, K. L.; Shailos, A.; Galatsis, K.; Kojima, R.; Strong, V.; Lech, A.; Wlodarski, W.; Kaner, R. B., Synthesis of nanometre-thick MoO3 sheets. *Nanoscale* **2010,** *2* (3), 429-433.
271. Li, X. L.; Liu, J. F.; Li, Y. D., Large-scale synthesis of tungsten oxide nanowires with high aspect ratio. *Inorganic Chemistry* **2003,** *42* (3), 921-924.
272. Xiao, Z. D.; Zhang, L. D.; Wang, Z. Y.; Lu, Q. F.; Tian, X. K.; Zeng, H. B., Low-temperature synthesis and structural characterization of single-crystalline tungsten oxide nanorods. *Materials Letters* **2007,** *61* (8-9), 1718-1721.
273. Horsley, J. A.; Wachs, I. E.; Brown, J. M.; Via, G. H.; Hardcastle, F. D., STRUCTURE OF SURFACE TUNGSTEN-OXIDE SPECIES IN THE WO3/AL2O3 SUPPORTED OXIDE SYSTEM FROM X-RAY ABSORPTION NEAR-EDGE SPECTROSCOPY AND RAMAN-SPECTROSCOPY. *Journal of Physical Chemistry* **1987,** *91* (15), 4014-4020.
274. Frey, G. L.; Rothschild, A.; Sloan, J.; Rosentsveig, R.; Popovitz-Biro, R.; Tenne, R., Investigations of nonstoichiometric tungsten oxide nanoparticles. *Journal of Solid State Chemistry* **2001,** *162* (2), 300-314.
275. Ard, S.; Dibble, C. J.; Akin, S. T.; Duncan, M. A., Ligand-Coated Vanadium Oxide Clusters: Capturing Gas-Phase Magic Numbers in Solution. *Journal of Physical Chemistry C* **2011,** *115* (14), 6438-6447.
276. Gharbi, N.; Sanchez, C.; Livage, J.; Lemerle, J.; Nejem, L.; Lefebvre, J., MIXED-VALENCE POLYVANADIC ACID GELS. *Inorganic Chemistry* **1982,** *21* (7), 2758-2765.
277. Song, J.; Ni, X. M.; Zhang, D.; Zheng, H. G., Fabrication and photoluminescence propertips of hexagonal MoO3 rods. *Solid State Sciences* **2006,** *8* (10), 1164-1167.
278. Navas, I.; Vinodkumar, R.; Pillai, V. P. M., Self-assembly and photoluminescence of molybdenum oxide nanoparticles. *Applied Physics a-Materials Science & Processing* **2011,** *103* (2), 373-380.
279. Su, C. Y.; Lin, H. C.; Yang, T. K.; Lin, C. K., Structure and optical properties of tungsten oxide nanomaterials prepared by a modified plasma arc gas condensation technique. *Journal of Nanoparticle Research* **2010,** *12* (5), 1755-1763.
280. Subrahmanyam, A.; Karuppasamy, A., Optical and electrochromic properties of oxygen sputtered tungsten oxide (WO3) thin films. *Solar Energy Materials and Solar Cells* **2007,** *91* (4), 266-274.
281. Jayatissa, A. H.; Cheng, S. T.; Gupta, T., Annealing effect on the formation of nanocrystals in thermally evaporated tungsten oxide thin films. *Materials Science and Engineering B-Solid State Materials for Advanced Technology* **2004,** *109* (1-3), 269-275.
282. Feng, M.; Pan, A. L.; Zhang, H. R.; Li, Z. A.; Liu, F.; Liu, H. W.; Shi, D. X.; Zou, B. S.; Gao, H. J., Strong photoluminescence of nanostructured crystalline tungsten oxide thin films. *Applied Physics Letters* **2005,** *86* (14).

283. Le, H. A.; Chin, S.; Park, E.; Bae, G.; Jurng, J., Chemical Vapor Synthesis and Physico-chemical Properties of V2O5 Nanoparticles. *Chemical Vapor Deposition* **2012,** *18* (1-3), 6-9.
284. Shpak, A. P.; Korduban, A. M.; Medvedskij, M. M.; Kandyba, V. O., XPS studies of active elements surface of gas sensors based on WO3-x nanoparticles. *Journal of Electron Spectroscopy and Related Phenomena* **2007,** *156*, 172-175.
285. Perera, S. D.; Liyanage, A. D.; Nijem, N.; Ferraris, J. P.; Chabal, Y. J.; Balkus Jr, K. J., Vanadium oxide nanowire – Graphene binder free nanocomposite paper electrodes for supercapacitors: A facile green approach. *Journal of Power Sources* **2013,** *230* (0), 130-137.
286. Guo, J.; Li, Y.; Zhu, S.; Chen, Z.; Liu, Q.; Zhang, D.; Moon, W.-J.; Song, D.-M., Synthesis of WO3@Graphene composite for enhanced photocatalytic oxygen evolution from water. *RSC Advances* **2012,** *2* (4), 1356-1363.
287. Sanjaya, Vanadium oxide nanowire e Graphene binder free nanocomposite paper electrodes for supercapacitors: A facile green approach *Power Sources* **2013,** *230* 130-137.
288. Rui, X.; Zhu, J.; Sim, D.; Xu, C.; Zeng, Y.; Hng, H. H.; Lim, T. M.; Yan, Q., Reduced graphene oxide supported highly porous V2O5 spheres as a high-power cathode material for lithium ion batteries. *Nanoscale* **2011,** *3* (11), 4752-4758.
289. Sun, Y.; Hu, X.; Luo, W.; Huang, Y., Self-Assembled Hierarchical MoO2/Graphene Nanoarchitectures and Their Application as a High-Performance Anode Material for Lithium-Ion Batteries. *Acs Nano* **2011,** *5* (9), 7100-7107.
290. Qin, J.; Cao, M.; Li, N.; Hu, C., Graphene-wrapped WO3 nanoparticles with improved performances in electrical conductivity and gas sensing properties. *Journal of Materials Chemistry* **2011,** *21* (43), 17167-17174.
291. An, X.; Yu, J. C.; Wang, Y.; Hu, Y.; Yu, X.; Zhang, G., WO3 nanorods/graphene nanocomposites for high-efficiency visible-light-driven photocatalysis and NO2 gas sensing. *Journal of Materials Chemistry* **2012,** *22* (17), 8525-8531.
292. Nakamoto, K., *Infrared and Raman Spectra of Inorganic and Coordination Compounds*. Wiley: New York: 1986.
293. Botto, I. L.; Vassallo, M. B.; Baran, E. J.; Minelli, G., IR spectra of VO2 and V2O3. *Materials Chemistry and Physics* **1997,** *50* (3), 267-270.
294. Seguin, L.; Figlarz, M.; Cavagnat, R.; Lassègues, J. C., Infrared and Raman spectra of MoO3 molybdenum trioxides and MoO3 · xH2O molybdenum trioxide hydrates. *Spectrochimica Acta Part A: Molecular and Biomolecular Spectroscopy* **1995,** *51* (8), 1323-1344.
295. Kortshagen, U., Nonthermal plasma synthesis of semiconductor nanocrystals. *Journal of Physics D-Applied Physics* **2009,** *42* (11).
296. Belomoin, G.; Therrien, J.; Smith, A.; Rao, S.; Twesten, R.; Chaieb, S.; Nayfeh, M. H.; Wagner, L.; Mitas, L., Observation of a magic discrete family of ultrabright Si nanoparticles. *Applied Physics Letters* **2002,** *80* (5), 841-843.
297. Rogozhina, E.; Belomoin, G.; Smith, A.; Abuhassan, L.; Barry, N.; Akcakir, O.; Braun, P. V.; Nayfeh, M. H., Si-N linkage in ultrabright, ultrasmall Si nanoparticles. *Applied Physics Letters* **2001,** *78* (23), 3711-3713.

298. Warner, J. H.; Hoshino, A.; Yamamoto, K.; Tilley, R. D., Water-soluble photoluminescent silicon quantum dots. *Angewandte Chemie-International Edition* **2005,** *44* (29), 4550-4554.
299. Zou, J.; Kauzlarich, S. M., Functionalization of silicon nanoparticles via silanization: Alkyl, halide and ester. *Journal of Cluster Science* **2008,** *19* (2), 341-355.
300. Sublemontier, O.; Lacour, F.; Leconte, Y.; Herlin-Boime, N.; Reynaud, C., CO2 laser-driven pyrolysis synthesis of silicon nanocrystals and applications. *Journal of Alloys and Compounds* **2009,** *483* (1-2), 499-502.
301. Wang, L.; Reipa, V.; Blasic, J., Silicon nanoparticles as a luminescent label to DNA. *Bioconjugate Chemistry* **2004,** *15* (2), 409-412.
302. Atkins, T. M.; Thibert, A.; Larsen, D. S.; Dey, S.; Browning, N. D.; Kauzlarich, S. M., Femtosecond Ligand/Core Dynamics of Microwave-Assisted Synthesized Silicon Quantum Dots in Aqueous Solution. *Journal of the American Chemical Society* **2011,** *133* (51), 20664-20667.
303. Sajti, C. L.; Petersen, S.; Menendez-Manjon, A.; Barcikowski, S., In-situ bioconjugation in stationary media and in liquid flow by femtosecond laser ablation. *Applied Physics a-Materials Science & Processing* **2010,** *101* (2), 259-264.
304. Sato, S.; Swihart, M. T., Propionic-acid-terminated silicon nanoparticles: Synthesis and optical characterization. *Chemistry of Materials* **2006,** *18* (17), 4083-4088.
305. Rosso-Vasic, M.; Spruijt, E.; Popovic, Z.; Overgaag, K.; van Lagen, B.; Grandidier, B.; Vanmaekelbergh, D.; Dominguez-Gutierrez, D.; De Cola, L.; Zuilhof, H., Amine-terminated silicon nanoparticles: synthesis, optical properties and their use in bioimaging. *Journal of Materials Chemistry* **2009,** *19* (33), 5926-5933.
306. Intartaglia, R.; Barchanski, A.; Bagga, K.; Genovese, A.; Das, G.; Wagener, P.; Di Fabrizio, E.; Diaspro, A.; Brandi, F.; Barcikowski, S., Bioconjugated silicon quantum dots from one-step green synthesis. *Nanoscale* **2012,** *4* (4), 1271-1274.
307. Granqvist, C. G.; Buhrman, R. A., Ultrafine metal particles. *Journal of Applied Physics* **1976,** *47* (5), 2200-2219.
308. Li, S. T.; El-Shall, M. S., Synthesis of nanoparticles by reactive laser vaporization: silicon nanocrystals in polymers and properties of gallium and tungsten oxides. *Applied Surface Science* **1998,** *127*, 330-338.
309. Wang, C. J.; Tsai, M. Y.; Chi, C. C.; Perng, T. P., Surface effects on the photoluminescence of Si quantum dots. *Journal of Nanoparticle Research* **2009,** *11* (3), 569-574.
310. Zaitseva, N.; Hamel, S.; Dai, Z. R.; Saw, C.; Williamson, A.; Galli, G., Effect of nitrogen on the stability of silicon nanocrystals produced by decomposition of alkyl silanes. *Journal of Physical Chemistry C* **2008,** *112* (10), 3585-3590.
311. Schwartz, M. P.; Hamers, R. J., Reaction of acetonitrile with the silicon(001) surface: A combined XPS and FTIR study. *Surface Science* **2007,** *601* (4), 945-953.
312. Tilley, R. D.; Warner, J. H.; Yamamoto, K.; Matsui, I.; Fujimori, H., Micro-emulsion synthesis of monodisperse surface stabilized silicon nanocrystals. *Chemical Communications* **2005,** (14), 1833-1835.
313. Ahire, J. H.; Wang, Q.; Coxon, P. R.; Malhotra, G.; Brydson, R.; Chen, R. J.; Chao, Y. M., Highly Luminescent and Nontoxic Amine-Capped Nanoparticles from Porous Silicon: Synthesis and Their Use in Biomedical Imaging. *Acs Applied Materials & Interfaces* **2012,** *4* (6), 3285-3292.

314. Okada, T.; Iwaki, T.; Yamamoto, K.; Kasahara, H.; Abe, K., Raman-Scattering From Gas-Evaporated Silicon Small Particles. *Solid State Communications* **1984,** *49* (8), 809-812.
315. Tsu, R.; Shen, H.; Dutta, M., CORRELATION OF RAMAN AND PHOTOLUMINESCENCE SPECTRA OF POROUS SILICON. *Applied Physics Letters* **1992,** *60* (1), 112-114.
316. Zhu, S.; Zhu, C.; Ma, J.; Meng, Q.; Guo, Z.; Yu, Z.; Lu, T.; Li, Y.; Zhang, D.; Lau, W. M., Controlled fabrication of Si nanoparticles on graphene sheets for Li-ion batteries. *RSC Advances* **2013,** *3* (17), 6141-6146.
317. Wilcoxon, J. P.; Samara, G. A.; Provencio, P. N., Optical and electronic properties of Si nanoclusters synthesized in inverse micelles. *Physical Review B* **1999,** *60* (4), 2704-2714.
318. Lockwood, R.; McFarlane, S.; Rodríguez Núñez, J. R.; Wang, X. Y.; Veinot, J. G. C.; Meldrum, A., Photoactivation of silicon quantum dots. *Journal of Luminescence* **2011,** *131* (7), 1530-1535.